PETROLOGIC AND MICROSTRUCTURAL CONSTRAINTS ON FOCUSED MELT TRANSPORT IN DUNITES AND THE RHEOLOGY OF THE SHALLOW MANTLE

by

MICHAEL GEOFFREY BRAUN
(Sc.B. Brown University, 1996)

submitted in partial fulfillment of the requirements for the degree of

DOCTOR OF PHILOSOPHY

at the

MASSACHUSETTS INSTITUTE OF TECHNOLOGY

and the

WOODS HOLE OCEANOGRAPHIC INSTITUTION

June 2004

Signature of Author _____
Joint Program in Oceanography/Applied Ocean Science and Engineering
Massachusetts Institute of Technology
and Woods Hole Oceanographic Institution
June 2004

Certified by _____
Dr. Peter B. Kelemen
Thesis Supervisor

Certified by _____
Dr. Greg Hirth
Thesis Supervisor

Accepted by _____
Dr. Greg Hirth
Chair, Joint Committee for Marine Geology and Geophysics
Woods Hole Oceanographic Institution

PETROLOGIC AND MICROSTRUCTURAL CONSTRAINTS ON FOCUSED MELT TRANSPORT IN DUNITES AND THE RHEOLOGY OF THE SHALLOW MANTLE

by

Michael Geoffrey Braun

Submitted in partial fulfillment of the requirements for the degree of Doctor of Philosophy at he Massachusetts Institute of Technology and the Woods Hole Oceanographic Institution

Abstract of Thesis

Observations at mid-ocean ridges indicate that magmas are focused to the ridge axis by a network of porous dunites in near chemical isolation. This thesis investigates several of the outstanding questions regarding the mechanisms of melt transport and its effects on the shallow mantle. Chapter 1 details the current understanding of melt migration from observations at mid-ocean ridges and ophiolites. Chapter 2 uses the size distribution and abundance of dunites measured in the Oman ophiolite to place limits on the potential mechanisms by which dunites form and subsequently estimate the flux of chemically unequilibrated melt which a network of dunites can supply. Chapter 3 characterizes the chemical composition of dunites and harzburgites from Oman to further constrain the process by which dunites form and relates the observed trends within dunites to variations in the time-integrated melt/rock ratio. Chapter 4 examines the microstructures of peridotites in Oman to constrain the deformation mechanisms which determine the viscosity of shallow mantle. Chapter 5 is a numerical investigation of advection beneath ridges incorporating the rheology inferred from the observed microstructures. Chapter 6 integrates the conclusions of the previous chapters, reevaluating the potential melt flux through dunites and constraining the permeability of the shallow mantle.

Thesis Advisors:

Dr. Peter B. Kelemen, WHOI

Dr. Greg Hirth, WHOI

Thesis Committee:

Dr. Glenn Gaetani, WHOI (Chair)

Dr. Nobumichi Shimizu, WHOI

Dr. John Whitehead, WHOI

Prof. Maria T. Zuber, MIT

Acknowledgments:

It would be impossible to adequately thank all the people who helped me to this point, but I feel I must try. It is with the most sincere sentiments that I thank my advisors Peter Kelemen and Greg Hirth, from whom I have learned to explore the Earth as a proper geologist, using a big hammer and a few more delicate tools. Through them, I have been given several 'once-in-a-lifetime' opportunities to see parts of the world I never would have dreamed of reaching. And it was on those trips that Peter and Greg encouraged me (physically, as well as intellectually) to reach many summits. Now that I think about it, nearly all my experiences with them can be related to one mountain or another: from the dark abyss of the Atlantic Ocean, where a chance observation at the top of a submerged mountain spawned several other cruises; to the East Cascades, where I learned that creative solutions to geologic problems are also fun and should always be encouraged (just bring good raingear and watch your step); to the moraines of Cape Cod, where I could teach them a thing or two. Of course the most memorable mountains are in the rugged interior of Oman, where I learned that I could climb mountains, a lot could be learned from the view at the top, and it's really important to follow the right goat. From the first day of my first ascent (of about six that week) into the Ingalls, Peter and Greg treated me as a colleague and taught me the value of interdisciplinary collaboration, and helicopters. In addition to being such capable mentors, they are also good friends; a quality which I realized very early on could actually make grad school pleasant.

I would also like to thank my committee for their continual encouragement and support and their patience with my ever-expanding array of projects. I would like to thank Jack Whitehead for his infectious enthusiasm in the lab and insistence on being able to explain why these things we study are important. From Nobu Shimizu I gained insight into analytical geochemistry as well as sound council. I would like to thank Maria Zuber for her perpetual efforts to maintain some organization and for fueling my excitement about space exploration which initially drove me into Earth science. And I would like to thank Glenn Gaetani who, although officially joining my committee just weeks prior to my defense, was a perpetual source of information, both petrologic and otherwise, throughout my years in grad school.

I also benefited greatly from the scientific interactions and amazing geotourism (often accompanied by climbing up more rocks), with Rob Reves-Sohn and Henry Dick. So many great things have come from attending the geodynamics seminar. Thank you to all the technical staff who make doing science at WHOI possible. In particular, Karen Hanghøj, who, in addition to making everything possible in the lab, has been a great friend and confidant; Graham Layne for his boundless of information and patience with me and the 1270, before its unfortunate demise; Louie Kerr for all his assistance despite our incursions on the SEM.

I would also like to express my deep appreciation for the people of the Sultanate of Oman, in particular Hilal al Azri, who provided me with access to their beautiful country. Every new person I met offered me genuinely warm hospitality; a complete stranger treated as an old friend. For this I am hopeful that peace will soon return to their home and their neighbors.

After seven and a half years of employment and schooling at WHOI and MIT, I have made many friends, without whom I would not have as many of the scars or entertaining pictures as I do. I would like extend a particular thanks to my officemate Jeff Standish for all the late-night and mid-day conversations, my former housemates Tom Marchitto and Lou St Laurent who made me think grad school would be fun and worth the pay cut and extra hours, and Mark Behn for initially perpetuating this notion then joining me in cynical denial. My time here was also enriched by Cara Santelli, Joe Warren, Sheri White, Ann Pearson, Greg Slater, Bridget Bergquist, Carrie Tuit, Christie Haupert, Margaret Boettcher, Mea Cook, Brian de Martin, Jessica Warren, Amy Draut, Dana and Will Gerlach, Liz Kujawinski, Steve Jayne, Kirsten Laarkamp, Stefan Hussnoeder, Kevin Frye, Joerg Renner, Frederik Simons, Jennifer Georgen, everyone who played G&G softball and after-school rugby. Special thanks to John Brown, my compatriot in mountain biking who, while never asking me hard science questions, always managed to find the most unpleasant hill to climb on the way back to the car.

I also need to thank my parents, Barbara and Alan Braun, who from the very beginning nurtured my interests in science and provided me with every opportunity to pursue my interests and advance my education.

Without a doubt, the most wonderful person I have ever met and the one with whom I have shared the most, is my wife Ana. We met while riding the JP bus between MIT and WHOI our first year, and she has been my best friend and constant companion ever since. She is endowed with a boundless zeal for life and continually challenges me to reach ever higher. Without her I would never have reached any of the pinnacles that I can now look back upon proudly.

Funding for my research was provided by The National Science Foundation through a Graduate Research Fellowship 2277600 and grants OCE-0118572, OCE-9819666, EAR-0230267, EAR-9405845, OCE-9521113. Additional support was generously provided by the Woods Hole Oceanographic Institution through the Office of Academic Programs and the Deep Ocean Exploration Institute.

TABLE OF CONTENTS

TABLE OF FIGURES

CHAPTER 2 – DUNITE DISTRIBUTION IN THE OMAN OPHIOLITE: IMPLICATIONS FOR MELT FLUX THROUGH POROUS DUNITE CONDUITS

CHAPTER 3 – DUNITES AS CONDUITS FOR PRIMITIVE MELT TRANSPORT: IMPLICATIONS OF THE GEOCHEMISTRY OF OMAN PERIDOTITES

TABLE OF TABLES

Chapter 1

INTRODUCTION

Our understanding of the dynamics of the upper mantle and the chemical evolution of the earth have been strongly influenced by the study of mid-ocean ridge basalts. Extraction of mid-ocean ridge basalts from the mantle has been a classical problem in igneous petrology and, more recently, magma dynamics. Some aspects of this problem are reasonably well understood. A mantle lherzolite source undergoes polybaric decompression melting, beginning at pressures greater than 2 GPa, with an average fraction of melting between ~5 and 10% and a maximum melt fraction (in the shallowest residues) of 15 to 20%. Melting and melt extraction processes produce an aggregate melt with the composition of olivine tholeiite. Because this overall picture is relatively simple, it is currently tractable to characterize the physical processes of melting, melt extraction, and transport from source to surface.

Much of what is known about the process of melt extraction from the mantle beneath oceanic spreading centers is inferred solely from the compositions of the lavas erupted at the surface. However, these lavas have undergone an uncertain amount of crystal fractionation, mixing, and/or assimilation on their way to the surface, which can obscure much of the melt extraction process. In contrast, ophiolitic peridotite exposures offer an unparalleled opportunity to examine the melt pathway itself. This work characterizes the structure and composition of mantle dunites in the Oman ophiolite in order to determine the process by which polybaric partial melts of the mantle are transported from their source, without equilibrating with the shallower mantle, and what influence this process has on the strength of the mantle.

The tectonic setting of the Oman ophiolite is debated [*Pearce et al.*, 1981] and some aspects of the lava composition – at least in the northern part of the ophiolite – are different from "normal" mid-ocean ridge basalt (MORB). However, a continuous layer of sheeted dikes underlying pillow lavas throughout most of the ophiolite indicates that the igneous crust formed at an oceanic spreading center. Furthermore, the composition of the lavas in the southern ophiolite massifs is very similar to MORB [*Pallister and Hopson*, 1981; *Pallister and Knight*, 1981], so that it is likely that the processes that formed the crust were analogous to those beneath mid-ocean ridges. The spreading rate during formation of the igneous crust in Oman is not known, but is estimated to be greater than ~50 mm/yr because

the ophiolite crust has a nearly continuous gabbroic layer [*Nicolas and Boudier*, 1995; *Nicolas et al.*, 2000], whereas mid-ocean ridges with spreading rates less than ~50 mm/yr have extensive exposures of peridotite on the seafloor, especially near fracture zones [*Cannat et al.*, 1996; *Dick*, 1989]. In addition, there is no evidence for significant crystal plastic deformation of gabbroic rocks [*Nicolas and Ildefonse*, 1996] such as observed in samples from the Mid-Atlantic Ridge [*Cannat et al.*, 1997].

Recent geophysical data indicate that the melting region beneath mid-ocean ridges is much larger than the seismically-determined zone of crustal accretion at the ridge axis. Seismic data from the MELT experiment (17°S along the East Pacific Rise) indicate that melt is present for several hundred kilometers off-axis [*Toomey et al.*, 1998; *Webb and Forsyth*, 1998] and to depths of 120-150 km [*Forsyth et al.*, 1998]. Similarly, modeling studies suggest that the deep melting region is on the order of 200 km wide at the depth where the mantle crosses the solidus, even where buoyancy driven flow focuses mantle upwelling at shallower levels [e.g. *Braun et al.*, 2000]. However, shallow seismic refraction data indicate the igneous oceanic crust attains its complete thickness within only 5-10 km of the ridge axis [*Dunn et al.*, 2000; *Vera et al.*, 1990]. Melt must therefore be efficiently extracted from a broad melting region and transported to the ridge axis to be accreted within a narrow zone.

The most important petrologic constraint on melt extraction is that MORB is not in chemical equilibrium with residual shallow-mantle harzburgite. Primitive MORBs are undersaturated in orthopyroxene (opx) with respect to the equilibrium cotectic melt composition at pressures commensurate with the base of the oceanic crust (1-2 kbar). These liquids were last saturated in opx at pressures in excess of 8-10 kbar [*Elthon*, 1989; *Elthon and Scarfe*, 1980; *O'Hara*, 1965; *Stolper*, 1980]. Spinel compositions from dunites exhibit high Cr/(Cr+Al) and high TiO_2 [*Augé*, 1987; *Kelemen et al.*, 1995; *Pallister and Knight*, 1981] similar to those found in MORB [*Dick and Bullen*, 1984] and distinct from residual harzburgites [*Allan and Dick*, 1996; *Arai and Matsukage*, 1996; *Dick and Bullen*, 1984; *Dick and Natland*, 1996; *Kelemen et al.*, 1997]. MORBs also preserve higher light/heavy rare-earth element ratios than predicted by equilibrium with residual peridotites dredged from mid-ocean ridges ("abyssal peridotites", [e.g. *Johnson et al.*, 1990]) and sampled in ophiolites [e.g. *Kelemen et al.*, 1995]. Thus, major and minor element data indicate that melts migrate through at least the shallowest 25-30 km the mantle with limited chemical interaction.

Some MORBs record melting and rapid extraction from even greater depths. Lu/Hf and Sm/Nd isotopic systematics [*Salters and Hart*, 1989] and $^{230}Th/^{238}U$ excesses [*Beattie*, 1993; *McKenzie*, 1985; *Sims et al.*, 2002] indicate the generation of small melt fractions in the presence of garnet, which is only stable in the mantle at depths greater than ~70 km [*Hirschmann and Stolper*, 1996; *Koga et al.*, 1998]. Therefore melt must be rapidly isolated from its source and delivered to the surface without equilibrating with the majority of rock through which it passes.

Although MORB is not in equilibrium with residual harzburgites, both the major and trace element concentrations from clinopyroxenes in mantle dunites from Oman are in equilibrium with the lavas that formed the overlying crust [*Kelemen et al.*, 1995], which are similar to MORB. Dunites as observed in the mantle section of the Oman ophiolite—one of the largest, best exposed sections of oceanic crust and mantle —are generally tabular bodies with sharp, replacive contacts and orientations at small angles to the foliation in the surrounding harzburgite and the crust-mantle transition zone (paleo-Moho) [e.g. *Boudier and Coleman*, 1981; *Lippard et al.*, 1986]. If the harzburgite foliation developed during deformation associated with 'corner-flow' beneath a spreading ridge, then the dunites must have formed prior to this deformation while still in the upwelling mantle beneath the ridge. These observations indicate that chemically isolated transport of melt to the surface occurred within high porosity dunite channels in the upwelling region.

Replacive dunites have been hypothesized to form by two processes: (1) as reaction zones around migrating melt-filled hydrofractures [*Nicolas*, 1986; *Nicolas*, 1990; *Suhr*, 1999] and (2) as high porosity conduits formed by a reactive infiltration instability [*Aharonov et al.*, 1995; *Kelemen*, 1990; *Kelemen and Dick*, 1995; *Spiegelman et al.*, 2001]. As melt migrates upward in the mantle, it becomes progressively undersaturated in pyroxene. In (1), silica-undersaturated melt within a hydrofracture forms dunite along the margins as the melt reacts with the wall rock. In (2), there is no crack, and high porosity dunite channels form as a result of a dissolution instability. Reaction between the melt and harzburgite dissolves pyroxene and precipitates olivine while increasing the liquid mass [*Daines and Kohlstedt*, 1994; *Kelemen*, 1990]. Kinetic studies show that these reactions can occur rapidly [*Brearley and Scarfe*, 1986; *Kuo and Kirkpatrick*, 1985a; *Kuo and Kirkpatrick*, 1985b; *Zhang et al.*, 1989]. The increased porosity increases the local permeability, which in turn increases the melt flux to the area. The increased flux draws in more undersaturated melt, resulting in further dissolution. Numerical models of this positive feedback, or 'reactive infiltration instability', indicate that a self-organized network

of high porosity dunite conduits can form within the melting region [*Aharonov et al.*, 1995; *Spiegelman et al.*, 2001].

My thesis consists of five chapters which explore the structural and petrologic evidence for chemically-isolated melt transport focused in porous dunite conduits, as well as the effects of dunite formation and melt migration on the rheology of the upper mantle. In the first chapter, measurements of the size, abundance, spatial distribution of dunites in the Oman ophiolite are extrapolated to assess the feasibility of various proposed mechanisms of dunite formation, and the ability of a porous dunite network to supply a flux of silica-undersaturated melt that is sufficient to form the oceanic crust. Dunite abundance exhibits a power-law dependence on dunite width as measured over four orders of magnitude. Dunites wider than 5-10 m, which are required to maintain chemical isolation of the migrating melts, cannot be formed by diffusive reaction around melt-filled hydrofractures. The merging of multiple reaction zones can generate wide dunites, but not in sufficient abundance to match the observed size/frequency data. Instead, dunites may be formed by reactive porous flow. As such, the unique size/frequency relationship which characterizes the distribution of dunites can be extrapolated to estimate melt flux through an interconnected network dunites in the melting region beneath mid-ocean ridges. If flux is conserved where dunites merge, the size/frequency relationship implies that melt fraction within the dunite varies non-linearly with dunite width. By incorporating this porosity variation, estimates of the total unequilibrated melt flux through a network of interconnected dunites match the observed mid-ocean ridge magma fluxes with porosities consistent with geophysical observations.

The second chapter relates the chemical variations observed in the Oman peridotites to the effects of dunite formation and progressive melt-rock interaction. The chemical trends observed in olivine and spinel in the Oman peridotites are similar to those observed in abyssal peridotites, suggesting the igneous processes which formed the Oman mantle are similar to those that occur beneath modern mid-ocean ridges. Additionally, the composition of dunites varies systematically with dunite width, with the widest dunites in equilibrium with the liquid parental to the Oman lavas. The sharp chemical gradients at lithologic contacts and the lack of significant variation within individual dunites is inconsistent with formation by diffusive reaction around melt-filled hydrofractures. In contrast, mass balance calculations incorporating orthopyroxene dissolution and olivine precipitation predict the differences between harzburgites and dunites. These models also indicate that the systematic changes in dunite composition with increasing width are the result of increased

melt-rock ratios, as high as 100 in the widest dunites. However, mixing between primitive and more depleted melts may also influence dunite composition, especially in narrow dunites which may have formed at shallower depths. This study is the first attempt to develop a geochemical proxy which quantifies the melt-rock ratio, or the amount of melt focusing, in dunites.

In the third chapter, microstructural analyses are used to quantify the differences in the rheology of harzburgite and dunites induced by dunite formation and focused melt migration. In the same suite of rocks as used in the geochemical study, the texture, grain size, and lattice preferred orientation are observed to vary systematically with dunite width. Harzburgites are typically fine-grained and exhibit a strong {0kl}[100] lattice preferred orientation and relatively small grain size. In contrast, dunites show a systematic transition in microstructure and grain size from the fine-grained {0kl}[100] harzburgite texture in the smallest dunites to a coarse-grained, (010)[100] lattice preferred orientation in the widest dunites. Comparison of these microstructures with recent laboratory experiments suggests that the harzburgites and small dunites were deforming by dislocation-accommodated grain boundary sliding, whereas the wide dunites were deforming predominantly by dislocation creep. The transition in deformation mechanism is most likely induced by grain growth driven by melt-rock reaction and enhanced grain boundary mobility associated with an increase in melt flux through the wider dunites. These microstructural observations imply that the bulk of the shallow mantle may have a viscosity as much as an order of magnitude lower than that predicted by dislocation creep.

The fourth chapter examines the effects of rheology on mantle flow and melt generation beneath mid-ocean ridges by incorporating the transition in deformation mechanism observed in the microstructural study, as well as experimental constraints on the effects of water and melt on the viscosity of peridotite, into hybrid finite-element/finite-difference numerical models. The increase in viscosity associated with dehydration significantly inhibits buoyant mantle flow in the dry melting region. However, buoyancy-driven flow is predicted in the damp melting region if the rheology in this depth interval is controlled by grain boundary sliding after the onset of melting. The models indicate that the magnitude of the effects of buoyant flow in the damp melting region become increasingly prominent at slower spreading ridges and provide a self-consistent explanation for a number of geophysical observations, including constant crustal thickness independent of spreading rate, short-wavelength mantle Bouguer anomalies at slow spreading ridges, as well as the

discrepancy between surface and body wave estimates of the magnitude of anisotropy observed along the East Pacific Rise.

The final chapter combines the dunite abundance data observed in outcrops with the microstructural observations from thin sections to re-assess the permeability of an interconnected network of dunites with the added constraint of satisfying the velocity requirements imposed by uranium-series disequilibria. The increase in grain size with dunite width increases permeability, allowing melt velocities in excess of 1 m/yr in the dunites that carry ~99% of the total melt flux. The high permeabilities imply that wide dunites are the primary conduits for the transport of primitive MORB, consistent with the geochemical data in the previous chapter.

In summary, large-scale field observations combined with detailed petrologic and microstructural analyses of peridotites from the Oman ophiolite indicate that dunites nucleate and widen by reactive porous flow of silica-undersaturated melts through depleted harzburgite and that wide dunites are the primary conduits for the transport of the primitive melts which form the oceanic crust. Dunite formation and focused melt transport increase the olivine grain size, thereby increasing the permeability within dunite conduits. Consistent with the observed textures, the increased melt flux through wider dunites can be quantified by comparison of observed geochemical variations with mass balance models. Variations in the major and minor elements of olivine and spinel serve as a proxy for variations in the melt-rock ratio within dunites. Assuming dunites form an interconnected network, the melt flux through wide dunites with moderate porosities is sufficient to form the oceanic crust and can occur on timescales short enough to satisfy the radiogenic isotopic constraints. The changes in grain size caused by this sustained melt transport also induce a transition in the deformation mechanism, from dislocation-accommodated grain boundary sliding in the harzburgite and small dunites to dislocation creep in wide dunites. The decrease in viscosity associated with the transition to grain boundary sliding can promote buoyancy–driven flow in the deep melting region despite the effects of dehydration during melting, and explain a variety of geophysical observations.

References:

Aharonov, E., J.A. Whitehead, P.B. Kelemen, and M. Spiegelman, Channeling instability of upwelling melt in the mantle, *J. Geophys. Res.*, *100*, 20,433-20,450, 1995.

Allan, J.F., and H.J.B. Dick, Cr-rich spinel as a tracer for melt migration and melt-wall rock interaction in the mantle: Hess Deep, Leg 147, in *Proc. ODP Sci. Results*, edited by C. Mével, K.M. Gillis, J.F. Allan, and P.S. Meyer, pp. 157-172, Ocean Drilling Program, College Station, TX, 1996.

Arai, S., and K. Matsukage, Petrology of gabbro-troctolite-peridotite complex from Hess Deep, Equatorial Pacific; implications for mantle-melt interaction within the oceanic lithosphere, *Proc. ODP, Sci. Res.*, *147*, 1996.

Augé, T., Chromite deposits in the northern Oman ophiolite: Mineralogical constraints, *Mineral. Deposita*, *22*, 1-10, 1987.

Beattie, P., Uranium-thorium disequilibria and partitioning on melting of garnet peridotite, *Nature*, *363*, 63-65, 1993.

Boudier, F., and R.G. Coleman, Cross section through the peridotite in the Samail ophiolite, southeastern Oman mountains, *J. Geophys. Res.*, *86*, 2573-2592, 1981.

Braun, M.G., G. Hirth, and E.M. Parmentier, The effects of deep damp melting on mantle flow and melt generation beneath mid-ocean ridges, *Earth Planet. Sci. Lett.*, *176*, 339-356, 2000.

Brearley, M., and C.M. Scarfe, Dissolution rates of upper mantle minerals in an alkali basalt melt at high presssure: An experimental study and implications for ultramafic xenolith survival, *J. Petrol.*, *27*, 1157-1182, 1986.

Cannat, M., G. Ceuleneer, and J. Fletcher, Localization of ductile strain and the magmatic evolution of gabbroic rocks drilled at the mid-atlantic ridge (23°N), in *Proc. ODP, Sci. Results*, edited by J.A. Karson, M. Cannat, D.J. Miller, and D. Elthon, pp. 77-98, 1997.

Cannat, M., Y. Lagabrielle, N. de Coutures, H. Bougault, J. Casey, L. Dmitriev, and Y. Fouquet, Ultramafic and gabbroic exposures at the Mid-Atlantic Ridge: Geological mapping in the 15°N region, *submitted to Tectonophysics February 1996*, 1-24, 1996.

Daines, M.J., and D.L. Kohlstedt, Transition from porous to channelized flow due to melt/rock reaction during melt migration, *Geophys. Res. Lett.*, *21*, 145-148, 1994.

Dick, H.J.B., Abyssal peridotites, very slow spreading ridges, and ocean ridge magmatism, in *Magmatism in the ocean basins*, edited by A.D. Saunders, and M.J. Norry, pp. 71-105, Geological Society of America, 1989.

Dick, H.J.B., and T. Bullen, Chromian spinel as a petrogenetic indicator in abyssal and alpine-type peridotites and spatially associated lavas, *Contrib. Mineral. Petrol.*, *86*, 54-76, 1984.

Dick, H.J.B., and J.H. Natland, Late-stage melt evolution and transport in the shallow mantle beneath the East Pacific Rise, in *Proc. ODP, Sci. Results*, edited by C. Mevel, K.M. Gillis, J.F. Allan, and P.S. Meyer, pp. 103-134, ODP, 1996.

Dunn, R.A., D.R. Toomey, and S.C. Solomon, Three dimensional seismic structure and physical properties of the crust and shallow mantle beneath the East Pacific Rise at 9°30' N, *J. Geophys. Res.*, *105*, 23,537-23,555, 2000.

Elthon, D., Pressure of origin of primary mid-ocean ridge basalts, in *Magmatism in the Ocean Basins*, edited by A.D. Saunders, and M.J. Norry, pp. 125-136, Geological Society, 1989.

Elthon, D., and C.M. Scarfe, High-pressure phase equilibria of a high-magnesia basalt: Implications for the origin of mid-ocean ridge basalts, *Carnegie Inst. Wa. Yrbk.*, 277-281, 1980.

Forsyth, D.W., S.C. Webb, L.M. Dorman, and Y. Shen, Phase velocity of rayleigh wave in the MELT experiment of the east pacific rise, *Science*, *280*, 1235-1238, 1998.

Hirschmann, M.M., and E.M. Stolper, A possible role for garner pyroxenite in the origin of the "garnet signature" in MORB, *Contrib. Mineral. Petrol.*, *124*, 185-208, 1996.

Johnson, K.T.M., H.J.B. Dick, and N. Shimizu, Melting in the oceanic upper mantle: an ion microprobe study of diopsides in abyssal peridotites, *J. Geophys. Res.*, *95*, 2661-2678, 1990.

Kelemen, P.B., Reaction between ultramafic rock and fractionating basaltic magma. I. Phase relations, the origin of calc-alkaline magma series, and the formation of discordant dunite, *J. Petrol.*, *31*, 51-98, 1990.

Kelemen, P.B., and H.J.B. Dick, Focused melt flow and localized deformation in the upper mantle: Juxtaposition of replacive dunite and ductile shear zones in the Josephine peridotite, SW Oregon, *J. Geophys. Res.*, *100*, 423-438, 1995.

Kelemen, P.B., G. Hirth, N. Shimizu, M. Spiegelman, and H.J.B. Dick, A review of melt migration processes in the adiabatically upwelling mantle beneath spreading ridges, *Phil. Trans. Roy. Soc., Lond. A*, *355*, 283-318, 1997.

Kelemen, P.B., N. Shimizu, and V.J.M. Salters, Extraction of mid-ocean ridge basalt from the upwelling mantle by focused flow of melt in dunite channels, *Nature*, *375*, 747-753, 1995.

Koga, K.T., N. Shimizu, and T.L. Grove, Disequilibrium trace element redistribution during garnet to spinel facies transformation, in *Proc. 7th Int. Kimberlite Conf.*, edited by J.L. Gurney, M.D. Pascoe, and S.H. Richardson, pp. 444-451, 1998.

Kuo, L.-C., and R.J. Kirkpatrick, Dissolution of mafic minerals and its implications for the ascent velocities of peridotite-bearing basaltic magmas, *J. Geol.*, *93*, 691-700, 1985a.

Kuo, L.-C., and R.J. Kirkpatrick, Kinetics of crystal dissolution in the system diopside-forsterite-silica, *Am. J. Sci.*, *285*, 51-90, 1985b.

Lippard, S.J., A.W. Shelton, and I.G. Gass, *The ophiolite of northern Oman*, 178 pp., Blackwell, Oxford, 1986.

McKenzie, D., 230Th-238U disequilibrium and the melting processes beneath ridges axes, *Earth Planet. Sci. Lett.*, *72*, 149-157, 1985.

Nicolas, A., A melt extraction model based on structural studies in mantle peridotites, *J. Petrol.*, *27*, 999-1022, 1986.

Nicolas, A., Melt extraction from mantle peridotites: Hydrofracturing and porous flow, with consequences for oceanic ridge activity, in *Magma Transport and Storage*, edited by M.P. Ryan, pp. 159-174, J. Wiley & Sons, New York, 1990.

Nicolas, A., and F. Boudier, Mapping oceanic ridge segments in Oman ophiolite, *J. Geophys. Res. 100*, 6179-6197, 1995.

Nicolas, A., F. Boudier, B. Ildefonse, and E. Ball, Accretion of Oman and United Arab Emirates ophiolite - Discussion of a new structural map, *Marine Geophys. Res.*, *21*, 147-179, 2000.

Nicolas, A., and B. Ildefonse, Flow mechanism and viscosity in basaltic magma chambers, *Geophys. Res. Lett.*, *16*, 2013-2016, 1996.

O'Hara, M.J., Primary magmas and the origin of basalts, *Scot. J. Geol.*, *1*, 19-40, 1965.

Pallister, J.S., and C.A. Hopson, Samail ophiolite plutonic suite: field relations, phase variation, cryptic variation and layering, and a model of a spreading ridge magma chamber, *J. Geophys. Res*, *86*, 2593-2644, 1981.

Pallister, J.S., and R.J. Knight, Rare-earth element geochemistry of the Samail ophiolite near Ibra, Oman, *J. Geophys. Res.*, *86*, 2673-2697, 1981.

Pearce, J., A., T. Alabaster, A. Shelton, W., and M. Searle, P., The Oman ophiolite as a Cretaceous arc-basin complex: Evidence and implications, *Phil. Trans. R. Soc. Lond. A*, *300*, 299-317, 1981.

Salters, V.J.M., and S.R. Hart, The hafnium paradox and the role of garnet in the source of mid-ocean-ridge basalts, *Nature*, *342*, 420-422, 1989.

Sims, K.W.W., S.J. Goldstein, J. Blichert-Toft, M.R. Perfit, P. Kelemen, D.J. Fornari, P.J. Michael, M.T. Murrell, S.R. Hart, D.J. DePaolo, G.D. Layne, L. Ball, M. Jull, and J.F. Bender, Chemical and isotopic constraints on the generation and transport of magma beneath the East Pacific Rise, *Geochim. Cosmochim. Acta*, *66* (19), 3481-3504, 2002.

Spiegelman, M., P.B. Kelemen, and E. Aharonov, Causes and consequences of flow organization during melt transport: The reaction infiltration instability, *J. Geophys. Res.*, *106*, 2061-2078, 2001.

Stolper, E., A phase diagram for mid-ocean ridge basalts: preliminary results and implications for petrogenesis, *Contrib. Mineral. Petrol.*, *74*, 13-27, 1980.

Suhr, G., Melt migration under oceanic ridges: Inferences from reactive transport modeling of upper mantle hosted dunites, *J. Petrol.*, *40*, 575-599, 1999.

Toomey, D.R., W.S.D. Wilcock, S.C. Solomon, W.C. Hammond, and J.A. Orcutt, Mantle Seismic strcutre beneath the MELT region of the east pacific ridge from P and S wave tomography, *Science*, *280*, 1224-1227, 1998.

Vera, E.E., J.C. Mutter, P. Buhl, A.A. Orcutt, A.J. Harding, M.E. Kappus, R.S. Detrick, and T.M. Brocher, The structure of 0- to .2-My-old crust at 9 N on the East Pacific Rise from expanded spread profiles, *J. Geophys. Res.*, *95*, 15529-15556, 1990.

Webb, S.C., and D.W. Forsyth, Structure of the upper mantle under the EPR from waveform inversion of regional events, *Science*, *280*, 1227-1229, 1998.

Zhang, Y., D. Walker, and C.E. Lesher, Diffusive crystal dissolution, *Contrib. Mineral. Petrol.*, *102*, 492-513, 1989.

Chapter 2

DUNITE DISTRIBUTION IN THE OMAN OPHIOLITE: IMPLICATIONS FOR MELT FLUX THROUGH POROUS DUNITE CONDUITS

Reprinted from Geochemistry, Geophysics, Geosystems, Vol. 3, No. 11, M.G. Braun and P.B. Kelemen, "Dunite Distribution in the Oman Ophiolite: Implications for Melt Flux Through Porous Dunite Conduits", doi: 10.1029/2001GC000289, with permission from the American Geophysical Union

Abstract

Dunites in the mantle section of the Oman ophiolite represent conduits for chemically isolated melt transport through the shallow mantle beneath oceanic spreading centers. These dunite melt conduits exhibit a scale-invariant power-law relationship between width and cumulative abundance, as measured over four orders of magnitude. We use this size/frequency distribution to assess several hypotheses for dunite formation and estimate the total melt flux that a dunite network can accommodate beneath an oceanic spreading center. Dunites, measured from one-dimensional lithologic sections and digital image mosaics at a variety of length scales, range in width from ~3mm to ~100 m and follow a power-law with a slope of ~1.1. Extrapolation of the power-law predicts that dunites as wide as 3.5 km may exist in the melting region beneath a mid-ocean ridge. Alternatively, perhaps the widest dunites we observe (~100 m) represent a maximum size.

Modeling of dunites as diffusive reaction zones around melt-filled hydrofractures cannot explain the existence of dunites wider than ~10 m in Oman. Instead, dunites may represent high porosity conduits formed by reactive porous flow. Using the observed size/frequency relationship, the assumption that dunites form a coalescing network, and the requirement that flux is conserved where dunites merge, we estimate the total flux through a porous dunite network and the fraction of that flux that remains chemically isolated. Our flux model predicts that the porosity in a dunite scales with the width. For maximum porosities of ~1-4% in the widest dunites, a network of porous dunite conduits with the abundances observed in Oman can supply a sufficient flux of melt (of which > 95% remains chemically unequilibrated with shallow residual peridotites) to satisfy the observed mid-ocean ridge flux.

Introduction

Geophysical and geochemical observations suggest that melt transport beneath oceanic spreading centers is strongly focused toward the ridge axis and rapidly extracted from the shallow mantle predominantly via chemically-isolating dunite conduits. In this study we examine the abundance and size distribution of dunite conduits preserved in the Oman Ophiolite to assess proposed mechanisms of dunite formation and place constraints on the melt flux that the dunite network can accommodate.

Recent geophysical data indicate that the melting region beneath mid-ocean ridges is much larger than the seismically-determined zone of crustal accretion at the ridge axis. Seismic data from the MELT experiment (17°S along the East Pacific Rise) indicate that melt is present for several hundred kilometers off-axis and to depths of 120-150 km [*Forsyth et al.*, 1998]. However, seismic velocity data indicate the igneous oceanic crust attains its complete thickness within 5 km of the ridge axis [*Dunn et al.*, 2000; *Vera et al.*, 1990]. Geochemical studies show that lateral melt migration from a broad region of corner flow is required to reproduce the trace element characteristics of MORB [*Spiegelman*, 1996]. Therefore melts must be efficiently extracted from a broad melting region and transported to the ridge axis to be accreted within the narrow ridge axis. Although our understanding of the exact path of melt migration through the upper mantle is incomplete, several geochemical and morphological constraints can be placed on the nature of the melt transport system.

Since mid-ocean ridge basalt (MORB) is not in chemical equilibrium with residual harzburgite in the shallow mantle, melt extraction must occur in chemically-isolated conduits. Primitive MORBs are undersaturated in orthopyroxene (opx) with respect to the equilibrium cotectic melt composition at pressures commensurate with the base of the oceanic crust (1-2 kbar). Figure 1 shows the major element composition of ~10,000 glasses from the global MORB database (blue dots), using the isomolar projections of Elthon [1983]. Liquids close to equilibrium with mantle olivine (i.e. molar Mg# (Mg/(Mg+Fe)) > 0.66, shown as red triangles) were last saturated in opx at pressures in excess of 8-10 kbar, in agreement with experimental data [e.g., *Elthon*, 1989;

Elthon and Scarfe, 1980; *O'Hara*, 1965; *Stolper*, 1980]. The high dissolution rate of opx in undersaturated basalts [*Brearley and Scarfe*, 1986; *Kuo and Kirkpatrick*, 1985a; *Kuo and Kirkpatrick*, 1985b] suggests that these melts must be isolated from the surrounding harzburgite during migration to preserve disequilibrium. MORBs also preserve higher light/heavy rare-earth element ratios than predicted for equilibrium with residual peridotites dredged from mid-ocean ridges ('abyssal peridotites', [e.g., *Johnson et al.*, 1990] and sampled in ophiolites [e.g., *Kelemen et al.*, 1995a]. In addition, numerical models of melt migration suggest that the concentrations of trace elements in MORB can also be used to distinguish two-dimensional melt transport from strictly vertical ascent [*Spiegelman*, 1996] when sufficient data becomes available. Thus, major and minor element data indicate that melts migrate through, at a minimum, the shallowest 25-30 km of the mantle with limited chemical interaction.

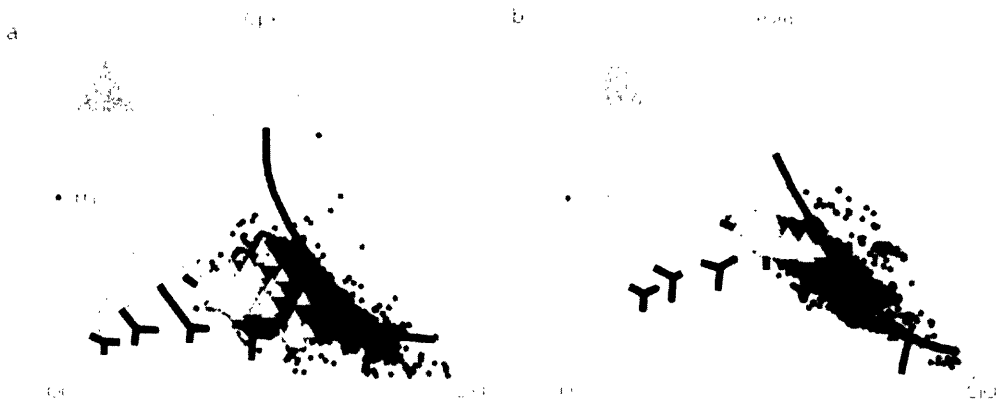

Figure 1. Pressures of equilibration of ~10,000 MORB glasses (circles) as inferred from pseudo-ternary phase diagrams projected from a) plagioclase and b) clinopyroxene [after *Elthon*, 1983]. Primitive MORB liquids (triangles), defined by Mg# (Mg/Mg+Fe) in excess of 0.66, were last saturated in orthopyroxene at pressures greater than 10 kb, suggesting these liquids passed through the upper 25-30 km of the mantle without reacting with the surrounding harzburgite. Glass compositions for this global compilation are from the RIDGE PetDB database (http://petdb.ldeo.columbia.edu). The positions of the cotectic lines at all pressures (1 bar - 25kb) are taken from Elthon [1983].

Some MORBs record melting and rapid extraction from even greater depths. Lu/Hf and Sm/Nd isotopic systematics [*Salters and Hart*, 1989] and $^{230}Th/^{238}U$ excesses [*Beattie*, 1993; *Lundstrom et al.*, 1995; *McKenzie*, 1985] suggest the generation of small

melt fractions in the presence of garnet, which is only stable in mantle peridotite at depths greater than ~70 km [*Hirschmann and Stolper*, 1996; *Koga et al.*, 1998]. To preserve the observed excesses of the shortest lived isotopes (i.e., ^{230}Th), melt must be rapidly isolated from the depths where fractionation occurs and delivered to the surface without achieving secular equilibrium or reacting with the majority of the rock through which it passes (see Kelemen et al. [1997] for a more complete discussion of melt velocity constraints).

Mantle dunites (>90% olivine) may be the chemically isolated conduits for melt transport. Although residual harzburgites are not in equilibrium with MORB, both the major and trace element concentrations from clinopyroxenes (cpx) in dunites in the mantle section of the Oman ophiolite are in equilibrium with the lavas (very similar to MORB) that formed the overlying crust [*Kelemen et al.*, 1995a]. In addition, spinel compositions from dunites exhibit high Cr/(Cr+Al) and high TiO_2 [*Augé*, 1987; *Kelemen et al.*, 1995a; *Pallister and Knight*, 1981] similar to those found in MORB [*Dick and Bullen*, 1984] and distinct from residual harzburgites [*Allan and Dick*, 1996; *Arai and Matsukage*, 1996; *Dick and Bullen*, 1984; *Dick and Natland*, 1996; *Kelemen et al.*, 1997]. Dunites as observed in the mantle section of the Oman ophiolite—one of the largest, best exposed sections of oceanic crust and mantle —are generally tabular bodies with sharp contacts and orientations subparallel to the foliation in the surrounding harzburgite and the crust-mantle transition zone (paleo-Moho) (e.g., [*Boudier and Coleman*, 1981; *Lippard et al.*, 1986]). Contact relationships between dunite and harzburgite (summarized by, e.g. Kelemen et al. [1995a], figure 2) indicate that dunites replaced the surrounding peridotite, via reactions which dissolved pyroxene (and precipitated a similar yet smaller mass of olivine). If the harzburgite foliation developed as the result of deformation associated with 'corner-flow' beneath a spreading ridge, then the dunites must have formed in the upwelling mantle beneath the ridge. Thus dunites accommodated chemically isolated transport of melt through the shallow mantle to the base of the crust.

The extent to which dunites are the *sole* conduits for melt transport is debatable. However, replacive dunites are abundant in the shallow mantle and certainly represent

regions of highly concentrated melt flux. As a result, the dunites embody a large part of the time-integrated history of melt migration beneath the spreading center. This study characterizes the abundance and distribution of dunites in the mantle section of the Oman ophiolite to assess (1) viable mechanisms for dunite formation and (2) the ability of a network of dunites to accommodate the observed melt flux to mid-ocean ridges.

Observations and Results

1. General Field Relations

The Oman ophiolite consists of ~13 large massifs which comprise a nearly continuous band of oceanic lithosphere more than 500 km long and 50-100 km wide. In this study we examine the distribution of replacive dunites exposed in the mantle sections of the Samail and Muscat massifs. Although there are a variety of interpretations of the structural data, detailed mapping efforts in the Samail massif and the adjacent Wadi Tayin massif indicate relatively little internal deformation since the initiation of obduction [e.g., *Jousselin et al.*, 1998; *Nicolas et al.*, 2000], and the peridotites represent residual mantle which passed beneath an oceanic spreading center.

The mantle section of the Wadi Tayin massif preserves a stratigraphic thickness of up to 9-12 km, composed almost entirely of residual harzburgite and dunite [e.g., *Boudier and Coleman*, 1981]. The peridotite is overlain by a 5-7 km thick gabbroic crustal section [e.g., *Pallister and Hopson*, 1981] with a nearly continuous layer of sheeted dikes underlying pillow lavas with compositions very similar to MORB [e.g., *Pallister and Hopson*, 1981; *Pallister and Knight*, 1981]. It is inferred that these observations are applicable to the Samail and Muscat massifs as well, though the crustal section in parts of the Samail massif may have been thinner (~4km) [*Nicolas et al.*, 1996].

Although the spreading rate during the formation of the Oman crust is unknown, the presence of the continuous igneous crustal layer [e.g., *Nicolas and Boudier*, 1995; *Nicolas et al.*, 2000] suggests a half-spreading rate greater than ~0.05 m/yr. Mid-ocean ridges with spreading rates less than ~0.05 m/yr exhibit extensive exposures of peridotite

on the seafloor, especially near fracture zones [e.g., *Cannat*, 1996; *Dick*, 1989]. In addition, there is little evidence for crystal plastic deformation in Oman gabbros [*Nicolas and Ildefonse*, 1996], whereas plastically deformed gabbros are commonly observed along the Mid-Atlantic Ridge [*Cannat et al.*, 1997]. We infer that the Oman ophiolite represents the igneous crust and residual peridotite generated at an intermediate- to fast-spreading oceanic spreading center.

The majority of dunites in the mantle section of the ophiolite occur as tabular veins, intersecting each other at small angles, with sharp contacts against the surrounding harzburgite. In this study we have chosen exposures which are planar over the length scale of the image and orthogonal to the intersection lineation formed by the planar dunites. Outcrops oriented orthogonal to the ones imaged show no intersections. The widths of dunites range from less than 1 cm to nearly 100 m, and lengths range from less than a meter to several kilometers. To avoid confusion with the large, partially cumulate, dunites formed at the base of the crust, we consider only dunites which are overlain by harzburgite. In some cases, our chosen map areas lie more than 1 km below the crust-mantle transition zone, though this is not possible to verify for outcrops in the Muscat massif.

2. Photomosaics and Image processing

We have measured dunite widths over 4 orders of magnitude (10^{-2} to 10^{2} m). Data was collected using one of several methods depending on scale: one-dimensional measured sections, outcrop mosaics for small dunites, hillside/mountainside photomosaics for intermediate scales, and airphoto analysis and chain and compass surveying for the largest dunites.

For the highest resolution, one-dimensional sections were collected in Wadi Lufti (Samail) along a chain line perpendicular to the strike of the predominant dunite orientation/peridotite foliation (335°/65°SW). Seven sample lines ranged in length from 7 to 66 m, for a composite section of 208 m, with every contact along the sample line measured to millimeter precision. (Figure 2a)

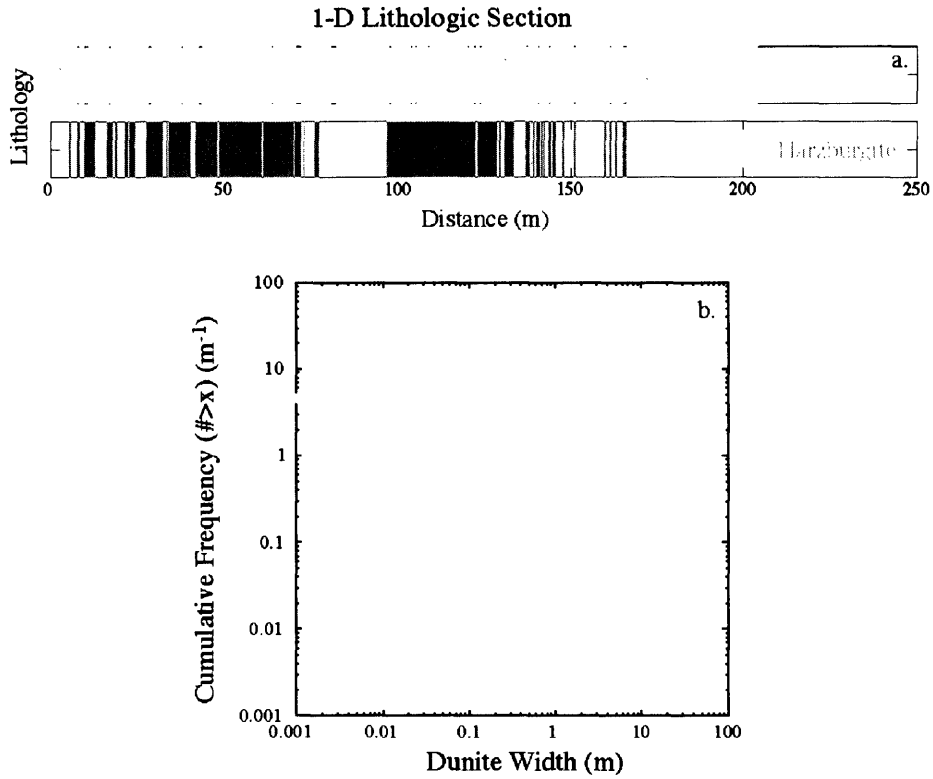

Figure 2. (a) Composite one-dimensional lithologic section of mantle peridotite (containing ~920 individual dunites) from 7 outcrops in Wadi Lufti, Oman. Dunite widths range from ~3 mm to 35 m. (b) Dunite size and abundance as measured along the composite section shows a robust power-law relationship between dunite width and frequency that extends over more than four orders of magnitude. Cumulative frequency is defined here as the number of dunites greater than a given width, *w*.

Dunite distributions over larger length scales are derived from two-dimensional image mosaics. Photomosaics of individual outcrops (figure 3a & b) were constructed from images of 0.5 m by 0.5 m areas along a grid superimposed on the outcrop. Lithologic contacts in each image were then retraced and reassembled into the mosaic using Adobe® Photoshop®. This is an improvement upon the method used by Kelemen et al. [2000], exploiting greater overlap, better camera positioning, and less image distortion. The prepared outcrops ranged in size from 3x3.5m to 16x5m, with a final precision of ~3 mm (determined by the width of the marker and the grain-size of the

rock). Where possible, one-dimensional sections traversed previously analyzed two-dimensional outcrops.

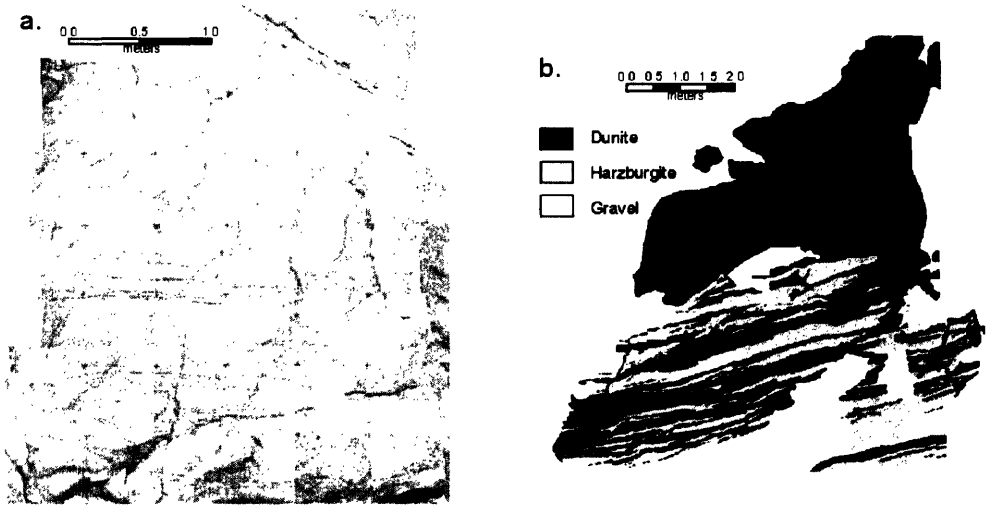

Figure 3. Outcrop mosaics from Wadi Lufti, Oman. The mosaics for (a) Outcrop #10 and (b) Outcrop #18 are composed of approximately 40 and 170 individual photographs, respectively, taken ~1.5 m above the outcrop surface. Contact information is determined at the outcrop and subsequently digitized from the scaled mosaic.

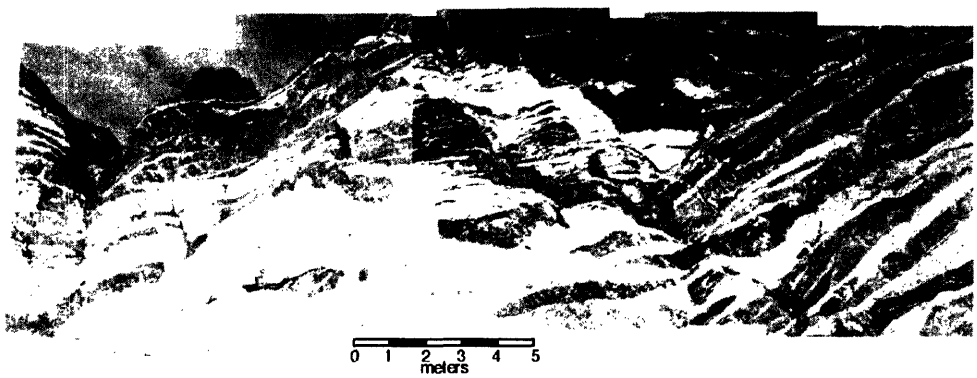

Figure 4. Photomosaic of dunites behind a mosque in Mutrah, part of the Muscat massif. Dunite locations were determined by image analysis and are seen here as the lighter regions in the image. Dunite orientations are measured in the field and used to correct the widths measured from each image.

At length scales larger than individual outcrops (figures 4 & 5), images were gathered and processed in a slightly different manner. For each location, a series of scaled photographs, taken from a fixed point at a known distance from the hillside were digitized and mosaicked, again using Adobe® Photoshop®. The mosaics were printed to

large sheets, over which the facies contacts were hand traced, then redigitized. This same process was used for airphoto analysis (figure 6) to fill in gaps in the ground survey. All mosaics are converted into scaled bitmap (binary) images containing just dunite (or harzburgite) objects for image processing.

3. Statistical Analysis

To evaluate the proposed mechanisms of dunite formation and to estimate the total potential flux through dunites, the abundance and distribution of dunites in the melt network must be determined. Kelemen et al, [2000] show that the abundance of dunites exhibits a power-law dependence on dunite width in the Ingalls ophiolite. In addition, Kelemen et al. extrapolate this dunite size/frequency relationship to predict the abundance of large dunites in the Wadi Tayin massif in Oman.

For the Oman ophiolite, the data from the composite 1-D section in Wadi Lufti show that a robust power-law relationship between dunite width and frequency does exist over at least four orders of magnitude in width (figure 2b). We collected additional dunite width data from images over a wide range of scales using an 'intercept width' technique, similar to that used by Kelemen et al [2000]. Dunite widths are measured along parallel lines perpendicular to the dominant dunite strike for each image mosaic. All widths are then corrected for apparent thickness based on field measurements of the true dunite orientation and camera position. In addition, several large dunites were measured using standard chain and compass techniques to further constrain the mosaics. The same width analysis is carried out for the harzburgite images, and therefore the percentage of dunite at each location can be determined by combining the dunite and harzburgite images. To account for the higher number of observations in larger areas, all frequency data are normalized by the total intercept length used in each image. Using cumulative frequency per meter allows for direct comparison of size/frequency data collected at different scales over different sized areas. (Using frequency per meter also allows for extrapolation to larger length scales, as will be discussed below.)

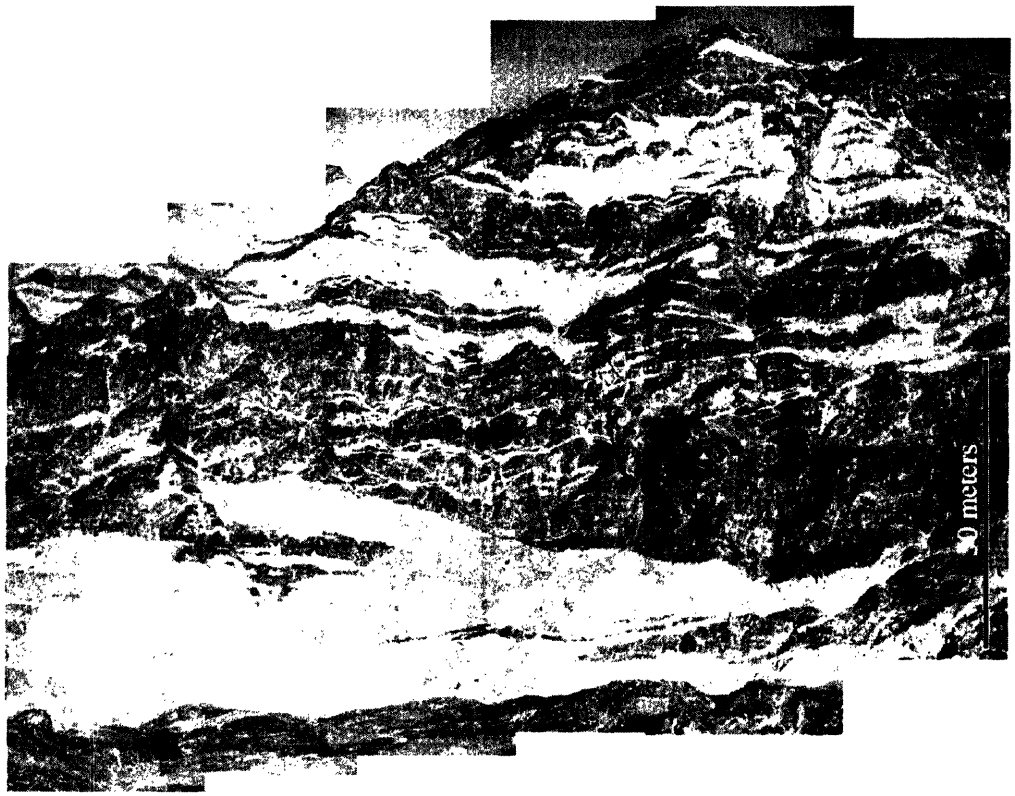

Figure 5. Photomosaic of a mountainside in the Muscat Massif. As at all scales, dunite orientations measured across the image area are used to correct dunite widths as measured from the image mosaic. The lighter rocks are dunite, the darker are harzburgites. The two geologists in the center of the image are standing ~ 50 m apart.

For each data set, a cumulative distribution function and probability density function can be established from histograms of the width data. The cumulative distribution function (CDF) is defined as the number of objects per meter greater than a given width, w. For a power-law, the CDF has the form

$$(1) \qquad F_w = \frac{a}{w^D}.$$

where D is the power-law exponent and a is related to the proportion of dunite in the image. The probability density function (PDF) is an estimate of the number of dunites of a given width per meter. The PDF is the derivative of the CDF and for the power-law above has the form

$$(2) \qquad f_w = -\frac{dF}{dw} = \frac{aD}{w^{D+1}}.$$

Ideally, the PDF could be determined directly from the width/frequency histogram. However, the values of both D and a are sensitive to the bin sizes used in creating the histogram. Therefore, we exploit the mathematical relationship between the distribution functions to calculate the PDF from the more robustly determined CDF.

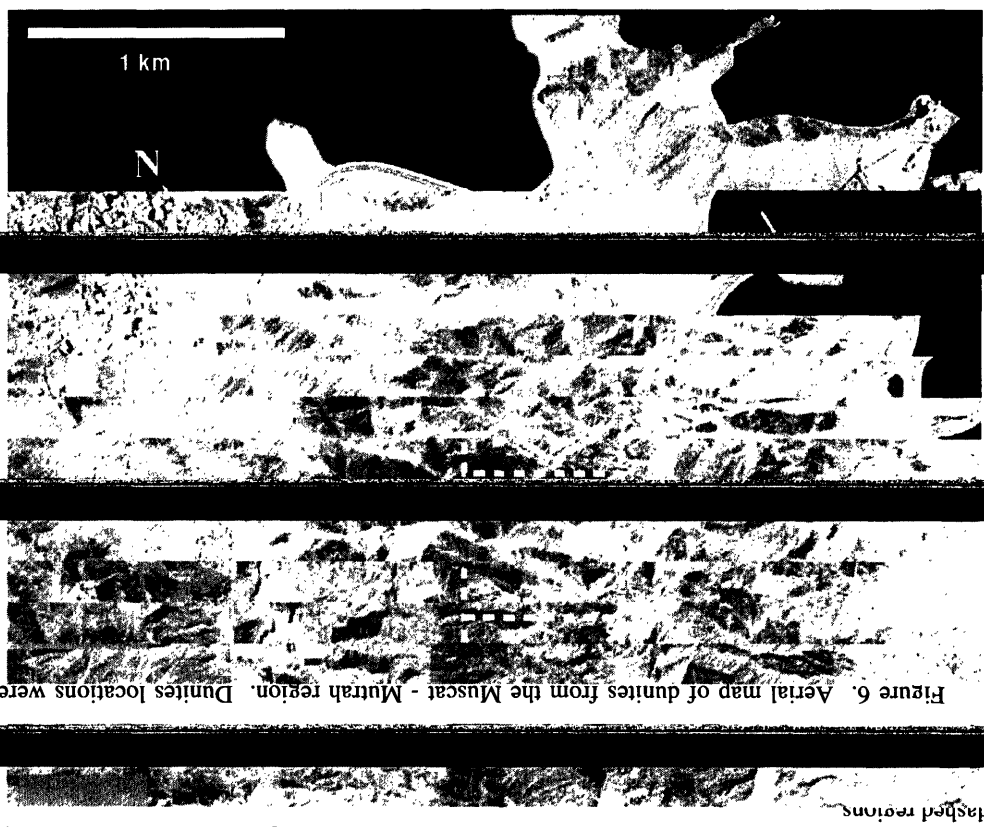

Figure 6. Aerial map of dunites from the Muscat - Mutrah region. Dunites locations were determined by both airphoto analysis and surface observations. Dunites are shown here as highlighted regions superimposed on the airphoto. The locations of figures 4 and 5 are shown by dashed regions.

If the true distribution of dunite widths is indeed scale-invariant over some range of widths, then the abundances of sampled dunites should fall along a common line. (Figure 7) However, any sampling of the true population is subject to truncation and censorship errors. Even samples derived from ideal power-law distributions will exhibit deviations from perfect power-law behavior. Truncation errors occur at the smallest scales since dunite width is limited by the resolution of the image. At the larger scales,

object width is limited by the size of the area of interest. In addition, censorship can systematically diminish the sampling frequency. At the grain scale (0.5 - 3cm) it is very difficult to distinguish the matrix of olivine around pyroxenes in the harzburgite from a discrete dunite vein. Even though all widths are subject to this precision limit, small scale features are most affected, since the error is a larger fraction of the true width. At the largest scale, the widths of dunites with one boundary outside the field of view are also underestimated. This type of censoring can occur for any object, but is more likely for larger objects, and more important for rare observations. For a combination of these reasons, the number of the largest and smallest dunites are underestimated. Several corrections have been developed to account for these errors in cumulative frequency plots (e.g. [*Barton and Zoback*, 1992; *Laslett*, 1982]). However, the effects of the corrections are minimal if the relationship is measured from the central linear portion of the distribution [*Pickering et al.*, 1995], which comprises the majority of the data. We define the central portion of the distribution as data which lie within the 80th percentile of absolute range from the median.

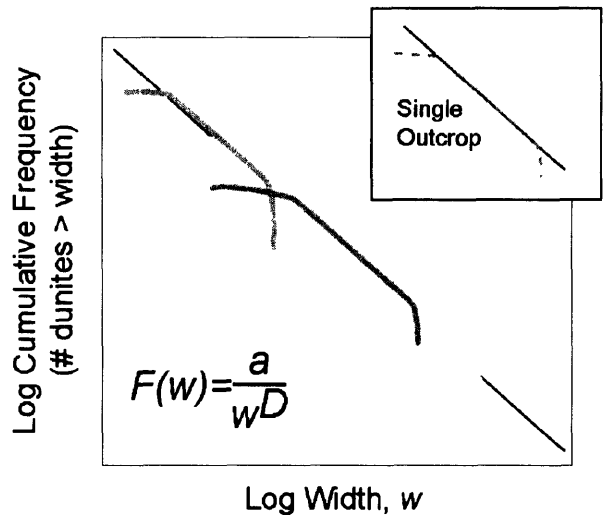

Figure 7. Idealized scale-invariant power-law distribution. This illustration demonstrates the how several data sets over a range of overlapping length scales can be used to determine the true power-law distribution of the dunite population. Individual outcrops exhibit a characteristic relationship between log width and log frequency (inset). If the distribution of dunite widths is scale-invariant, then every outcrop will lie along a common line.

Values of D and a are obtained from the culled CDF data using a linear regression with data weighted by the studentized residuals to eliminate outliers with high leverage. We initially fit the linearized system, $\log F = \log a - D \log w$, using a least squares method. Outliers are culled based on the value of their studentized residuals, and the retained data are refit. In all cases, the retained data (figure 8 – open circles) represent approximately 80% of the total data set. For a more complete description, see Weisburg [1985, p109-117]. Values of the fitted parameters for individual locations, as well as their average (D=1.11, a=0.088), are shown in table 1. For a given dunite size, there exists 10^D, or ~13 times as many dunites of that size compared to the number of dunites that are an order of magnitude narrower. The CDFs for the data collected in Oman fall on a common distribution line spanning approximately four orders of magnitude. (Figure 8 – gray band) Because the areas mapped in detail have variable percentages of dunite (18-68%), individual data sets may fall above or below the average line, reflected in the value for a. For this reason we use the mean values of D and a for extrapolation to larger length scales.

Table 1:	Figure	D	a	R^2	% dunite
Lufti 1D composite	2	0.78	0.098	0.99	65.7
Lufti o/c #10	3a	1.38	0.014	0.83	68.2
Lufti o/c #18	3b	0.78	0.075	0.98	49.9
Mosque	4	1.07	0.079	0.98	45.5
Mountainside	5	1.00	0.061	0.96	44.3
Muscat Airphoto	6	1.64	0.198	0.98	17.7
Parameter Mean		1.11	0.088		

Table 1. Fit parameters derived from each dunite image presented in this study, including the least-squares correlation coefficient, R^2. For each image, the corresponding figure number and percentage of dunite in the image are also listed. The details of the parameter fitting are described in the text.

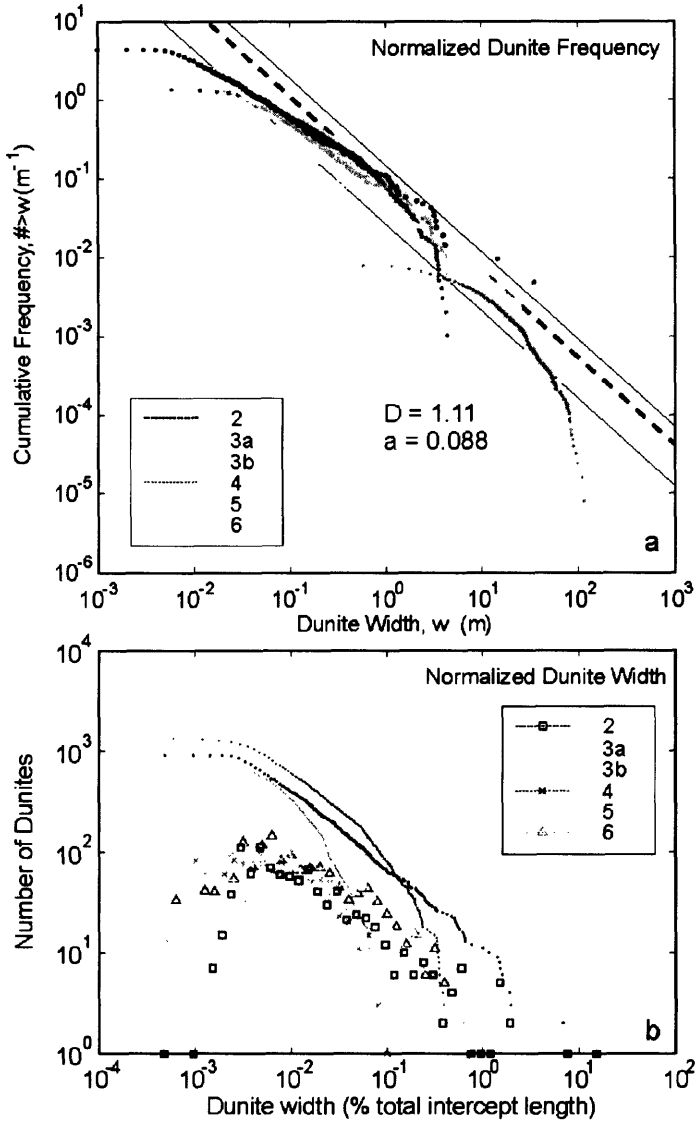

Figure 8. Width distribution data from dunites in the mantle section of the Oman ophiolite. These data (dots) are collected from lithologic sections and photomosaics with length scales spanning more than 4 orders of magnitude. (a) To reduce the effects of truncation and censorship errors, only data within 80% of the range from the median value (circled) are used in the fits. The mean of the fits to the individual data sets is shown by the gray band (dashed line ± 1s in a to account for differences in dunite density between images). (b) Width-normalized dunite size/frequency statistics. Although difficult for extrapolation to larger length scales, normalization of dunite width the total intercept length collapses the data sets onto each other. In addition to the CDF data, the binned PDF data are shown with discrete symbols corresponding to each image.

Discussion

Dunite melt conduits as observed in the shallow mantle section of the Oman ophiolite range in size from less than 1 cm to nearly 100 meters. In addition, the abundance of these dunites exhibits a power-law dependence on width as measured over four orders of magnitude. In the following section, we use the size/frequency distribution of dunites as measured in Oman to assess the proposed mechanisms for the formation of replacive dunites and subsequently estimate the total unequilibrated melt flux a dunite network can accommodate beneath oceanic spreading centers.

1. Extrapolation to the melting region

By extrapolating the power-law size frequency distribution measured in this study, we can estimate the size and abundance of dunite melt conduits over larger length scales (i.e. the melting region beneath mid-ocean ridges). The CDF data are normalized per unit of observation length to enable comparison of data from regions of different size. This normalization also allows for easy extrapolation, simply by multiplying the distribution function by the desired length scale, L. Therefore, the number of dunites wider than w predicted in L meters of observation perpendicular to the general strike of the tabular dunites is defined as

$$F_w = \frac{a}{w^D} L. \quad (3)$$

Extrapolation in this manner adequately predicts the abundance of the largest dunites observed in individual massifs in Oman (L=10 km) as reported by Kelemen et al [2000]. (Figure 9) Estimating dunite abundance over length scales commensurate with the melting region beneath mid-ocean ridges requires one order of magnitude of additional extrapolation (L=100 km). This approach suggests that there may be at least one dunite as wide as ~3.5 km in the melting region beneath an oceanic spreading center (figure 9). A dunite of this width, even with a 3-5% steady state melt fraction, is as yet undetectable by seafloor broadband seismic networks [*Hung et al.*, 2000], so unfortunately, this hypothesis cannot be tested. Alternatively, there could be a smaller

maximum size limit. The widest dunites observed in the Oman mantle section (~100 m) could be the largest present beneath mid-ocean ridges.

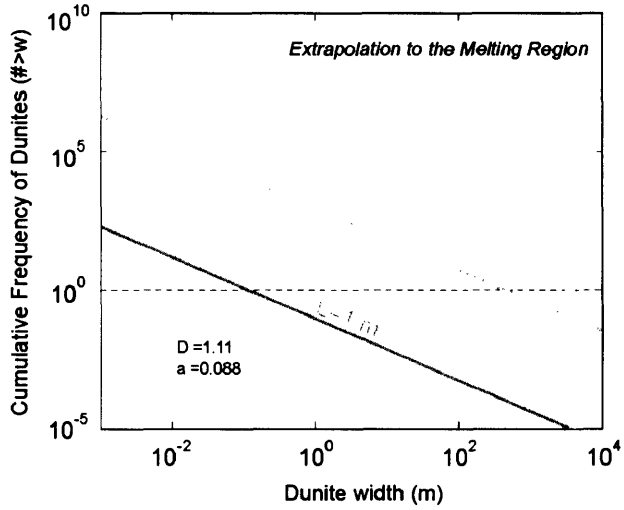

Figure 9. Extrapolation for dunite abundance to larger length scales using the power-law size/frequency distribution determined from the dunite width data from Oman. For length scales on order of individual massifs in Oman, (10 km) the extrapolation predicts dunite abundances consistent with field observations (red dashed line). [*Kelemen et al.*, 2000] Extrapolation to length scales commensurate with the melting region beneath mid-ocean ridges (100 km) predicts the existence of dunites as wide as several kilometers (blue dashed line). Alternatively, perhaps the larges dunites are no larger than the widest dunites we observe in Oman (~100 m).

2. Mechanisms of Dunite Formation

Dunites have been hypothesized to form by (1) diffusive reaction around melt-filled hydrofractures [*Nicolas*, 1986; *Nicolas*, 1990; *Suhr*, 1999]; (2) random merging of growing reaction zones around several hydrofractures [*Kelemen et al.*, 2000]; and (3) a reactive infiltration instability resulting in high porosity conduits. [*Aharonov et al.*, 1995; *Kelemen and Dick*, 1995; *Kelemen et al.*, 1995b; *Spiegelman et al.*, 2001] (Figure 10a-c)

For all three hypotheses, replacive dunites are formed by reaction between ascending MORB melts and the surrounding peridotite. As pressure decreases, the solubility of silica-rich phases (opx and cpx) in basalt increases [*Dick*, 1977; *Quick*, 1981; *Kelemen*, 1990]. Therefore, ascending melts dissolve pyroxene and precipitate olivine, increasing the liquid mass and, where the time integrated melt flux is large

enough, creating dunite in their wake. [*Daines and Kohlstedt*, 1994; *Kelemen*, 1990; *Kelemen et al.*, 1995b] Kinetic studies show that these reactions can occur rapidly [*Brearley and Scarfe*, 1986; *Kuo and Kirkpatrick*, 1985a; *Kuo and Kirkpatrick*, 1985b; *Zhang et al.*, 1989]. The discriminating difference between hypotheses is the melt transport mechanism. In (1) and (2), pyroxene-undersaturated melt within hydrofractures forms dunite along the margins as the melt reacts with the wall rock. In (3), there is no crack, and high porosity dunite channels form as a result of a dissolution instability. The increased porosity resulting from the dissolution reaction increases the local permeability, which in turn increases the melt flux to the area. The increased flux draws in more undersaturated melt, resulting in further dissolution.

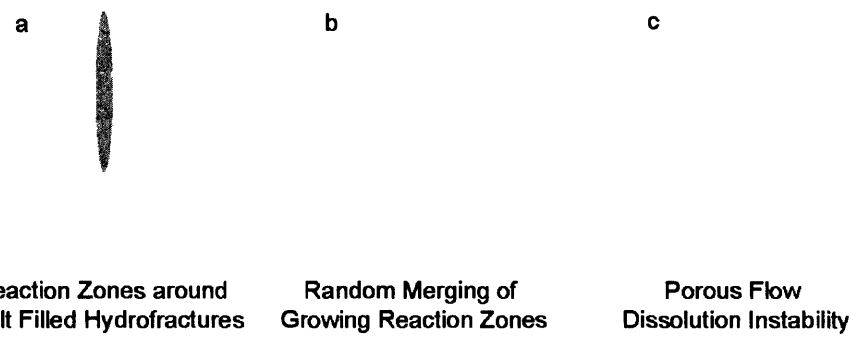

Figure 10. Three hypotheses for replacive dunite formation in the shallow mantle based on reaction of silica-undersaturated basalts with shallow mantle harzburgites. (a) Dunites may form as diffusive reaction zones around melt filled hydrofractures. (b) Random merging of growing reaction zones may give the appearance of large dunites. (c) Dunites may form by a reactive infiltration instability creating high porosity dunite melt conduits.

3. Dunites as diffusive reaction zones

Dunite growth as reaction zones around melt filled hydrofractures is limited by silica diffusion in the melt. Whether in hydrofractures or in the surrounding porous rock, buoyancy-driven melt transport is predominantly vertical, whereas, dunite margins grow in the direction orthogonal to melt transport. Since the kinetics of pyroxene dissolution are fast, silica must be continually moved from the reaction front back to the hydrofracture in order to drive continued dissolution. Because the melt transport velocity in the host peridotite is small, (~1 m/yr; e.g. [*Kelemen et al.*, 1997]) hydrodynamic

dispersion will also be very small [*Freeze and Cherry*, 1979]. Therefore, dunite growth is limited by the lateral transport of silica by diffusion.

This is a limiting case with no horizontal advection of melt. Focused flow networks require that melt, initially formed along grain boundaries uniformly distributed in a porous source rock, flow laterally into channels of focused transport. This lateral advection into the channels (10^{-1} – 10^{-4} times the vertical velocity of ~1 m/yr in porous models [*Spiegelman et al.*, 2001]) may be generally faster than the diffusive transport velocity of SiO_2.

If dunites are diffusive reaction zones, then the time required for formation via Fickian diffusion can be estimated by,

$$\frac{dC}{dt} = -D_{eff}\frac{d^2C}{dw^2}. \quad (4)$$

Assuming the melt composition in the hydrofracture, (i.e. degree of undersaturation) remains constant, the dunite width, w, is proportional to the square root of the formation time, t. The effective diffusivity, D_{eff}, of a particular species in the two phase system is defined as

$$D_{eff} = \phi D_{melt} + (1-\phi)D_{rock}, \quad (5)$$

[*Crank*, 1975] where ϕ is the interconnected porosity and D_{melt} and D_{rock} are the diffusivities of silicon in the melt and solid phases, respectively. Given a moderate porosity of 1-3%, $D_{melt} \approx 10^{-11}$ m^2/s, and $D_{rock} \approx 10^{-15}$ m^2/s [*Lesher et al.*, 1996], the time required to form the largest observed dunites in Oman (~100m) is 250-750 Ma. However, the lifetime of solid material rising through the melting region beneath a spreading center is only ~1-10 Ma for spreading rates of 120-10 mm/yr, respectively. Therefore, the widest dunites that could be formed by diffusion around melt-filled hydrofractures is ~3-20 m (depending on porosity and spreading rate). (Figure 11) If the spreading rate during the formation of the igneous crust in Oman was at least 0.05 m/yr, then dunites wider than ~3-10 m could not be formed as the result of diffusion alone.

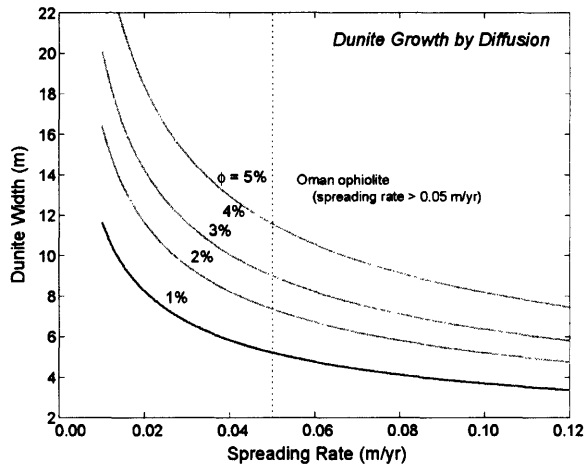

Figure 11. Width of dunite reaction zones around melt filled hydrofractures as a function of spreading rate. As spreading rate increases, the time available for diffusive transport of material in the melting region decreases. For moderate porosities and spreading rates greater than 5 cm/yr, dunites wider than ~12 m cannot form by diffusion around a melt filled hydrofracture within the residence time of solid material in the melting region. To maximize the time for diffusion, these calculations assume dunites begin forming at the base of the melting region and remain active until reaching the surface.

4. Dunites as merging reaction zones

Large dunites (>10 m wide) are present in the Oman ophiolite in the abundances predicted by the observed power-law (~10/km). However, diffusion around individual melt-filled hydrofractures cannot explain their formation. In modeling dunite formation as reaction zones around a static distribution of cracks, Kelemen et al. [2000] suggested that wide dunites may be the result of random merging of reaction zones around individual hydrofractures.

To test this hypothesis, we examined a series of forward models in which reaction zones around dunites are allowed to grow and merge, and compared the results to the distribution of observed dunite widths in Oman. These models start with an initial, spatially-random distribution of five parallel cracks. Reaction zones around each crack grow with the square root of time. In addition, five new dunites nucleate at each time step (unlike Kelemen et al. [2000]). With time, the merging of reaction zones create increasingly wider dunites, and a weak power-law size/frequency distribution begins to emerge. However, the merging process fills space rapidly. After 200 timesteps, the

largest dunites are only ~20 times wider than the initial width, but the dunites occupy approximately 42% of the total area (Figure 12a). By the time very wide dunites (>10^3 times the initial width) form, more than 94% of the model space is filled with dunite and the power-law has degraded (Figure 12b).

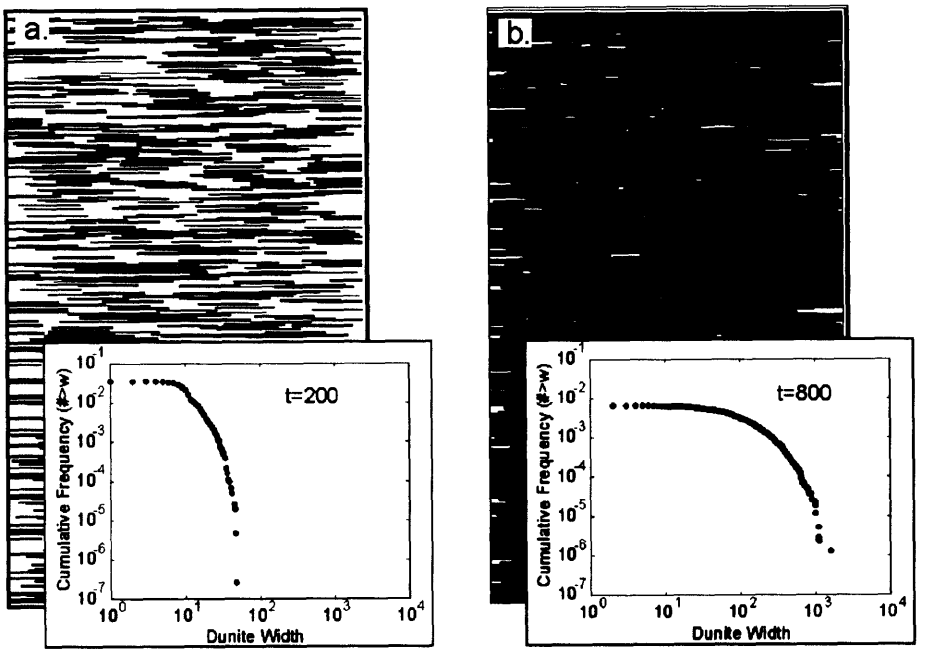

Figure 12. Forward model of merging reaction zones around melt filled hydrofractures. An initially spatially random set of 5 cracks of width 1 are allowed to grow diffusively with the square root of time. At each timestep, 5 new cracks randomly nucleate and begin to grow. (a) At time t=200, a weak power-law begins to form, but dunite widths span less than 2 orders of magnitude. At this point, dunites occupy ~42% of the total area. (b) By t=800, dunite widths range ~3 orders of magnitude, but now 94% of the total area is occupied by dunites. Although merging of growing reaction zones as shown here can produce very wide dunites, the abundance statistics are not consistent with the field observations.

We examined a range of growth and nucleation rates, which affect the time required to fill space with dunites, but in all cases, the range in dunite size never spanned more than 1.5 orders of magnitude before dunites filled more than 50% of the available space. Additional model parameters could be added to modify the fracture mechanics or diffusive growth as a function of dunite width (i.e. new dunites may preferentially nucleate near larger dunites, or larger dunites may grow faster). Such feedback effects

may produce a power-law size/frequency distribution over several orders of magnitude in width, by analogy with the feedback mechanisms examined for purely porous conduits in the next section of this paper. However, there is as yet no evidence to suggest either of these are necessary. Preliminary size/frequency data for harzburgites (the space between dunites) in the images presented here exhibit exponential distributions, suggesting the random spatial distribution of dunites within the areas we mapped in detail. (We have concentrated on areas with high dunite density, and suspect that on the massif and ophiolite scale, dunites may be clustered in a non-random fashion.) Regardless of the nature of the spatial distribution, the diffusion equation (4) specifies that the growth rate for any given dunite should decrease with time, preventing larger dunites from growing faster.

5. Dunites as Porous Conduits

Dunites may represent high porosity melt channels formed as a result of the reactive migration of melt in a solubility gradient [*Aharonov et al.*, 1995; *Kelemen and Dick*, 1995; *Kelemen et al.*, 1995b; *Spiegelman et al.*, 2001]. As melt migrates upward, it becomes progressively undersaturated in pyroxene. The resulting reaction between the melt and harzburgite dissolves pyroxene and precipitates olivine while increasing the liquid mass [*Daines and Kohlstedt*, 1994; *Kelemen*, 1990; *Kelemen et al.*, 1995b]. The increased porosity increases the local permeability, which in turn increases the melt flux to the area. The increased flux draws in more undersaturated melt, resulting in further dissolution. Numerical models of this positive feedback, or reactive infiltration instability, indicate that a self-organized network of high porosity dunite conduits, coalescing downstream, can rapidly form within the melting region [*Aharonov et al.*, 1995; *Spiegelman et al.*, 2001]. Modeled widths of these porous conduits, measured in terms of the width over which the soluble solid phase has been completely removed by dissolution, are ~1 km wide when scaled to the size of the melting region beneath mid-ocean ridges.

The primary requirement of the melt transport process is that it provides a sufficient flux of unequilibrated melt to the ridge axis to form the oceanic crust. We can assess the ability of a high-porosity dunite network to accommodate this flux using the dunite size/frequency relationship established from our field observations. The total melt flux to the ridge can be estimated as the product of the crustal thickness, half-spreading rate, and ridge length. Assuming a constant global crustal thickness of 6 km, the estimated melt flux to the ridge is 60-900 m^3/yr per meter of ridge segment along axis for slow- and fast-spreading ridges (0.01 to 0.15 m/yr), respectively.

The total flux through the dunite network can be estimated by integrating the predicted flux in a dunite of a given size with the observed size/frequency data. The 2-dimensional flux (volume per unit time per unit length) in an individual dunite, J_w, can be defined as

(6) $$J_w = \phi v w ,$$

which is the product of the dunite width, w, and the Darcy flux

(7) $$\phi v = \frac{k \Delta \rho g}{\eta},$$

where $\Delta\rho g$ is the driving pressure gradient due to melt buoyancy, η is the melt viscosity, and the permeability, k, is a function of porosity, ϕ, grain size, d, and geometry, C:

(8) $$k = \frac{\phi^n d^2}{C}.$$

For an interconnected porous network around tetrakaidecahedral grain edges, n=2 and C=1600 [*von Bargen and Waff*, 1986]. The grain size, d, is assumed to be ~4 mm, consistent with the observations from dunites in Oman [*Boudier and Coleman*, 1981]. The driving pressure gradient is derived from the density difference, ~500 kg/m^3, between basaltic melt and olivine. The total flux of the system, J_{tot}, is the integral of the product of the flux function, J_w, and the dunite PDF, f_w, over the range of dunite sizes predicted for the given length scale, L, where

(9a) $$J_{tot} = \int_{w_{min}}^{w_{max}} J_w f_w dw$$

(9b) $$J_{tot} = \int_{w_{min}}^{w_{max}} \phi v w \cdot \frac{aD}{w^{D+1}} L \cdot dw .$$

To estimate the total flux through all dunites, the minimum bound for the integral, w_{min}, is equivalent to the width of the smallest observed dunite, (~1 cm). The upper integration bound, w_{max}, is determined from the extrapolation of the power-law at the length scale of the melting region. However, as discussed above, only dunites greater than the length scale of diffusive equilibration can preserve chemical disequilibrium. Therefore the total flux of unequilibrated melt, J_{uneq}, occurs only through dunites wider than 3-10 m.

In addition, we assume that the dunites form a network of channels that coalesce downstream. As discussed by Kelemen et al. [2000] this is consistent with, though not required by, the observed power-law relationship between dunite width and frequency. In such a network, flux must be conserved where porous conduits merge. In systems where flux is conserved at binary intersections the number of channels is inversely proportional to the flux they carry, or $f_w \propto J^{-1}_w$ [e.g., *Hart*, 1993]. In its simplest form, at each intersection, two channels each carrying one unit of flux join to form one channel carrying twice the flux.

Using a series of stochastic models, we show that this relationship between the number of channels and the flux they carry holds regardless of the initial distribution of flux or the order in which channels merge. In each case, approximately 4100 channels are initially assigned a flux according to a particular probability density function – continuous uniform, exponential, or gaussian – with a fixed maximum allowable flux ranging from 1-100 times the smallest initial flux. (Figure 13, a, c, & e respectively) The channels randomly merge in pairs until all the flux is in one channel. This process is repeated 100 times for each class of initial flux distribution. For any given maximum initial flux, the total flux through the system is constant, regardless of the shape of the initial distribution. In all cases, the number of channels is inversely proportional to the flux they carry as measured over approximately 4 orders of magnitude. (Figure 13, b, d, & f) This consequence of flux conservation is also observed in theoretical [*Aharonov et*

al., 1995] and numerical [*Spiegelman et al.*, 2001] models of reactive porous flow, where $f_w \propto J_w^{-1}$.

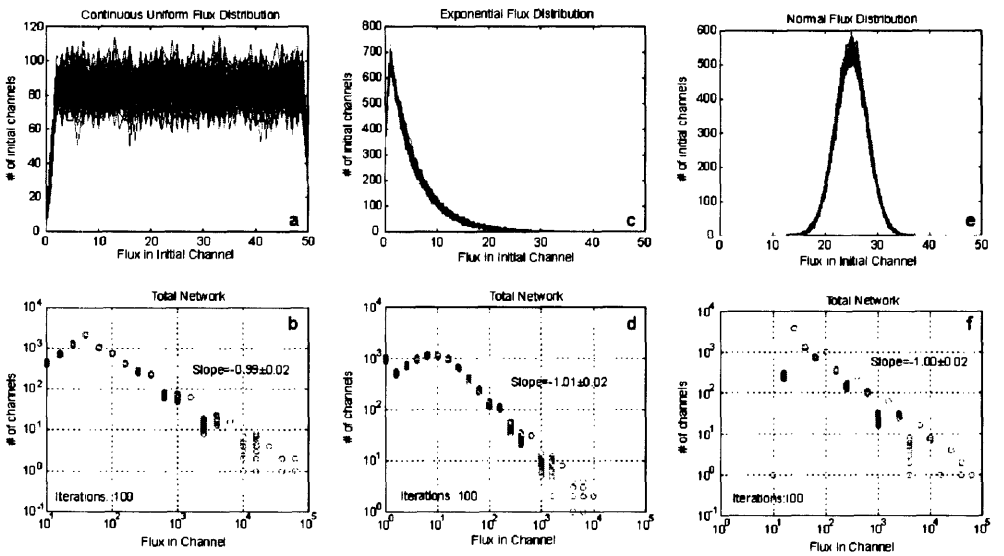

Figure 13. Relationship between flux and number of channels for a system of binary merging conduits for different initial flux distributions: continuous uniform, exponential, Gaussian. In each case a starting population of ~4000 channels, with flux distributions shown in the upper panels (a, c, & e), is allowed to randomly merge in pairs. Merging continues until all the flux is carried in one channel. The probability density function (PDF) of the resultant network in each run (b, d, & f) is below each initial distribution. This process was repeated 100 times for each of the different initial distributions. In all cases, the maximum flux in any initial channel is constant (50 times the minimum flux in runs shown here), and the total flux through the system is constant. In all cases, there exists a robust power-law relationship, with a slope of –1, between flux and number of channels. This relationship holds over nearly 4 orders of magnitude, regardless of the initial distribution of flux or order in which channels merge.

Our dunite size/frequency observations from Oman indicate that $f_w \propto w^{-(D+1)}$. Equating these relationships for f_w suggests that flux is non-linearly proportional to dunite width, or

$$J_w \propto w^{D+1}.$$

Using this width-flux relation, we can define a porosity scaling as a function of dunite width. After substitution of equation (6) into the above relation, it follows that $\phi v w \propto w^{D+1}$.

Canceling w from both sides and substituting (8) into (7) yields the following relationship between porosity, ϕ, and channel width, w:

$$\frac{\phi^n d^2}{C\eta}\Delta\rho g \propto w^D.$$

Assuming grain size, d, melt viscosity, η, grain boundary geometry, C, or the driving pressure gradient, $\Delta\rho g$, do not vary significantly between dunites of different sizes, the only free parameter is the interconnected porosity. Therefore, by specifying the maximum porosity, ϕ_{max}, in the largest dunite, w_{max}, the porosity in any given dunite can be written as

$$\phi = \phi_{max}\left(\frac{w}{w_{max}}\right)^{D/n}. \quad (10)$$

The Darcy flux (7) can then be expressed as

$$\phi v = \frac{\phi_{max}^n d^2 \Delta\rho g}{C\eta}\left(\frac{w}{w_{max}}\right)^D. \quad (11)$$

After substitution of (11) into (9b), if flux is non-linearly proportional to dunite width, the total flux can be expressed as

$$J_{tot} = \frac{\phi_{max}^n d^2 \Delta\rho g a D L}{C\eta w_{max}^D}\left(w_{max} - w_{min}\right). \quad (12)$$

Adopting the spreading rate constraint for Oman, we assume that all flux through dunites wider than 5 m will preserve disequilibrium between migrating melt and the surrounding harzburgite. For length scales commensurate with mid-ocean ridge spreading centers (L=100 km), the largest dunites in the network may be as wide as ~3500 m. Given a maximum porosity in the widest dunites of 1-3%, the total flux through the dunite network is comparable to the observed ridge flux. (Figure 14a) More importantly, the flux of unequilibrated melt accounts for greater than 99% of the total melt flux. Alternatively, if the largest dunite widths in the melting region are limited to the widest dunites observed in Oman (w_{max}=100 m), this "non-linear flux model" (Figure 14b) still supplies a sufficient unequilibrated melt flux (~95% of the total flux) to satisfy the mid-ocean ridge constraints at reasonable porosities (ϕ_{max}<4%). These results indicate that melt transport through dunites wide enough to preserve disequilibrium with the

shallow mantle can be accommodated entirely by porous flow, and thus, there is no requirement for transport through melt-filled cracks.

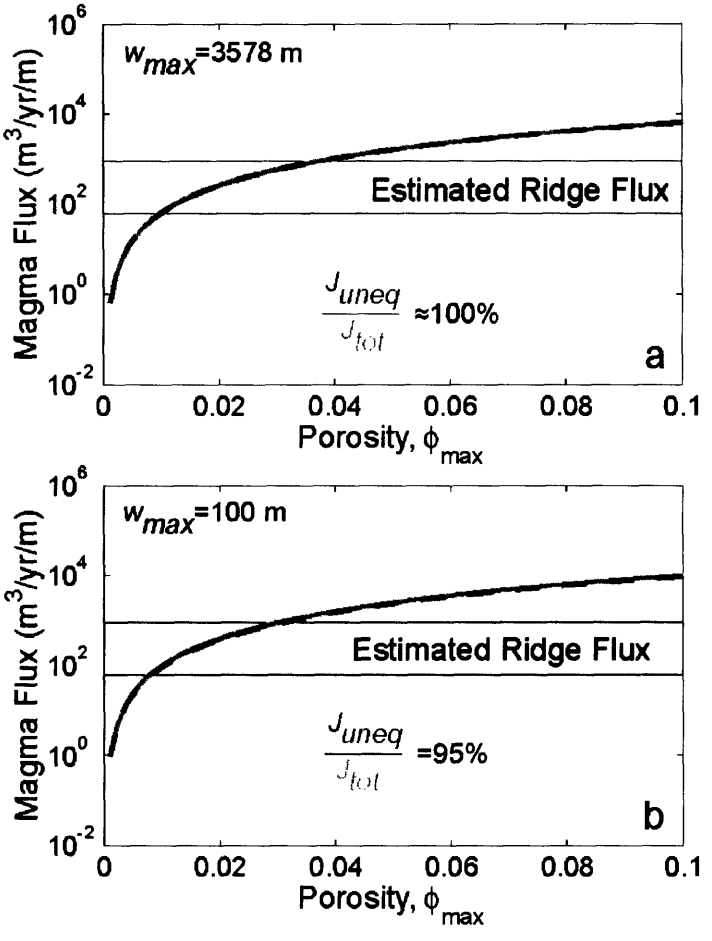

Figure 14. Calculated melt flux through a porous dunite network as a function of porosity, given the power-law abundance relationship derived from field observations. These calculations assume that only dunites wider than 10 m can accommodate chemically unequilibrated melt flux. These "non-linear flux model" calculations incorporate the flux conservation constraint. (a) If the largest dunites have widths predicted by the power-law for a length scale of 100 km, the unequilibrated flux (J_{uneq} - dashed line) is nearly 100% of the total flux (J_{tot} - solid line) through the system and satisfies the observed ridge flux constraint (gray field) over a range of moderate porosities. (b) If the largest dunites are limited to the widest dunites observed in the mantle section of the Oman ophiolite (100 m), the observed ridge flux constraint is still satisfied.

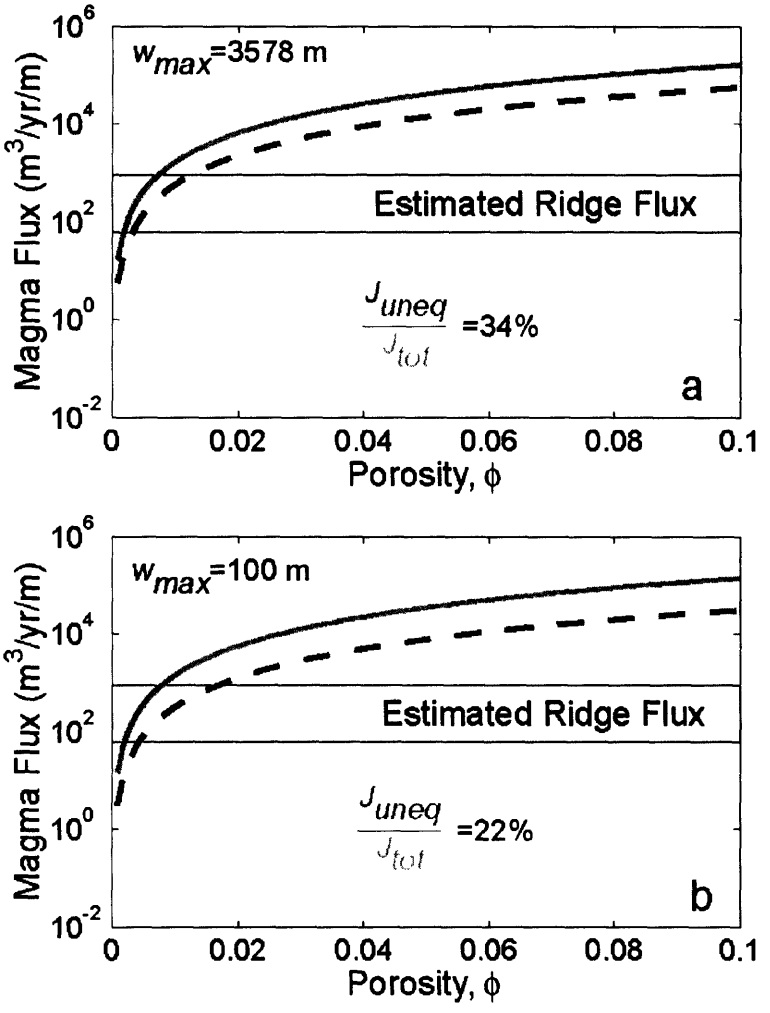

Figure 15. Calculated melt flux through a porous dunite network in which all dunites have a single porosity. (a) The "linear flux model" with the maximum width suggested by extrapolation of the power-law predicts the unequilibrated flux (dashed line) accounts for only 34% of the total flux (solid line). (b) The unequilibrated flux accounts for only 22% of the total flux if the maximum dunite width is limited to the widest observed dunites in Oman, ~100 m. In either case, the predicted fluxes satisfy the observed ridge flux constraint (gray field) over a narrow range in porosities less than ~1-2%.

Flux conservation is a necessary constraint on the melt flux model. A "linear melt flux" model which assumes a constant Darcy flux (e.g. integration of (9b) assuming the porosity in channels is constant and therefore independent of dunite width), does not reproduce the observed fluxes of unequilibrated melt at mid-ocean ridges. The total ridge flux in the "linear melt flux" model can be accommodated if all dunites have porosities of

1 to 2%. However, the unequilibrated melt flux accounts for only ~34% of the total flux, if the maximum dunite width is 3578 m (Figure 15a), and only 22% of the total flux if the maximum dunite width is 100 m (Figure 15b). Such volumes of equilibrated melt would result in an andesitic composition for the igneous oceanic crust, corresponding to a liquid composition in equilibrium with olivine, pyroxene, and spinel in the shallow mantle immediately below the base of the crust (~2 kb), very different from the observed basaltic bulk composition of oceanic crust and primitive MORB (figure 1). Thus, dunite channels can only accommodate the flux of unequilibrated melt through the shallow mantle if the porosity within the dunites is proportional to their width.

Conclusions

Dunite widths as measured in the mantle section of the Oman ophiolite exhibit a scale-invariant power-law size/frequency distribution over 4 orders of magnitude. The power law slope ($D \approx 1.1$) predicts that there exist ~13 times more dunites for every order of magnitude decrease in dunite width. Extrapolation to larger length scales is consistent with field observations at the massif scale and suggests that dunites as wide as 3.5 km may exist in the melting region beneath oceanic spreading centers. Alternatively, dunites may never exceed 100 m, equivalent to the width of the largest we observe in the Oman mantle section.

Diffusive reaction zones around individual melt-filled hydrofractures cannot explain the formation of wide dunites, as the time required to form the largest observed dunites is greater than the transport time of solid material through the melting region. For the inferred minimum spreading rate of the spreading center that formed the Oman ophiolite, dunites more than ~3-10 m wide could not have been formed by this process. Forward models for the formation of wide dunites by the random merging of reaction zones rapidly fill space and do not generate the power-law relationship observed in the field. Instead, our data are most consistent with the formation of dunites as a network of high porosity dissolution channels.

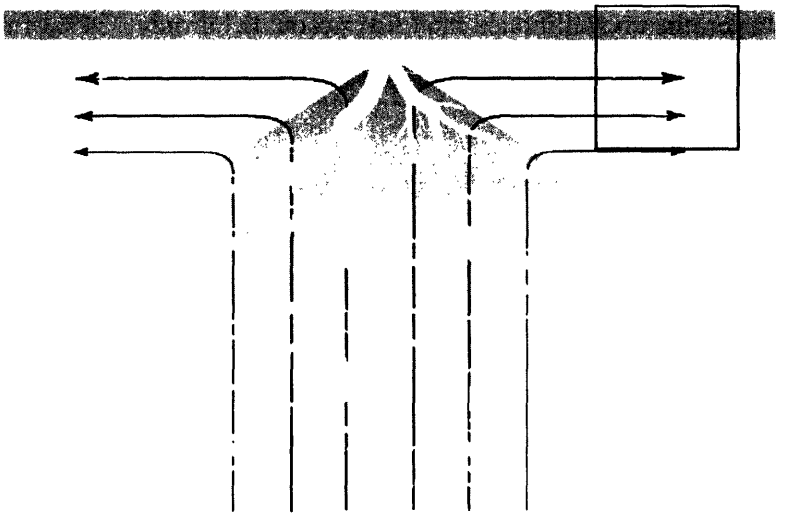

Figure 16. Schematic illustration of a coalescing dunite network beneath an oceanic spreading center based on observations in the Oman Ophiolite. Dunites are shown in green, the crust in blue, and melt is presumed to be present throughout the red and yellow region. The box in the upper right corner indicates the scale of the lithologic section preserved in Oman. The preserved dunites may have been thinned, e.g. via simple shear, during transposition resulting from corner flow. We have implicitly assumed that this thinning affected all dunite widths by the same percentage. Thinning in this manner would affect the magnitudes of the dunite widths but not change the ratio of smaller dunites to larger ones. Therefore the power-law slope would remain unaffected.

We use the dunite width/frequency statistics and diffusive equilibration length constraints to estimate the total flux of melt through porous dunite channels to the ridge axis. In a system of coalescing channels that conserves flux, porous flow in dunite dissolution channels can accommodate the observed melt flux to the ridge over a wide range of spreading rates and moderate porosities, and can preserve the observed disequilibrium between ridge basalts and the shallow, residual mantle.

Based on our observations of dunite shape, size, abundance, and distribution, we offer the following schematic illustration of the melt migration network beneath a spreading center. (Figure 16) In the melting region beneath a spreading center, ascending melts have the potential to dissolve pyroxene and precipitate olivine, leaving dunite in its wake. These high porosity dunite channels coalesce upward and toward the ridge axis.

Merging increases dunite width and porosity while decreasing the number of conduits, thus focusing melt transport toward the ridge axis.

Acknowledgements

We would like to thank Greg Hirth, Marc Parmentier, Jack Whitehead, and Maria Zuber for a thorough examination and insightful comments regarding this work, as well as Günter Suhr, Kazuhito Ozawa and Susumu Umino for their thoughtful reviews. This work was funded by a NSF Graduate Research Fellowship and NSF grants OCE-0118572 and OCE-9819666.

Bibliography

Aharonov, E., J.A. Whitehead, P.B. Kelemen, and M. Spiegelman, Channeling instability of upwelling melt in the mantle, *J. Geophys. Res.*, *100*, 20433-20450, 1995.

Allan, J.F., and H.J.B. Dick, Cr-rich spinels as a tracer for melt migration and melt-wall rock interaction in the mangle: Hess Deep, leg 147, *Sci. Res. Ocean Drill. Prog.*, *147*, 157-172, 1996.

Arai, S., and K. Matsukage, Petrology of gabbro-troctolite-peridotite complex from Hess Deep, Equatorial Pacific: implications for mantle-melt interaction within the oceanic lithosphere, *Sci. Res. Ocean Drill. Prog.*, *147*, 135-155, 1996.

Augé, T., Chromite deposits in the northern Oman ophiolite: mineralogical constraints, *Mineral. Deposita*, *22*, 1-10, 1987.

Barton, C.A., and M.D. Zoback, Self-similar distribution and properties of macroscopic fractures at depth in crystalline rock in the Cajon Pass Scientific borehole., *J. Geophys. Res.*, *97*, 5181-5200, 1992.

Beattie, P., Uranium- thorium disequilibria and partitioning on melting of garnet peridotite, *Nature*, *363*, 63-65, 1993.

Boudier, F., and R.G. Coleman, Cross section through the peridotite in the Samail ophiolite, southeastern Oman mountains, *J. Geophys. Res.*, *86*, 2573-2592, 1981.

Brearley, M., and C.M. Scarfe, Dissolution rates of upper mantle minerals in an alkali basalts melt at high pressure: An experimental study and implications for ultramafic xenolith survival, *J. Petrol.*, *27*, 1157-1182, 1986.

Cannat, M., How thick is the magmatic crust at slow spreading oceanic ridges?, *J. Geophys. Res.*, *101*, 2847-2857, 1996.

Cannat, M., G. Ceuleneer, and J. Fletcher, Localization of ductile strain and the magmatic evolution of gabbroic rocks drilled at the mid-Atlantic ridge (23°N), in *Proc. ODP, Sci. Results*, edited by J.A. Karson, M. Cannat, D.J. Miller, and D. Elthon, pp. 77-98, 1997.

Crank, J., *The Mathematics of Diffusion*, 414 pp., Oxford University Press, New York, 1975.

Daines, M.J., and D.L. Kohlstedt, Transition from porous to channelized flow due to melt/rock reaction during melt migration, *Geophys. Res. Lett.*, *21*, 145-148, 1994.

Dick, H.J.B., Partial melting in the Josephine Peridotite; I, The effect on mineral composition and its consequence for geobarometry and geothermometry, American Journal of Science, 277 (7), 801-832, 1977.

Dick, H.J.B., Abyssal peridotites, very slow spreading ridges, and ocean ridge magmatism, in *Magmatism in the ocean basins*, edited by A.D. Saunders, and M.J. Norry, pp. 71-105, Geological Society of America, 1989.

Dick, H.J.B., and T. Bullen, Chromian spinel as a petrogenetic indicator in abyssal and alpine-type peridotites and spatially associated lavas, *Contrib. Mineral. Petrol.*, *86*, 54-76, 1984.

Dick, H.J.B., and J.H. Natland, Late-stage melt evolution and transport in the shallow mantle beneath the East Pacific Rise, in *Proceedings of the Ocean Drilling Program, Scientific Results*, edited by C. Mevel, K.M. Gillis, J.F. Allan, and P.S. Meyer, pp. 103-134, ODP, 1996.

Dunn, R.A., D.R. Toomey, and S.C. Solomon, Three dimensional seismic structure and physical properties of the crust and shallow mantle beneath the East Pacific Rise at 9°30' N, *J. Geophys. Res.*, *105*, 23,537-23,555, 2000.

Elthon, D., Isomolar and isostructural pseudo-liquidus phase diagrams for oceanic basalts, *Amer. Mineral.*, *68*, 506-511, 1983.

Elthon, D., Pressure of origin of primary mid-ocean ridge basalts, in *Magmatism in the Ocean Basins*, edited by A.D. Saunders, and M.J. Norry, pp. 125-136, Geological Society, 1989.

Elthon, D., and C.M. Scarfe, High pressure phase equilibria of a high-magnesia basalt: implications for the origin of mid-ocean ridge basalts, *Carnegie Inst. Wa. Yrbk.*, 277-281, 1980.

Forsyth, D.W., S.C. Webb, L.M. Dorman, and Y. Shen, Phase velocity of Raleigh wave in the MELT experiment of the east pacific rise, *Science*, *280*, 1235-1238, 1998.

Freeze, R.A., and J.A. Cherry, Groundwater, 604 pp., Prentice Hall, Englewood Cliffs, 1979.

Hart, S.R., Equilibration during mantle melting: A fractal tree model, *Proc. Natl. Acad. Sci. USA*, *90*, 11914-11918, 1993.

Hirschmann, M.M., and E.M. Stolper, A possible role for garner pyroxenite in the origin of the "garnet signature" in MORB, *Contrib. to Mineral. Pet.*, *124*, 185-208, 1996.

Hung, S.-H., D.W. Forsyth, and D.R. Toomey, Can a narrow, melt-rich, low-velocity zone of mantle upwelling be hidden beneath the East Pacific Rise? Limits from waveform modeling and the MELT experiment, *J. Geophys. Res.*, *105* (4), 7945-7960, 2000.

Johnson, K.T.M., H.J.B. Dick, and N. Shimizu, Melting in the oceanic upper mantle: an ion microprobe study of diopsides in abyssal peridotites, *J. Geophys. Res.*, *95*, 2661-2678, 1990.

Jousselin, D., A. Nicolas, and F. Boudier, Detailed mapping of a mantle diapir below a paleo-spreading center in the Oman Ophiolite, *J. Geophys. Res.*, *103*, 18,153-18,170, 1998.

Kelemen, P.B., Reaction between ultramafic rock and fractionating basaltic magma. I. Phase relations, the origin of calc-alkaline magma series, and the formation of discordant dunite, *J. Petrol.*, *31*, 51-98, 1990.

Kelemen, P.B., M.G. Braun, and G. Hirth, Spatial distribution of melt conduits in the mantle beneath oceanic spreading ridges: Observations from the Ingalls and Oman ophiolites, *Geochem. Geophys. Geosyst.*, 2000.

Kelemen, P.B., and H.J.B. Dick, Focused melt flow and localized deformation in the upper mantle: juxtaposition of replacive dunite and ductile shear zones, *J. Geophys. Res.*, *100*, 423-438, 1995.

Kelemen, P.B., G. Hirth, N. Shimizu, M. Spiegelman, and H.J.B. Dick, A review of melt migration processes in the adiabatically upwelling mantle beneath spreading ridges, *Phil. Trans. Roy. Soc., Lond. A*, *355*, 283-318, 1997.

Kelemen, P.B., N. Shimizu, and V.J.M. Salters, Extraction of mid-ocean ridge basalt from the upwelling mantle by focused flow of melt in dunite channels, *Nature*, *375*, 747-753, 1995a.

Kelemen, P.B., J.A. Whitehead, E. Aharonov, and K.A. Jordahl, Experiments on flow focusing in soluble porous media, with applications to melt extraction from the mantle, *J. Geophys. Res.*, *100*, 475-496, 1995b.

Koga, K.T., N. Shimizu, and T.L. Grove, Disequilibrium trace element redistribution during garnet to spinel facies transformation, in *Proc. 7th Int. Kimberlite Conf.*, edited by J.L. Gurney, M.D. Pascoe, and S.H. Richardson, pp. 444-451, 1998.

Kuo, L.-C., and R.J. Kirkpatrick, Dissolution of mafic minerals and its implications for the ascent velocities of peridotite-bearing basaltic magmas, *J. Geol.*, *93*, 691-700, 1985a.

Kuo, L.-C., and R.J. Kirkpatrick, Kinetics of crystal dissolution in the system diopside-forsterite-silica, *Am. J. Sci.*, *285*, 51-90, 1985b.

Laslett, G.M., Censoring and edge effects in areal and line transect sampling of rock joint traces, *Math. Geol.*, *14*, 125-140, 1982.

Lesher, C.E., R.L. Hervig, and D. Tinker, Self-diffusion of network formers (silicon and oxygen) in naturally occurring basaltic liquid, *Geochim. Cosmochim. Acta*, *60*, 405-413, 1996.

Lippard, S.J., A.W. Shelton, and I.G. Gass, *The ophiolite of northern Oman*, 178 pp., Blackwell, Oxford, 1986.

Lundstrom, C.C., J. Gill, Q. Williams, and M.R. Perfit, Mantle melting and basalt extraction by equilibrium porous flow, *Science*, *270*, 1958-1961, 1995.

McKenzie, D., 230Th-238U disequilibrium and the melting processes beneath ridges axes, *Earth Planet. Sci. Lett.*, *72*, 149-157, 1985.

Nicolas, A., A melt extraction model based on structural studies in mantle peridotites, *J. Petrol.*, *27*, 999-1022, 1986.

Nicolas, A., Melt extraction from mantle peridotites: Hydrofracturing and porous flow, with consequences fro oceanic ridge activity, in *Magma Transport and storage*, edited by M.P. Ryan, pp. 1-26, Wiley, 1990.

Nicolas, A., and F. Boudier, Mapping oceanic ridge segments in Oman ophiolite, *J. Geophys. Res.*, *100*, 6179-6197, 1995.

Nicolas, A., F. Boudier, and B. Ildefonse, Variable crustal thickness in the Oman Ophiolite; implication for oceanic crust, Journal of Geophysical Research, B, Solid Earth and Planets, 101 (8), 17,941-17,950, 1996.

Nicolas, A., F. Boudier, B. Ildefonse, and E. Ball, Accretion of Oman and United Arab Emirates ophiolite - Discussion of a new structural map, *Mar. Geophys. Res.*, *21*, 147-179, 2000.

Nicolas, A., and B. Ildefonse, Flow mechanism and viscosity in basaltic magma chambers, *Geophysical Research Letters*, *16*, 2013-2016, 1996.

O'Hara, M.J., Primary magmas and the origin of basalts, *Scot. J. Geol.*, *1*, 19-40, 1965.

Pallister, J.S., and C.A. Hopson, Samail ophiolite plutonic suite: field relations, phase variation, cryptic variation and layering, and a model of a spreading ridge magma chamber, *J. Geophys. Res.*, *86*, 2593-2644, 1981.

Pallister, J.S., and R.J. Knight, Rare-earth element geochemistry of the Samail ophiolite near Ibra, Oman, *J. Geophys. Res.*, *86*, 2673-2697, 1981.

Pickering, G., J.M. Bull, and D.L. Sanderson, Sampling power-law distributions, *Tectonophysics*, *248*, 1-20, 1995.

Quick, J.E., Petrology and petrogenesis of the Trinity Peridotite, an upper mantle diapir in the eastern Klamath Mountains, northern California, *J. Geophys. Res. 86,* 11,837-11,863, 1981.

Salters, V.J.M., and S.R. Hart, The hafnium paradox and the role of garnet in the source of mid-ocean-ridge basalts, *Nature*, *342*, 420-422, 1989.

Spiegelman, M., Geochemical consequences of melt transport in 2-D: The sensitivity of trace elements to mantle dynamics, *Earth Planet. Sci. Lett.*, *139*, 115-132, 1996.

Spiegelman, M., P.B. Kelemen, and E. Aharonov, Causes and consequences of flow organization during melt transport: The reaction infiltration instability, *J. Geophys. Res.*, *106*, 2061-2078, 2001.

Stolper, E., A phase diagram for mid-ocean ridge basalts: preliminary results and implications for petrogenesis, *Contrib. Mineral. Petrol.*, *74*, 13-27, 1980.

Suhr, G., Melt migration under oceanic ridges: Inferences from reactive transport modeling of upper mantle hosted dunites, *J. Petrol.*, *40*, 575-599, 1999.

Vera, E.E., J.C. Mutter, P. Buhl, A.A. Orcutt, A.J. Harding, M.E. Kappus, R.S. Detrick, and T.M. Brocher, The structure of 0- to .2-My-old crust at 9 N on the East Pacific Rise from expanded spread profiles, *J. Geophys. Res.*, *95*, 15529-15556, 1990.

von Bargen, N., and H.S. Waff, Permeablilities, interfacial areas and curvatures of partially molten systems: Results of numerical computations of equilibrium microstructures, *J. Geophys. Res.*, *91*, 9261-9276, 1986.

Weisburg, S., *Applied Linear Regression*, 324 pp., Wiley and Sons, New York, 1985.

Zhang, Y., D. Walker, and C.E. Lesher, Diffusive crystal dissolution, *Contrib. Mineral. Petrol.*, *102*, 492-513, 1989.

Chapter 3

DUNITES AS CONDUITS FOR PRIMITIVE MELT TRANSPORT: IMPLICATIONS OF THE GEOCHEMISTRY OF OMAN PERIDOTITES

Abstract:

Composition and structural relationships preserved in residual mantle peridotites have established the framework for our understanding of melt generation and transport in the shallow mantle beneath mid-ocean ridges. In particular, geochemical data and field observations from ophiolites indicate that dunites form by reaction of harzburgite with ascending orthopyroxene-undersaturated melts and subsequently serve as conduits for the transport of those melts to the surface. In this study we present detailed geochemical transects across several dunites from the Oman ophiolite to test whether dunites are the primary conduits for the melts that form the oceanic crust.

Chemical profiles across dunites from Wadi Lufti, Oman are relatively flat with sharp boundaries that coincide with the macroscopic lithologic contacts observed in the field. The compositions of olivines, pyroxenes, and spinels in peridotites exhibit trends similar to those observed in abyssal peridotites and extend to slightly more depleted compositions. Relative to the surrounding harzburgite, dunites have olivines with lower NiO and higher Mg# and spinels with higher TiO_2 and Cr# and lower Mg#.

The major and trace element composition of dikes and lavas from the region indicate that their parental liquid was similar to MORB. Dunite compositions also vary systematically with the width of the dunite; the widest dunite preserving equilibrium with the primitive liquid parental to the dikes and lavas in the region. These observations suggest that the melt transport processes which occurred in the Oman mantle were similar to those which operate beneath modern mid-ocean ridges.

The observed trends in the data are best explained by dunite formation by reactive porous flow followed by focused melt transport. The reaction of peridotite with primitive liquid imparts a distinct chemical signature, observed in the small dunites, which is then progressively overprinted in wider dunites by an increasing flux of primitive melt. These calculations suggest that the widest dunites preserve melt/rock ratios in excess of 100-1000. These large melt/rock ratios, coupled with field observations on the abundance of dunites, indicate that wide dunites are the primary conduits for the transport of primitive melts that form the oceanic crust.

Introduction:

Mid-ocean ridge basalt (MORB) is not in equilibrium with residual mantle peridotites at pressures less than 1 GPa or more. Most MORBs are undersaturated in orthopyroxene relative to the low pressure equilibrium composition expected for melts at the base of the oceanic crust. In fact, the major element composition of the most primitive MORB liquids indicates they were last in equilibrium with the shallow mantle at pressures in excess of 8 kb [*Elthon*, 1989; *Elthon and Scarfe*, 1980; *O'Hara*, 1965; *Stolper*, 1980]. Although the compositions of ultra-depleted melt inclusions [*Sobolev and Shimizu*, 1993] and some interpretations of ^{226}Ra excesses in MORB [*Jull et al.*, 2002; *Kelemen et al.*, 1997; *Lundstrom et al.*, 1995; *Sims et al.*, 2002] imply that some melts are in intimate contact with residual harzburgite at low pressure, the fundamental observation of major element disequilibrium requires that the majority of melts erupted at mid-ocean ridges ascend thorough the uppermost 25-30 km of residual peridotite with minimal chemical interaction with the shallow mantle.

At least some chemically-isolated melt transport in the upper mantle occurs through dunite conduits, which form in the melting region beneath mid-ocean ridges. Primitive MORB liquids at low pressure are saturated only in olivine and spinel. Therefore dunites (rocks with greater than 90% olivine) can serve as non-reactive conduits for the transport of basaltic melts and preserve geochemical signatures indicative of melt transport. Olivines from dunites exhibit a narrow distribution in Mg# (molar Mg/(Mg+Fe)$\times$100) [*Kelemen*, 1990; *Kelemen et al.*, 1997], typical of residual mantle dunites [e.g. *Dick and Natland*, 1996] and distinct from cumulate olivine precipitated at low pressure from pooled polybaric melts [*Nicolas and Prinzhofer*, 1983]. Clinopyroxenes in dunites preserve rare earth element (REE) concentrations in equilibrium with MORB [*Alabaster et al.*, 1982; *Kelemen et al.*, 1995]. In contrast, clinopyroxenes in harzburgites are significantly more light rare earth depleted, consistent with residues of moderate degrees of partial melting [*Johnson et al.*, 1990]. Major and minor element compositions from spinels are consistent with the trace element data. The Cr# (molar Cr/(Cr+Al)$\times$100) and TiO_2 content of spinels in dunites dredged from mid-

ocean ridges are similar to those in MORB and significantly higher than in spinels from residual harzburgites [e.g. *Allan and Dick*, 1996; *Dick and Bullen*, 1984].

The geochemistry of peridotites dredged from mid-ocean ridges ("abyssal peridotites") provides the framework for our understanding of melt transport beneath oceanic spreading centers. However, dredged peridotites in general, and dunites in particular, are so heavily serpentinized that few primary minerals remain. Also dredging obscures the spatial relationships between samples necessary to address questions regarding the size, shape, and 'interconnectedness' of the melt migration conduits.

Ophiolites provide a crucial extension to our understanding of melt transport beneath mid-ocean ridges. The Oman ophiolite in particular has long been the focus of study because of the geochemical similarity of the mantle peridotites, gabbros, and lavas to abyssal rocks [e.g. *Augé*, 1987; *Kelemen et al.*, 1995; *Lippard et al.*, 1986; *Pallister and Hopson*, 1981] particularly in the southern massifs. The original mineralogy of the peridotites is well preserved, in some areas with <20% serpentine and the extensive exposures provide the geographic context and contact relationships unobtainable by dredging. Dunites in Oman are generally tabular bodies moderately discordant to the orthopyroxene foliation in the host harzburgite [e.g. *Boudier and Coleman*, 1981; *Kelemen et al.*, 1995; *Lippard et al.*, 1986]. Both the dunites and surrounding harzburgites are sheared parallel to the base of the overlying crust [e.g. *Braun and Hirth*, in prep; *Dijkstra et al.*, 2002]. If the observed peridotite fabric was imposed by transposition of the mantle during corner flow away from the spreading center, then the dunites formed in the melting region in a near-vertical orientation, consistent with the melt conduit hypothesis.

Field relationships preserved in ophiolites indicate that dunites replace harzburgite by reaction with ascending melts which dissolve pyroxene and precipitate additional olivine and spinel [*Boudier and Nicolas*, 1972; *Kelemen et al.*, 1995; *Nicolas and Prinzhofer*, 1983; *Savel'yeva et al.*, 1980]. As basaltic melts rise to lower pressure, they become increasingly orthopyroxene-undersaturated and are forced to dissolve orthopyroxene to re-establish equilibrium. The dissolution of orthopyroxene leads to

increased liquid mass and precipitation of additional olivine [*Daines and Kohlstedt*, 1994; *Kelemen*, 1990]. With a sufficient flux of pyroxene-undersaturated melt, all the orthopyroxene can be dissolved and dunite is formed along the melt migration path.

What remains to be resolved is whether dunites are shallow melt migration features formed by depleted melts or the primary conduits for transport of the primitive melts which form the bulk of the oceanic crust. This distinction depends strongly on the manner in which dunites nucleate and the composition and flux of melt they carry. To better constrain these uncertainties, we examine geochemical profiles across a suite of dunites and their adjacent harzburgites from the Samail and Wadi Tayin massifs in the southern portion of the Oman ophiolite (figure 1) and compare them to the compositions of dikes and lavas in the region. With these data we can discern between the proposed models of dunite nucleation and quantify the flux of melt through dunites.

Methods:

The majority of the residual peridotite samples come from the Wadi Lufti region of the Samail massif. This area contains some of the freshest peridotites in Oman and preserves detailed lithologic structures ordinarily obscured by the extensive weathering typical of peridotites in other regions of Oman. Dunites in Oman vary dramatically in size, from a few centimeters in width to nearly 100 m [*Braun and Kelemen*, 2002]. To encompass this wide range, we collected detailed transects across four dunites (7 cm, 3 m, 20 m, and 50 m wide) as well as the surrounding harzburgites from Wadi Lufti.

One drawback to the high density of dunites in Wadi Lufti, is that it is difficult to get far away from one dunite without approaching another one. Therefore, to augment our chemical characterization of the harzburgite far from dunites, we include data from the Wadi Tayin massif (see figure 1) where dunite abundance is much smaller and the harzburgites are still reasonably fresh. To constrain the compositions of the melts which may have passed through these dunites, we also collected a suite of 41 basaltic dikes and lavas from the Samail and Wadi Tayin massifs (figure 1).

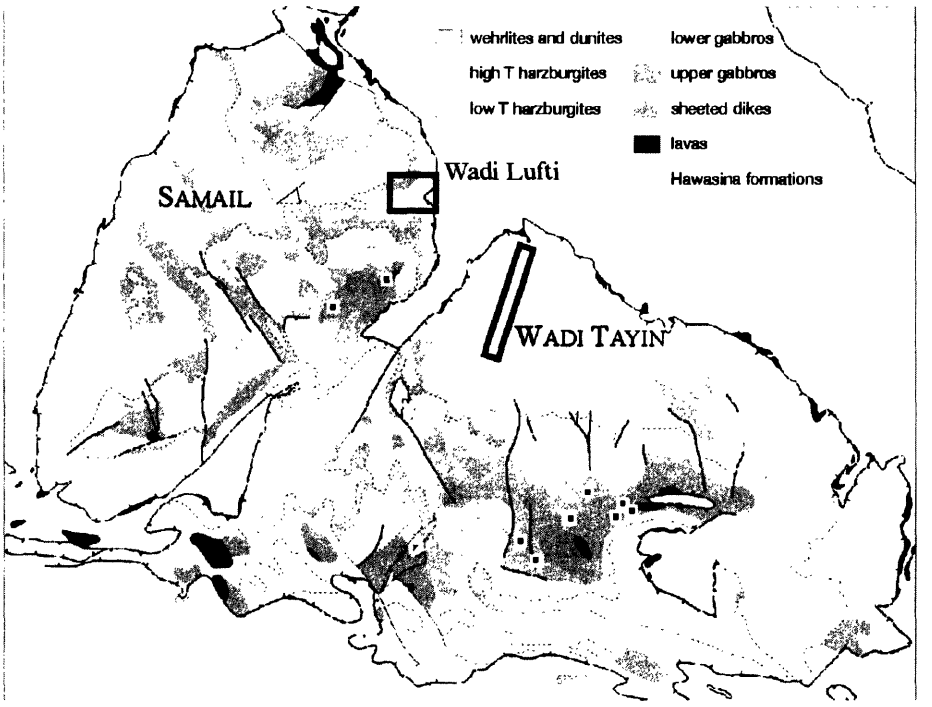

Figure 1: Sample locations within the Samail and Wadi Tayin massifs in the southern portion of the Oman ophiolite. Black boxes delineate regions in which peridotites were collected. White squares indicate dike and lava sample locations. Underlying geologic map is taken from Nicolas et al. [2002].

Compositional data for all major peridotite phases were collected using the JEOL JXA-733 Superprobe at the MIT Electron Microprobe Facility. The least-altered samples in each transect were chosen for analysis. Except for the smallest dunite which is completely contained in two large thin sections, this sub-sampling results a sample spacing of ~0.5 m (with only a few small gaps). For each thin section, we measured cores of mineral clasts with little visible alteration (critical for spinels) and present the average of at least 4 distinct grains for each phase. In total, the four transects encompass 188 samples with 1088 olivines, 1279 spinels, and 123 pyroxenes. Sample mean compositions with 1σ standard deviations are listed in tables B1, B2, and B3, respectively, available as electronic supplements at http://www.Journal.com.

Beam currents were adjusted to obtain high precision minor element concentrations in each phase. Olivine analyses were conducted using a 100 nA, 15 kV

beam with a 1 μm spot size. For Ni and Ca, the high beam current and long count times (240 sec on peak/180 sec on background) yield a 1σ uncertainty associated with counting statistics of ±1.5%. Spinels were measured using a 30 nA, 15kV beam. For Ti in spinel, an 80 sec count time results in less than 7% uncertainty. Only minimal gains in precision were obtained with longer count times. Pyroxenes were measured using the standard beam current and accelerating voltage (10 nA, 15 kV) but with increased count times on Ni and Ti.

Trace element concentrations in clinopyroxenes preserved in dunites were measured using the Cameca IMS 3f Ion Microprobe at the Woods Hole Oceanographic Institution by Dr. Karen Hanghøj. Equilibrium liquid compositions for the observed clinopyroxenes were calculated using the mineral/melt partition coefficients of *Hart & Dunn*, [1993]. Major and trace element concentrations for the suite of dikes and lavas were measured by ICP-MS by Dr. Julian Pearce at Cardiff University.

Results:

Our detailed transects through the residual peridotites in conjunction with the analyses of the dikes and lavas have yielded several observations which we can use to improve our understanding of melt supply to oceanic spreading centers. First, the compositions of harzburgites and dunites measured in Wadi Lufti samples are similar to abyssal residual peridotites. Second, transects across the dunites show that the geochemical boundaries between dunites and the surrounding harzburgites are well defined, with sharp transitions in both major and minor element chemistry that coincide with the macroscopic changes in lithology. Third, dunite composition is fairly uniform within each transect, but varies systematically as a function of dunite width, with wide dunites close to equilibrium with liquids parental to the observed lavas and dikes in the region, which in turn are similar to MORB.

1. Peridotite Composition

Numerous studies have demonstrated that the major and trace element

composition of peridotites from Oman are similar to peridotites dredged from the seafloor near mid-ocean ridges [e.g. *Boudier and Coleman*, 1981; *Kelemen et al.*, 1995; *Pallister and Knight*, 1981]. The peridotites from Wadi Lufti show a similar relationship. The Cr# (molar Cr/(Cr+Al)*100) of spinels ranges from 31-75. Although there is significant overlap, dunite Cr#s are typically higher than ~55 whereas harzburgites generally fall below this value. The observed co-variation of Cr# and Mg# in the spinels follows the abyssal peridotite trend (figure 2a) but is offset slightly to lower Mg# at a given Cr#. The Cr# in spinels from Oman dunites, as in other alpine peridotites, extends to higher values than the majority of abyssal peridotites but do not reach as low, suggestive of a higher degree of partial melting [*Dick and Bullen*, 1984]. The variation in the TiO_2 content of spinels (figure 2b) is also similar to that observed in abyssal peridotites (as compiled by Kelemen et al. [1997; 1995]), with the concentration in the dunites (0.25-0.6 wt%) distinctly higher than in harzburgite (<0.25 wt%). The TiO_2 in the Oman dunites, however, do not extend to concentrations as high as those observed in abyssal rocks.

The major element composition of the majority of olivine in the peridotites is consistent with a residual, rather than cumulate origin. Olivine Mg# ranges from 90-93 with Ni contents of 0.3-0.4 wt%, similar to abyssal peridotites (figure 3b). However, a few harzburgites show evidence for impregnation. These samples exhibit abundant clinopyroxene, olivines with low Ni contents (<0.35 wt %) and Mg#s (<88-90.5), orthopyroxene with Mg#<88, and interstitial spinels with low Cr#, high TiO_2 and a translucent brown (rather than opaque black) appearance in plane light. Rocks with these anomalous compositions (shown in light gray – figure 3) typically reside at dunite/harzburgite contacts and reflecting a late stage of "impregnation" during cooling in which igneous phases crystallize from a liquid migrating along grain boundaries, rather than representing a trapped melt.

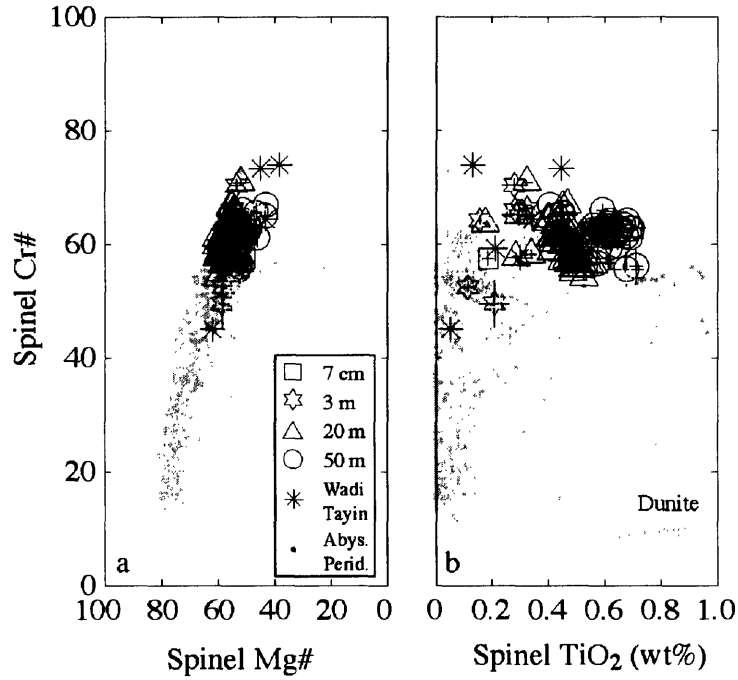

Figure 2: Major element composition of spinel from dunites of various widths (black) and the surrounding harzburgites (gray) from Wadi Lufti. The Oman spinel data follow the trends observed in abyssal peridotites (closed circles), suggesting that the petrogenic processes which occurred in Oman are similar to those beneath active mid-ocean ridges. a) Spinel Cr# as a function of Mg#. The Oman samples sit at the upper end of the abyssal peridotite trend with dunites generally exhibiting higher Cr# than harzburgites. b) Cr# versus TiO_2 in Oman spinels. Dunites consistently exhibit higher TiO_2 contents than the adjacent harzburgites. "Impregnated" samples are shown in light gray. Error bars indicate 1σ standard deviation around the mean based on at least 4 points per thin section.

The olivine and spinel compositions also correlate well with each other. Figure 3a shows that with increasing in TiO_2 in spinel, there is a monotonic decrease in the Ni content in olivine, excluding the impregnated harzburgites. Additionally, there is a distinct relationship in the dunites between the Mg# of the olivines and the TiO_2 content of the coexisting spinels (figure 3c). Dunites with higher TiO_2 have lower Mg# olivines.

2. Dunite/Harzburgite contacts

In the field, dunite-harzburgite boundaries are clearly defined by the difference in orthopyroxene mode. Individual pyroxenes are easily observed in smooth, stream-cut outcrop surfaces and also affect the overall weathering of the rocks. The dunites in Wadi

Lufti are tabular bodies free of orthopyroxene with mutually-parallel contacts. However, large dunites can contain lens-shaped "islands" of harzburgite which approach several meters wide. In general, dunite-harzburgite contacts are sharp, with the orthopyroxene (opx) mode dropping from ~20% in the harzburgite to zero in the dunite over distances on the order of the grain size [*Braun and Hirth*, in prep]. In only a few cases is a diffuse

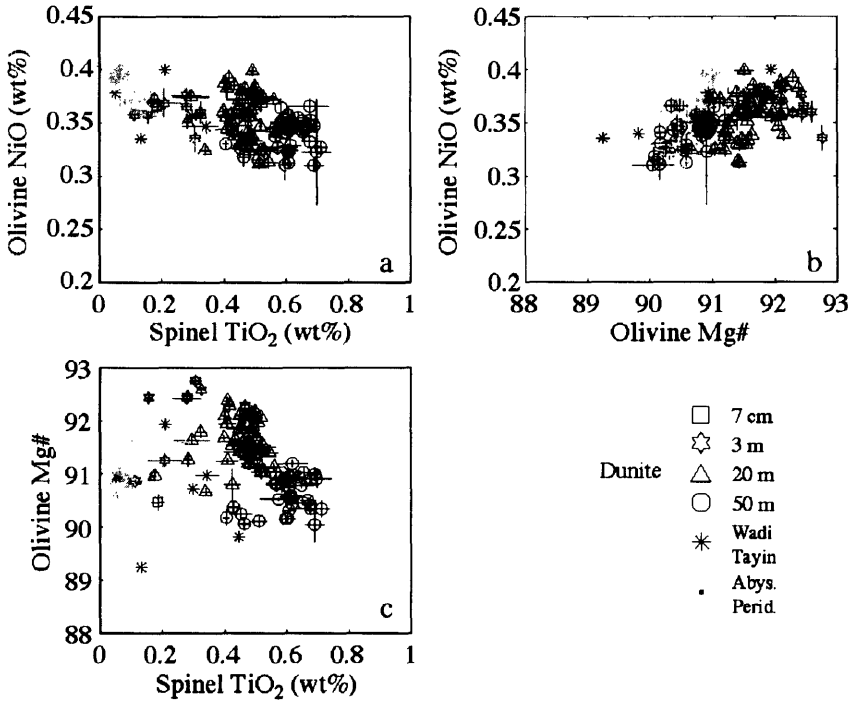

Figure 3. Major and minor element covariations in olivines and spinels from southern Oman. a) NiO in olivine decreases as TiO_2 in spinel increases. b) Olivine NiO versus Mg# in comparison to data from abyssal peridotites (closed circles – see text for references). c) Olivine Mg# versus TiO_2 in coexisting spinel. TiO_2 in dunites is consistently higher than in harzburgites and is correlated with olivine major element composition. Dunites are black, harzburgites are gray and symbol shape indicates dunite width. "Impregnated" samples are shown in light gray. Error bars indicate 1σ standard deviation around the mean based on at least 4 points per thin section.

interface with intermediate opx mode observed. These opx-poor regions are small (< 0.5 m wide), discontinuous, and occur toward the periphery of clusters of dunites. Olivine dominates the mode at greater than 80%. However, variations in spinel abundance are also observed. The spinel mode in the dunites is higher than in the harzburgite, by as much as a factor of two, although the spinel proportion in both rock types is generally

less than 1%. In addition to these small variations over large length scales, we also observe punctuated excursions in spinel mode in the form of narrow spinel-rich bands (< 1 cm wide) which typically parallel the dunite-harzburgite contacts. These spinel-rich bands occur within the dunite or at the contact, but not within the harzburgite.

Transitions in the major and minor element compositions of olivine and spinel between the harzburgite and dunite are also sharp and coincident with the changes in opx mode. Figures 4-8 show profiles for Mg#, Ni, and CaO in olivine, and Cr# and TiO_2 in spinel respectively, across each of the four dunites. Vertical lines mark the dunite/harzburgite contacts. Horizontal lines indicate the mean harzburgite composition. For each of these elements, with the exception of CaO in olivine, the chemical change occurs almost entirely at the lithologic contacts observed in the field. The Ca contents of olivine, in contrast, exhibit a gradual transition over several meters within the dunite as well as greater chemical variation within each sample.

The boundaries of harzburgite islands within dunites are also sharp. As seen in the 20 m wide dunite, the harzburgite island at the 5 m mark exhibits a coincident decrease in CaO and TiO_2 with an increase in Ni. Similar changes within the dunites (at 18 m in the 20 m wide dunite and near 30 m in the 50 m wide dunite) may reflect the locations of former harzburgite islands recently relieved of all their pyroxene.

3. Compositional variation with dunite width

Although dunite compositions are relatively constant across each transect, we observe systematic changes in the mean composition of minerals in dunites with increasing dunite width. The smallest dunite has mineral compositions similar to those in the harzburgite. However, with increasing width, dunites exhibit a 10% drop in the Ni content, a 2-unit drop in Mg#, a 300% increase in TiO_2, and a 7-unit increase in Cr# (figure 9a-d). Possible explanations for these variations are addressed in the discussion section.

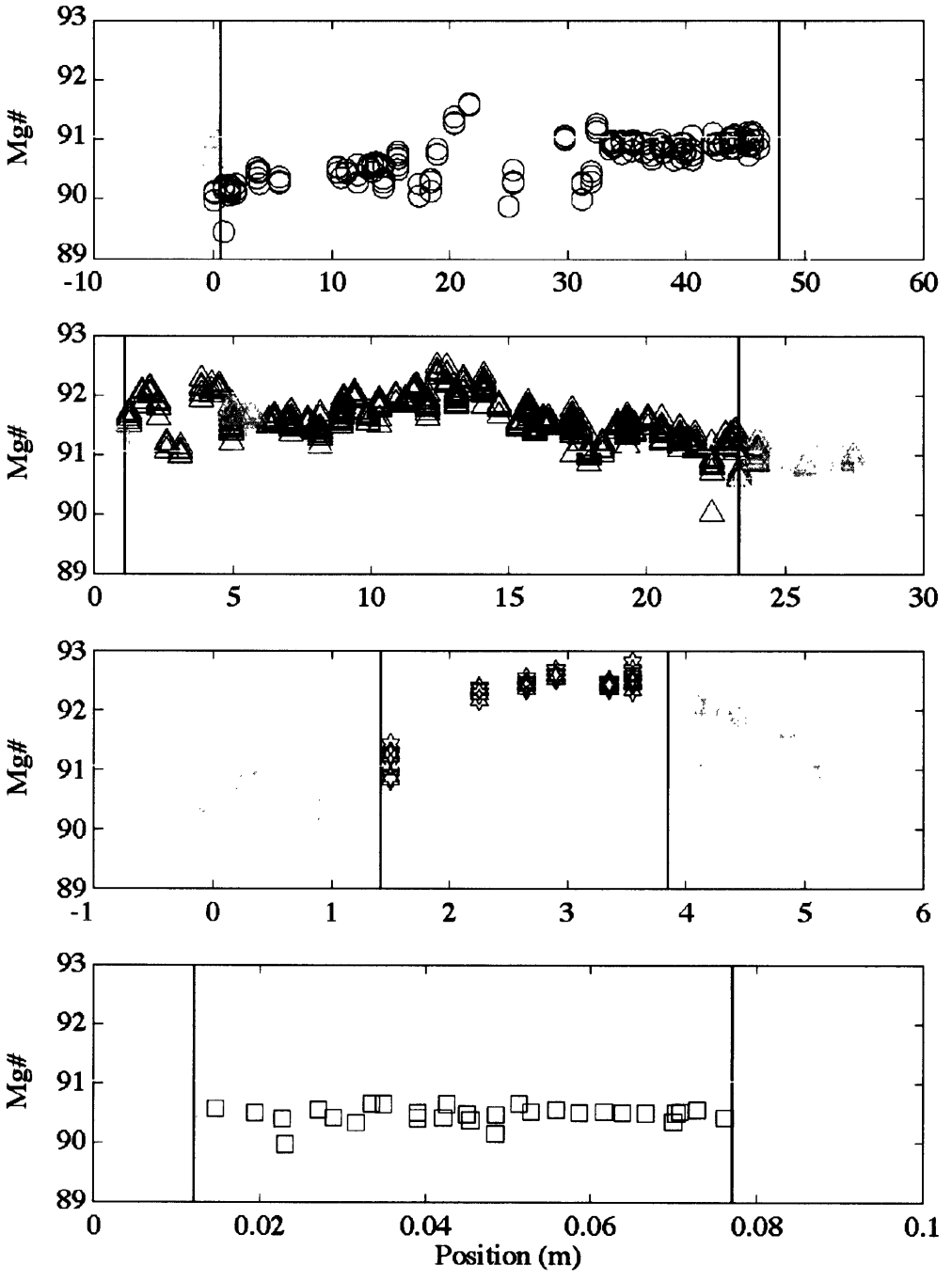

Figure 4. Profiles of Mg# across a) 50 m, b) 25 m, c) 3m, and d) 7cm wide dunites. Each symbol represents an individual analysis. Vertical lines indicate the position of the lithologic contacts observed in the field between each dunite (black) and the surrounding harzburgite. Horizontal dashed line indicates the mean harzburgite composition which includes the data from Wadi Tayin. Symbols are the same as in figures 2 and 3.

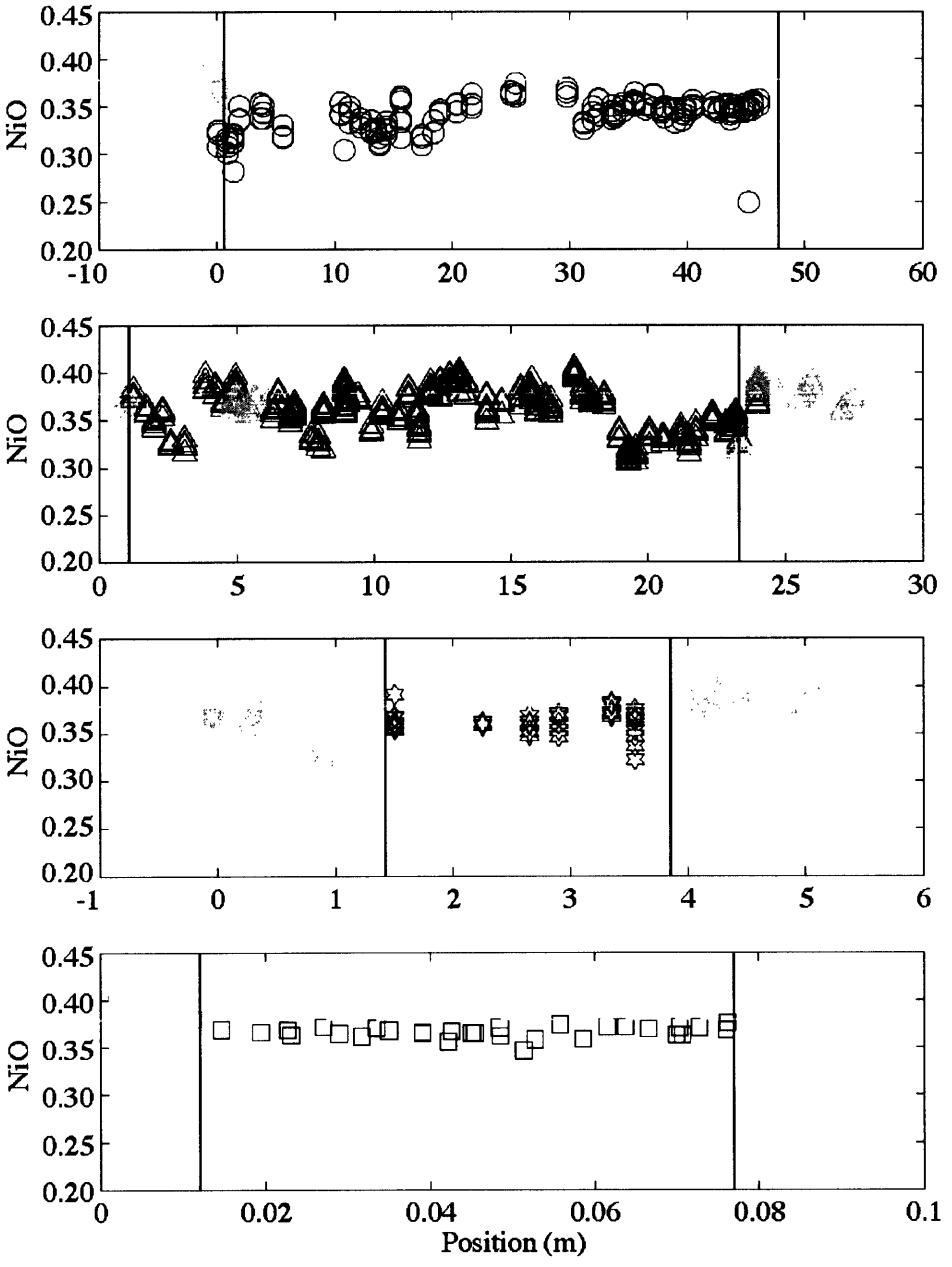

Figure 5. Profiles of NiO (wt%) in olivine across a) 50 m, b) 25 m, c) 3m, and d) 7cm wide dunites. See figure 4 for additional details.

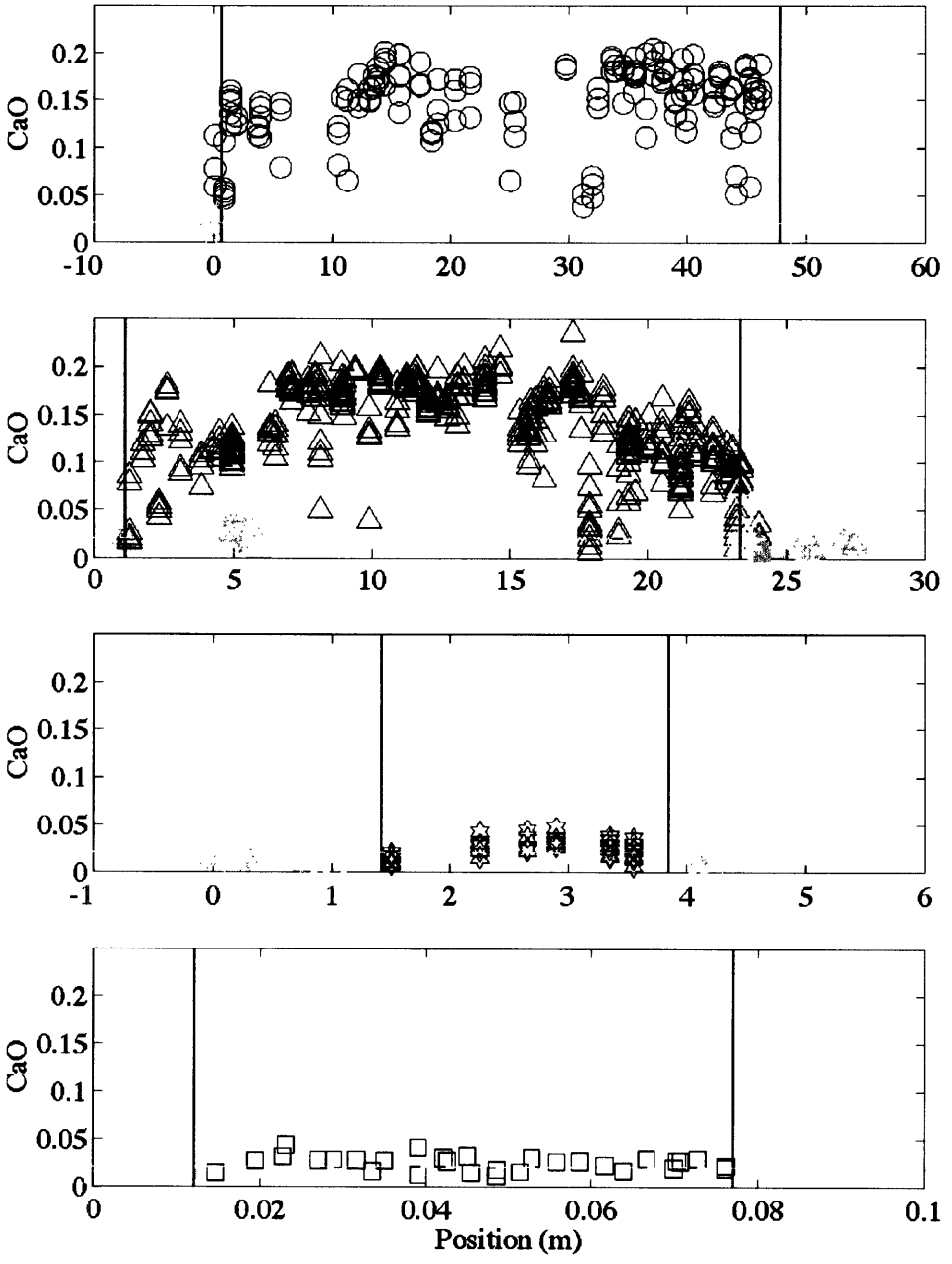

Figure 6. Profiles of CaO (wt%) in olivine across a) 50 m, b) 25 m, c) 3m, and d) 7cm wide dunites. The CaO contents in olivines at the centers of dunites are in equilibrium with the liquid parental to the Oman dikes and lavas. However, the low CaO values within 1-2 m of the contact are likely related to subsolidus exchange with pyroxenes in the harzburgite. See figure 4 for additional details.

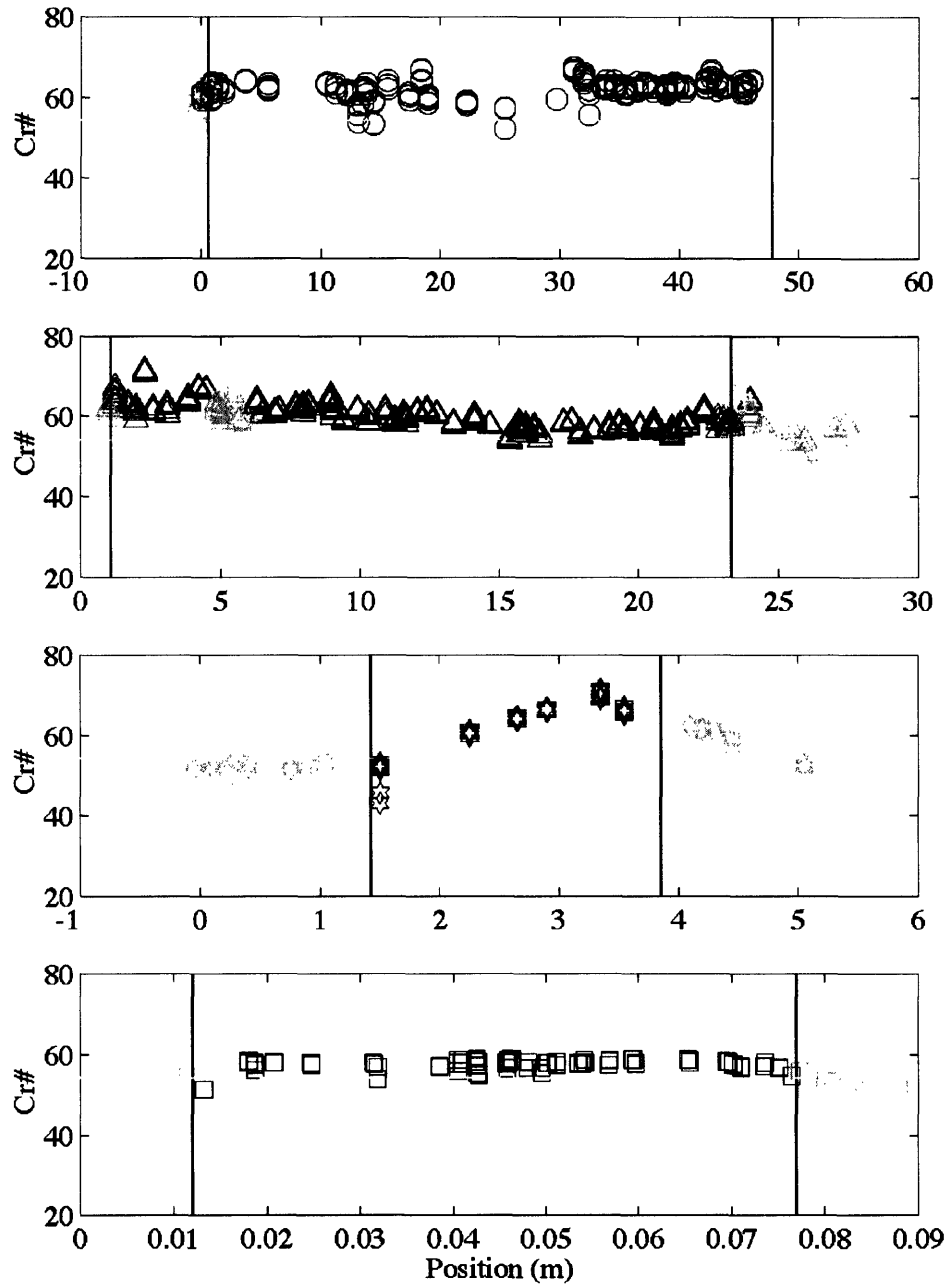

Figure 7. Profiles of spinel Cr# across a) 50 m, b) 25 m, c) 3m, and d) 7cm wide dunites. Cr# is typically higher in the dunites than in the harzburgite. See figure 4 for additional details.

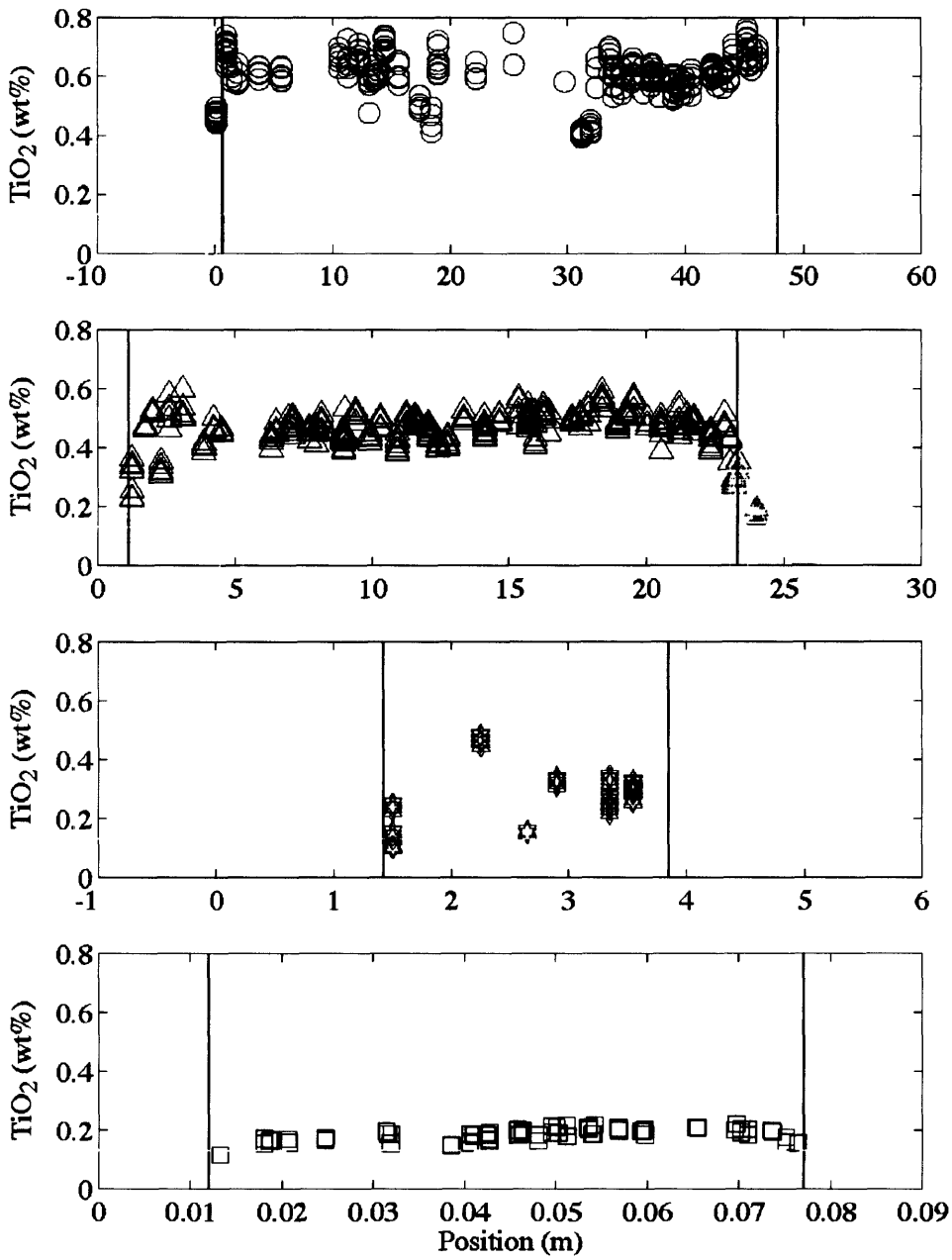

Figure 8. Profiles of TiO_2 (wt%) in spinel across a) 50 m, b) 25 m, c) 3m, and d) 7cm wide dunites. TiO_2 is consistently higher in dunites than harzburgites and increases with increasing dunite width. See figure 4 for additional details.

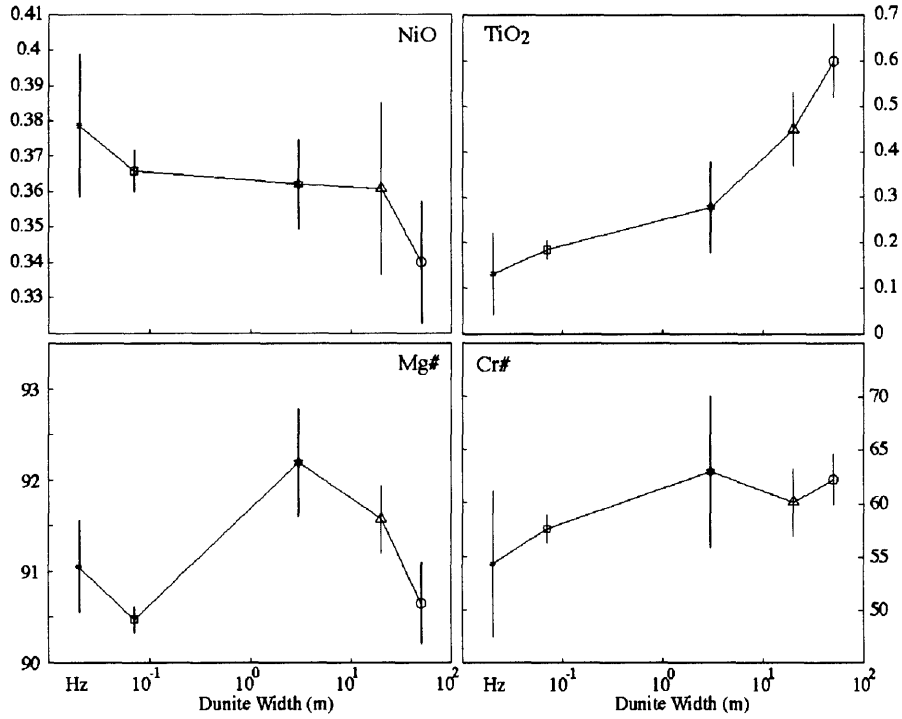

Figure 9. Variation in olivine and spinel composition with dunite width. a) NiO decreases with increasing dunite width, whereas b) TiO_2 and d) Cr# increase. c) The variation in olivine Mg# is more complex. Mg# increases rapidly between small and moderate width dunites then decreases with increasing width.

In the widest dunite, the major and minor element compositions of olivine and spinel, and to a lesser extent trace element concentrations in clinopyroxene, are close to equilibrium with the inferred composition of primitive Oman lavas (Table 1). The major elements in the dikes and lavas vary systematically with the Mg# of the liquid (figure 10) and may therefore represent a single liquid line of descent. From these trends, the composition of the liquid parental to the Oman lavas and dikes can be estimated by back-fractionating olivine and spinel (± plagioclase and clinopyroxene) from the most primitive of the observed compositions. During back-fractionation, equilibrium olivine and spinel are progressively added, in 0.5% increments, to the liquid until it reaches equilibrium with olivine in the widest dunite (Mg#=90.8). Equilibrium compositions are determined using partition coefficients derived from experiments, for Fe-Mg [*Gaetani*

and Grove, 1998], Ni [*Hart and Davis*, 1978], and Ca [*Libourel*, 1999], assuming equilibration at 1300°C and 5 kb. Based on the observed proportion of olivine to spinel in mantle peridotites, for each unit mass of olivine added back to the liquid, 1% of that mass in spinel is added. The total mass added is 15% of the mass of the initial liquid. The composition of the inferred parental liquid is indicated by the star in figure 10.

The observed increase in the CaO and Al_2O_3 contents with increasing Mg# in the lavas suggests that these lavas may have fractionated substantial amounts of plagioclase and clinopyroxene in addition to olivine and spinel. To address this possibility, we performed a similar back-fractionation calculation which included these phases. For each mass of equilibrium olivine added, twice the mass in both plagioclase and clinopyroxene were added to the liquid. The liquid reach equilibrium with Fo90.8 olivine after ~37% mass addition, relative to the initial liquid mass. Representative plagioclase and clinopyroxene compositions were taken from Oman gabbros reported by Pallister and Hopson [1981]. The estimated parental liquid composition after gabbro back-fractionation is shown by the squares in figure 10.

The true liquid line of descent, if only one unique path generated all the lavas measured in this study, is unlikely to involve saturation in only olivine and spinel or all four phases during the entire cooling history. Instead, each of the phases would appear at various points along the descent path. Therefore, these two back-fractionated liquids are potential end-members, between which lies the composition of the real parental liquid.

Because Ni is compatible in olivine, equilibrium olivine addition increases the NiO content of the liquid. Back-fractionation to equilibrium with Fo90.8 olivines predicts a primitive liquid with 0.02-0.04 wt% NiO (150-300 ppm Ni). Given the Ni partition coefficient (in wt%) based on the MgO content of the liquid (14.25 wt%) [*Hart and Davis*, 1978] is ~8, the NiO content of olivines in equilibrium with the primitive liquid would have ~0.3 wt% NiO, which is the concentration observed in olivines from the widest dunite.

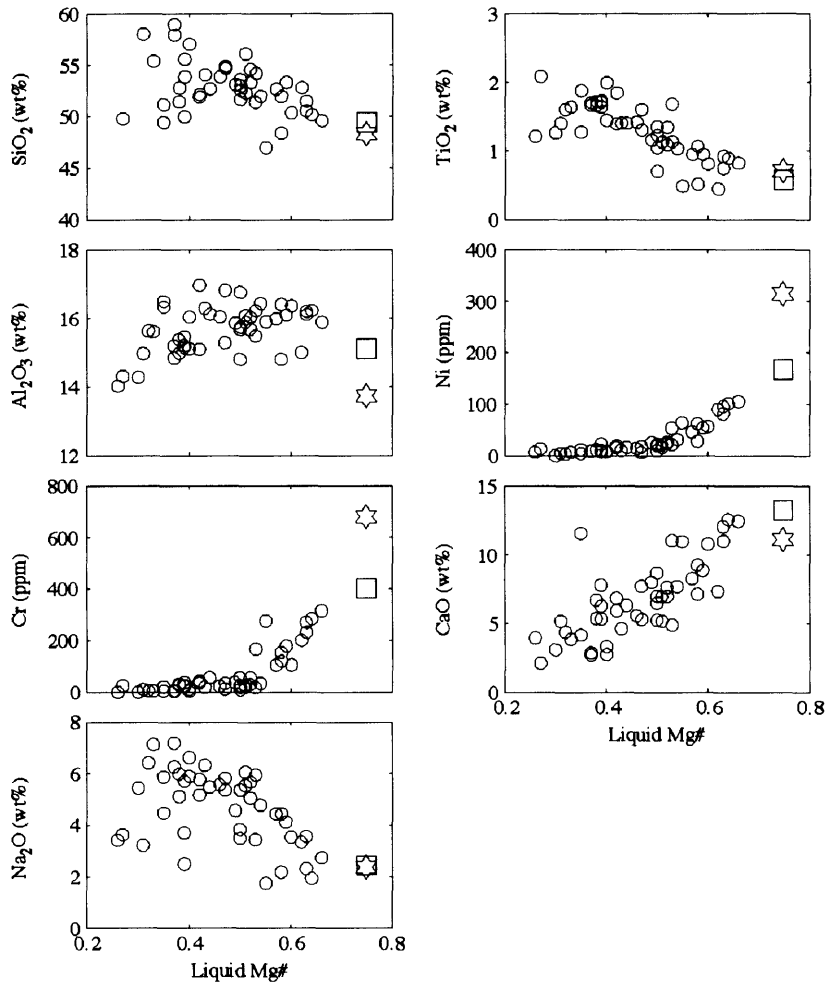

Figure 10. Composition of dikes and lavas from the Samail and Wadi Tayin massifs. Oxides exhibit systematic variation with the lava Mg#, indicative of a liquid line of descent from a common parental liquid. Back fractionation of olivine+spinel (✡) and olivine+spinel+plagioclase+clinpyroxene ( ) bound the composition of the parental liquid.

The Ca contents of olivines in the centers of the wide dunites (~0.2 wt%) may also reflect equilibrium with the primitive mantle-derived liquid. The lavas and dikes from Oman indicate parental liquids with Ca contents of ~11-13 wt%, similar to primitive MORB (as defined by liquids with Mg#> 66 taken from PetDB, the global MORB database). Based on olivine/melt partitioning experiments [*Libourel*, 1999], the predicted olivine CaO content is 0.19-0.26 wt%, similar to the olivines in the centers of wide dunites.

The CaO content of olivines in the wider dunites decreases substantially within a

few meters of the contact with the harzburgite. This variation is most likely related to subsolidus redistribution of Ca rather than differences in melt composition in the dunite during formation at igneous conditions. Although, the high, uniform CaO contents of olivines away from the contacts of the wide dunites likely record equilibration with primitive Oman melt, applying the same partition coefficient argument (using Libourel, [1999]) to the composition of the low-Ca olivines predicts a liquid with less than 4.25 wt% CaO. Although glasses with such low CaO contents have been observed at mid-ocean ridges, they uniformly have ~70 wt% SiO_2, Mg#'s less than 20, and represent less than 0.4% of the total MORB database. Because these are not the compositions of primitive melts in the mantle, we infer that the low Ca contents in olivines within a few meters of the harzburgite contacts (which includes all the samples from the two narrow dunites) are the result of subsolidus loss of Ca from olivine to proximal orthopyroxene.

TiO_2 contents of spinel also reflect equilibrium with the primitive liquid. For the purposes of back-fractionation, we assume that Ti is completely incompatible in olivine. After back-fractionation, the primitive liquid contains approximately 0.6-0.7 wt% TiO_2. Thermodynamic solution models for Ti equilibrium between spinel and melt suggest partitioning is a complex function of the major element composition of both the solid and liquid [*Poustovetov et al.*, 2001]. However, for simplicity in calculation, we employ the exponential relationship between the Cr# of the spinel and the concentration ratio of the spinel and coexisting melt observed in natural oceanic samples [*Allan et al.*, 1988; *Gaetani et al.*, 1995; *Hawkins and Melchior*, 1983; *Hawkins and Melchior*, 1985] (figure 11). An exponential fit to the data yields the following partitioning relationship: $K_{Ti}^{sp}=\exp(0.0359\times Cr\#-2.26)$. Given the Cr# of the spinels in the widest dunite are ~62, the predicted TiO_2 content of the spinels in equilibrium with the primitive liquid is 0.58-0.68 wt%, similar to what is observed in the spinels.

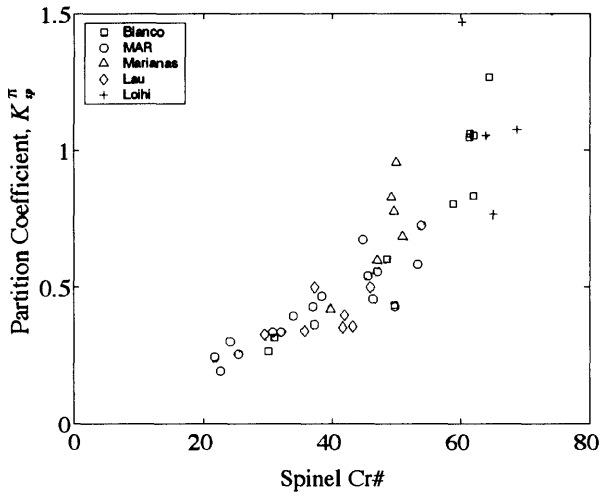

Figure 11. Relationship for TiO_2 partitioning as a function of spinel Cr# between spinel and basaltic melt. The compositions of spinels and coexisting basalt are taken from a variety of marine volcanic environments [*Allan et al.*, 1988; *Gaetani et al.*, 1995; *Hawkins and Melchior*, 1983; *Hawkins and Melchior*, 1985].

Clinopyroxenes preserved in the widest dunite also suggest near-equilibrium with the liquids parental to the dikes and lavas in Oman. The estimated REE content of the parental lavas is based on back-fractionation of olivine from dikes and lavas with measured Mg#s greater than 60. Of the 41 samples, 6 fit this criterion. Figure 12 shows that the chondrite-normalized REE concentrations of these lavas are nearly indistinguishable from primitive MORB glass [*Frey et al.*, 1993]. The trace element compositions of the observed liquids are listed in table 1. Clinopyroxenes from the 50 m wide dunite are moderately depleted in rare earth elements, but significantly more light-REE enriched than residual harzburgites from Oman [*Kelemen et al.*, 1995] or the seafloor [e.g. *Johnson et al.*, 1990]. Calculated liquids in equilibrium with these clinopyroxenes are determined using the mineral/melt partition coefficients of Hart and Dunn [1993]. The liquid composition based on the median of 42 clinopyroxenes falls slightly below that of the Oman and MORB lavas, similar to previous measurements [*Kelemen et al.*, 1995].

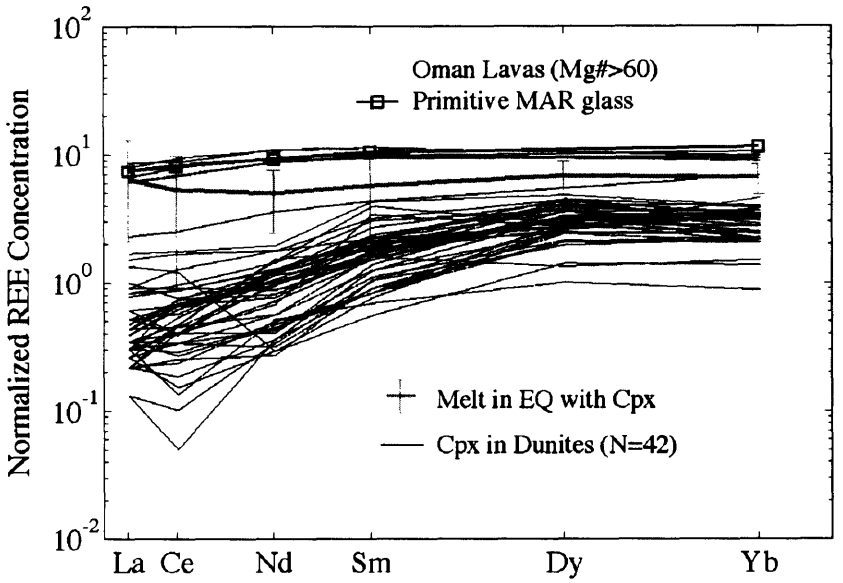

Figure 12. Rare earth element (REE) concentrations in lavas (Mg#>60) and dunite hosted clinopyroxenes (cpx) from Oman. Measured lava concentrations have been adjusted via olivine back-fractionation as described in the text. Calculated liquids in equilibrium with the mean cpx composition (thick gray line with 1σ error) are similar to the primitive liquids which are indistinguishable from primitive MORB glass [*Frey et al.*, 1993].

The major and trace elements of both the solid and liquid phases measured in Oman, particularly in wide dunites, are distinct from the compositions of other ophiolitic peridotites that exhibit equilibration with highly-depleted liquids. Suhr et al. [2003] present a comprehensive suite of geochemical profiles across dunites from the Bay of Islands (BOI) ophiolite. Although several aspects of these data are similar to our observations in Oman, Suhr et al show that the composition of the large dunites in BOI record transport of strongly depleted melts. In particular, the dunites are dominated by olivines with high Mg#'s (92-95), spinels with less than 0.15 wt% TiO_2, and replete with REE-depleted clinopyroxenes. Additionally, Suhr et al. observe a monotonic increase in Mg# with dunite width but no relationship between either TiO_2 or NiO with width.

The variations in mineral compositions with width in BOI dunites are distinct from the trends seen in Oman and are consistent with equilibration of increasingly depleted melts in wider dunites. Primarily, BOI dunites exhibit a monotonic increase in olivine Mg# with width to values much higher than observed in residual peridotites in

Oman. The olivine NiO contents are slightly higher than in Oman and the spinel TiO_2 contents are lower, as is observed in ultra-depleted melt inclusions in olivine [*Sobolev and Shimizu*, 1993] and the more refractory dikes in BOI [*Suhr et al.*, 2003] and Oman [*Python and Ceuleneer*, 2003]. Neither Ni or Ti show any appreciable change with dunite width.

Discussion:

Rather than inferring chemical interactions solely from compositional variations in erupted lavas or dredged peridotites, the exposures in Oman offer the opportunity to integrate the variations in the composition of residual peridotites with the spatially-associated lavas and the morphology of the melt conduits themselves to constrain the mechanisms by which dunites form and the composition and flux of melts they transport. The geochemical trends observed in Oman peridotites, and in particular from Wadi Lufti, closely follow those documented in abyssal peridotites (figures 2 and 3). The similarities in chemical trends seen in Oman and abyssal peridotites suggest that the igneous processes which formed the rocks now in the ophiolite are comparable to those that occur beneath modern oceanic spreading centers. The similarities between the Oman lavas and dikes presented here and primitive MORB (figure 12) augment this hypothesis. Whether or not the Oman ophiolite was formed at a mid-ocean ridge or back-arc spreading center is still a matter of debate [*Pearce et al.*, 1981]. However, we do observe that multiple phases in the widest dunites are in major, minor, and, to a lesser extent, trace element equilibrium with liquids parental to the Oman extrusives, implying these wide dunites are conduits for the transport of primitive melts to the surface.

Given the paucity of compositional and morphological data on dunites from active mid-ocean ridges, the observed covariations in olivine and spinel composition from Oman and their relationship to dunite width are the best constraints for addressing how dunites form beneath oceanic spreading centers in general and whether they could be the primary conduits for chemically-isolated melt transport in the sub-ridge mantle.

Two distinct melt migration mechanisms have been proposed to explain the

formation of replacive dunites in the adiabatically upwelling mantle. One option is that melt migration occurs in fractures induced by melt overpressure [*Nicolas*, 1990; *Suhr*, 1999]. In this view, dunites are produced by diffusive interaction between the melt migrating through a fracture and interstitial melts in the host rock. Alternatively, melt may migrate entirely by porous flow, and dunites could represent high-porosity conduits into which undersaturated melts are focused. The detailed geochemical transects presented here provide a means to discriminate between these mechanisms of dunite formation.

1. Dunite nucleation around cracks

If dunites form by reaction around melt-filled fractures, then the compositional profiles should reflect the lateral diffusive transport of material between the fracture and the reaction front, or from the reaction front into the harzburgite, as is observed in laboratory experiments [*Morgan and Liang*, 2003]. Specifically, profiles of elements with significantly different diffusivities and partition coefficients (such as Ni, Fe, Ca, and Ti) should exhibit different gradients away from the melt source. However, we observe sharp dunite/harzburgite transitions in both olivine and spinel composition (figures 4-8) and in the orthopyroxene mode (the primary reflection of the silica transport inherent to the dissolution reaction). Additionally, the time required for silicon diffusion around a melt-filled fracture to form the wide dunites (which preserve the most primitive melt signatures) is longer than the residence time of solid material in the melting region. [*Braun and Kelemen*, 2002]. Instead, dunite compositions are relatively constant across their width. No distinct centralized peak in concentration, indicative of the location of the annealed fracture, was observed.

Takahashi [1991; 1992] and Suhr [1999] argued that flat profiles across dunites with sharp contacts form within fractures which drained melt from the adjacent harzburgite and/or precipitated olivine in the fracture. Because the melts drained from the harzburgite were generated in situ, they are in equilibrium with the harzburgite and cannot dissolve any orthopyroxene. Precipitation of significant volumes of olivine within

the hydrofracture, enough to produce dunites several meters wide, is inconsistent with replacive nature of the contacts observed in the field [*Kelemen et al.*, 1995].

From the geochemical data presented here we find no conclusive evidence that requires the presence of melt-filled fractures existing within dunites. The absence of evidence, however, cannot disprove the hypothesis. A hydrofracture origin is plausible for the small dunites which cross-cut the peridotite foliation at high angles. These dunite dikes, which locally contain several percent plagioclase and clinopyroxene [*Python and Ceuleneer*, 2003] likely formed in the conductive boundary layer just below the crust. However, the formation of hydrofractures in the melting region beneath a ridge is mechanically unlikely. A permeability barrier is required to develop significant melt overpressures to initiate hydrofracture, but such a sharp decrease in permeability in the adiabatically-upwelling portion of the melting region would be difficult to maintain because the melt fraction is typically increasing due to melting and reaction with primitive melts [*Kelemen et al.*, 1997]. Additionally, mechanical data from laboratory experiments indicate that the viscosity of peridotite at upper mantle conditions is sufficiently low to deform at geologic strain rates at very small differential stresses (~1 MPa) [*Hirth and Kohlstedt*, 2003]. Therefore, if a localized melt overpressure were to develop, the stress around it would easily be dissipated by viscous decompaction before it was large enough to induce hydrofracture.

2. Dunite nucleation by reactive porous flow

An increasing body of evidence indicates that dunites represent high-permeability conduits initiated as dissolution instabilities during reactive porous flow. The reaction of harzburgite at shallow pressure with melt derived from higher pressure results in dissolution of orthopyroxene, crystallization of a smaller mass of olivine, and an increase in the liquid mass [*Kelemen*, 1990]. The increase in porosity increases the local permeability, allowing an increased flux of reactive melt into the region, enhancing dissolution. This positive feedback can rapidly form a coalescing network of high

permeability channels which focus melt transport [*Aharonov et al.*, 1995; *Kelemen et al.*, 1995; *Spiegelman et al.*, 2001].

The dunite channels, once formed, would grow wider with time. Percolation models based on melt topology in peridotites indicate that dunites are more permeable than harzburgites. The decrease in mean dihedral angle associated with the decreasing abundance of pyroxene [*Toramaru and Fujii*, 1986; *Zhu and Hirth*, 2003] coupled with the increase in porosity by reaction suggest that, once formed, dunites may serve as high permeability conduits for continued focused melt transport. Sustained transport of opx-undersaturated melts will widen the conduit with time by reaction along the margins [e.g. *Spiegelman et al.*, 2001].

The peridotites from Wadi Lufti exhibit distinct compositional variations which imply that dunite width is related to composition of melt which passed through it. Because the chemical covariations also follow trends commonly observed in abyssal peridotites (figures 2 and 3), we can use our observations from Oman to address whether porous dunites conduits are the primary conduits for the transport of primitive MORBs which form the oceanic crust.

The variation in mineral composition with dunite width (figure 9) may reflect either variations in melt composition derived from mixing of depleted and primitive liquids, or the reaction of harzburgite with a primitive liquid and the continued flux of that melt through the resulting dunite. By comparing the predictions of these two models to the observed geochemical variations, we can constrain the proportion of primitive melt which flowed through the dunites and quantify the melt/rock ratio.

3. Variable magma composition

The widest dunites in Oman are in equilibrium with primitive melts from deep in the melting column. In contrast, the harzburgites are the residues of high-degree, polybaric partial melting in equilibrium with shallow depleted melts. In this section, we compare the observed chemical variations with the calculated composition of dunites in equilibrium with mixtures of primitive and depleted melts.

We offer three probable mechanisms which could result in mixing of primitive and depleted liquids in a coalescing network of porous conduits: 1) diffusive chemical exchange between melts in the dunite and the surrounding harzburgite; 2) compaction-enhanced "suction" of melts into the dunite from the adjacent, lower-permeability harzburgite [*Spiegelman and Kelemen*, 2003]; and 3) addition of more depleted melts from smaller tributaries in the coalescing network. Any combination of these mechanisms could be responsible for contributing depleted melts to the deeper-derived melts ascending in dunites, independent of the dunite width. However, melt addition along dunite margins is more likely to affect narrow dunites because the added melt represents a larger fraction of the total flux in narrow dunites in comparison with the total flux in wider dunites. The increased mixing in small dunites could therefore create the observed compositional variations with width. Field evidence from Oman suggests that porosity may increase with increasing dunite width [*Braun and Kelemen*, 2002] making the effect of peripheral melt addition even more pronounced in narrow dunites than in wide ones.

To test this mixing hypothesis, we calculated the composition of dunites in equilibrium with mixtures of depleted and primitive end-member liquids to compare them with the observed geochemical variations. The primitive melt composition is assumed to be that of the liquid parental to the dikes and lavas observed in Oman (table 2). For the depleted end-member, we use the composition of ultra-depleted melt (UDM) inferred from olivine-hosted melt inclusions collected from the seafloor [*Sobolev and Shimizu*, 1993]. The major element composition of UDM is close to equilibrium with the Oman harzburgites. However, the Ni content of UDM has not been measured, so we assert the Ni content of the depleted melt is 0.036 wt%, to be in equilibrium with the observed harzburgite composition. The higher Ni content, relative to the parental Oman liquid, is justifiable because Ni is compatible in olivine. Partial melting of harzburgite will increase the Ni content of the depleted residue relative to the more-fertile source rock.

The compositions of olivine and spinel in equilibrium with these liquids are best

reproduced using the following mineral/liquid partition coefficients, several of which vary with the composition of the liquid: K_{ol}^{Fe-Mg}=0.28-0.30 [*Gaetani and Grove*, 1998], K_{ol}^{Ni}=10.5-11.7 (wt%) [*Hart and Davis*, 1978], K_{sp}^{Ti} =0.76-0.25 (wt%), and K_{sp}^{Cr}=400, K_{sp}^{Al}=1.8. As described in the results section, the spinel partition coefficients used here are derived from the compositions of natural spinels (figure 13) and the coexisting basalts from a variety of oceanic environments [*Allan et al.*, 1988; *Gaetani et al.*, 1995; *Hawkins and Melchior*, 1983; *Hawkins and Melchior*, 1985]

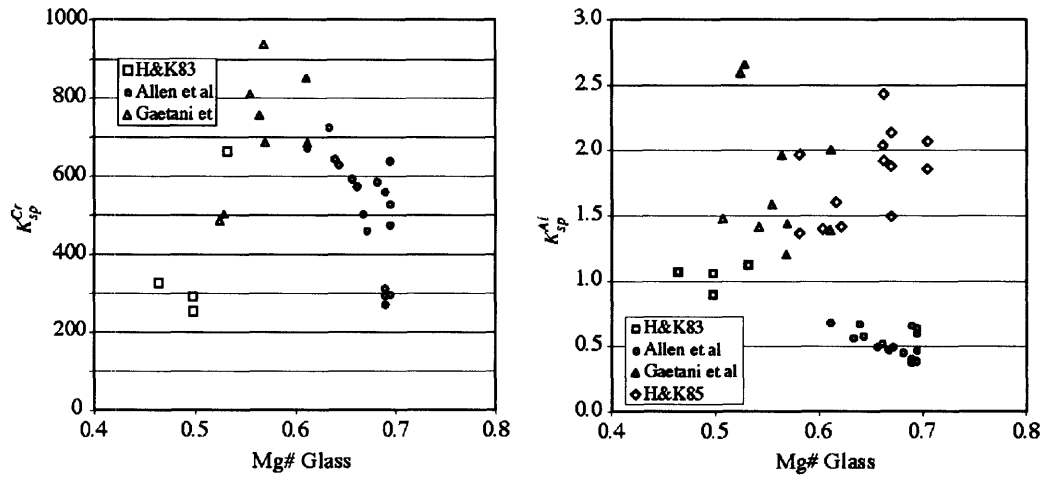

Figure 13. Observed partitioning of Cr and Al between natural spinels and their basaltic host lavas from several marine environments.

Figure 14 shows the evolution of the calculated equilibrium dunite composition as the ratio of depleted to primitive melt in the mixture varies from 0.01 to 100. The general compositional trends in the data are reproduced in this model. However, the model fails to reproduce the observed variation in olivine Mg# (figure14 b and c) because simple mixing cannot increase the Mg# beyond that of either end-member. As a result, the systematic trend of decreasing olivine Mg# with increasing TiO_2 and increasing dunite width is not seen in the model.

Using a depleted melt composition in equilibrium with the higher Mg# dunite samples would yield a better fit to the data. However, simply defining a melt based on

the dunite composition is circular in reasoning and provides no explanation for the origin of a liquid more depleted than the most depleted residues.

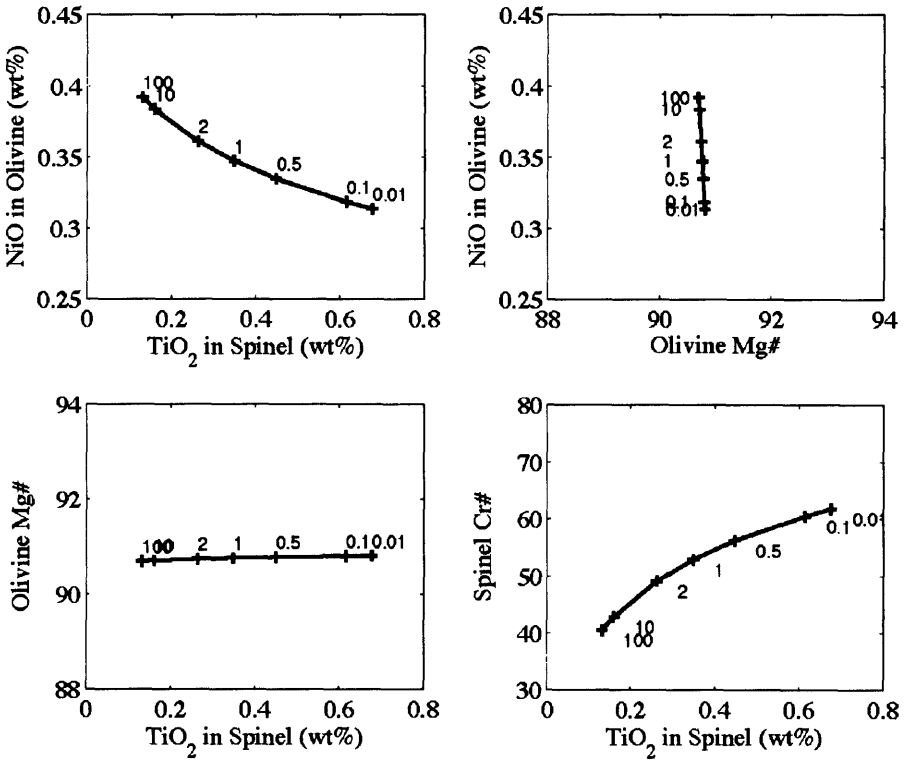

Figure 14. Dunite compositions in equilibrium with various mixtures of depleted and primitive melts. The depleted end-member is taken to be UDM and the primitive end-member is derived by back-fractionation of olivine and spinel. The ratio of depleted to primitive melt in the mixture is indicated at each tick mark. The mixing model reproduces much of the observed variation in Oman dunites (closed circles) and harzburgites (open circles) but cannot account for the observed high in Mg# in small dunites.

4. Reaction with a Primitive Liquid

We can better match the observed chemical variations, especially the changes in Mg# with dunite width, by incorporating orthopyroxene dissolution into a mass-balance model for peridotite composition with increasing melt/rock ratio. We approximate the geochemical evolution of peridotite during reactive melt transport by calculating the equilibrium composition of a fixed mass of harzburgite with an increasing mass of melt.

The mass balance between the initial peridotite and the increasing mass of primitive liquid is accomplished in two stages: a dunite formation stage to account for

mass redistribution during reaction of the harzburgite and a dunite flux stage which describes the equilibration of the newly formed dunite with an increasing melt mass.

During reaction, the change in phase proportions is dependent upon the reaction stoichiometry and the melt/rock ratio. As opx is consumed by reaction with the primitive liquid, olivine and spinel are precipitated and the liquid mass increases. This reaction is described (in mass units) as

1 OPX + 1 $MELT_1$ --> n_{ol} OLIVINE + (2-n_{ol}) $MELT_2$,

where n_{ol} is the mass of olivine precipitated per unit mass of opx consumed. The reaction stoichiometry is not known precisely. Based on the ratio of the apparent heats of fusion of olivine and opx at 1300°C, Kelemen [1990] estimated n_{ol} to be approximately 0.7 for isobaric and either isothermal or isenthalpic conditions and constant pressure. This result has been confirmed experimentally by Daines and Kohlstedt [*Daines and Kohlstedt*, 1994]. However, n_{ol} less than 0.7 could result, for example, from reaction during adiabatic decompression. For the purposes of testing the sensitivity of the model in relation to the data observed in Oman, we explore a range in n_{ol} of 0.1 to 0.7.

We define the melt/rock ratio, ξ, as the mass of the melt phase relative to that of the initial harzburgite mass. To adequately resolve the chemical changes during the initial stages of dissolution as well as the evolution of the dunite at high ξ, the melt/rock ratio is varied from 0.001 to 1000 with a non-linear step size. The critical melt/rock ratio, ξ_{crit}, at which dissolution is complete is determined by the degree of opx-undersaturation and the abundance of opx in the initial harzburgite. A harzburgite with ~20% orthopyroxene reacting at 2 kb with melt formed at an average pressure of 12 kb, would require approximately twice its mass in liquid to dissolve opx completely [*Kelemen*, 1990; *Kelemen and Dick*, 1995; *Kelemen et al.*, 1997]. Based on the observations of solid phase abundance in the harzburgites from Oman, the initial harzburgite mode used for these calculations is 79% olivine, 20% orthopyroxene, and 1% spinel. Given the natural variation in the opx mode and, more importantly, the uncertainties in the silica activity of the primitive liquid, we allow the critical melt/rock ratio to vary from 0.5-4.

The equilibrium phase compositions for each melt/rock ratio are calculated via

three steps: determination of the bulk composition prior to reaction, modal adjustment due to reaction, and redistribution of elements into the new phase assemblage. The total content of each element, i, in the system, C^i_{tot}, is the sum of the initial composition, C^i_p, of each phase, p, times the modal proportion of the phase prior to reaction, X_p, or

$$C^i_{tot} = \sum C^i_p X_p . \qquad (1)$$

The initial compositions of each of the solid phases is listed in table 2.

The mass proportions of each phase after reaction (denoted with *) are a function of the reaction stoichiometry, n_p, the melt/rock ratio, ξ, and ξ_{crit} and can be expressed as

$$X^*_p = X_p - \frac{X_p}{\xi_{crit}} n_p \xi \quad \text{for } \xi \le \xi_{crit}. \qquad (2)$$

With each unit mass of primitive melt added, the elemental components of the dissolved mass of opx are redistributed amongst the remaining phases. The kinetics of opx dissolution are sufficiently rapid [*Brearley and Scarfe*, 1986; *Kuo and Kirkpatrick*, 1985] and the grain size in the harzburgites is small enough [*Braun and Hirth*, in prep] to assume local equilibrium is achieved between the peridotite and the pervasive interstitial melt. Therefore, by substituting the appropriate partition coefficient,

$$K^i_p = \frac{C^i_p}{C^i_{melt}}, \qquad (3)$$

for equilibrium between the phase p and the melt into equation (1), the concentration of each element in each phase can be determined,

$$C^i_{p^*} = \frac{C^i_{tot} K^i_p}{X^*_{melt} + X^*_{ol} K^i_{ol} + X^*_{opx} K^i_{opx} + X^*_{sp} K^i_{sp}}. \qquad (4)$$

Olivine partition coefficients are the same as those used for the olivine back-fractionation and melt-mixing models. For simplicity, we assume Ti, Cr, and Al are perfectly incompatible in olivine as is Ni in spinel. Orthopyroxene-melt partition coefficients are fixed at K^{Mg}_{op}=2.8, K^{Fe}_{op}=0.65, K^{Ni}_{op}=2.15, and K^{Al}_{op}=0.07 [*Colson et al.*, 1988]. Spinel partition coefficients are derived from ratios observed in natural spinels and the

coexisting basalts [*Allan et al.*, 1988; *Gaetani et al.*, 1995; *Hawkins and Melchior*, 1983; *Hawkins and Melchior*, 1985]. Partition coefficients for elements in phases without empirically determined values are based on the observed compositions of coexisting solid phases in the harzburgites. See table 3 for a complete listing of the partition coefficients and their sources.

The mass balance model with reaction produces simultaneous variation in olivine Mg#, NiO, and TiO_2 as a function of the melt/rock ratio (figure 15). Because opx has a lower Fe/Mg than the coexisting olivine, the incorporation of that Mg and Fe from opx into olivine by reaction subsequently raises the Mg#. Additionally, Fe is less compatible than Mg in olivine, so the increased liquid mass preferentially partitions Fe into the liquid, further increasing the olivine Mg#.

Once the melt/rock ratio increases beyond complete orthopyroxene dissolution, the Mg# drops as the bulk composition shifts towards olivine and spinel compositions in equilibrium with the ever increasing mass of primitive liquid. The Mg# of the primitive liquid is sufficiently low to draw the olivine Mg# back down.

The magnitude of the increase in the olivine Mg# is dependent upon the reaction stoichiometry, n_{ol}, and the critical melt/rock ratio, ξ_{crit}. As n_{ol} increases, the Mg# variation decreases because the high-Mg# opx reactant is diluted in a larger reservoir of olivine product. Over the range of n_{ol} examined, reaction raises the Mg# to 91.2-91.8 from its initial value of 90.8 (figure 15a – gray lines). At a fixed value of n_{ol}, increasing the critical melt/rock ratio, ξ_{crit}, decreases the influence of opx dissolution on the Mg# of the olivine by diluting the high-Mg# opx component in a larger mass of liquid (figure 15a – dashed lines). These results are similar to those of Suhr et al. [2003], although they were derived in a slightly different manner. Our model also continues past complete opx dissolution to model the return of the dunite composition to equilibrium with the primitive melt that formed it.

The model predicts that the concentration of Ni in olivine decreases moderately during opx dissolution and then drops further with increasing melt/rock ratio (figure 15b). Reaction decreases the olivine Ni content in proportion to the mass of olivine

precipitated. Orthopyroxene has a low Ni content, so reaction increases the olivine mass without appreciably changing the bulk Ni concentration. As a result, the finite mass of Ni in the system is diluted in an increasing mass of olivine. Increasing n_{ol} decreases the NiO concentration in the olivine. Regardless of the reaction stoichiometry, after dissolution is complete, the NiO content drops further as the dunite interacts with an increasing amount of melt with a low Ni concentration.

The observed differences in NiO between the dunites and harzburgite are larger than can be accounted for simply by Ni exchange between olivine and opx during cooling. For 1000°C of cooling, loss of Ni from opx would result in an increase of only 0.01 wt% (80 ppm) in the olivine NiO content [*Kelemen et al.*, 1998]. Although, cooling could account for some of the variation within harzburgite samples.

The model also predicts an increase in the spinel TiO_2 content with increasing melt/rock ratio (figure 15c). Reaction induces a sharp increase in Cr# as Cr is added to spinel from both the primitive liquid and the dissolving orthopyroxene. The elevated Cr content and Cr# of the primitive liquid relative to MORB perhaps reflect this effect of melt/rock reaction. The increase in Cr# has a distinct effect on the TiO_2 concentration. The Ti partition coefficient increases with the progressive increase in Cr#, raising the TiO_2 content in spinel. The increase in TiO_2 content after complete opx dissolution is mitigated slightly as Al previously held in the opx is distributed between the melt and the spinel, dropping the Cr#. However, once the liquid mass is large enough that the bulk Al content is not influenced by the opx component, the Cr# increases and the TiO_2 increase continues unfettered.

Although the model can reproduce the bulk of the Mg# variation, it can not explain the very high Mg#s (>92) observed in the data. The calculations are based on a fixed harzburgite composition. However, the Mg# of the harzburgites in Wadi Lufti vary considerably (figure 3). If instead of the average composition, a higher Mg# harzburgite is used as the starting composition, then higher olivine Mg#s can be attained by reaction. Some of the observed variations in harzburgite Mg# may be related to local variations in source composition and/or the degree of melting.

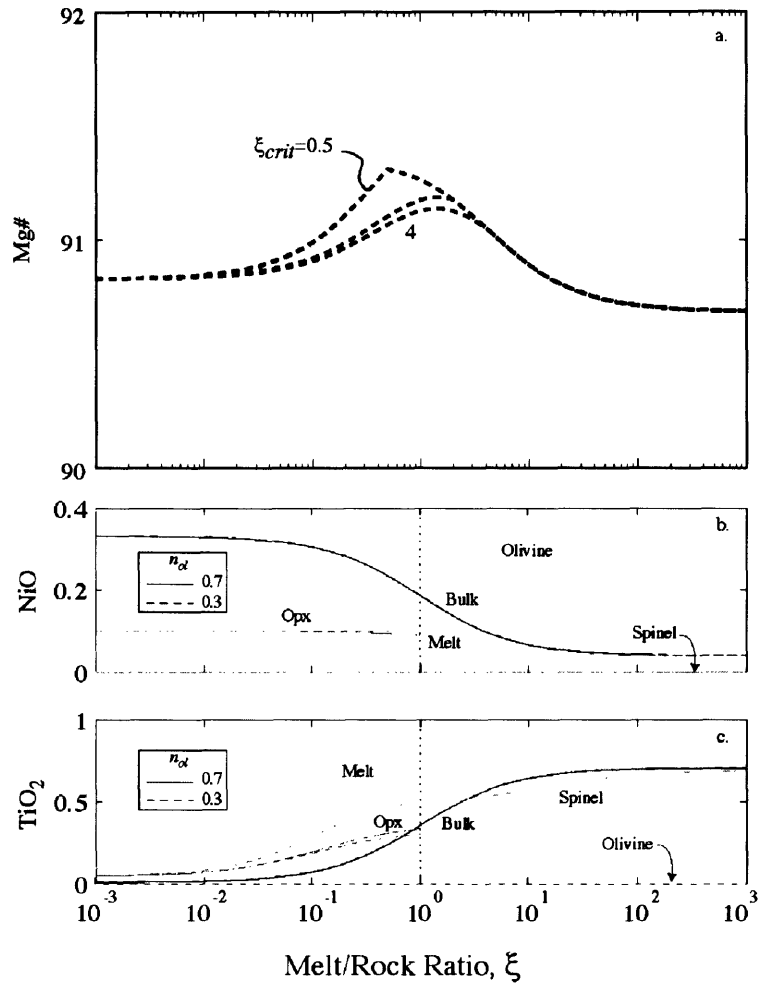

Figure 15. Variation in olivine Mg#, NiO, and TiO_2 as a function of melt/rock ratio derived from the mass balance model incorporating orthopyroxene dissolution. a) Progressive dissolution of opx with increasing ξ increases the Mg# in olivine which is then reset by the continued increase in liquid mass. The increase in Mg# depends strongly on the ratio of olivine precipitated during reaction to opx dissolved, n_{ol} (gray lines) as well as on the mass of melt required to completely dissolve opx from the rock, ξ_{crit} (dashed lines). Based on theoretical and experimental constraints, we assume n_{ol}=0.7 and ξ_{crit}=1 (dashed gray line) for the reaction modeling. b) NiO and c) TiO_2 variations within each phase as a function of melt/rock ratio for ξ_{crit}=1 and n_{ol}=0.3 and 0.7. As reaction progresses, the increase in olivine mass reduces it NiO content, as opx contains comparatively little NiO. Reaction also increases the TiO_2 content of the melt and spinel. The magnitude of the changes is sensitive to the value of n_{ol}, which dictates the mass changes during reaction.

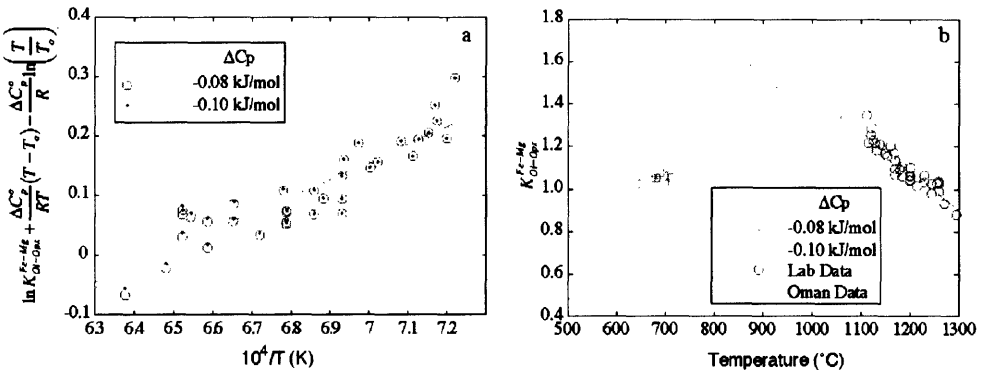

Figure 16. Calibration and performance of a preliminary olivine-orthopyroxene geothermometer. a) The thermometer is calibrated on olivine-orthopyroxene pairs from experiments at a variety of temperature and pressure conditions. Open circles represent data inverted using ΔC_p=-0.08425 kJ/mol. Dots are the same data inverted using ΔC_p=-0.1. b) The thermometer based on the experiments (open circles) predicts the temperatures derived from olivine-spinel thermometry [*Sack and Ghiorso*, 1991] and the measured K_{Ol-Opx}^{Fe-Mg}.

In addition to igneous compositional variations, the olivine Mg# in the harzburgite may be reduced by subsolidus diffusion. Olivine-spinel thermometry in the dunites indicates that significant diffusive exchange of Fe and Mg occurred down to temperatures of approximately 700°C. Although the spinel represents only a small fraction of the mass of the harzburgite, similar subsolidus re-equilibration with orthopyroxene may have significantly affected the Mg# of the olivines in the harzburgites.

Following Loucks [1996] we develop a preliminary olivine-opx thermometer to estimate the change in the Fe/Mg distribution coefficient, K_{Ol-Opx}^{Fe-Mg}, between the two phases with decreasing temperature. By assuming the heat capacities of olivine and opx are similar and do not vary significantly with temperature, olivine-orthopyroxene pairs from experiments [*Colson et al.*, 1988; *Gaetani and Grove*, 1998; *Gaetani et al.*, 1994; *Grove and Juster*, 1989; *Gudfinnsson and Presnall*, 2000; *Kinzler*, 1997] can be inverted to develop an predictive relationship between K_{Ol-Opx}^{Fe-Mg} and temperature (Figure 16a). The derivation and calibration of the thermometric relation is described in Appendix A.

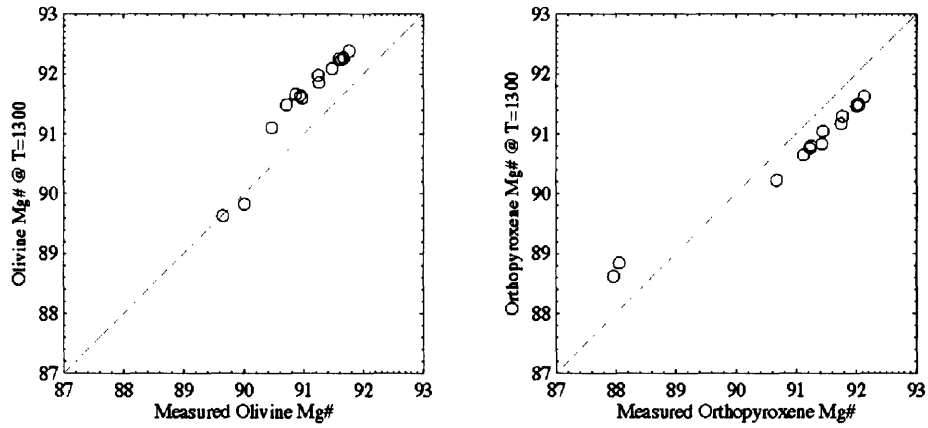

Figure 17. Olivine and orthopyroxene Mg#s following Fe-Mg repartitioning at 1300°C based on variations in K_{Ol-Opx}^{Fe-Mg} predicted by olivine-opx geothermometry. The derivation of repartitioning functions for each phase is described in appendix A.

The increase in K_{Ol-Opx}^{Fe-Mg} with decreasing temperature (Figure 16b) implies that more Fe was partitioned to the olivine while more Mg was segregated to the opx during cooling. Therefore, at igneous conditions, olivines in the harzburgites had a higher Mg# than the measured values would indicate. The 15% decrease in K_{Ol-Opx}^{Fe-Mg} associated with increasing the temperature from ~700°C to 1300°C implies, the mean Mg# would increase from 90.8 to 92 (figure 17), bringing the harzburgite olivines up to values commensurate with those measured in the narrowest dunite.

Given the uncertainties in the composition of the initial peridotite and the primitive liquid, we focus on four probable model solutions which reproduce the data from Oman. Figure 18 shows each of these models superimposed on the data from Oman. In all models, n_{ol}=0.7 and ξ_{crit}=1, consistent with the theoretical and experimental values, as discussed above.

The composition of the estimated parental liquid is dependent upon the crystal fractionation path and subsequently affects the Mg# of the olivines during reaction. Using the liquid composition obtained by back fractionation of olivine and spinel (figure 18a – open circles), the model predicts only a modest change in the olivine Mg# during reaction. However, a much larger increase in Mg# during reaction is observed if the gabbro fractionated liquid is used as the reacting liquid (figure 18a – open squares). The

change in model response is due to the differences in absolute concentrations of Fe and Mg between the two liquids. The Fe/Mg ratio is the same in both liquids, which is why the olivines evolve to the same Mg# at high melt rock ratios. However, the lower Fe content coupled with a partition coefficient less than 1 induces lower Fe contents in the coexisting olivine and orthopyroxene. Subsequently, the addition of that Fe-poor opx back into the system via reaction further boosts the Mg# of the olivine which is preferentially taking Mg over Fe.

As a consequence of the different concentrations (including K, Na, and Al) the partition coefficients are also slightly different. The effect on the magnitude of Fe-Mg is small. Using a purely temperature-dependent K_{ol}^{Fe-Mg} [*Roeder and Emslie*, 1970] rather than one which incorporates aluminate melt components [*Gaetani and Grove*, 1998] demonstrates that the effect of composition of the partition coefficient is small. However, the lower Cr/Al ratio in gabbro-fractionated liquid produces lower Cr# spinels during reaction which in turn reduces the change in TiO_2 of spinel (figure 18d).

In addition to the variations in the liquid composition, we have discussed the possibility that the composition of the initial harzburgite could vary due to subsolidus Fe-Mg exchange. Figures 18b and c also show the effects of varying the starting harzburgite Mg# between the mean of the observed values and the repartitioned value assuming Fe-Mg subsolidus exchange was important (solid and dashed lines, respectively). By correcting for Fe-Mg exchange at low temperature, the Mg# of the olivine increases and the Mg# of the coexisting opx decreases. The change in olivine Mg# during reaction is reduced owing to the smaller Fe/Mg ratio in the opx component, but less of an increase is necessary to fit the model to the data. Correcting for subsolidus Fe-Mg exchange has no effect on the evolution of the NiO content in olivine or Cr# and TiO_2 in spinel (figure 18 a,d)

These results suggest that the geochemical covariations observed in Oman reflect the time-integrated melt/rock ratio of the peridotite. In our model all dunites undergo the same formation process. The systematic variations in dunite composition with width imply a progressive overprinting of the reaction signature with that of the primitive melt.

Narrow dunites have not been completely overprinted and thus carried a smaller time-integrated flux. Whereas, wide dunites, which preserve equilibrium with primitive melts, were conduits for large masses of primitive melt (> 100 times that of the dunite).

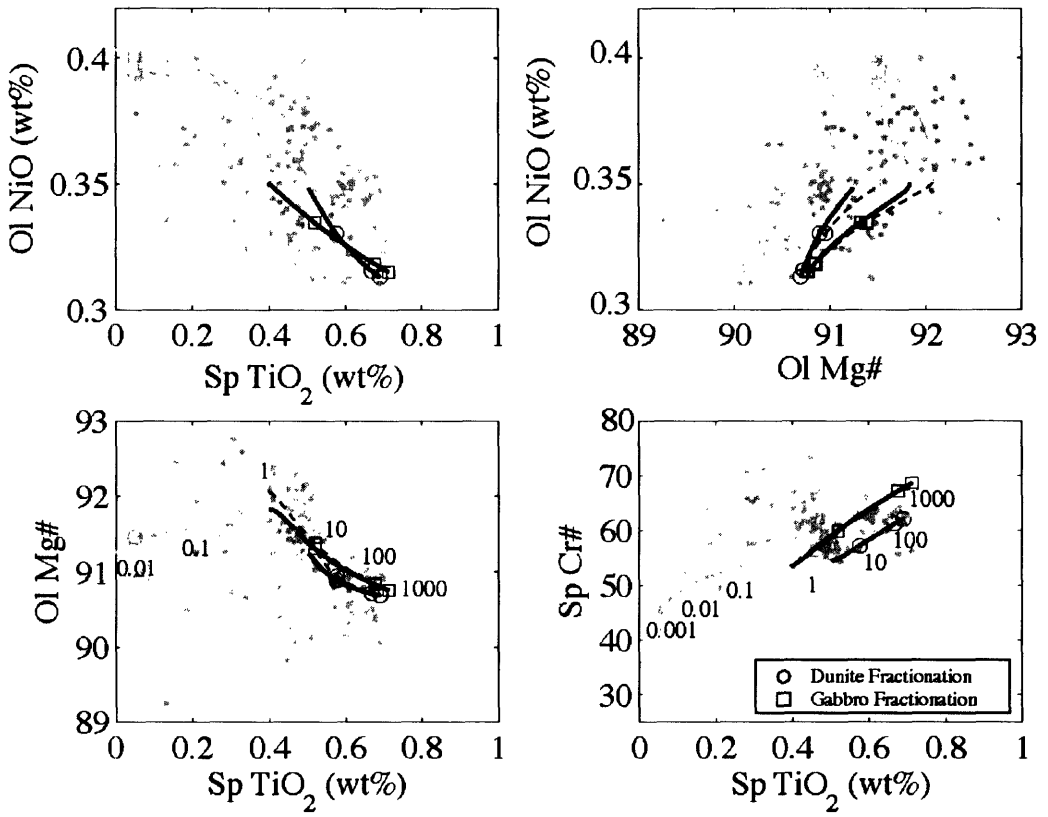

Figure 18. Model results for the evolution of the peridotite composition with increasing melt/rock interaction. Melt-rock reaction increases the olivine Mg# and spinel TiO_2 and Cr#, while decreasing NiO in olivine. Equilibration of the resulting dunite with an increasing mass of liquid drives the Mg# back down along with NiO, while the Cr# and TiO_2 continue to rise. The model curves reproduce the general trends observed in the data (figure 3). Harzburgites are plotted as small open circles, dunites as small filled circles. During opx dissolution, the line is shown in gray. Once reaction is complete, the line is black. Curves with large open circles delineate the peridotite evolution using the "dunite"-back-fractionated liquid. Squares designate the curves which used the "gabbro"-back-fractionated liquid. Symbols along each curve represent melt/rock ratios, from left to right in a,c,d, of 0.001, 0.01, 0.1, 1, 10, 100, 100.

Although the predicted changes in peridotite composition due to reaction span the range of the observed data, it does not imply that all compositional variation is related to reaction with opx-undersaturated melt. Analyses of numerous spinels in abyssal harzburgites show large variations in Cr# and Mg# which can arise from variations in

degree of melting and olivine fractionation, which certainly are occurring in the polybaric fractional melting regime beneath spreading centers. Because dunites are forming over a range of depths in the melting region, the melts which form them must also be variable. Mixing of these variable degree melts, by diffusion, compaction-driven flow, or injection from tributaries cannot be ruled out. The misfit between observed in composition of dunites and the model predictions likely reflect the variable contributions of these multiple processes.

5. Mass Balance in a Network of Dunites

The geochemical data in the context of the reaction-flux model presented here are consistent with field observations that suggest wider dunites have a higher melt/rock ratio than smaller dunites. Assuming dunites form a coalescing network of porous conduits in which magma flux is conserved, the observed power-law relationship between the abundance of dunites in Oman and their width suggests that the permeability of wide dunites is substantially higher than that in narrow dunites. As a result, magma flux estimates derived from the observed size-frequency relationship indicate the majority of the magma flux to mid-ocean ridges is transported through dunites greater than ~10 m wide [*Braun and Kelemen*, 2002] . As discussed above, the composition of the wide dunites presented here are in equilibrium with melts which form the bulk of the Oman crust.

Grain size variations from the same suite of dunites as examined in this study support the hypothesis that the permeability was higher in wider dunites. Olivine grain size in these dunites increases with dunite width [*Braun and Hirth*, in prep]. The textures and lattice preferred orientations indicate that grain boundaries were highly mobile prior to transposition during corner flow, consistent with the hypothesis that the grain size increase forms in the melting region. The grain size increase can be therefore translated into an increase in permeability with increasing dunite width which existed when these dunites were active conduits.

Conclusion:

Detailed transects across several dunites of various widths show that the geochemical boundaries between dunites and the surrounding harzburgites are well defined, with changes in both major and minor element chemistry coincident with the macroscopic lithologic contacts. Additionally, dunite compositions are uniform within each transect, but vary systematically as a function of dunite width, with wide dunites close to equilibrium with liquids parental to the observed lavas and dikes in the region.

The data from Oman can be used to constrain the processes of dunite formation and melt migration beneath oceanic spreading centers. The composition of residual peridotites measured in Wadi Lufti are similar to abyssal peridotites, and the inferred parent to the Oman lavas is similar to MORB. Therefore, we can extend the spatial information afforded by well-preserved outcrops to dunite inter-relationships in the melting region beneath ridges.

Geochemical profiles across the dunites are inconsistent with formation by diffusion around melt-filled hydrofractures. Instead, the data are better fit by models which approximate focused porous flow through dunites. The observed covariations in peridotite mineral compositions are only partly explained by simple mixing of depleted and primitive magmas in porous conduits of varying widths. As an alternative, we present a model for melt-rock reaction which reproduces the main features of the observed geochemical variations. The model suggests the compositional variations with dunite width reflect an increase in the time-integrated melt/rock ratio in wider dunites. Because dunites grow by reaction along their margins, narrow dunites may be formed shallower in the melting column than wide dunites. Therefore, the observations likely reflect combination of the two porous flow models, that is reaction of harzburgite with a liquid of variable composition. Regardless, the geochemical data from Oman, coupled with field observations and microstructural data collected on the same rocks, indicate that wide dunites are the primary conduits for chemically-isolated transport of melts with sufficient flux to form the oceanic crust.

Acknowledgements:

MGB would like to thank Karen Hanghøj and Julian Pearce for providing the clinopyroxene and lava data, Deborah Hassler for the Wadi Tayin samples, Glenn Gaetani, Nobu Shimizu, and Henry Dick for their advice and access to their data and Greg Hirth for his comments and encouragement.

Bibliography:

Aharonov, E., J.A. Whitehead, P.B. Kelemen, and M. Spiegelman, Channeling instability of upwelling melt in the mantle, *J. Geophys. Res.*, *100*, 20,433-20,450, 1995.

Alabaster, T., J. Pearce, A., and J. Malpas, The volcanic stratigraphy and petrogenesis of the Oman ophiolite complex, *Contrib. Mineral. Petrol.*, *81*, 168-183, 1982.

Allan, J.F., and H.J.B. Dick, Cr-rich spinel as a tracer for melt migration and melt-wall rock interaction in the mantle: Hess Deep, Leg 147, in *Proc. Ocean Drilling Prog. Scientific Results*, edited by C. Mével, K.M. Gillis, J.F. Allan, and P.S. Meyer, pp. 157-172, Ocean Drilling Program, College Station, TX, 1996.

Allan, J.F., R. Sack, O., and R. Batiza, Cr-rich spinels as petrogenetic indicators: MORB-type lavas from the Lamont seamount chain, eastern Pacific, *Amer. Mineral.*, *73*, 741-753, 1988.

Augé, T., Chromite deposits in the northern Oman ophiolite: Mineralogical constraints, *Mineral. Deposita*, *22*, 1-10, 1987.

Boudier, F., and R.G. Coleman, Cross section through the peridotite in the Samail ophiolite, southeastern Oman mountains, *J. Geophys. Res.*, *86*, 2573-2592, 1981.

Boudier, F., and A. Nicolas, Fusion partielle gabbroique dans la Iherzolite de Lanzo, *Suisse Min. Pet.*, *52*, 39-56, 1972.

Braun, M.G., and G. Hirth, Microstructural Evolution in Naturally-Deformed Dunites: Grain Boundary Sliding and the Strength of the Shallow Mantle, *J. Geophys. Res.*, in prep.

Braun, M.G., and P.B. Kelemen, Dunite distribution in the Oman Ophiolite; implications for melt flux through porous dunite conduits, *Geochem., Geophys., Geosyst. 3* (11), 21, 2002.

Brearley, M., and C.M. Scarfe, Dissolution rates of upper mantle minerals in an alkali basalt melt at high presssure: An experimental study and implications for ultramafic xenolith survival, *J. Petrol.*, *27*, 1157-1182, 1986.

Colson, R.O., G.A. McKay, and L.A. Taylor, Temperature and composition dependencies of trace element partitioning: Olivine/melt and low-Ca pyroxene /melt, *Geochim. Cosmochim. Acta*, *52*, 539-553, 1988.

Daines, M.J., and D.L. Kohlstedt, Transition from porous to channelized flow due to melt/rock reaction during melt migration, *Geophys. Res. Lett.*, *21*, 145-148, 1994.

Dick, H.J.B., and T. Bullen, Chromian spinel as a petrogenetic indicator in abyssal and alpine-type peridotites and spatially associated lavas, *Contrib. Mineral. Petrol., 86*, 54-76, 1984.

Dick, H.J.B., and J.H. Natland, Late-stage melt evolution and transport in the shallow mantle beneath the East Pacific Rise, in *Proc. Ocean Drilling Prog., Scientific Results*, edited by C. Mevel, K.M. Gillis, J.F. Allan, and P.S. Meyer, pp. 103-134, ODP, 1996.

Dijkstra, A.H., M.R. Drury, and R.M. Frijhoff, Microstructures and lattice fabrics in the Hilti mantle section (Oman Ophiolite): Evidence for shear localization in the crust-mantle transition zone?, *J. Geophys. Res., 107* (11), 2002.

Elthon, D., Pressure of origin of primary mid-ocean ridge basalts, in *Magmatism in the Ocean Basins*, edited by A.D. Saunders, and M.J. Norry, pp. 125-136, Geological Society, 1989.

Elthon, D., and C.M. Scarfe, High-pressure phase equilibria of a high-magnesia basalt: Implications for the origin of mid-ocean ridge basalts, *Carnegie Inst. Wa. Yrbk.*, 277-281, 1980.

Frey, F.A., N. Walker, D. Stakes, S.R. Hart, and R. Nielsen, Geochemical characteristics of basaltic glasses from the AMAR and FAMOUS axial valleys, Mid-Atlantic Ridge (36°-37°N): Petrogenetic implications, *Earth Planet. Sci. Lett., 115*, 117-136, 1993.

Gaetani, G.A., S.E. DeLong, and D.A. Wark, Petrogenesis of basalts from the Blanco Trough, northeast Pacific: Inferences for off-axis melt generation, *J. Geophys. Res., 100*, 4197-4214, 1995.

Gaetani, G.A., and T.L. Grove, The influence of water on melting of mantle peridotite, *Contrib. Mineral. Petrol., 131*, 323-346, 1998.

Gaetani, G.A., T.L. Grove, and W.B. Bryan, Experimental phase rlations of basaltic andesite from hole 839B under hydroud conditions, *Proc. Ocean Drilling Prog., Scientific Results, 135*, 557-563, 1994.

Grove, T.L., and T.C. Juster, Experimental investigations of low-Ca pyroxene stability and olivine-pyroxene - liquid equilibria at 1-atm in natural basaltic and andesitic liquids, *Contrib. Mineral Petrol, 103*, 287-305, 1989.

Gudfinnsson, G.H., and D.C. Presnall, Melting behavior of model lherzolite in the system CaO-MgO-Al_2O_3-SiO_2-FeO at 0.7-2.8 GPa, *J. Petrol., 41* (8), 1241-1269, 2000.

Hart, S.A., and T. Dunn, Experimental cpx/melt partitioning of 24 trace elements, *Contrib. Mineral. Petrol., 113*, 1-8, 1993.

Hart, S.R., and K.E. Davis, Nickel Partitioning Between Olivine and Silicate Melt, *40*, 203-219, 1978.

Hawkins, J., W., and J. Melchior, T., Petrology of basalts from Loihi Seamounts, Hawaii, *Earth Planet. Sci. Lett., 66*, 356-368, 1983.

Hawkins, J., W., and J. Melchior, T., Petrology of Mariana Trough and Lau Basin basalts, *J. Geophys. Res., 90*, 11,431-11,468, 1985.

Hirth, G., and D. Kohlstedt, L., Rheology of the upper mantle and the mantle wedge: a view from the experimentalists, in *The Subduction Factory*, edited by J.M. Eiler, 2003.

Holland, T.J.B., and R. Powell, An enlarged and updated internally consistent thermodynamic dataset with uncertainties and correlations: the system K_2O-Na_2O-CaO-MgO-MnO-FeO-Fe_2O_3-Al_2O_3-TiO_2-SiO_2-C-H_2-O_2, *J. Metamorphic Geol.*, *8*, 89-124, 1990.

Johnson, K.T.M., H.J.B. Dick, and N. Shimizu, Melting in the oceanic upper mantle: an ion microprobe study of diopsides in abyssal peridotites, *J. Geophys. Res.*, *95*, 2661-2678, 1990.

Jull, M., P.B. Kelemen, and K.W.W. Sims, Consequences of diffuse and channelled porous melt migration on uranium series disequilibria, *Geochim. Cosmochim. Acta*, *66* (23), 4133-4148, 2002.

Kelemen, P.B., Reaction between ultramafic rock and fractionating basaltic magma. I. Phase relations, the origin of calc-alkaline magma series, and the formation of discordant dunite, *J. Petrol.*, *31*, 51-98, 1990.

Kelemen, P.B., and H.J.B. Dick, Focused melt flow and localized deformation in the upper mantle: Juxtaposition of replacive dunite and ductile shear zones in the Josephine peridotite, SW Oregon, *J. Geophys. Res.*, *100*, 423-438, 1995.

Kelemen, P.B., S.R. Hart, and S. Bernstein, Silica enrichment in the continental upper mantle via melt/rock reaction, *Earth Planet. Sci. Lett.*, *164*, 387-406, 1998.

Kelemen, P.B., G. Hirth, N. Shimizu, M. Spiegelman, and H.J.B. Dick, A review of melt migration processes in the adiabatically upwelling mantle beneath spreading ridges, *Phil. Trans. Roy. Soc., Lond. A*, *355*, 283-318, 1997.

Kelemen, P.B., N. Shimizu, and V.J.M. Salters, Extraction of mid-ocean ridge basalt from the upwelling mantle by focused flow of melt in dunite channels, *Nature*, *375*, 747-753, 1995.

Kinzler, R.J., Melting of mantle peridotite at pressures approaching the spinel to garnet transition: Application to mid-ocean ridge basalt petrogenesis, *J. Geophys. Res.*, *102* (B1), 853-874, 1997.

Kuo, L.-C., and R.J. Kirkpatrick, Dissolution of mafic minerals and its implications for the ascent velocities of peridotite-bearing basaltic magmas, *J. Geol.*, *93*, 691-700, 1985.

Libourel, G., Systematics of valcum partitioning between olivine and silicatemelt: implications for melt sttructure and calcium content of magmatic olivines, *Contrib. Mineral. Petrol.*, *136*, 63-80, 1999.

Lippard, S.J., A.W. Shelton, and I.G. Gass, *The ophiolite of nothern Oman*, 178 pp., Blackwell, Oxford, 1986.

Loucks, R.R., A precise olivine-augite Mg-Fe-exchange geothermometer, *Contrib. Mineral. Petrol.*, *125*, 140-150, 1996.

Lundstrom, C.C., J. Gill, Q. Williams, and M.R. Perfit, Mantle melting and basalt extraction by equilibrium porous flow, *Science*, *270*, 1958-1961, 1995.

Morgan, Z., and Y. Liang, An experimental and numerical study of the kinetics of harzburgite reactive dissolution with applications to dunite dike formation, *Earth Planet. Sci. Lett.*, *214* (1-2), 59-74, 2003.

Nicolas, A., Melt extraction from mantle peridotites: Hydrofracturing and porous flow, with consequences for oceanic ridge activity, in *Magma Transport and Storage*, edited by M.P. Ryan, pp. 159-174, J. Wiley & Sons, New York, 1990.

Nicolas, A., and A. Prinzhofer, Cumulative or residual origin for the transition zone in ophiolites: Structural evidence, *J. Petrol., 24, Part 2*, 188-206, 1983.

O'Hara, M.J., Primary magmas and the origin of basalts, *Scot. J. Geol., 1*, 19-40, 1965.

Pallister, J.S., and C.A. Hopson, Samail ophiolite plutonic suite: field relations, phase variation, cryptic variation and layering, and a model of a spreading ridge magma chamber, *J. Geophys. Res, 86*, 2593-2644, 1981.

Pallister, J.S., and R.J. Knight, Rare-earth element geochemistry of the Samail ophiolite near Ibra, Oman, *J. Geophys. Res., 86*, 2673-2697, 1981.

Pearce, J., A., T. Alabaster, A. Shelton, W., and M. Searle, P., The Oman ophiolite as a Cretaceous arc-basin complex: Evidence and implications, *Phil. Trans. R. Soc. Lond. A, 300*, 299-317, 1981.

Poustovetov, A.A., P.L. Roeder, D. Canil, H.E. Jamieson, and R.F. Martin, The distribution of Cr between basaltic melt and chromian spinel as an oxygen geobarometer; Phase equilibria in basaltic systems; a tribute to Peter L. Roeder, *Can. Mineral., 39, Part 2*, 309-317, 2001.

Python, M., and G. Ceuleneer, Nature and distribution of dykes and related melt migration structures in the mantle section of the Oman ophiolite, *Geochem., Geophys., Geosyst., 4* (7), 10.1029/2002GC000354, 2003.

Roeder, P.L., and R.F. Emslie, Olivine-liquid equilibrium, *Contrb. Mineral. Petrol., 29* (4), 275-289, 1970.

Sack, R.O., and M.S. Ghiorso, Chromian spinels as petrogenetic indicators; thermodynamics and petrological applications, *Amer. Mineral., 76* (5-6), 827-847, 1991.

Savel'yeva, G.N., S. Shcherbakov, A., and Y.A. Denisova, The role of high-temperature deformation in the development of dunite bodies in harzburgites, *Geotectonics, 14*, 175-182, 1980.

Sims, K.W.W., S.J. Goldstein, J. Blichert-Toft, M.R. Perfit, P. Kelemen, D.J. Fornari, P.J. Michael, M.T. Murrell, S.R. Hart, D.J. DePaolo, G.D. Layne, L. Ball, M. Jull, and J.F. Bender, Chemical and isotopic constraints on the generation and transport of magma beneath the East Pacific Rise, *Geochim. Cosmochim. Acta, 66* (19), 3481-3504, 2002.

Sobolev, A.V., and N. Shimizu, Ultra-depleted primary melt included in an olivine from the Mid-Atlantic Ridge, *Nature, 363*, 151-154, 1993.

Spiegelman, M., and P. Kelemen, Extreme chemical variability as a consequence of channelized melt transport, *Geochem., Geophys., Geosyst., 4* (7), 2003.

Spiegelman, M., P.B. Kelemen, and E. Aharonov, Causes and consequences of flow organization during melt transport: The reaction infiltration instability, *J. Geohys. Res., 106*, 2061-2078, 2001.

Stolper, E., A phase diagram for mid-ocean ridge basalts: preliminary results and implications for petrogenesis, *Contrib. Mineral. Petrol., 74*, 13-27, 1980.

Suhr, G., Melt migration under oceanic ridges; inferences from reactive transport modelling of upper mantle hosted dunites, *J. Petrol.*, *40*, 575-599, 1999.
Suhr, G., E. Hellebrand, J.E. Snow, H.A. Seck, and A. Hofmann, W., Significance of large, refractory dunite bodies in the upper mantle of the Bay of Islands Ophiolite, *Geochem., Geophys., Geosyst.*, *4* (3), 10.1029/2001GC000277, 2003.
Takahashi, N., Origin of three peridotite suites from Horoman peridotite complex, Hokkaido, Japan: Melting, melt segregation, and solidification processes in the upper mantle, *J. Min. Petr. Econ. Geol.*, *86*, 199-215, 1991.
Takahashi, N., Evidence for melt segregation towards fractures in the Horoman mantle peridotite complex, *Nature*, *359*, 52-55, 1992.
Toramaru, A., and N. Fujii, Connectivity of melt phase in a partially molten peridotite, *J. Geophys. Res.*, *91*, 9239-9252, 1986.
Zhu, W., and G. Hirth, A network model for permeability in partially molten rocks, *Earth Planet. Sci. Lett.*, *212*, 407-416, 2003.

Appendix A

We have calibrated a preliminary olivine-orthopyroxene thermometer from mineral pairs measured in laboratory experiments to estimate the variation in subsolidus Fe-Mg partitioning. The exchange of Fe and Mg between olivine and orthopyroxene is governed by the reaction

$$X_{Ol}^{Mg} + X_{Opx}^{Fe} = X_{Ol}^{Fe} + X_{Opx}^{Mg}. \qquad \text{(A1)}$$

The partitioning of the components between phases is related to the changes in the standard enthalpy, ΔH°, and entropy, ΔS°, of the reaction at a given temperature by the relation,

$$\begin{aligned} RTl\ln K_{Ol-Opx}^{Fe-Mg} &= -\Delta G_T^o \\ &= -\Delta H_T^o + T\Delta S_T^o \end{aligned} \qquad \text{(A2)}$$

where the enthalpy and entropy at temperature, T, are defined by the properties at a reference state, T_o, and the excess enthalpy and entropy or reaction, respectively, associated with the difference in temperature between the reference and desired temperatures,

$$\begin{aligned} \Delta H_T &= \Delta H_T^o + \Delta H_T^{xs} = \Delta H_{To} + \Delta C_p(T - T_o) \\ \Delta S_T &= \Delta S_T^o + \Delta S_T^{xs} = \Delta S_{To} + \Delta C_p \ln\left(\frac{T}{T_o}\right) \end{aligned} \qquad \text{(A3)}$$

Substituting (A3) into (A2) yields

$$\ln K_{Ol-Opx}^{Fe-Mg} + \frac{\Delta C_p^o}{RT}(T - T_o) - \frac{\Delta C_p^o}{R}\ln\left(\frac{T}{T_o}\right) = -\frac{\Delta H_{To}}{R}\frac{1}{T} + \frac{\Delta S_{To}}{R}. \qquad \text{(A4)}$$

Using the standard state heat capacities of olivine and orthopyroxene at 1400K from the thermodynamic database of Holland and Powell [1990], Loucks [1996] estimates ΔC_p=-0.08425 kJ/mol.

A preliminary database of petrologic experiments which contain equilibrated olivine-orthopyroxene pairs is compiled from [*Colson et al.*, 1988; *Gaetani and Grove*, 1998; *Gaetani et al.*, 1994; *Grove and Juster*, 1989; *Gudfinnsson and Presnall*, 2000; *Kinzler*, 1997]. A least-squares fit to the data assuming the relationship in (A4) and ΔC_p=-0.08425 kJ/mol yields

$$\ln K_{Ol-Opx}^{Fe-Mg} + \frac{\Delta C_p^o}{RT}(T - T_o) - \frac{\Delta C_p^o}{R}\ln\left(\frac{T}{T_o}\right) = \lambda_1 \frac{10^4}{T} + \lambda_2 \qquad \text{(A5)}$$

where λ_1=-1.952 and λ_2=0.3012, with a correlation coefficient, R^2=0.82 (figure 16a). Additional data, especially at low temperatures (less than 1150°C) will better constrain the accuracy of the extrapolation.

The measured K_{Ol-Opx}^{Fe-Mg} from olivine-orthopyroxene pairs in Oman harzburgites along with the olivine-spinel thermometry results suggest that the extrapolation of the laboratory data is reasonably accurate. The red squares in figure 16b show the inferred Fe-Mg partitioning and equilibration temperature for each of the Oman samples in which olivine, orthopyroxene, and spinel have been measured. The extrapolation fits the trend in the data remarkably well considering the extent of the extrapolation. If the functional form of the inversion were inappropriate, the extrapolation would not come close.

The extrapolation is moderately sensitive to the prescribed magnitude of ΔC_p. to better fit the temperatures inferred from olivine-spinel thermometry requires a value of ΔC_p.=-0.1 kJ/mol. With this change, λ_1=-1.865 and λ_2=0.2888, and the inversion still fits the experimental data reasonably well, with R^2=0.79 (figure 16a – dashed line and solid symbols), and the extrapolation (figure 16b – dashed line) goes through the Oman data. Arbitrarily large changes, however, substantially reduce the quality of the fit to the laboratory experiments.

Using this empirically-derived expression for K_{Ol-Opx}^{Fe-Mg} as a function of temperature, the Fe/Mg ratio in each phase can be determined at any given temperature by repartitioning. The Fe-Mg distribution coefficient between olivine and orthopyroxene at any temperature is defined as

$$K_{Ol-Opx}^{Fe-Mg} = \frac{\left(\frac{X_{Fe}^{Ol}}{X_{Mg}^{Ol}}\right)}{\left(\frac{X_{Fe}^{Opx}}{X_{Mg}^{Opx}}\right)}, \qquad \text{(A6)}$$

where X_j^i is the cation fraction of element j in phase i. Subsolidus exchange assumes that for every Fe cation transferred from olivine to orthopyroxene, a Mg cation moves

in the opposite direction. Therefore mass balance requires that

$$X_j^{Ol}\Big|_{T_1} + X_j^{Opx}\Big|_{T_1} = X_j^{Ol}\Big|_{T_2} + X_j^{Opx}\Big|_{T_2} \qquad \text{(A7)}$$

be satisfied for any two temperatures, T_1 and T_2. For simplicity in notation, numerical subscripts 1 and 2 indicate the value at temperatures T_1 and T_2, respectively. For the purposes of these calculations, it is assumed that $X_{Fe_1}^{Ol}$, $X_{Mg_1}^{Ol}$, $X_{Fe_1}^{Opx}$, and $X_{Mg_1}^{Opx}$ have been measured and T_1 is known by some independent means.

Substituting (A7) for Fe into (A6) yields

$$K_2 = \frac{\frac{1}{2}\left(\frac{1}{X_{Fe_1}^{Ol} + X_{Fe_1}^{Opx} - X_{Fe_2}^{Ol}}\right) - 1}{\frac{2}{3X_{Fe_2}^{Ol}} - 1}. \qquad \text{(A8)}$$

For a given temperature T_2, (A5) predicts the Fe/Mg partition coefficient, K_2. Solving (A8) is most easily solved numerically to yield $X_{Fe_2}^{Ol}$. Subsequently, resubstitution of $X_{Fe_2}^{Ol}$ into (A7) yields the value for $X_{Fe_2}^{Opx}$.

Finally, mineral stoichiometry requires $X_{Fe}^{Ol} + X_{Mg}^{Ol} = 2/3$ for olivine and $X_{Fe}^{Ol} + X_{Mg}^{Ol} = 1/2$ for orthopyroxene, from which, $X_{Mg_2}^{Ol}$ and $X_{Mg_2}^{Ol}$ can be explicitly determined.

Table 1 Oman Dike and Lava Compsitions

Sample	SiO_2	TiO_2	Al_2O_3	FeO	MnO	MgO	CaO	Na_2O	K_2O	P_2O_5	Total	Cr	Ni	La	Ce	Nd	Sm	Dy	Yb
om01-2A	57.03	1.99	15.11	10.86	0.37	4.01	2.72	5.88	0.39	0.34	98.7	8	7	9.15	25.46	21.02	6.49	9.5	5.72
om01-2B	58.96	1.67	15.2	9.62	0.13	3.23	2.69	7.18	0.08	0.35	99.11	4	8	9.48	27.97	22.3	6.96	10.16	6.35
om01-2C	57.93	1.7	14.84	10.35	0.34	3.34	2.85	6.25	0.03	0.37	98	2	8	9.56	27.73	22.79	7.09	10.21	6.18
om01-3B	51.41	1.68	15.49	9.71	0.12	6.16	11.01	3.43	0.15	0.17	99.32	167	53	5.52	16.15	13.27	4.17	6.06	3.43
om01-3C	49.6	0.82	15.88	8.2	0.14	8.89	12.45	2.74	0.03	0.06	98.81	316	105	1.62	4.67	4.5	1.64	2.98	1.94
om01-3D	51.48	0.74	16.11	7.81	0.11	7.53	10.99	3.54	0.07	0.07	98.45	230	81	1.64	4.79	4.57	1.61	2.74	1.76
om01-9	52.64	0.95	15.98	8.74	0.17	6.51	8.22	4.44	0.34	0.09	98.08	104	46	1.97	5.87	5.54	2.02	3.27	2.05
om01-10	54.6	1.34	15.68	8.54	0.15	5.29	6.96	5.67	0.5	0.13	98.86	56	23	2.87	9.28	8.73	2.93	4.67	2.78
om01-11	53.08	1.16	15.86	9.84	0.14	5.25	8	4.56	0.11	0.1	98.1	36	25	3.35	9.22	7.71	2.47	3.87	2.36
om01-12	53.61	1.35	15.68	9.26	0.15	5.11	6.97	5.36	0.38	0.13	97.99	55	22	2.83	8.44	7.84	2.68	4.35	2.61
om01-13A	51.96	1.03	16.43	9.51	0.12	6.34	7.68	4.78	0.38	0.1	98.33	33	31	2.95	8.35	7.09	2.31	3.6	2.18
om01-13B	53.29	1.09	16.04	9.3	0.11	5.56	7.58	5.06	0.45	0.1	98.59	29	26	3.55	9.61	7.84	2.5	3.8	2.28
om01-14	50.37	0.81	16.36	8.17	0.11	6.97	10.79	3.53	0.05	0.08	97.24	105	56	2.42	6.33	5.96	1.98	3.08	1.89
om01-15	53.91	1.41	16.04	10.31	0.18	4.9	5.56	5.56	0.54	0.14	98.55	22	14	3.77	10.48	10.05	3.37	5.21	3.15
om01-16	56.11	1.12	15.88	8.53	0.16	4.99	5.18	6.06	0.33	0.1	98.46	27	16	2.98	8.35	7.22	2.41	3.71	2.26
om01-17	54.2	1.13	16.23	9.57	0.17	6.16	4.91	5.93	0.26	0.11	98.66	18	21	3.01	8.76	7.56	2.48	3.87	2.44
om01-18	52.29	1.13	16.08	9.96	0.17	5.81	6.95	5.55	0.15	0.09	98.19	19	21	2.93	8.21	7.09	2.32	3.57	2.15
om01-20	51.67	1.22	16.76	10.93	0.18	6.16	5.25	5.36	0.24	0.12	97.89	20	22	3.35	9.59	8.15	2.65	4.11	2.52
om01-21	54.68	1.31	15.28	10.27	0.15	5.01	5.31	5.8	0.35	0.12	98.27	33	17	3.11	9.18	8.37	2.82	4.55	2.84
om01-22	51.98	1.06	16.41	9.16	0.16	7.07	7.11	4.43	0.55	0.09	98.02	154	62	2.24	6.76	6.46	2.29	3.91	2.42
om01-23	51.14	1.27	16.34	10.68	0.06	3.18	11.54	4.47	0.03	0.11	98.82	20	4	3.19	9.39	8.49	2.79	4.36	2.75
om01-24	52.52	1.05	15.74	9.93	0.07	5.55	8.68	3.83	0.36	0.1	97.82	25	19	2.62	8	7.25	2.43	3.95	2.47
om01-26	51.93	1.39	16.97	11.33	0.13	4.54	5.92	5.77	0.16	0.13	98.26	42	18	3.57	10.46	9.62	3.2	5.06	3.19
om01-27	52.73	1.4	16.12	11.14	0.14	4.82	6.3	5.46	0.18	0.12	98.41	55	16	3.4	9.87	9.07	3.05	4.81	2.96
om01-28	54.07	1.4	16.3	10.79	0.14	4.51	4.6	6.32	0.11	0.14	98.38	18	10	3.48	10.3	9.73	3.25	5.18	3.27
om01-29	54.85	1.6	16.82	7.22	0.12	3.66	7.69	5.35	0.08	0.17	97.56	11	6	3.77	10.99	9.55	3.31	5.55	3.52
om01-30	53.91	1.73	15.21	11.8	0.09	4.18	6.27	5.72	0.26	0.15	99.31	26	9	5.16	13.31	9.9	3.23	5.07	3.15

Table 1 Cont.

Sample	SiO_2	TiO_2	Al_2O_3	FeO	MnO	MgO	CaO	Na_2O	K_2O	P_2O5	Total	Cr	Ni	La	Ce	Nd	Sm	Dy	Yb
om01-31	51.46	1.72	14.98	13.31	0.12	4.57	6.69	5.11	0.13	0.13	98.22	28	10	3.71	10.51	8.71	2.98	4.83	2.92
om01-33	52.15	1.84	15.1	12.35	0.1	4.93	6.81	5.16	0.23	0.15	98.82	35	16	4.73	14.85	12.07	3.85	5.87	3.52
om01-34	52.82	1.66	15.38	12.79	0.09	4.48	5.33	5.97	0.23	0.13	98.89	31	11	4.17	14.2	12.8	3.97	5.7	3.33
om01-35	49.8	2.08	14.3	20.8	0.28	4.39	2.1	3.63	0.06	0.14	97.58	23	13	4.14	11.67	10.16	3.32	5.25	3.19
om01-36	58.04	1.4	14.97	10.94	0.28	2.7	5.16	3.21	0.53	0.19	97.42	8	4	5.06	14.72	12.88	4.17	6.46	4.03
om01-37	61.08	1.21	14.03	10.74	0.13	2.08	3.92	3.42	0.73	0.21	97.54	0	6	5.32	15.98	13.15	4.27	6.91	4.27
om01-38	61.55	1.26	14.28	9.92	0.12	2.41	3.08	5.43	0.25	0.2	98.49	0	0	5.25	14.74	12.74	4.4	6.79	3.84
om01-39	60.18	1.6	15.63	7.81	0.28	2.06	4.37	6.41	0.4	0.23	98.97	5	3	6.58	18.57	15.2	4.78	7.23	4.64
om01-40	63.31	1.44	16.04	5.09	0.19	1.92	3.31	6.62	0.47	0.36	98.74	2	7	8.58	25.59	21.6	6.75	9.75	6.11
om01-41	55.6	1.71	15.13	11.54	0.18	4.16	5.31	3.7	0.76	0.2	98.29	36	22	5.7	16.33	13.71	4.3	6.39	3.8
om01-42	49.98	1.64	15.46	13.71	0.14	4.83	7.77	2.49	0.53	0.11	96.67	21	7	2.8	8.31	7.72	2.74	4.78	2.99
om01-46	50.54	0.92	16.19	8.83	0.15	8.4	12.03	2.3	0.1	0.07	99.54	270	96	1.87	5.76	5.13	1.77	2.88	1.74
om01-47	50.17	0.89	16.23	8.91	0.14	8.8	12.53	1.93	0.07	0.06	99.72	283	101	2.22	6.81	5.9	1.99	3.17	1.91
om01-48	53.31	0.95	16.09	8.72	0.11	7.1	8.84	4.12	0.12	0.09	99.44	177	54	2.22	7.26	6.87	2.3	3.57	2.2

Table 2 Initial Compositions

	Olivine	Orthopyroxene	Spinel	Melt 1	Melt 2
MgO	50.45	34.00	15.30	14.34	11.09
FeO	9.08	5.40	14.00	8.62	6.64
NiO	0.40	0.08	0.00	0.04	0.03
TiO_2	-	0.04	0.14	0.70	0.59
Cr_2O_3	-	0.56	27.36	0.04	0.06
Al_2O_3	-	1.67	40.25	13.84	15.37
Fe_2O_3	-	-	2.80	-	-
SiO_2	40.36	57.33	0.00	48.66	50.28
CaO	0.02	0.00	-	11.17	13.27
MnO	0.13	0.13	-	0.12	0.12
Na_2O	-	1.14	-	2.39	2.48
P_2O_5	-	-	-	0.05	0.04
K_2O	-	-	-	0.03	0.02
Total	100.44	100.36	99.85	100.00	100.00

Melt 1: Dunite Backfractionated

Melt 2: Gabbro Backfractionated

Table 3 Mineral/Melt Partition Coefficients

	Olivine	Orthopyroxene	Spinel
MgO	var[a]	2.1 [c]	0.833 [e]
FeO	var[a]	0.56 [c]	1.7 [e]
NiO	var[b]	2.15 [c]	0
TiO2	0	0.5 [d]	var[ef]
Cr2O3	0	13.23 [d]	1000 [e]
Al2O3	0	0.07 [d]	1.6[e]

var=partition coefficient varies with liquid composition

[a]Gaetani & Grove, 1998, [b]Hart & Davis, 1978

[c]Beattie et al., 1991, [d]Colson et al., 1991

[e]Hawkins & Melchior, 1983, 1985, Allen et al., 1988, Gaetani et al, 1995

[f]K_{Ti}^{sp}=exp(0.0359×Cr#-2.26)

Table B1 - Olivine Composition

Sample	suite	N	SiO_2	TiO_2	Al_2O_3	Cr_2O_3	FeO	MnO	MgO	CaO	NiO	Total	Mg#
om00-13	50	3	39.53	0.0047	0.0000	0.0003	10.68	0.1647	49.68	0.0560	0.2974	100.41	89.24
			(0.123)	(0.005)	(0.000)	(0.000)	(0.184)	(0.012)	(0.312)	(0.027)	(0.005)		(0.221)
om00-14a	50	5	39.97	0.0000	0.0000	0.0010	10.71	0.1680	48.67	0.0383	0.3024	99.86	89.01
			(0.524)	(0.000)	(0.000)	(0.002)	(0.142)	(0.010)	(0.385)	(0.020)	(0.005)		(0.202)
om00-14b	50	4	40.09	0.0000	0.0000	0.0000	11.11	0.1701	48.54	0.0127	0.2795	100.20	88.62
			(0.149)	(0.000)	(0.000)	(0.000)	(0.163)	(0.003)	(0.167)	(0.006)	(0.005)		(0.182)
om00-15	50	3	40.12	0.0005	0.0000	0.0000	9.06	0.1268	50.85	0.1668	0.3530	100.68	90.91
			(0.082)	(0.001)	(0.000)	(0.000)	(0.081)	(0.010)	(0.026)	(0.019)	(0.004)		(0.078)
om00-16	50	4	40.10	0.0034	0.0007	0.0000	9.01	0.1258	51.26	0.1533	0.3522	101.00	91.03
			(0.069)	(0.001)	(0.001)	(0.000)	(0.109)	(0.009)	(0.033)	(0.010)	(0.004)		(0.097)
om00-17	50	4	39.95	0.0024	0.0000	0.0000	9.10	0.1068	51.09	0.1304	0.3228	100.70	90.91
			(0.195)	(0.004)	(0.000)	(0.000)	(0.188)	(0.056)	(0.218)	(0.054)	(0.049)		(0.159)
om00-18	50	3	40.16	0.0022	0.0000	0.0000	9.02	0.1288	51.15	0.1736	0.3480	100.99	91.00
			(0.057)	(0.004)	(0.000)	(0.000)	(0.040)	(0.006)	(0.281)	(0.023)	(0.004)		(0.040)
om00-19	50	3	40.39	0.0008	0.0005	0.0000	9.05	0.1340	51.31	0.0829	0.3472	101.32	91.00
			(0.032)	(0.001)	(0.001)	(0.000)	(0.123)	(0.008)	(0.090)	(0.039)	(0.004)		(0.123)
om00-20	50	4	40.18	0.0016	0.0000	0.0000	9.08	0.1259	51.26	0.1498	0.3432	101.13	90.97
			(0.169)	(0.002)	(0.000)	(0.000)	(0.075)	(0.003)	(0.130)	(0.026)	(0.006)		(0.078)
om00-21	50	2	40.31	0.0005	0.0000	0.0006	9.10	0.1291	51.22	0.1551	0.3506	101.25	90.94
			(0.021)	(0.001)	(0.000)	(0.001)	(0.021)	(0.001)	(0.177)	(0.000)	(0.001)		(0.009)
om00-22	50	3	40.15	0.0013	0.0001	0.0009	9.14	0.1293	51.28	0.1772	0.3456	101.22	90.91
			(0.120)	(0.001)	(0.000)	(0.002)	(0.058)	(0.003)	(0.090)	(0.003)	(0.002)		(0.065)
om00-23	50	3	40.24	0.0012	0.0006	0.0002	9.06	0.1311	51.24	0.1522	0.3499	101.17	90.98
			(0.059)	(0.002)	(0.001)	(0.000)	(0.133)	(0.002)	(0.178)	(0.010)	(0.003)		(0.110)
om00-24	50	4	40.19	0.0013	0.0017	0.0002	9.18	0.1248	50.97	0.1761	0.3509	101.00	90.83
			(0.078)	(0.002)	(0.002)	(0.000)	(0.173)	(0.010)	(0.168)	(0.017)	(0.004)		(0.174)
om00-25	50	3	39.81	0.0015	0.0000	0.0017	9.06	0.1308	50.39	0.1359	0.3450	99.88	90.84
			(0.090)	(0.003)	(0.000)	(0.002)	(0.097)	(0.013)	(0.042)	(0.022)	(0.004)		(0.086)

Sample	suite	N	SiO_2	TiO_2	Al_2O_3	Cr_2O_3	FeO	MnO	MgO	CaO	NiO	Total	Mg#
om00-26	50	3	39.85	0.0008	0.0000	0.0013	9.08	0.1301	50.45	0.1734	0.3375	100.02	90.83
			(0.101)	(0.001)	(0.000)	(0.002)	(0.135)	(0.005)	(0.150)	(0.020)	(0.004)		(0.127)
om00-27	50	3	39.91	0.0009	0.0000	0.0048	9.16	0.1248	50.73	0.1445	0.3422	100.42	90.81
			(0.055)	(0.001)	(0.000)	(0.003)	(0.125)	(0.004)	(0.075)	(0.009)	(0.008)		(0.126)
om00-28	50	3	39.79	0.0005	0.0000	0.0011	9.10	0.1374	50.51	0.1820	0.3457	100.06	90.82
			(0.187)	(0.000)	(0.000)	(0.001)	(0.050)	(0.001)	(0.197)	(0.002)	(0.006)		(0.053)
om00-29	50	3	39.97	0.0000	0.0008	0.0033	8.98	0.1242	50.52	0.1807	0.3451	100.12	90.94
			(0.040)	(0.000)	(0.001)	(0.006)	(0.057)	(0.003)	(0.131)	(0.018)	(0.002)		(0.063)
om00-30	50	3	40.39	0.0004	0.0000	0.0048	9.24	0.1271	50.89	0.1910	0.3575	101.20	90.75
			(0.135)	(0.001)	(0.000)	(0.003)	(0.086)	(0.011)	(0.046)	(0.015)	(0.008)		(0.084)
om00-31	50	3	40.35	0.0000	0.0000	0.0032	9.14	0.1287	51.11	0.1507	0.3483	101.22	90.89
			(0.085)	(0.000)	(0.000)	(0.003)	(0.081)	(0.004)	(0.068)	(0.045)	(0.003)		(0.085)
om00-32	50	3	40.35	0.0009	0.0000	0.0029	9.13	0.1336	51.21	0.1732	0.3542	101.35	90.91
			(0.150)	(0.001)	(0.000)	(0.003)	(0.091)	(0.010)	(0.095)	(0.013)	(0.002)		(0.085)
om00-32.5	50	4	40.31	0.0003	0.0000	0.0038	9.08	0.1280	51.18	0.1826	0.3551	101.24	90.95
			(0.066)	(0.001)	(0.000)	(0.002)	(0.045)	(0.007)	(0.054)	(0.009)	(0.006)		(0.038)
om00-33	50	3	40.36	0.0000	0.0000	0.0052	9.11	0.1224	51.02	0.1721	0.3494	101.13	90.90
			(0.118)	(0.000)	(0.000)	(0.002)	(0.100)	(0.008)	(0.146)	(0.022)	(0.004)		(0.114)
om00-34	50	3	40.52	0.0032	0.0000	0.0081	9.10	0.1314	51.12	0.1830	0.3404	101.42	90.92
			(0.129)	(0.002)	(0.000)	(0.004)	(0.064)	(0.014)	(0.045)	(0.004)	(0.002)		(0.053)
om00-35	50	3	40.27	0.0000	0.0000	0.0046	9.05	0.1294	50.82	0.1901	0.3440	100.81	90.92
			(0.059)	(0.000)	(0.000)	(0.002)	(0.075)	(0.004)	(0.059)	(0.008)	(0.007)		(0.069)
om00-37	50	3	40.24	0.0006	0.0000	0.0007	8.77	0.1230	50.97	0.1522	0.3517	100.61	91.20
			(0.111)	(0.001)	(0.000)	(0.001)	(0.080)	(0.002)	(0.055)	(0.010)	(0.010)		(0.065)
om00-38	50	3	40.06	0.0009	0.0000	0.0066	9.58	0.1374	50.51	0.0600	0.3426	100.70	90.38
			(0.061)	(0.002)	(0.000)	(0.005)	(0.082)	(0.003)	(0.160)	(0.011)	(0.007)		(0.088)
om00-39	50	3	40.07	0.0000	0.0000	0.0054	9.78	0.1327	50.40	0.0428	0.3303	100.77	90.18
			(0.110)	(0.000)	(0.000)	(0.004)	(0.138)	(0.011)	(0.182)	(0.008)	(0.004)		(0.153)
om00-41	50	3	40.26	0.0000	0.0007	0.0040	8.89	0.1324	50.62	0.1850	0.3645	100.45	91.03
			(0.085)	(0.000)	(0.001)	(0.007)	(0.035)	(0.004)	(0.067)	(0.003)	(0.005)		(0.031)

Sample	suite	N	SiO_2	TiO_2	Al_2O_3	Cr_2O_3	FeO	MnO	MgO	CaO	NiO	Total	Mg#
om00-42	50	3	40.36	0.0012	0.0000	0.0020	9.55	0.1398	50.16	0.1296	0.3658	100.71	90.35
			(0.131)	(0.001)	(0.000)	(0.004)	(0.136)	(0.005)	(0.053)	(0.018)	(0.007)		(0.119)
om00-48	50	3	40.00	0.0000	0.0000	0.0000	8.66	0.1243	51.09	0.1535	0.3496	100.37	91.32
			(0.146)	(0.000)	(0.000)	(0.000)	(0.062)	(0.003)	(0.052)	(0.022)	(0.005)		(0.060)
om00-49	50	3	40.00	0.0000	0.0000	0.0010	9.17	0.1375	50.71	0.1458	0.3440	100.51	90.79
			(0.204)	(0.000)	(0.000)	(0.001)	(0.055)	(0.012)	(0.023)	(0.024)	(0.002)		(0.052)
om00-50	50	3	39.80	0.0000	0.0000	0.0000	9.66	0.1453	50.20	0.1135	0.3264	100.25	90.25
			(0.053)	(0.000)	(0.000)	(0.000)	(0.097)	(0.008)	(0.105)	(0.005)	(0.008)		(0.103)
om00-51	50	3	39.80	0.0000	0.0002	0.0029	9.79	0.1445	50.10	0.1741	0.3153	100.33	90.12
			(0.130)	(0.000)	(0.000)	(0.005)	(0.121)	(0.010)	(0.056)	(0.014)	(0.005)		(0.120)
om00-52	50	3	39.96	0.0000	0.0000	0.0009	9.35	0.1438	50.48	0.1563	0.3288	100.41	90.59
			(0.112)	(0.000)	(0.000)	(0.002)	(0.101)	(0.007)	(0.055)	(0.019)	(0.011)		(0.091)
om00-53	50	4	40.00	0.0000	0.0005	0.0008	9.59	0.1370	50.35	0.1880	0.3272	100.59	90.35
			(0.036)	(0.000)	(0.001)	(0.002)	(0.176)	(0.011)	(0.175)	(0.015)	(0.006)		(0.153)
om00-54	50	3	39.62	0.0000	0.0029	0.0026	9.31	0.1409	50.24	0.1759	0.3128	99.80	90.59
			(0.116)	(0.000)	(0.005)	(0.005)	(0.050)	(0.005)	(0.092)	(0.008)	(0.004)		(0.031)
om00-55	50	3	39.80	0.0000	0.0004	0.0012	9.35	0.1381	50.23	0.1681	0.3242	100.01	90.55
			(0.064)	(0.000)	(0.001)	(0.002)	(0.064)	(0.008)	(0.100)	(0.007)	(0.002)		(0.075)
om00-56	50	3	39.82	0.0000	0.0000	0.0000	9.36	0.1342	50.21	0.1539	0.3273	100.00	90.53
			(0.059)	(0.000)	(0.000)	(0.000)	(0.036)	(0.004)	(0.061)	(0.007)	(0.007)		(0.026)
om00-57	50	3	39.72	0.0000	0.0000	0.0004	9.44	0.1426	50.01	0.1570	0.3326	99.81	90.42
			(0.071)	(0.000)	(0.000)	(0.001)	(0.130)	(0.002)	(0.199)	(0.018)	(0.004)		(0.153)
om00-58	50	3	39.85	0.0000	0.0015	0.0012	9.41	0.1417	50.07	0.1255	0.3420	99.94	90.46
			(0.044)	(0.000)	(0.002)	(0.002)	(0.046)	(0.003)	(0.092)	(0.052)	(0.009)		(0.028)
om00-58.5	50	3	40.14	0.0000	0.0002	0.0008	9.40	0.1325	50.26	0.1068	0.3458	100.38	90.51
			(0.035)	(0.000)	(0.000)	(0.001)	(0.031)	(0.002)	(0.148)	(0.022)	(0.007)		(0.052)
om00-65	50	3	40.12	0.0000	0.0000	0.0026	9.47	0.1390	49.53	0.1219	0.3219	99.71	90.31
			(0.121)	(0.000)	(0.000)	(0.002)	(0.070)	(0.003)	(0.123)	(0.037)	(0.007)		(0.050)
om00-66	50	3	40.12	0.0000	0.0000	0.0011	9.33	0.1450	49.56	0.1191	0.3481	99.63	90.44
			(0.091)	(0.000)	(0.000)	(0.002)	(0.085)	(0.008)	(0.061)	(0.005)	(0.009)		(0.086)

Sample	suite	N	SiO_2	TiO_2	Al_2O_3	Cr_2O_3	FeO	MnO	MgO	CaO	NiO	Total	Mg#
om00-67	50	4	39.92	0.0172	0.2112	0.3312	9.98	0.1556	48.89	0.1335	0.3439	99.98	89.70
			(0.790)	(0.034)	(0.422)	(0.659)	(1.071)	(0.029)	(1.984)	(0.016)	(0.006)		(1.393)
om00-68	50	3	40.43	0.0000	0.0000	0.0035	9.66	0.1560	49.70	0.1274	0.3409	100.42	90.16
			(0.060)	(0.000)	(0.000)	(0.001)	(0.093)	(0.004)	(0.277)	(0.005)	(0.008)		(0.081)
om00-69	50	6	39.95	0.0000	0.0000	0.0029	9.77	0.1451	50.21	0.1453	0.3106	100.53	90.16
			(0.202)	(0.000)	(0.000)	(0.003)	(0.092)	(0.011)	(0.134)	(0.013)	(0.015)		(0.064)
om00-70	50	5	39.71	0.0000	0.0051	0.0021	9.75	0.1421	49.54	0.0625	0.3104	99.53	90.05
			(0.183)	(0.000)	(0.011)	(0.004)	(0.246)	(0.004)	(0.603)	(0.025)	(0.006)		(0.338)
om00-71	50	3	39.88	0.0000	0.0002	0.0030	9.14	0.1242	50.33	0.0196	0.3748	99.88	90.75
			(0.136)	(0.000)	(0.000)	(0.002)	(0.100)	(0.014)	(0.032)	(0.002)	(0.005)		(0.095)
om00-72	50	3	39.80	0.0000	0.0000	0.0030	9.82	0.1496	49.94	0.0836	0.3180	100.11	90.07
			(0.061)	(0.000)	(0.000)	(0.003)	(0.110)	(0.014)	(0.110)	(0.027)	(0.009)		(0.082)
om00-73	50	4	40.02	0.0000	0.0000	0.0015	9.11	0.1237	50.17	0.0173	0.3662	99.81	90.75
			(0.088)	(0.000)	(0.000)	(0.002)	(0.090)	(0.008)	(0.124)	(0.007)	(0.005)		(0.079)
om00-74	50	4	40.14	0.0000	0.0004	0.0027	8.83	0.1224	50.59	0.0189	0.3860	100.08	91.08
			(0.053)	(0.000)	(0.000)	(0.002)	(0.099)	(0.005)	(0.109)	(0.006)	(0.006)		(0.089)
om98-105	50	2	40.45	0.0100	0.0030	0.0095	9.87	0.1391	49.18	0.1065	0.3639	100.13	89.88
			(0.057)	(0.001)	(0.001)	(0.010)	(0.071)	(0.003)	(0.332)	(0.058)	(0.002)		(0.004)
om98-107	50	3	40.39	0.0152	0.0061	0.0033	8.23	0.1353	50.33	0.1582	0.3545	99.62	91.60
			(0.289)	(0.006)	(0.002)	(0.006)	(0.017)	(0.023)	(0.188)	(0.023)	(0.008)		(0.013)
om98-110	50	3	40.25	0.0093	0.0069	0.0000	9.12	0.1111	50.15	0.1910	0.3578	100.20	90.75
			(0.176)	(0.010)	(0.004)	(0.000)	(0.085)	(0.007)	(0.337)	(0.013)	(0.003)		(0.054)
om98-113	50	1	39.70	0.0248	0.0007	0.0000	9.28	0.1243	48.80	0.1530	0.3040	98.39	90.36
			(0.000)	(0.000)	(0.000)	(0.000)	(0.000)	(0.000)	(0.000)	(0.000)	(0.000)		(0.000)
om98-116	50	3	40.42	0.0115	0.0046	0.0039	9.16	0.1033	49.41	0.0293	0.3635	99.51	90.58
			(0.180)	(0.005)	(0.003)	(0.006)	(0.159)	(0.023)	(0.309)	(0.002)	(0.008)		(0.181)
om00-149	3	5	39.94	0.0004	0.0000	0.0008	8.79	0.1093	49.94	0.0213	0.3843	99.18	91.02
			(0.228)	(0.001)	(0.000)	(0.001)	(0.080)	(0.009)	(0.348)	(0.005)	(0.018)		(0.084)
om00-150	3	6	40.06	0.0134	0.0000	0.0021	8.20	0.1226	50.41	0.0199	0.3649	99.18	91.64
			(0.078)	(0.004)	(0.000)	(0.003)	(0.083)	(0.008)	(0.167)	(0.006)	(0.008)		(0.083)

Sample	suite	N	SiO_2	TiO_2	Al_2O_3	Cr_2O_3	FeO	MnO	MgO	CaO	NiO	Total	Mg#
om00-151	3	5	40.13	0.0007	0.0000	0.0000	7.91	0.0955	50.82	0.0181	0.4073	99.39	91.97
			(0.133)	(0.002)	(0.000)	(0.000)	(0.153)	(0.011)	(0.138)	(0.009)	(0.013)		(0.158)
om00-152b	3	7	40.50	0.0008	0.0000	0.0001	7.84	0.1001	50.99	0.0140	0.3814	99.83	92.06
			(0.079)	(0.001)	(0.000)	(0.000)	(0.113)	(0.004)	(0.124)	(0.006)	(0.009)		(0.116)
om00-153.1	3	6	40.70	0.0021	0.0000	0.0000	8.04	0.1005	51.06	0.0303	0.3835	100.31	91.88
			(0.060)	(0.003)	(0.000)	(0.000)	(0.079)	(0.006)	(0.137)	(0.021)	(0.007)		(0.088)
om00-154	3	6	40.62	0.0003	0.0000	0.0000	7.89	0.1050	50.84	0.0248	0.3735	99.85	91.99
			(0.079)	(0.001)	(0.000)	(0.000)	(0.104)	(0.007)	(0.159)	(0.006)	(0.004)		(0.100)
om00-155a	3	6	40.54	0.0189	0.0000	0.0020	7.58	0.1206	52.14	0.0240	0.3655	100.79	92.46
			(0.050)	(0.003)	(0.000)	(0.003)	(0.077)	(0.004)	(0.100)	(0.008)	(0.007)		(0.080)
om00-155b	3	3	40.13	0.0092	0.0000	0.0005	7.11	0.1151	51.11	0.0146	0.3356	98.83	92.76
			(0.055)	(0.003)	(0.000)	(0.001)	(0.101)	(0.008)	(0.112)	(0.008)	(0.012)		(0.081)
om00-156	3	6	40.92	0.0000	0.0000	0.0000	7.48	0.0951	51.23	0.0261	0.3764	100.13	92.43
			(0.085)	(0.000)	(0.000)	(0.000)	(0.051)	(0.007)	(0.102)	(0.009)	(0.006)		(0.052)
om00-158	3	5	40.61	0.0007	0.0000	0.0000	7.27	0.1090	51.00	0.0340	0.3598	99.39	92.59
			(0.202)	(0.002)	(0.000)	(0.000)	(0.074)	(0.004)	(0.415)	(0.008)	(0.010)		(0.052)
om00-160	3	5	40.74	0.0018	0.0000	0.0012	7.39	0.1081	50.71	0.0332	0.3581	99.34	92.44
			(0.099)	(0.003)	(0.000)	(0.002)	(0.064)	(0.006)	(0.240)	(0.009)	(0.008)		(0.068)
om00-162	3	5	40.69	0.0041	0.0000	0.0006	7.53	0.1126	50.60	0.0273	0.3592	99.32	92.29
			(0.190)	(0.003)	(0.000)	(0.001)	(0.095)	(0.007)	(0.242)	(0.010)	(0.002)		(0.083)
om00-165a	3	3	40.44	0.0056	0.0000	0.0002	8.93	0.1293	49.84	0.0161	0.3576	99.72	90.87
			(0.059)	(0.000)	(0.000)	(0.000)	(0.065)	(0.004)	(0.215)	(0.001)	(0.003)		(0.030)
om00-166b	3	5	40.62	0.0056	0.0000	0.0004	8.55	0.1220	50.10	0.0124	0.3687	99.79	91.26
			(0.106)	(0.005)	(0.000)	(0.001)	(0.138)	(0.003)	(0.174)	(0.005)	(0.013)		(0.118)
om00-168	3	3	40.61	0.0019	0.0000	0.0037	8.90	0.1224	50.30	0.0263	0.3563	100.32	90.97
			(0.050)	(0.002)	(0.000)	(0.003)	(0.053)	(0.005)	(0.841)	(0.006)	(0.014)		(0.089)
om00-170	3	8	40.21	0.0000	0.0029	0.0001	9.71	0.1291	50.00	0.0165	0.3212	100.39	90.17
			(0.133)	(0.000)	(0.008)	(0.000)	(0.161)	(0.018)	(0.218)	(0.008)	(0.019)		(0.169)
om00-171	3	5	40.15	0.0000	0.0000	0.0023	9.51	0.1128	49.96	0.0154	0.3209	100.07	90.35
			(0.130)	(0.000)	(0.000)	(0.002)	(0.057)	(0.005)	(0.225)	(0.008)	(0.007)		(0.059)

Sample	suite	N	SiO_2	TiO_2	Al_2O_3	Cr_2O_3	FeO	MnO	MgO	CaO	NiO	Total	Mg#
om00-173	3	5	40.18	0.0000	0.0000	0.0000	9.43	0.1100	50.22	0.0159	0.3284	100.28	90.47
			(0.193)	(0.000)	(0.000)	(0.000)	(0.073)	(0.005)	(0.270)	(0.004)	(0.027)		(0.105)
om00-174a	3	6	40.54	0.0179	0.0000	0.0010	9.06	0.1423	50.87	0.0158	0.3750	101.01	90.92
			(0.140)	(0.002)	(0.000)	(0.001)	(0.104)	(0.006)	(0.129)	(0.005)	(0.004)		(0.106)
om00-175	3	5	40.24	0.0000	0.0002	0.0003	9.40	0.1154	50.18	0.0354	0.3309	100.29	90.49
			(0.168)	(0.000)	(0.000)	(0.001)	(0.151)	(0.008)	(0.199)	(0.049)	(0.009)		(0.166)
om00-176a	3	3	40.33	0.0000	0.0000	0.0007	9.00	0.1013	50.46	0.0185	0.3622	100.27	90.91
			(0.058)	(0.000)	(0.000)	(0.001)	(0.032)	(0.004)	(0.190)	(0.004)	(0.005)		(0.046)
om00-176b	3	4	40.65	0.0219	0.0004	0.0018	9.37	0.1466	50.67	0.0186	0.3602	101.24	90.60
			(0.163)	(0.006)	(0.001)	(0.003)	(0.021)	(0.008)	(0.127)	(0.008)	(0.010)		(0.023)
om00-176c	3	2	40.50	0.0000	0.0004	0.0036	9.15	0.1041	50.19	0.0170	0.3708	100.33	90.72
			(0.000)	(0.000)	(0.000)	(0.002)	(0.170)	(0.009)	(0.134)	(0.008)	(0.000)		(0.179)
om00-176d	3	6	40.35	0.0209	0.0001	0.0023	9.69	0.1529	50.62	0.0146	0.3667	101.21	90.30
			(0.176)	(0.003)	(0.000)	(0.003)	(0.080)	(0.004)	(0.238)	(0.002)	(0.004)		(0.087)
om98-118d	0.07	30	40.27	0.0138	0.0052	0.0007	9.32	0.1178	49.66	0.0251	0.3658	99.77	90.48
			(0.196)	(0.008)	(0.002)	(0.002)	(0.145)	(0.020)	(0.276)	(0.008)	(0.006)		(0.143)
om98-118h	0.07	11	40.30	0.0093	0.0043	0.0010	9.30	0.1097	49.73	0.0146	0.3746	99.85	90.51
			(0.197)	(0.009)	(0.002)	(0.002)	(0.091)	(0.016)	(0.295)	(0.004)	(0.010)		(0.083)
om00-75	20	6	40.43	0.0045	0.0004	0.0012	8.64	0.1227	50.58	0.0202	0.3638	100.16	91.25
			(0.200)	(0.004)	(0.001)	(0.001)	(0.097)	(0.007)	(0.119)	(0.005)	(0.013)		(0.090)
om00-76	20	7	40.25	0.0012	0.0000	0.0019	8.26	0.1287	50.72	0.0370	0.3747	99.77	91.63
			(0.091)	(0.002)	(0.000)	(0.001)	(0.064)	(0.008)	(0.130)	(0.030)	(0.004)		(0.075)
om00-77	20	5	40.32	0.0026	0.0001	0.0018	7.91	0.1297	50.81	0.1104	0.3599	99.64	91.97
			(0.108)	(0.003)	(0.000)	(0.002)	(0.107)	(0.005)	(0.134)	(0.008)	(0.003)		(0.112)
om00-78	20	5	40.38	0.0008	0.0032	0.0029	7.83	0.1305	50.96	0.1386	0.3469	99.80	92.06
			(0.115)	(0.001)	(0.007)	(0.006)	(0.061)	(0.009)	(0.135)	(0.012)	(0.004)		(0.053)
om00-79	20	6	40.20	0.0000	0.0000	0.0020	8.08	0.1276	50.65	0.0517	0.3583	99.46	91.79
			(0.057)	(0.000)	(0.000)	(0.001)	(0.095)	(0.006)	(0.097)	(0.005)	(0.003)		(0.095)
om00-80	20	5	40.20	0.0030	0.0000	0.0001	8.67	0.1318	49.94	0.1688	0.3243	99.45	91.12
			(0.069)	(0.004)	(0.000)	(0.000)	(0.061)	(0.007)	(0.053)	(0.018)	(0.002)		(0.066)

Sample	suite	N	SiO_2	TiO_2	Al_2O_3	Cr_2O_3	FeO	MnO	MgO	CaO	NiO	Total	Mg#
om00-81	20	5	40.29	0.0049	0.0003	0.0043	8.76	0.1447	49.93	0.1145	0.3248	99.58	91.04
			(0.125)	(0.002)	(0.001)	(0.006)	(0.046)	(0.009)	(0.172)	(0.023)	(0.006)		(0.061)
om00-83	20	5	40.46	0.0002	0.0010	0.0029	7.80	0.1341	50.97	0.0971	0.3877	99.85	92.10
			(0.095)	(0.000)	(0.002)	(0.005)	(0.126)	(0.013)	(0.167)	(0.014)	(0.007)		(0.130)
om00-84	20	4	40.46	0.0021	0.0000	0.0009	7.79	0.1341	50.87	0.1149	0.3826	99.75	92.09
			(0.129)	(0.002)	(0.000)	(0.001)	(0.071)	(0.005)	(0.097)	(0.004)	(0.005)		(0.075)
om00-85	20	5	40.34	0.0003	0.0000	0.0039	7.76	0.1276	50.84	0.1165	0.3670	99.56	92.11
			(0.123)	(0.001)	(0.000)	(0.003)	(0.061)	(0.004)	(0.132)	(0.011)	(0.003)		(0.042)
om00-86.2	20	5	40.71	0.0027	0.0001	0.0018	8.27	0.1160	50.62	0.0265	0.3678	100.13	91.60
			(0.257)	(0.003)	(0.000)	(0.002)	(0.138)	(0.006)	(0.288)	(0.003)	(0.005)		(0.155)
om00-86.4	20	6	40.61	0.0040	0.0000	0.0008	8.15	0.1166	50.96	0.0181	0.3623	100.22	91.76
			(0.154)	(0.003)	(0.000)	(0.002)	(0.061)	(0.008)	(0.076)	(0.007)	(0.006)		(0.060)
om00-87.1	20	6	40.60	0.0043	0.0000	0.0028	8.23	0.1187	50.83	0.0484	0.3665	100.20	91.67
			(0.237)	(0.002)	(0.000)	(0.002)	(0.127)	(0.012)	(0.234)	(0.008)	(0.006)		(0.142)
om00-87.3	20	5	40.61	0.0023	0.0002	0.0044	8.23	0.1165	50.63	0.0328	0.3723	100.00	91.64
			(0.082)	(0.002)	(0.000)	(0.006)	(0.030)	(0.009)	(0.128)	(0.010)	(0.004)		(0.024)
om00-88.1	20	6	40.83	0.0042	0.0017	0.0086	8.28	0.1207	50.63	0.0512	0.3605	100.29	91.60
			(0.113)	(0.004)	(0.003)	(0.016)	(0.057)	(0.007)	(0.186)	(0.020)	(0.004)		(0.059)
om00-89	20	6	40.69	0.0051	0.0001	0.0005	8.26	0.1204	51.00	0.0191	0.3752	100.47	91.67
			(0.167)	(0.003)	(0.000)	(0.001)	(0.039)	(0.007)	(0.126)	(0.008)	(0.005)		(0.040)
om00-90	20	4	40.72	0.0068	0.0000	0.0011	8.41	0.1198	50.64	0.0148	0.3802	100.29	91.48
			(0.161)	(0.003)	(0.000)	(0.001)	(0.066)	(0.008)	(0.107)	(0.005)	(0.004)		(0.076)
om00-91	20	5	40.15	0.0014	0.0005	0.0007	8.31	0.1391	50.43	0.1404	0.3577	99.53	91.54
			(0.055)	(0.001)	(0.001)	(0.001)	(0.043)	(0.004)	(0.070)	(0.024)	(0.005)		(0.043)
om00-92.2	20	6	40.20	0.0025	0.0006	0.0012	8.25	0.1401	50.38	0.1255	0.3724	99.47	91.59
			(0.115)	(0.004)	(0.001)	(0.002)	(0.049)	(0.006)	(0.122)	(0.014)	(0.007)		(0.061)
om00-93	20	5	40.29	0.0022	0.0000	0.0033	8.26	0.1361	50.30	0.1831	0.3512	99.52	91.57
			(0.156)	(0.002)	(0.000)	(0.002)	(0.061)	(0.003)	(0.133)	(0.007)	(0.003)		(0.055)
om00-94	20	5	40.27	0.0045	0.0001	0.0004	8.32	0.1311	50.49	0.1727	0.3296	99.72	91.54
			(0.089)	(0.003)	(0.000)	(0.001)	(0.040)	(0.007)	(0.103)	(0.013)	(0.003)		(0.051)

Sample	suite	N	SiO_2	TiO_2	Al_2O_3	Cr_2O_3	FeO	MnO	MgO	CaO	NiO	Total	Mg#
om00-95	20	5	40.24	0.0048	0.0003	0.0011	8.40	0.1301	50.28	0.1805	0.3285	99.57	91.43
			(0.149)	(0.003)	(0.001)	(0.001)	(0.031)	(0.006)	(0.068)	(0.010)	(0.005)		(0.033)
om00-98	20	6	40.19	0.0068	0.0006	0.0026	8.15	0.1300	50.37	0.1667	0.3611	99.38	91.68
			(0.116)	(0.005)	(0.001)	(0.002)	(0.036)	(0.006)	(0.107)	(0.012)	(0.005)		(0.041)
om00-99	20	5	40.18	0.0048	0.0003	0.0023	7.96	0.1262	50.39	0.1710	0.3717	99.21	91.86
			(0.095)	(0.004)	(0.001)	(0.002)	(0.107)	(0.004)	(0.076)	(0.015)	(0.004)		(0.100)
om00-100	20	6	40.32	0.0040	0.0000	0.0035	7.87	0.1275	50.57	0.1954	0.3718	99.46	91.97
			(0.085)	(0.002)	(0.000)	(0.002)	(0.053)	(0.010)	(0.113)	(0.002)	(0.003)		(0.057)
om00-101	20	5	40.34	0.0061	0.0000	0.0017	8.19	0.1238	50.32	0.1170	0.3384	99.44	91.64
			(0.127)	(0.004)	(0.000)	(0.002)	(0.061)	(0.005)	(0.114)	(0.045)	(0.004)		(0.063)
om00-104	20	5	39.96	0.0033	0.0000	0.0025	7.85	0.1247	50.29	0.1553	0.3555	98.74	91.95
			(0.033)	(0.003)	(0.000)	(0.004)	(0.048)	(0.009)	(0.142)	(0.019)	(0.005)		(0.055)
om00-105a	20	6	40.09	0.0057	0.0004	0.0027	7.89	0.1281	50.20	0.1831	0.3778	98.88	91.90
			(0.080)	(0.005)	(0.000)	(0.003)	(0.051)	(0.007)	(0.069)	(0.005)	(0.005)		(0.044)
om00-106	20	6	40.14	0.0071	0.0009	0.0052	7.70	0.1240	50.30	0.1832	0.3557	98.82	92.09
			(0.037)	(0.003)	(0.002)	(0.006)	(0.054)	(0.006)	(0.105)	(0.008)	(0.004)		(0.045)
om00-107	20	7	40.00	0.0043	0.0001	0.0043	7.66	0.1252	50.36	0.1861	0.3385	98.67	92.14
			(0.082)	(0.001)	(0.000)	(0.004)	(0.038)	(0.004)	(0.134)	(0.009)	(0.006)		(0.033)
om00-108	20	7	40.20	0.0054	0.0009	0.0014	7.43	0.1216	50.54	0.1710	0.3824	98.86	92.38
			(0.037)	(0.003)	(0.002)	(0.002)	(0.067)	(0.004)	(0.065)	(0.012)	(0.009)		(0.061)
om00-109.1	20	7	40.27	0.0046	0.0001	0.0029	7.52	0.1283	50.48	0.1597	0.3923	98.96	92.28
			(0.041)	(0.003)	(0.000)	(0.003)	(0.103)	(0.006)	(0.136)	(0.007)	(0.005)		(0.112)
om00-110	20	5	41.08	0.0057	0.0000	0.0021	7.75	0.1150	51.22	0.1849	0.3840	100.75	92.17
			(0.085)	(0.003)	(0.000)	(0.003)	(0.105)	(0.007)	(0.108)	(0.011)	(0.007)		(0.104)
om00-112	20	5	41.17	0.0072	0.0000	0.0024	7.81	0.1208	51.07	0.1946	0.3728	100.75	92.10
			(0.224)	(0.004)	(0.000)	(0.002)	(0.066)	(0.008)	(0.166)	(0.009)	(0.006)		(0.079)
om00-113	20	5	41.03	0.0055	0.0001	0.0027	8.12	0.1251	50.86	0.2015	0.3661	100.72	91.78
			(0.147)	(0.003)	(0.000)	(0.003)	(0.068)	(0.011)	(0.084)	(0.010)	(0.006)		(0.073)
om00-115	20	6	40.85	0.0070	0.0007	0.0064	8.37	0.1284	50.59	0.1306	0.3742	100.46	91.51
			(0.117)	(0.004)	(0.002)	(0.011)	(0.048)	(0.008)	(0.096)	(0.013)	(0.007)		(0.048)

Sample	suite	N	SiO_2	TiO_2	Al_2O_3	Cr_2O_3	FeO	MnO	MgO	CaO	NiO	Total	Mg#
om00-117	20	6	41.12	0.0072	0.0000	0.0036	8.19	0.1225	50.80	0.1490	0.3781	100.78	91.71
			(0.161)	(0.004)	(0.000)	(0.003)	(0.078)	(0.005)	(0.106)	(0.012)	(0.008)		(0.065)
om00-119	20	5	41.14	0.0080	0.0003	0.0027	8.44	0.1274	50.45	0.1434	0.3626	100.67	91.42
			(0.143)	(0.001)	(0.001)	(0.006)	(0.050)	(0.007)	(0.088)	(0.019)	(0.004)		(0.052)
om00-122a	20	6	40.88	0.0052	0.0000	0.0023	8.34	0.1256	50.74	0.1469	0.3684	100.61	91.56
			(0.062)	(0.003)	(0.000)	(0.003)	(0.071)	(0.004)	(0.130)	(0.036)	(0.007)		(0.051)
om00-124	20	6	40.77	0.0048	0.0002	0.0009	8.31	0.1326	50.33	0.1696	0.3627	100.07	91.53
			(0.085)	(0.003)	(0.001)	(0.001)	(0.060)	(0.010)	(0.078)	(0.010)	(0.006)		(0.062)
om00-127	20	6	40.84	0.0052	0.0002	0.0045	8.47	0.1260	50.44	0.1653	0.3778	100.43	91.39
			(0.115)	(0.002)	(0.000)	(0.003)	(0.152)	(0.007)	(0.279)	(0.019)	(0.006)		(0.126)
om00-129	20	7	40.83	0.0087	0.0000	0.0006	8.73	0.1314	50.32	0.1583	0.3718	100.56	91.13
			(0.092)	(0.003)	(0.000)	(0.001)	(0.059)	(0.006)	(0.128)	(0.018)	(0.005)		(0.069)
om00-130	20	5	40.83	0.0042	0.0000	0.0007	8.36	0.1378	50.33	0.0639	0.3343	100.07	91.48
			(0.133)	(0.001)	(0.000)	(0.001)	(0.053)	(0.004)	(0.114)	(0.041)	(0.005)		(0.055)
om00-131	20	5	41.07	0.0064	0.0000	0.0018	8.44	0.1348	50.35	0.1172	0.3134	100.43	91.41
			(0.105)	(0.002)	(0.000)	(0.002)	(0.061)	(0.003)	(0.140)	(0.031)	(0.006)		(0.066)
om00-132	20	6	41.00	0.0007	0.0000	0.0002	8.32	0.1360	50.68	0.1233	0.3334	100.59	91.57
			(0.086)	(0.001)	(0.000)	(0.000)	(0.078)	(0.005)	(0.170)	(0.014)	(0.006)		(0.065)
om00-135	20	6	40.97	0.0014	0.0000	0.0005	8.64	0.1386	50.24	0.1529	0.3236	100.46	91.20
			(0.115)	(0.002)	(0.000)	(0.001)	(0.026)	(0.006)	(0.122)	(0.011)	(0.006)		(0.038)
om00-136	20	6	41.15	0.0018	0.0000	0.0013	8.72	0.1405	50.69	0.1174	0.3367	101.16	91.20
			(0.151)	(0.002)	(0.000)	(0.002)	(0.100)	(0.009)	(0.207)	(0.013)	(0.006)		(0.105)
om00-138	20	6	41.03	0.0012	0.0000	0.0031	8.70	0.1385	50.60	0.0986	0.3408	100.91	91.20
			(0.114)	(0.001)	(0.000)	(0.003)	(0.122)	(0.008)	(0.176)	(0.015)	(0.005)		(0.124)
om00-139	20	7	41.06	0.0031	0.0000	0.0012	8.63	0.1311	50.47	0.0982	0.3439	100.74	91.25
			(0.106)	(0.003)	(0.000)	(0.002)	(0.036)	(0.009)	(0.218)	(0.011)	(0.005)		(0.046)
om00-140.3	20	6	41.45	0.0055	0.0000	0.0010	9.21	0.1408	50.17	0.0871	0.3243	101.39	90.67
			(0.089)	(0.003)	(0.000)	(0.001)	(0.058)	(0.006)	(0.204)	(0.011)	(0.004)		(0.069)
om00-141.1	20	5	40.48	0.0069	0.0002	0.0013	9.27	0.1429	49.90	0.0648	0.3109	100.18	90.56
			(0.112)	(0.003)	(0.000)	(0.003)	(0.097)	(0.011)	(0.174)	(0.018)	(0.007)		(0.107)

Sample	suite	N	SiO_2	TiO_2	Al_2O_3	Cr_2O_3	FeO	MnO	MgO	CaO	NiO	Total	Mg#
om00-141.2	20	5	40.28	0.0078	0.0000	0.0004	9.81	0.1446	49.58	0.0186	0.2540	100.10	90.01
			(0.097)	(0.003)	(0.000)	(0.001)	(0.217)	(0.006)	(0.164)	(0.005)	(0.009)		(0.216)
om00-141.3	20	6	40.48	0.0102	0.0000	0.0017	10.15	0.1466	49.57	0.0130	0.2417	100.61	89.70
			(0.168)	(0.002)	(0.000)	(0.004)	(0.119)	(0.007)	(0.215)	(0.004)	(0.009)		(0.134)
om00-141.4	20	4	40.48	0.0073	0.0002	0.0016	10.17	0.1477	49.39	0.0109	0.2461	100.45	89.65
			(0.176)	(0.004)	(0.000)	(0.003)	(0.170)	(0.013)	(0.100)	(0.004)	(0.003)		(0.174)
om00-141.5	20	6	40.17	0.0067	0.0000	0.0019	9.95	0.1429	49.52	0.0182	0.2828	100.10	89.87
			(0.147)	(0.004)	(0.000)	(0.002)	(0.289)	(0.006)	(0.327)	(0.010)	(0.020)		(0.314)
om00-142.1	20	6	40.46	0.0052	0.0004	0.0020	9.34	0.1407	49.83	0.0281	0.3110	100.12	90.48
			(0.079)	(0.004)	(0.001)	(0.004)	(0.124)	(0.002)	(0.141)	(0.006)	(0.006)		(0.117)
om00-142.2	20	6	40.39	0.0075	0.0006	0.0072	9.55	0.1474	49.88	0.0281	0.3168	100.32	90.30
			(0.231)	(0.003)	(0.001)	(0.007)	(0.092)	(0.008)	(0.221)	(0.010)	(0.010)		(0.092)
om00-142.3	20	4	40.33	0.0052	0.0000	0.0015	9.44	0.1450	49.69	0.0220	0.3275	99.95	90.37
			(0.223)	(0.002)	(0.000)	(0.001)	(0.053)	(0.004)	(0.070)	(0.009)	(0.004)		(0.055)
om00-143.2	20	5	40.50	0.0040	0.0000	0.0026	8.94	0.1268	50.36	0.0112	0.3920	100.33	90.94
			(0.059)	(0.004)	(0.000)	(0.004)	(0.106)	(0.002)	(0.117)	(0.005)	(0.006)		(0.109)
om00-144	20	5	40.67	0.0039	0.0000	0.0022	9.17	0.1285	50.21	0.0106	0.3707	100.56	90.71
			(0.115)	(0.004)	(0.000)	(0.003)	(0.123)	(0.003)	(0.154)	(0.003)	(0.006)		(0.138)
om00-145b	20	6	40.50	0.0026	0.0000	0.0012	9.14	0.1333	50.34	0.0157	0.3748	100.50	90.76
			(0.109)	(0.003)	(0.000)	(0.001)	(0.108)	(0.003)	(0.166)	(0.006)	(0.008)		(0.112)
om00-146	20	6	40.39	0.0015	0.0000	0.0033	8.78	0.1286	50.92	0.0140	0.3920	100.62	91.18
			(0.210)	(0.002)	(0.000)	(0.004)	(0.092)	(0.010)	(0.195)	(0.007)	(0.006)		(0.112)
om00-147	20	6	40.66	0.0016	0.0000	0.0007	9.05	0.1344	50.41	0.0180	0.3596	100.63	90.85
			(0.165)	(0.002)	(0.000)	(0.001)	(0.117)	(0.005)	(0.166)	(0.004)	(0.008)		(0.114)
om00-148	20	7	40.70	0.0018	0.0002	0.0016	8.93	0.1384	50.45	0.0176	0.3701	100.61	90.97
			(0.152)	(0.001)	(0.001)	(0.002)	(0.123)	(0.005)	(0.158)	(0.009)	(0.006)		(0.124)
om99-20	20	26	40.38	0.0006	0.0004	0.0015	8.36	0.1412	50.73	0.1137	0.3848	100.12	91.54
			(0.164)	(0.002)	(0.001)	(0.003)	(0.148)	(0.014)	(0.170)	(0.010)	(0.005)		(0.138)
om99-21	20	10	40.48	0.0142	0.0014	0.0010	8.51	0.1054	50.79	0.1455	0.3560	100.41	91.41
			(0.278)	(0.009)	(0.002)	(0.002)	(0.156)	(0.016)	(0.227)	(0.049)	(0.013)		(0.158)

Sample	suite	N	SiO_2	TiO_2	Al_2O_3	Cr_2O_3	FeO	MnO	MgO	CaO	NiO	Total	Mg#
om99-22	20	10	40.54	0.0136	0.0040	0.0014	8.30	0.1096	50.60	0.1776	0.3589	100.11	91.57
			(0.133)	(0.009)	(0.002)	(0.003)	(0.143)	(0.013)	(0.229)	(0.008)	(0.005)		(0.136)
om99-23	20	20	40.27	0.0004	0.0011	0.0000	8.17	0.1446	50.31	0.1726	0.3850	99.46	91.65
			(0.201)	(0.001)	(0.001)	(0.000)	(0.095)	(0.015)	(0.186)	(0.009)	(0.004)		(0.094)
om99-24	20	10	40.64	0.0110	0.0025	0.0000	8.19	0.1045	51.23	0.1865	0.3594	100.73	91.77
			(0.211)	(0.008)	(0.002)	(0.000)	(0.148)	(0.015)	(0.149)	(0.006)	(0.004)		(0.129)
om99-25	20	10	40.65	0.0129	0.0030	0.0009	8.06	0.1069	50.83	0.1610	0.3801	100.20	91.83
			(0.188)	(0.007)	(0.002)	(0.002)	(0.125)	(0.025)	(0.165)	(0.007)	(0.005)		(0.118)
om99-26	20	10	40.52	0.0148	0.0016	0.0005	7.92	0.1099	50.76	0.1734	0.3940	99.89	91.95
			(0.223)	(0.010)	(0.002)	(0.002)	(0.083)	(0.016)	(0.178)	(0.018)	(0.008)		(0.092)
om99-27	20	9	40.54	0.0057	0.0033	0.0022	7.71	0.1102	50.43	0.1777	0.3572	99.35	92.10
			(0.183)	(0.006)	(0.002)	(0.003)	(0.147)	(0.016)	(0.141)	(0.006)	(0.004)		(0.152)
om99-28	20	10	40.29	0.0115	0.0018	0.0025	8.04	0.1093	50.29	0.1275	0.3803	99.25	91.77
			(0.102)	(0.010)	(0.002)	(0.004)	(0.087)	(0.018)	(0.210)	(0.017)	(0.004)		(0.083)
om99-29	20	20	40.20	0.0006	0.0006	0.0000	8.41	0.1571	50.35	0.1159	0.3122	99.54	91.44
			(0.186)	(0.002)	(0.001)	(0.000)	(0.110)	(0.019)	(0.196)	(0.024)	(0.005)		(0.115)
om99-30	20	10	40.83	0.0087	0.0029	0.0012	8.54	0.1151	50.87	0.1166	0.3304	100.81	91.40
			(0.225)	(0.005)	(0.002)	(0.002)	(0.121)	(0.016)	(0.187)	(0.027)	(0.003)		(0.120)
om99-31	20	20	40.54	0.0000	0.0004	0.0004	8.62	0.1606	50.56	0.0955	0.3339	100.31	91.27
			(0.174)	(0.000)	(0.001)	(0.002)	(0.092)	(0.011)	(0.270)	(0.024)	(0.004)		(0.093)
om99-32	20	10	40.42	0.0113	0.0266	0.0792	9.09	0.1240	50.29	0.1062	0.3500	100.50	90.80
			(0.339)	(0.007)	(0.077)	(0.243)	(0.248)	(0.023)	(0.470)	(0.022)	(0.004)		(0.302)
om99-33	20	10	40.34	0.0091	0.0012	0.0012	8.61	0.1144	50.48	0.0454	0.3505	99.95	91.27
			(0.178)	(0.009)	(0.002)	(0.002)	(0.119)	(0.020)	(0.218)	(0.023)	(0.005)		(0.127)
om99-34	20	25	40.40	0.0006	0.0016	0.0040	8.35	0.1551	50.53	0.1839	0.3989	100.03	91.52
			(0.169)	(0.001)	(0.002)	(0.017)	(0.147)	(0.025)	(0.202)	(0.012)	(0.004)		(0.147)
om99-35	20	10	40.20	0.0083	0.0016	0.0024	8.75	0.1131	49.84	0.0408	0.3725	99.33	91.03
			(0.144)	(0.006)	(0.001)	(0.005)	(0.121)	(0.017)	(0.265)	(0.028)	(0.005)		(0.118)
om99-36a	20	10	40.26	0.0115	0.0038	0.0008	8.80	0.1009	49.73	0.0182	0.3722	99.29	90.97
			(0.171)	(0.010)	(0.002)	(0.002)	(0.068)	(0.015)	(0.231)	(0.011)	(0.005)		(0.079)

Sample	suite	N	SiO_2	TiO_2	Al_2O_3	Cr_2O_3	FeO	MnO	MgO	CaO	NiO	Total	Mg#
om99-36c	20	25	40.42	0.0017	0.0021	0.0014	8.78	0.1393	50.00	0.0095	0.3840	99.73	91.04
			(0.163)	(0.004)	(0.003)	(0.004)	(0.127)	(0.025)	(0.254)	(0.004)	(0.010)		(0.131)
om00-145a.1	WT	7	40.46	0.0020	0.0000	0.0024	9.04	0.1354	50.35	0.0117	0.3641	100.37	90.85
			(0.225)	(0.002)	(0.000)	(0.003)	(0.109)	(0.007)	(0.124)	(0.004)	(0.007)		(0.111)
om00-145a.2	WT	6	40.42	0.0028	0.0000	0.0020	9.17	0.1377	50.12	0.0132	0.3722	100.24	90.69
			(0.131)	(0.003)	(0.000)	(0.003)	(0.088)	(0.005)	(0.092)	(0.004)	(0.005)		(0.081)
om94-100	WT	3	40.20	0.0033	0.0133	0.0033	9.02	0.1400	50.60	0.0367	0.3967	100.41	90.91
			(0.163)	(0.006)	(0.006)	(0.006)	(0.078)	(0.010)	(0.096)	(0.006)	(0.006)		(0.066)
om94-101	WT	3	40.22	0.0000	0.0233	0.0000	9.41	0.1400	50.34	0.0233	0.4000	100.55	90.51
			(0.133)	(0.000)	(0.006)	(0.000)	(0.095)	(0.000)	(0.081)	(0.012)	(0.000)		(0.075)
om94-102	WT	4	40.44	0.0012	0.0164	0.0007	9.23	0.1300	50.26	0.0285	0.3907	100.49	90.66
			(0.099)	(0.002)	(0.001)	(0.001)	(0.075)	(0.003)	(0.075)	(0.008)	(0.007)		(0.080)
om94-103	WT	5	40.37	0.0060	0.0100	0.0000	10.03	0.1440	50.64	0.0200	0.4020	101.62	90.00
			(0.243)	(0.005)	(0.007)	(0.000)	(0.618)	(0.009)	(0.450)	(0.000)	(0.015)		(0.626)
om94-104	WT	4	40.44	0.0000	0.0050	0.0025	9.09	0.1225	49.91	0.0200	0.4200	100.00	90.73
			(0.140)	(0.000)	(0.006)	(0.005)	(0.521)	(0.010)	(1.043)	(0.008)	(0.014)		(0.566)
om94-106	WT	2	40.54	0.0000	0.0100	0.0050	8.73	0.1300	51.86	0.0250	0.4200	101.72	91.38
			(0.141)	(0.000)	(0.000)	(0.007)	(0.106)	(0.014)	(0.481)	(0.021)	(0.000)		(0.169)
om94-114	WT	2	40.51	0.0050	0.0150	0.0050	9.79	0.1450	50.82	0.0400	0.3650	101.68	90.25
			(0.064)	(0.007)	(0.007)	(0.007)	(0.163)	(0.007)	(0.276)	(0.000)	(0.021)		(0.194)
om94-115	WT	3	40.54	0.0000	0.0300	0.0233	9.11	0.1200	51.30	0.0833	0.3933	101.61	90.94
			(0.071)	(0.000)	(0.010)	(0.006)	(0.049)	(0.010)	(0.121)	(0.006)	(0.006)		(0.026)
om94-52	WT	3	40.14	0.0000	0.0167	0.0000	9.13	0.1200	51.16	0.0167	0.3933	100.98	90.90
			(0.081)	(0.000)	(0.006)	(0.000)	(0.130)	(0.010)	(0.225)	(0.006)	(0.006)		(0.150)
om94-53	WT	8	40.70	0.0000	0.0088	0.0000	8.77	0.1200	50.13	0.0150	0.3975	100.14	91.06
			(0.188)	(0.000)	(0.006)	(0.000)	(0.143)	(0.011)	(0.846)	(0.005)	(0.007)		(0.250)
om94-55	WT	5	40.85	0.0000	0.0120	0.0000	8.73	0.1220	49.16	0.0540	0.3780	99.30	90.94
			(0.257)	(0.000)	(0.004)	(0.000)	(0.108)	(0.013)	(0.168)	(0.015)	(0.004)		(0.107)
om94-57	WT	10	40.85	0.0000	0.0070	0.0000	8.75	0.1340	49.70	0.0660	0.3640	99.87	91.01
			(0.158)	(0.000)	(0.009)	(0.000)	(0.197)	(0.007)	(0.278)	(0.011)	(0.008)		(0.218)

Sample	suite	N	SiO_2	TiO_2	Al_2O_3	Cr_2O_3	FeO	MnO	MgO	CaO	NiO	Total	Mg#
om94-59	WT	3	40.31	0.0000	0.0210	0.0000	8.88	0.1152	51.48	0.0207	0.4032	101.23	91.18
			(0.030)	(0.000)	(0.002)	(0.000)	(0.110)	(0.006)	(0.055)	(0.003)	(0.007)		(0.091)
om94-60	WT	3	40.22	0.0000	0.0117	0.0024	9.00	0.1182	51.07	0.0188	0.3917	100.83	91.00
			(0.078)	(0.000)	(0.003)	(0.002)	(0.135)	(0.005)	(0.104)	(0.002)	(0.002)		(0.107)
om94-61	WT	3	40.48	0.0033	0.0167	0.0000	7.90	0.1000	51.78	0.0167	0.3967	100.70	92.12
			(0.204)	(0.006)	(0.006)	(0.000)	(0.087)	(0.000)	(0.067)	(0.006)	(0.006)		(0.071)
om94-64	WT	3	40.40	0.0006	0.0155	0.0014	8.85	0.1251	50.63	0.0226	0.4004	100.45	91.07
			(0.197)	(0.001)	(0.003)	(0.002)	(0.049)	(0.004)	(0.070)	(0.008)	(0.007)		(0.034)
om94-65	WT	3	40.15	0.0018	0.0176	0.0018	9.00	0.1265	51.09	0.0164	0.3915	100.80	91.01
			(0.101)	(0.002)	(0.008)	(0.002)	(0.062)	(0.004)	(0.260)	(0.003)	(0.009)		(0.063)
om94-67	WT	3	40.17	0.0033	0.0133	0.0033	8.74	0.1167	51.25	0.0233	0.4033	100.72	91.27
			(0.134)	(0.006)	(0.006)	(0.006)	(0.087)	(0.006)	(0.056)	(0.006)	(0.006)		(0.085)
om94-69	WT	3	41.27	0.0000	0.0100	0.0000	7.93	0.1267	50.71	0.1900	0.4000	100.64	91.94
			(0.040)	(0.000)	(0.000)	(0.000)	(0.071)	(0.006)	(0.161)	(0.000)	(0.000)		(0.077)
om94-72	WT	3	39.92	0.0029	0.0130	0.0013	9.44	0.1267	50.82	0.0242	0.3846	100.74	90.56
			(0.111)	(0.003)	(0.005)	(0.002)	(0.150)	(0.005)	(0.219)	(0.005)	(0.009)		(0.147)
om94-73	WT	4	40.06	0.0027	0.0114	0.0003	8.86	0.1173	51.09	0.0211	0.3970	100.55	91.13
			(0.059)	(0.004)	(0.001)	(0.000)	(0.117)	(0.006)	(0.146)	(0.004)	(0.013)		(0.123)
om94-74	WT	3	40.52	0.0000	0.0400	0.0000	8.99	0.1400	50.88	0.0233	0.4000	101.00	90.99
			(0.110)	(0.000)	(0.000)	(0.000)	(0.064)	(0.000)	(0.084)	(0.006)	(0.010)		(0.066)
om94-76	WT	3	39.65	0.0009	0.0137	0.0006	10.59	0.1481	49.33	0.0170	0.3355	100.09	89.25
			(0.132)	(0.001)	(0.003)	(0.001)	(0.108)	(0.002)	(0.035)	(0.002)	(0.000)		(0.103)
om94-78	WT	3	40.73	0.0000	0.0233	0.0000	9.15	0.1567	50.23	0.0733	0.3567	100.73	90.73
			(0.072)	(0.000)	(0.006)	(0.000)	(0.031)	(0.006)	(0.015)	(0.006)	(0.006)		(0.026)
om94-79	WT	3	40.32	0.0000	0.0233	0.0000	8.97	0.1167	50.54	0.0200	0.3967	100.39	90.95
			(0.103)	(0.000)	(0.006)	(0.000)	(0.165)	(0.006)	(0.110)	(0.010)	(0.015)		(0.170)
om94-80	WT	3	39.94	0.0000	0.0300	0.0000	9.05	0.1500	51.16	0.0567	0.3467	100.73	90.98
			(0.292)	(0.000)	(0.000)	(0.000)	(0.138)	(0.000)	(0.151)	(0.012)	(0.006)		(0.102)
om94-81	WT	3	40.08	0.0000	0.0200	0.0033	9.20	0.1267	51.12	0.0267	0.3967	100.96	90.83
			(0.046)	(0.000)	(0.000)	(0.006)	(0.172)	(0.012)	(0.023)	(0.006)	(0.006)		(0.155)

Sample	suite	N	SiO_2	TiO_2	Al_2O_3	Cr_2O_3	FeO	MnO	MgO	CaO	NiO	Total	Mg#
om94-83	WT	3	40.96	0.0099	0.0229	0.0158	4.28	0.0449	55.04	0.0184	0.6421	101.03	95.82
			(0.286)	(0.002)	(0.008)	(0.008)	(0.240)	(0.008)	(0.471)	(0.006)	(0.061)		(0.248)
om94-87	WT	3	40.42	0.0000	0.0152	0.0007	8.74	0.1297	51.45	0.0214	0.4051	101.17	91.30
			(0.097)	(0.000)	(0.006)	(0.001)	(0.035)	(0.014)	(0.182)	(0.003)	(0.005)		(0.060)
om94-91	WT	4	40.28	0.0020	0.0130	0.0007	9.39	0.1447	50.55	0.0256	0.3998	100.81	90.56
			(0.113)	(0.004)	(0.001)	(0.001)	(0.059)	(0.005)	(0.171)	(0.008)	(0.012)		(0.081)
om94-98	WT	7	40.14	0.0057	0.0143	0.0000	9.13	0.1257	50.82	0.0229	0.3971	100.66	90.84
			(0.250)	(0.005)	(0.013)	(0.000)	(0.108)	(0.005)	(0.099)	(0.010)	(0.005)		(0.107)
om94-99	WT	2	40.35	0.0000	0.0000	0.0000	9.86	0.1500	48.79	0.0900	0.3400	99.58	89.82
			(0.042)	(0.000)	(0.000)	(0.000)	(0.064)	(0.000)	(0.014)	(0.014)	(0.000)		(0.056)

Table B2 - Spinel Compositions

sample	Width	N	SiO_2	TiO_2	Al_2O_3	Cr_2O_3	Fe_2O_3	FeO	MnO	MgO	CaO	NiO	Total	Mg#	Cr#	Fe^{3+}#
om00-13	50	14	0.2108	0.6758	21.89	38.75	8.41	20.03	0.3576	9.55	0.0010	0.1163	100	45.93	54.29	10.09
			(0.647)	(0.028)	(0.732)	(0.793)	(0.437)	(0.685)	(0.047)	(0.395)	(0.002)	(0.023)		(1.852)	(1.247)	(0.547)
om00-14a	50	10	0.0319	0.6028	25.12	38.28	6.05	18.49	0.3515	10.99	0.0000	0.0851	100	51.44	50.56	7.07
			(0.008)	(0.019)	(0.845)	(0.608)	(1.154)	(0.504)	(0.014)	(0.309)	(0.000)	(0.016)		(1.364)	(0.933)	(1.373)
om00-14b	50	10	0.0244	0.2732	31.80	35.85	1.55	17.96	0.3018	12.20	0.0000	0.0341	100	54.77	43.06	1.74
			(0.008)	(0.030)	(0.401)	(0.418)	(0.186)	(0.523)	(0.018)	(0.365)	(0.000)	(0.009)		(1.459)	(0.569)	(0.209)
om00-15	50	4	0.0337	0.6785	17.14	45.60	7.98	17.05	0.3609	11.05	0.0000	0.1067	100	53.59	64.10	9.65
			(0.004)	(0.024)	(0.134)	(0.134)	(0.107)	(0.260)	(0.018)	(0.191)	(0.000)	(0.005)		(0.809)	(0.237)	(0.122)
om00-16	50	4	0.0100	0.6542	17.86	44.11	8.49	17.72	0.3248	10.70	0.0007	0.1334	100	51.84	62.36	10.25
			(0.003)	(0.030)	(0.613)	(0.829)	(0.523)	(0.301)	(0.010)	(0.196)	(0.001)	(0.013)		(0.871)	(1.158)	(0.652)
om00-17	50	10	0.0524	0.6972	17.51	44.08	8.67	18.21	0.3511	10.32	0.0023	0.1140	100	50.24	62.80	10.52
			(0.026)	(0.047)	(0.386)	(1.151)	(1.070)	(0.633)	(0.039)	(0.443)	(0.004)	(0.017)		(1.936)	(0.768)	(1.335)
om00-19	50	3	0.0236	0.6914	18.04	45.50	6.49	18.70	0.3438	10.09	0.0019	0.1160	100	49.02	62.85	7.87
			(0.003)	(0.019)	(0.175)	(0.277)	(0.456)	(0.356)	(0.024)	(0.259)	(0.003)	(0.029)		(1.112)	(0.113)	(0.560)
om00-20	50	4	0.0371	0.6095	18.16	45.81	6.58	17.36	0.3577	11.00	0.0000	0.0913	100	53.03	62.85	7.92
			(0.006)	(0.027)	(0.189)	(0.263)	(0.190)	(0.407)	(0.007)	(0.282)	(0.000)	(0.004)		(1.221)	(0.374)	(0.210)
om00-21	50	6	0.0265	0.6102	17.21	44.89	8.33	18.02	0.3274	10.44	0.0000	0.1423	100	50.80	63.63	10.10
			(0.005)	(0.025)	(0.391)	(0.912)	(0.552)	(0.522)	(0.026)	(0.307)	(0.000)	(0.016)		(1.456)	(0.948)	(0.676)
om00-22	50	3	0.0683	0.5926	16.27	47.22	7.12	17.75	0.2965	10.55	0.0038	0.1365	100	51.44	66.08	8.66
			(0.042)	(0.021)	(0.737)	(0.320)	(1.292)	(0.499)	(0.043)	(0.207)	(0.004)	(0.037)		(1.190)	(0.893)	(1.586)
om00-23	50	11	0.0249	0.6195	17.17	44.79	8.49	17.96	0.3662	10.47	0.0010	0.1026	100	50.95	63.63	10.30
			(0.006)	(0.019)	(0.363)	(0.647)	(0.435)	(0.407)	(0.010)	(0.288)	(0.001)	(0.006)		(1.253)	(0.753)	(0.531)
om00-24	50	6	0.0286	0.5839	17.85	44.14	8.49	17.79	0.3237	10.66	0.0033	0.1409	100	51.64	62.39	10.25
			(0.038)	(0.032)	(0.299)	(0.397)	(0.301)	(0.487)	(0.012)	(0.331)	(0.008)	(0.009)		(1.459)	(0.497)	(0.389)
om00-25	50	4	0.0077	0.5647	17.96	44.79	7.71	17.93	0.3109	10.63	0.0000	0.1032	100	51.38	62.59	9.30
			(0.002)	(0.029)	(0.173)	(0.428)	(0.345)	(0.509)	(0.031)	(0.357)	(0.000)	(0.018)		(1.551)	(0.250)	(0.446)
om00-26	50	6	0.0214	0.5637	17.41	44.93	8.08	18.12	0.3368	10.42	0.0009	0.1191	100	50.61	63.38	9.79
			(0.009)	(0.017)	(0.321)	(0.268)	(0.274)	(0.270)	(0.019)	(0.188)	(0.002)	(0.019)		(0.818)	(0.525)	(0.344)
om00-27	50	11	0.0344	0.5668	18.28	44.66	7.58	17.53	0.3359	10.91	0.0026	0.0940	100	52.59	62.10	9.12
			(0.014)	(0.032)	(0.401)	(0.502)	(0.378)	(0.193)	(0.027)	(0.146)	(0.005)	(0.018)		(0.603)	(0.715)	(0.465)
om00-29	50	4	0.0177	0.5794	17.95	44.55	8.08	17.49	0.3266	10.88	0.0014	0.1280	100	52.57	62.48	9.74
			(0.007)	(0.033)	(0.263)	(0.460)	(0.155)	(0.252)	(0.008)	(0.156)	(0.002)	(0.021)		(0.716)	(0.577)	(0.188)
om00-30	50	13	0.0231	0.6069	17.58	44.83	8.31	17.16	0.3445	11.05	0.0024	0.1029	100	53.44	63.11	10.02
			(0.017)	(0.022)	(0.204)	(0.441)	(0.425)	(0.203)	(0.009)	(0.149)	(0.003)	(0.005)		(0.629)	(0.377)	(0.523)

sample	Width	N	SiO_2	TiO_2	Al_2O_3	Cr_2O_3	Fe_2O_3	FeO	MnO	MgO	CaO	NiO	Total	Mg#	Cr#	Fe^{3+}#
om00-31	50	5	0.0123	0.5984	18.04	44.83	7.50	18.04	0.3164	10.54	0.0000	0.1292	100	51.00	62.51	9.05
			(0.005)	(0.033)	(0.364)	(0.721)	(0.565)	(0.663)	(0.021)	(0.461)	(0.000)	(0.025)		(2.016)	(0.835)	(0.650)
om00-32	50	3	0.0461	0.5922	18.03	44.20	8.40	17.25	0.3034	11.05	0.0000	0.1234	100	53.33	62.17	10.11
			(0.012)	(0.012)	(0.291)	(1.438)	(1.083)	(0.212)	(0.012)	(0.151)	(0.000)	(0.030)		(0.645)	(1.153)	(1.300)
om00-32.5	50	6	0.0245	0.6389	18.19	43.52	8.83	17.40	0.3488	10.94	0.0010	0.1074	100	52.86	61.61	10.63
			(0.005)	(0.017)	(0.471)	(0.563)	(0.451)	(0.265)	(0.008)	(0.218)	(0.002)	(0.007)		(0.875)	(0.816)	(0.565)
om00-33	50	6	0.0051	0.5897	17.82	44.72	7.99	17.69	0.3238	10.74	0.0000	0.1266	100	51.97	62.74	9.64
			(0.004)	(0.033)	(0.486)	(0.731)	(0.509)	(0.595)	(0.011)	(0.430)	(0.000)	(0.013)		(1.834)	(0.866)	(0.648)
om00-34	50	7	0.0259	0.5949	17.74	44.90	7.97	17.42	0.3167	10.91	0.0004	0.1272	100	52.75	62.94	9.61
			(0.006)	(0.040)	(0.364)	(0.611)	(0.445)	(0.384)	(0.008)	(0.263)	(0.001)	(0.016)		(1.149)	(0.703)	(0.552)
om00-35	50	6	0.0219	0.6585	17.61	44.29	8.49	17.94	0.3666	10.52	0.0009	0.0981	100	51.11	62.79	10.28
			(0.002)	(0.040)	(0.171)	(0.523)	(0.502)	(0.084)	(0.009)	(0.075)	(0.001)	(0.011)		(0.288)	(0.364)	(0.619)
om00-37	50	3	0.3248	0.6184	20.02	43.85	6.19	17.58	0.2743	11.00	0.0078	0.1413	100	52.71	59.52	7.40
			(0.503)	(0.051)	(1.737)	(2.267)	(0.516)	(1.289)	(0.027)	(0.773)	(0.007)	(0.023)		(3.575)	(3.331)	(0.603)
om00-38	50	6	0.0136	0.4277	16.76	46.39	6.61	20.47	0.3838	8.83	0.0043	0.1067	100	43.48	65.00	8.10
			(0.004)	(0.015)	(0.528)	(0.461)	(0.402)	(0.365)	(0.018)	(0.275)	(0.008)	(0.019)		(1.193)	(0.889)	(0.506)
om00-39	50	10	0.0340	0.4056	15.77	47.69	6.37	20.58	0.4195	8.66	0.0045	0.0651	100	42.87	66.99	7.85
			(0.006)	(0.009)	(0.202)	(0.333)	(0.338)	(0.299)	(0.009)	(0.191)	(0.004)	(0.009)		(0.893)	(0.394)	(0.411)
om00-41	50	1	0.0000	0.5836	19.82	43.73	6.87	17.46	0.2940	11.15	0.0000	0.1006	100	53.23	59.68	8.19
			(0.000)	(0.000)	(0.000)	(0.000)	(0.000)	(0.000)	(0.000)	(0.000)	(0.000)	(0.000)		(0.000)	(0.000)	(0.000)
om00-42	50	3	0.0199	0.6759	21.92	41.01	7.05	17.76	0.3396	11.10	0.0039	0.1248	100	52.69	55.63	8.35
			(0.002)	(0.063)	(1.161)	(2.754)	(0.965)	(1.324)	(0.026)	(0.793)	(0.002)	(0.010)		(3.646)	(2.988)	(1.155)
om00-46	50	4	0.0024	0.6119	20.78	44.09	6.10	15.49	0.2884	12.53	0.0007	0.1111	100	59.05	58.74	7.17
			(0.003)	(0.027)	(0.250)	(0.448)	(0.185)	(0.294)	(0.008)	(0.198)	(0.001)	(0.018)		(0.838)	(0.505)	(0.227)
om00-49	50	9	0.0184	0.6461	19.82	44.00	6.64	17.12	0.3318	11.32	0.0042	0.1026	100	54.09	59.82	7.91
			(0.004)	(0.041)	(0.362)	(0.671)	(0.269)	(0.710)	(0.019)	(0.480)	(0.003)	(0.006)		(2.077)	(0.751)	(0.333)
om00-50	50	4	0.0229	0.4529	16.77	47.68	5.62	19.52	0.3731	9.48	0.0021	0.0807	100	46.40	65.61	6.86
			(0.008)	(0.037)	(0.796)	(1.139)	(0.444)	(0.514)	(0.025)	(0.413)	(0.003)	(0.014)		(1.732)	(1.588)	(0.521)
om00-51	50	5	0.0093	0.5114	19.32	43.52	7.57	17.77	0.3027	10.89	0.0000	0.1039	100	52.21	60.17	9.06
			(0.006)	(0.023)	(0.403)	(0.586)	(0.149)	(0.298)	(0.015)	(0.164)	(0.000)	(0.016)		(0.791)	(0.811)	(0.182)
om00-52	50	5	0.0265	0.6134	17.88	45.66	6.82	18.02	0.3200	10.54	0.0000	0.1095	100	51.05	63.15	8.24
			(0.010)	(0.034)	(0.391)	(0.701)	(0.570)	(0.342)	(0.025)	(0.204)	(0.000)	(0.020)		(0.956)	(0.757)	(0.698)
om00-53	50	8	0.0226	0.7108	21.33	40.84	7.86	17.74	0.3394	11.03	0.0076	0.1106	100	52.57	56.19	9.33
			(0.005)	(0.023)	(1.187)	(2.794)	(1.471)	(0.718)	(0.019)	(0.427)	(0.005)	(0.010)		(1.963)	(3.035)	(1.718)

sample	Width	N	SiO_2	TiO_2	Al_2O_3	Cr_2O_3	Fe_2O_3	FeO	MnO	MgO	CaO	NiO	Total	Mg#	Cr#	Fe^{3+}#
om00-54	50	4	0.0085	0.6080	18.25	44.56	7.59	17.88	0.2999	10.69	0.0000	0.1072	100	51.59	62.09	9.15
			(0.004)	(0.011)	(0.510)	(0.901)	(0.209)	(0.587)	(0.013)	(0.348)	(0.000)	(0.016)		(1.632)	(1.130)	(0.250)
om00-55	50	5	0.0105	0.6079	18.54	44.01	7.79	17.95	0.3141	10.64	0.0069	0.1271	100	51.38	61.43	9.38
			(0.007)	(0.028)	(0.880)	(0.968)	(0.420)	(0.331)	(0.017)	(0.289)	(0.011)	(0.025)		(1.132)	(1.587)	(0.534)
om00-56	50	5	0.0063	0.5736	21.58	42.24	6.45	17.33	0.2900	11.41	0.0000	0.1213	100	53.99	56.77	7.62
			(0.005)	(0.060)	(1.106)	(1.231)	(0.292)	(0.279)	(0.011)	(0.256)	(0.000)	(0.022)		(0.923)	(1.945)	(0.355)
om00-57	50	8	0.0266	0.6754	18.67	44.13	7.57	17.62	0.3497	10.85	0.0050	0.1036	100	52.33	61.32	9.10
			(0.006)	(0.024)	(0.171)	(0.292)	(0.121)	(0.348)	(0.017)	(0.248)	(0.003)	(0.006)		(1.064)	(0.345)	(0.148)
om00-58	50	7	0.0171	0.6525	18.09	44.96	7.14	18.38	0.3293	10.32	0.0000	0.0977	100	50.02	62.51	8.64
			(0.005)	(0.040)	(0.384)	(0.520)	(0.205)	(0.350)	(0.021)	(0.241)	(0.000)	(0.015)		(1.056)	(0.761)	(0.233)
om00-58.5	50	6	0.0219	0.6677	17.50	45.27	7.40	18.56	0.3812	10.12	0.0009	0.0880	100	49.28	63.45	8.99
			(0.002)	(0.024)	(0.169)	(0.449)	(0.383)	(0.583)	(0.016)	(0.415)	(0.001)	(0.007)		(1.814)	(0.167)	(0.499)
om00-65	50	6	0.0256	0.6064	18.01	45.01	7.27	18.24	0.3151	10.43	0.0005	0.0924	100	50.49	62.64	8.79
			(0.013)	(0.021)	(0.362)	(0.453)	(0.170)	(0.173)	(0.027)	(0.119)	(0.001)	(0.026)		(0.516)	(0.693)	(0.206)
om00-66	50	5	0.0098	0.6162	17.41	46.35	6.61	18.12	0.3396	10.42	0.0006	0.1207	100	50.62	64.10	8.01
			(0.007)	(0.018)	(0.192)	(0.227)	(0.423)	(0.348)	(0.017)	(0.242)	(0.001)	(0.012)		(1.056)	(0.156)	(0.521)
om00-68	50	6	0.0180	0.6020	18.40	44.74	7.17	18.11	0.2997	10.57	0.0005	0.0926	100	50.97	61.99	8.64
			(0.006)	(0.026)	(0.274)	(0.313)	(0.374)	(0.472)	(0.012)	(0.322)	(0.001)	(0.009)		(1.409)	(0.381)	(0.466)
om00-69	50	5	0.0195	0.5968	17.50	44.32	8.44	18.53	0.3269	10.17	0.0006	0.0925	100	49.45	62.94	10.24
			(0.004)	(0.021)	(0.395)	(0.668)	(0.650)	(0.378)	(0.015)	(0.273)	(0.001)	(0.012)		(1.180)	(0.655)	(0.817)
om00-70	50	12	0.0224	0.6897	19.16	45.00	5.39	19.78	0.3835	9.52	0.0000	0.0656	100	46.18	61.19	6.52
			(0.006)	(0.031)	(0.943)	(0.811)	(0.489)	(0.279)	(0.013)	(0.168)	(0.000)	(0.009)		(0.756)	(1.584)	(0.607)
om00-71	50	6	0.0382	0.0854	20.25	49.35	1.18	17.19	0.3169	11.55	0.0059	0.0310	100	54.50	62.05	1.39
			(0.059)	(0.012)	(0.412)	(0.416)	(0.177)	(0.170)	(0.011)	(0.094)	(0.015)	(0.006)		(0.426)	(0.667)	(0.209)
om00-72	50	14	0.0304	0.4635	19.78	45.55	4.86	18.26	0.3502	10.65	0.0038	0.0560	100	50.97	60.71	5.81
			(0.030)	(0.015)	(0.389)	(0.494)	(0.280)	(0.328)	(0.008)	(0.232)	(0.009)	(0.009)		(0.991)	(0.681)	(0.342)
om00-73	50	4	0.0209	0.0846	22.80	46.75	0.94	17.33	0.3005	11.75	0.0000	0.0180	100	54.72	57.91	1.10
			(0.003)	(0.004)	(0.984)	(0.815)	(0.237)	(0.222)	(0.014)	(0.248)	(0.000)	(0.008)		(0.834)	(1.473)	(0.281)
om00-74	50	6	0.0114	0.0369	25.35	44.32	0.76	16.91	0.2889	12.30	0.0000	0.0237	100	56.46	53.98	0.87
			(0.005)	(0.009)	(0.788)	(1.055)	(0.067)	(0.472)	(0.011)	(0.241)	(0.000)	(0.010)		(1.165)	(1.364)	(0.076)
om00-149	3	10	0.0101	0.1666	25.38	42.03	3.21	16.09	0.2532	12.75	0.0091	0.1109	100	58.54	52.63	3.68
			(0.029)	(0.016)	(0.398)	(0.499)	(0.112)	(0.254)	(0.016)	(0.137)	(0.020)	(0.008)		(0.638)	(0.683)	(0.129)
om00-150	3	5	0.0045	0.1044	24.50	43.17	3.17	15.84	0.2642	12.84	0.0024	0.1008	100	59.09	54.18	3.65
			(0.007)	(0.009)	(0.492)	(0.485)	(0.204)	(0.223)	(0.015)	(0.111)	(0.005)	(0.028)		(0.540)	(0.767)	(0.241)

sample	Width	N	SiO_2	TiO_2	Al_2O_3	Cr_2O_3	Fe_2O_3	FeO	MnO	MgO	CaO	NiO	Total	Mg#	Cr#	Fe^{3+}#
om00-151	3	12	0.0027	0.0776	20.42	47.99	2.79	16.07	0.2761	12.28	0.0032	0.0841	100	57.67	61.19	3.28
			(0.005)	(0.006)	(0.661)	(0.505)	(0.511)	(0.387)	(0.010)	(0.207)	(0.010)	(0.011)		(0.996)	(1.003)	(0.606)
om00-152b	3	13	0.0027	0.2875	19.50	48.27	3.18	16.59	0.2968	11.78	0.0002	0.0954	100	55.85	62.42	3.77
			(0.003)	(0.020)	(0.211)	(0.294)	(0.145)	(0.365)	(0.011)	(0.249)	(0.001)	(0.008)		(1.061)	(0.364)	(0.174)
om00-153	3	13	0.0002	0.3095	21.76	45.18	3.87	16.27	0.2806	12.22	0.0000	0.1036	100	57.24	58.22	4.54
			(0.001)	(0.063)	(0.969)	(0.775)	(0.654)	(0.528)	(0.015)	(0.392)	(0.000)	(0.015)		(1.560)	(1.371)	(0.784)
om00-154	3	15	0.0031	0.3374	19.92	46.53	4.25	17.10	0.2919	11.47	0.0004	0.1066	100	54.44	61.05	5.04
			(0.003)	(0.011)	(0.476)	(0.434)	(0.327)	(0.844)	(0.015)	(0.580)	(0.001)	(0.007)		(2.472)	(0.712)	(0.399)
om00-155a	3	6	0.0000	0.2814	17.39	50.19	3.54	16.79	0.3063	11.45	0.0019	0.0614	100	54.85	65.95	4.23
			(0.000)	(0.018)	(0.467)	(0.361)	(0.243)	(0.288)	(0.022)	(0.177)	(0.004)	(0.014)		(0.801)	(0.752)	(0.300)
om00-155b	3	8	0.0047	0.3069	17.51	50.28	3.32	16.70	0.3094	11.52	0.0011	0.0548	100	55.14	65.83	3.98
			(0.009)	(0.019)	(0.107)	(0.564)	(0.239)	(1.051)	(0.026)	(0.704)	(0.002)	(0.025)		(3.081)	(0.318)	(0.297)
om00-156	3	10	0.0381	0.2794	14.83	52.69	3.72	17.05	0.3215	10.98	0.0017	0.0906	100	53.44	70.44	4.53
			(0.007)	(0.046)	(0.591)	(0.504)	(0.257)	(0.575)	(0.025)	(0.436)	(0.003)	(0.010)		(1.826)	(1.000)	(0.320)
om00-158	3	4	0.0429	0.3260	17.26	50.75	3.01	16.87	0.3078	11.37	0.0022	0.0592	100	54.56	66.36	3.61
			(0.014)	(0.013)	(0.210)	(0.651)	(0.588)	(0.304)	(0.012)	(0.224)	(0.001)	(0.004)		(0.936)	(0.513)	(0.701)
om00-160	3	4	0.0362	0.1568	18.47	49.36	3.45	16.21	0.2951	11.96	0.0022	0.0625	100	56.80	64.20	4.10
			(0.004)	(0.005)	(0.307)	(0.614)	(0.406)	(0.551)	(0.012)	(0.358)	(0.003)	(0.008)		(1.567)	(0.596)	(0.487)
om00-162	3	6	0.0186	0.4661	20.57	47.17	3.22	15.82	0.2771	12.38	0.0084	0.0647	100	58.24	60.61	3.79
			(0.006)	(0.014)	(0.321)	(0.623)	(0.435)	(0.580)	(0.019)	(0.392)	(0.018)	(0.012)		(1.665)	(0.564)	(0.522)
om00-165a	3	4	0.0147	0.1137	25.52	42.03	3.03	16.29	0.2518	12.68	0.0000	0.0688	100	58.13	52.49	3.48
			(0.003)	(0.020)	(0.508)	(0.590)	(0.112)	(0.399)	(0.011)	(0.224)	(0.000)	(0.009)		(1.021)	(0.838)	(0.134)
om00-166b	3	6	0.0121	0.2087	27.48	40.19	2.65	16.27	0.2434	12.89	0.0021	0.0570	100	58.54	49.59	3.02
			(0.004)	(0.053)	(2.793)	(2.647)	(0.536)	(0.560)	(0.010)	(0.268)	(0.005)	(0.022)		(1.178)	(4.130)	(0.640)
om00-168	3	9	0.0158	0.1604	24.89	42.52	3.11	16.53	0.2586	12.44	0.0000	0.0770	100	57.29	53.41	3.59
			(0.002)	(0.030)	(0.594)	(0.567)	(0.106)	(0.336)	(0.014)	(0.243)	(0.000)	(0.009)		(0.965)	(0.927)	(0.128)
om00-170	3	4	0.0200	0.2599	24.07	41.69	4.43	17.44	0.2864	11.67	0.0000	0.1244	100	54.40	53.75	5.15
			(0.007)	(0.042)	(0.670)	(0.604)	(0.054)	(0.524)	(0.014)	(0.384)	(0.000)	(0.017)		(1.561)	(1.055)	(0.077)
om00-171	3	6	0.0311	0.3007	25.18	40.18	4.37	18.32	0.2930	11.21	0.0010	0.1050	100	52.17	51.71	5.08
			(0.034)	(0.031)	(0.919)	(0.881)	(0.445)	(0.437)	(0.018)	(0.237)	(0.002)	(0.010)		(1.110)	(1.420)	(0.532)
om00-173	3	8	0.0137	0.2653	24.88	41.28	4.11	17.00	0.2622	12.07	0.0000	0.1193	100	55.86	52.67	4.75
			(0.005)	(0.016)	(0.571)	(0.497)	(0.211)	(0.290)	(0.015)	(0.209)	(0.000)	(0.012)		(0.841)	(0.861)	(0.254)
om00-174a	3	5	0.0019	0.1589	24.44	42.49	3.64	16.54	0.2607	12.37	0.0006	0.0915	100	57.13	53.84	4.21
			(0.004)	(0.012)	(0.096)	(0.165)	(0.085)	(0.266)	(0.009)	(0.174)	(0.001)	(0.029)		(0.738)	(0.181)	(0.096)

sample	Width	N	SiO_2	TiO_2	Al_2O_3	Cr_2O_3	Fe_2O_3	FeO	MnO	MgO	CaO	NiO	Total	Mg#	Cr#	Fe3*#
om00-175	3	9	0.0241	0.3038	25.62	40.22	4.30	17.07	0.2473	12.10	0.0003	0.1130	100	55.82	51.29	4.97
			(0.026)	(0.017)	(0.493)	(0.468)	(0.194)	(0.326)	(0.015)	(0.213)	(0.001)	(0.013)		(0.897)	(0.750)	(0.234)
om00-176a	3	12	0.0081	0.1357	25.41	41.17	3.82	16.78	0.2482	12.31	0.0000	0.1067	100	56.67	52.09	4.40
			(0.005)	(0.018)	(0.422)	(0.338)	(0.234)	(0.184)	(0.015)	(0.135)	(0.000)	(0.014)		(0.534)	(0.600)	(0.277)
om00-176b	3	5	0.1030	0.1888	26.15	39.88	4.00	17.30	0.2664	12.01	0.0018	0.1017	100	55.30	50.58	4.61
			(0.230)	(0.037)	(1.609)	(2.007)	(0.262)	(0.484)	(0.034)	(0.223)	(0.003)	(0.026)		(1.103)	(2.779)	(0.281)
om00-176c	3	14	0.0367	0.1907	25.93	40.69	3.79	16.39	0.2532	12.59	0.0004	0.1193	100	57.80	51.28	4.35
			(0.023)	(0.032)	(0.507)	(0.590)	(0.155)	(0.217)	(0.014)	(0.143)	(0.001)	(0.012)		(0.590)	(0.840)	(0.181)
om00-176d	3	6	0.0000	0.0818	25.55	41.04	3.82	16.86	0.2696	12.27	0.0020	0.1033	100	56.47	51.86	4.39
			(0.000)	(0.012)	(0.537)	(0.994)	(0.368)	(0.734)	(0.011)	(0.440)	(0.002)	(0.019)		(1.945)	(1.088)	(0.429)
om98-118d	0.07	71	0.0067	0.1859	21.62	43.70	4.79	18.63	0.3149	10.67	0.0040	0.0789	100	50.51	57.57	5.67
			(0.011)	(0.020)	(0.832)	(0.915)	(0.733)	(0.761)	(0.020)	(0.555)	(0.005)	(0.016)		(2.319)	(1.277)	(0.883)
om98-118h	0.07	26	0.0001	0.1310	24.43	42.41	3.31	17.83	0.2764	11.54	0.0009	0.0676	100	53.58	53.81	3.84
			(0.001)	(0.016)	(1.001)	(1.295)	(0.363)	(0.480)	(0.021)	(0.278)	(0.002)	(0.014)		(1.248)	(1.751)	(0.423)
om00-75	20	7	0.0000	0.1057	20.40	48.83	1.52	17.39	0.2707	11.48	0.0000	0.0000	100	54.06	61.63	1.80
			(0.000)	(0.021)	(0.742)	(0.834)	(0.288)	(0.626)	(0.013)	(0.374)	(0.000)	(0.000)		(1.691)	(1.238)	(0.345)
om00-76	20	7	0.0071	0.2947	17.97	49.90	3.01	17.23	0.2943	11.22	0.0029	0.0669	100	53.72	65.11	3.62
			(0.005)	(0.058)	(1.321)	(0.556)	(1.599)	(0.228)	(0.013)	(0.199)	(0.003)	(0.034)		(0.662)	(1.641)	(1.937)
om00-77	20	5	0.0099	0.4662	18.43	46.24	6.22	16.69	0.2884	11.53	0.0006	0.1143	100	55.17	62.73	7.43
			(0.012)	(0.005)	(0.426)	(0.212)	(0.200)	(0.495)	(0.022)	(0.373)	(0.001)	(0.015)		(1.528)	(0.613)	(0.267)
om00-78	20	6	0.0021	0.5180	19.34	45.22	6.45	16.01	0.2961	12.05	0.0010	0.1115	100	57.30	61.07	7.65
			(0.003)	(0.005)	(0.616)	(0.754)	(0.333)	(0.441)	(0.012)	(0.283)	(0.002)	(0.011)		(1.242)	(1.105)	(0.408)
om00-79	20	6	0.0139	0.3239	14.81	54.00	2.23	17.58	0.3166	10.66	0.0048	0.0620	100	51.93	70.98	2.72
			(0.004)	(0.017)	(0.273)	(0.331)	(0.361)	(0.890)	(0.024)	(0.618)	(0.004)	(0.017)		(2.706)	(0.439)	(0.434)
om00-80	20	5	0.0025	0.5177	18.89	44.78	7.19	16.63	0.2720	11.61	0.0006	0.1120	100	55.44	61.40	8.58
			(0.003)	(0.044)	(0.244)	(0.533)	(0.318)	(0.620)	(0.024)	(0.433)	(0.001)	(0.004)		(1.838)	(0.447)	(0.409)
om00-81	20	5	0.0124	0.5280	18.64	45.17	6.64	17.77	0.3023	10.82	0.0006	0.1053	100	52.06	61.92	7.98
			(0.006)	(0.041)	(0.494)	(0.676)	(0.142)	(0.449)	(0.022)	(0.267)	(0.001)	(0.013)		(1.242)	(0.969)	(0.176)
om00-83	20	6	0.0141	0.4017	18.25	48.31	4.58	16.13	0.3110	11.90	0.0068	0.0966	100	56.79	63.98	5.46
			(0.025)	(0.011)	(0.300)	(0.411)	(0.099)	(0.487)	(0.021)	(0.294)	(0.009)	(0.008)		(1.348)	(0.571)	(0.117)
om00-84	20	5	0.0118	0.4679	16.52	49.92	4.69	16.53	0.3269	11.44	0.0064	0.0978	100	55.23	66.97	5.65
			(0.005)	(0.018)	(0.207)	(0.282)	(0.126)	(0.235)	(0.019)	(0.159)	(0.004)	(0.015)		(0.694)	(0.393)	(0.149)
om00-85	20	3	0.0124	0.4511	16.78	49.87	4.42	16.67	0.3101	11.40	0.0000	0.0900	100	54.93	66.59	5.32
			(0.008)	(0.011)	(0.145)	(0.241)	(0.072)	(0.279)	(0.018)	(0.184)	(0.000)	(0.019)		(0.815)	(0.295)	(0.087)

sample	Width	N	SiO_2	TiO_2	Al_2O_3	Cr_2O_3	Fe_2O_3	FeO	MnO	MgO	CaO	NiO	Total	Mg#	Cr#	Fe^{3+}#
om00-86.2	20	7	0.0000	0.0424	20.15	49.88	1.06	16.61	0.2648	11.99	0.0000	0.0000	100	56.29	62.43	1.25
			(0.000)	(0.019)	(0.694)	(0.418)	(0.408)	(0.222)	(0.011)	(0.147)	(0.000)	(0.000)		(0.607)	(0.986)	(0.483)
om00-86.4	20	6	0.0085	0.1297	20.52	49.76	0.64	16.76	0.2467	11.90	0.0015	0.0365	100	55.87	61.94	0.75
			(0.004)	(0.020)	(0.780)	(0.767)	(0.203)	(0.326)	(0.026)	(0.213)	(0.004)	(0.014)		(0.899)	(1.252)	(0.240)
om00-87.1	20	6	0.0000	0.1573	19.51	49.33	1.74	17.99	0.2886	10.98	0.0000	0.0000	100	52.09	62.92	2.07
			(0.000)	(0.010)	(0.539)	(0.599)	(0.209)	(0.576)	(0.015)	(0.401)	(0.000)	(0.000)		(1.707)	(0.888)	(0.252)
om00-87.3	20	6	0.0156	0.0898	21.65	48.58	0.67	16.52	0.2337	12.19	0.0015	0.0400	100	56.82	60.09	0.79
			(0.001)	(0.027)	(0.855)	(0.623)	(0.318)	(0.263)	(0.020)	(0.275)	(0.003)	(0.015)		(0.939)	(1.235)	(0.376)
om00-88.1	20	7	0.0139	0.2633	18.61	50.57	1.73	17.00	0.2712	11.48	0.0004	0.0554	100	54.60	64.59	2.07
			(0.006)	(0.044)	(1.022)	(0.203)	(0.764)	(0.832)	(0.028)	(0.671)	(0.001)	(0.010)		(2.637)	(1.293)	(0.922)
om00-89	20	5	0.0104	0.1180	22.56	47.76	0.53	16.37	0.2415	12.38	0.0006	0.0330	100	57.42	58.68	0.62
			(0.007)	(0.007)	(0.210)	(0.161)	(0.179)	(0.382)	(0.012)	(0.233)	(0.001)	(0.014)		(1.030)	(0.300)	(0.209)
om00-90	20	5	0.0084	0.1154	22.63	47.72	0.44	16.51	0.2270	12.30	0.0000	0.0459	100	57.03	58.59	0.52
			(0.005)	(0.007)	(0.948)	(0.968)	(0.271)	(0.702)	(0.015)	(0.393)	(0.000)	(0.015)		(1.819)	(1.508)	(0.316)
om00-91	20	5	0.0069	0.4241	18.33	47.37	5.13	17.00	0.2838	11.36	0.0012	0.0852	100	54.35	63.42	6.14
			(0.006)	(0.019)	(0.363)	(0.627)	(0.305)	(0.309)	(0.006)	(0.209)	(0.002)	(0.005)		(0.903)	(0.751)	(0.358)
om00-92.2	20	4	0.0040	0.4596	20.17	45.87	4.86	16.13	0.2953	12.08	0.0022	0.1256	100	57.18	60.41	5.74
			(0.004)	(0.018)	(0.192)	(0.185)	(0.092)	(0.365)	(0.018)	(0.259)	(0.004)	(0.015)		(1.079)	(0.289)	(0.116)
om00-93	20	5	0.0025	0.4699	19.85	45.56	5.52	16.18	0.2843	12.03	0.0018	0.1055	100	56.99	60.62	6.54
			(0.003)	(0.021)	(0.227)	(0.493)	(0.378)	(0.438)	(0.019)	(0.312)	(0.003)	(0.016)		(1.299)	(0.425)	(0.459)
om00-94	20	6	0.0135	0.4494	18.79	45.99	6.09	16.68	0.3071	11.56	0.0048	0.1117	100	55.26	62.15	7.26
			(0.022)	(0.015)	(0.302)	(0.347)	(0.152)	(0.365)	(0.012)	(0.267)	(0.008)	(0.016)		(1.114)	(0.525)	(0.185)
om00-95	20	6	0.0088	0.4542	18.93	45.75	6.13	16.83	0.2917	11.50	0.0029	0.1013	100	54.92	61.84	7.31
			(0.004)	(0.023)	(0.392)	(0.702)	(0.242)	(0.351)	(0.014)	(0.228)	(0.003)	(0.010)		(1.003)	(0.833)	(0.292)
om00-98	20	5	0.0031	0.3991	17.82	48.26	4.98	16.54	0.2955	11.59	0.0029	0.1076	100	55.53	64.51	5.96
			(0.003)	(0.016)	(0.362)	(0.503)	(0.177)	(0.081)	(0.006)	(0.022)	(0.003)	(0.009)		(0.164)	(0.695)	(0.209)
om00-99	20	6	0.0016	0.4498	19.62	46.07	5.39	15.88	0.2706	12.21	0.0000	0.1141	100	57.82	61.17	6.37
			(0.004)	(0.041)	(0.286)	(0.617)	(0.208)	(0.276)	(0.015)	(0.181)	(0.000)	(0.008)		(0.785)	(0.660)	(0.248)
om00-100	20	5	0.0019	0.5091	20.74	44.61	5.63	15.67	0.2705	12.44	0.0006	0.1212	100	58.61	59.06	6.62
			(0.003)	(0.016)	(0.100)	(0.305)	(0.201)	(0.267)	(0.016)	(0.164)	(0.001)	(0.016)		(0.730)	(0.272)	(0.235)
om00-101	20	6	0.0016	0.4340	19.55	46.47	4.70	16.92	0.3100	11.52	0.0010	0.0897	100	54.83	61.45	5.59
			(0.002)	(0.012)	(0.159)	(0.288)	(0.355)	(0.584)	(0.011)	(0.368)	(0.002)	(0.008)		(1.648)	(0.280)	(0.416)
om00-104	20	7	0.0108	0.4088	19.63	46.21	5.03	16.50	0.2834	11.81	0.0000	0.1138	100	56.05	61.23	5.97
			(0.005)	(0.027)	(0.392)	(0.541)	(0.496)	(0.277)	(0.016)	(0.180)	(0.000)	(0.016)		(0.781)	(0.639)	(0.597)

sample	Width	N	SiO_2	TiO_2	Al_2O_3	Cr_2O_3	Fe_2O_3	FeO	MnO	MgO	CaO	NiO	Total	Mg#	Cr#	Fe^{3+}#
om00-105a	20	6	0.0026	0.4919	21.06	44.85	5.05	15.66	0.2624	12.49	0.0000	0.1290	100	58.70	58.82	5.93
			(0.004)	(0.018)	(0.154)	(0.564)	(0.301)	(0.366)	(0.016)	(0.231)	(0.000)	(0.020)		(1.013)	(0.478)	(0.356)
om00-106	20	6	0.0010	0.4873	20.33	45.14	5.46	15.98	0.2868	12.18	0.0005	0.1366	100	57.61	59.83	6.44
			(0.003)	(0.018)	(0.344)	(0.311)	(0.234)	(0.546)	(0.012)	(0.381)	(0.001)	(0.010)		(1.597)	(0.492)	(0.298)
om00-107	20	5	0.0006	0.4885	20.82	45.03	5.21	15.47	0.2659	12.59	0.0000	0.1223	100	59.18	59.19	6.12
			(0.001)	(0.007)	(0.330)	(0.605)	(0.258)	(0.195)	(0.017)	(0.119)	(0.000)	(0.013)		(0.527)	(0.705)	(0.295)
om00-108	20	6	0.0048	0.4101	20.00	46.81	4.58	14.94	0.2648	12.87	0.0000	0.1230	100	60.56	61.10	5.38
			(0.007)	(0.014)	(0.300)	(0.267)	(0.124)	(0.200)	(0.014)	(0.159)	(0.000)	(0.013)		(0.612)	(0.491)	(0.144)
om00-109.1	20	5	0.0070	0.4159	20.27	45.98	4.89	15.55	0.2721	12.49	0.0006	0.1259	100	58.88	60.34	5.75
			(0.008)	(0.017)	(0.160)	(0.133)	(0.050)	(0.162)	(0.014)	(0.130)	(0.001)	(0.023)		(0.504)	(0.254)	(0.062)
om00-110	20	5	0.0064	0.4997	21.43	44.43	5.20	15.28	0.2752	12.77	0.0030	0.1109	100	59.84	58.17	6.08
			(0.003)	(0.015)	(0.201)	(0.226)	(0.159)	(0.192)	(0.008)	(0.127)	(0.004)	(0.013)		(0.535)	(0.325)	(0.190)
om00-112	20	5	0.0032	0.4886	21.18	44.50	5.41	15.26	0.2769	12.75	0.0053	0.1170	100	59.83	58.49	6.34
			(0.003)	(0.018)	(0.120)	(0.165)	(0.166)	(0.234)	(0.021)	(0.160)	(0.004)	(0.013)		(0.670)	(0.181)	(0.196)
om00-113	20	5	0.0064	0.4945	21.67	44.12	5.29	15.12	0.2764	12.89	0.0071	0.1277	100	60.30	57.74	6.18
			(0.008)	(0.015)	(0.140)	(0.225)	(0.184)	(0.395)	(0.023)	(0.263)	(0.003)	(0.016)		(1.113)	(0.241)	(0.213)
om00-115	20	5	0.0007	0.5258	24.07	42.61	4.03	15.43	0.2567	12.96	0.0060	0.1094	100	59.95	54.29	4.66
			(0.001)	(0.039)	(0.297)	(0.463)	(0.308)	(0.501)	(0.027)	(0.343)	(0.003)	(0.023)		(1.409)	(0.488)	(0.365)
om00-117	20	5	0.0058	0.5026	22.47	43.47	4.82	15.80	0.2749	12.54	0.0048	0.1145	100	58.59	56.48	5.62
			(0.004)	(0.013)	(0.319)	(0.347)	(0.096)	(0.121)	(0.031)	(0.080)	(0.005)	(0.004)		(0.334)	(0.545)	(0.112)
om00-119	20	5	0.0109	0.4483	22.36	44.23	4.05	16.25	0.2900	12.25	0.0101	0.0978	100	57.33	57.03	4.73
			(0.011)	(0.049)	(0.330)	(0.622)	(0.382)	(0.341)	(0.015)	(0.238)	(0.004)	(0.020)		(0.990)	(0.686)	(0.440)
om00-122a	20	5	0.0134	0.5202	22.16	43.43	5.05	16.15	0.2971	12.26	0.0006	0.1220	100	57.50	56.80	5.91
			(0.016)	(0.016)	(0.452)	(0.289)	(0.434)	(0.274)	(0.019)	(0.193)	(0.001)	(0.011)		(0.790)	(0.589)	(0.523)
om00-124	20	3	0.0000	0.4869	23.13	42.26	5.34	15.71	0.2736	12.65	0.0000	0.1380	100	58.94	55.07	6.21
			(0.000)	(0.038)	(0.457)	(0.564)	(0.105)	(0.246)	(0.022)	(0.147)	(0.000)	(0.005)		(0.653)	(0.810)	(0.122)
om00-127	20	5	0.0038	0.4975	20.96	44.32	5.45	16.32	0.2925	12.03	0.0000	0.1171	100	56.78	58.65	6.43
			(0.003)	(0.018)	(0.154)	(0.217)	(0.121)	(0.345)	(0.011)	(0.220)	(0.000)	(0.005)		(0.968)	(0.287)	(0.137)
om00-129	20	6	0.0032	0.5599	22.11	42.65	5.81	16.29	0.2973	12.13	0.0010	0.1414	100	57.03	56.41	6.81
			(0.004)	(0.022)	(0.223)	(0.479)	(0.402)	(0.608)	(0.012)	(0.431)	(0.002)	(0.014)		(1.784)	(0.279)	(0.497)
om00-130	20	5	0.0076	0.4733	22.41	43.77	3.85	17.91	0.3376	11.14	0.0012	0.0932	100	52.58	56.72	4.53
			(0.008)	(0.011)	(0.383)	(0.458)	(0.337)	(0.370)	(0.013)	(0.261)	(0.003)	(0.016)		(1.095)	(0.661)	(0.390)
om00-131	20	5	0.0038	0.5437	22.17	43.03	5.20	16.82	0.3118	11.82	0.0030	0.1042	100	55.59	56.56	6.11
			(0.003)	(0.028)	(0.383)	(0.390)	(0.249)	(0.827)	(0.024)	(0.547)	(0.003)	(0.019)		(2.352)	(0.612)	(0.291)

sample	Width	N	SiO_2	TiO_2	Al_2O_3	Cr_2O_3	Fe_2O_3	FeO	MnO	MgO	CaO	NiO	Total	Mg#	Cr#	Fe^{3+}#
om00-132	20	4	0.0032	0.4863	21.60	42.98	5.98	16.69	0.2947	11.85	0.0029	0.1110	100	55.87	57.17	7.04
			(0.003)	(0.017)	(0.201)	(0.409)	(0.200)	(0.261)	(0.023)	(0.146)	(0.004)	(0.016)		(0.688)	(0.455)	(0.232)
om00-135	20	5	0.0019	0.4837	21.10	42.58	6.76	17.22	0.2998	11.44	0.0000	0.1169	100	54.23	57.51	7.99
			(0.002)	(0.017)	(0.238)	(0.324)	(0.170)	(0.443)	(0.015)	(0.293)	(0.000)	(0.019)		(1.270)	(0.416)	(0.213)
om00-136	20	5	0.0044	0.4825	20.82	43.32	6.40	16.97	0.2949	11.57	0.0018	0.1264	100	54.86	58.26	7.58
			(0.002)	(0.020)	(0.392)	(0.477)	(0.387)	(0.349)	(0.015)	(0.221)	(0.003)	(0.021)		(0.978)	(0.674)	(0.459)
om00-138	20	5	0.0050	0.4762	20.96	44.00	5.28	17.80	0.3122	11.06	0.0023	0.1030	100	52.54	58.48	6.26
			(0.006)	(0.023)	(0.599)	(0.957)	(0.403)	(0.599)	(0.015)	(0.416)	(0.001)	(0.022)		(1.780)	(1.158)	(0.490)
om00-139	20	5	0.0057	0.4101	20.89	44.45	5.08	17.47	0.3017	11.30	0.0000	0.1033	100	53.55	58.80	6.01
			(0.004)	(0.035)	(0.235)	(0.209)	(0.253)	(0.191)	(0.012)	(0.150)	(0.000)	(0.021)		(0.599)	(0.316)	(0.308)
om00-140.3	20	6	0.0121	0.3388	21.21	44.02	5.04	17.91	0.3027	11.05	0.0015	0.1010	100	52.38	58.19	5.97
			(0.005)	(0.019)	(0.349)	(0.912)	(0.768)	(0.403)	(0.011)	(0.286)	(0.002)	(0.019)		(1.208)	(0.748)	(0.918)
om00-141.1	20	7	0.0000	0.2198	24.32	41.53	4.31	17.75	0.2616	11.61	0.0048	0.0000	100	53.83	53.40	5.01
			(0.000)	(0.015)	(0.990)	(0.754)	(0.809)	(0.135)	(0.025)	(0.115)	(0.013)	(0.000)		(0.379)	(1.358)	(0.959)
om00-141.2	20	6	0.0000	0.0903	36.89	32.07	0.54	16.17	0.1606	14.04	0.0000	0.0315	100	60.75	36.86	0.59
			(0.000)	(0.028)	(1.668)	(1.521)	(0.295)	(0.225)	(0.016)	(0.332)	(0.000)	(0.008)		(0.896)	(2.158)	(0.324)
om00-141.3	20	4	0.0000	0.0418	34.72	34.04	0.77	16.89	0.1812	13.37	0.0000	0.0000	100	58.52	39.69	0.84
			(0.000)	(0.028)	(1.696)	(1.828)	(0.155)	(0.295)	(0.030)	(0.370)	(0.000)	(0.000)		(1.084)	(2.453)	(0.166)
om00-141.4	20	4	0.0000	0.0520	33.68	35.14	0.79	16.88	0.1866	13.26	0.0000	0.0000	100	58.33	41.17	0.88
			(0.000)	(0.009)	(0.203)	(0.324)	(0.115)	(0.771)	(0.013)	(0.505)	(0.000)	(0.000)		(2.036)	(0.357)	(0.125)
om00-141.5	20	7	0.0055	0.2276	28.27	39.75	1.73	17.65	0.2351	12.09	0.0009	0.0458	100	54.87	48.83	1.99
			(0.006)	(0.112)	(5.747)	(5.269)	(0.674)	(0.984)	(0.054)	(1.289)	(0.001)	(0.018)		(3.994)	(8.328)	(0.828)
om00-142.1	20	8	0.0253	0.3270	16.93	49.40	3.73	19.78	0.3286	9.41	0.0054	0.0620	100	45.89	66.19	4.55
			(0.007)	(0.020)	(0.517)	(0.561)	(0.852)	(0.883)	(0.038)	(0.638)	(0.004)	(0.014)		(2.806)	(0.514)	(1.057)
om00-142.2	20	7	0.0260	0.2562	17.36	49.56	3.23	19.56	0.3192	9.64	0.0045	0.0531	100	46.76	65.72	3.92
			(0.005)	(0.048)	(1.325)	(0.787)	(1.033)	(0.444)	(0.025)	(0.291)	(0.004)	(0.013)		(1.264)	(1.960)	(1.272)
om00-142.3	20	6	0.0441	0.2117	18.09	50.06	2.00	19.35	0.3294	9.86	0.0039	0.0419	100	47.61	64.99	2.41
			(0.035)	(0.036)	(0.871)	(0.984)	(0.322)	(0.351)	(0.047)	(0.262)	(0.002)	(0.012)		(1.101)	(1.521)	(0.391)
om00-143.2	20	6	0.0059	0.0614	23.38	45.13	2.01	17.25	0.2358	11.88	0.0015	0.0547	100	55.11	56.42	2.33
			(0.005)	(0.026)	(0.706)	(1.030)	(0.166)	(0.589)	(0.026)	(0.331)	(0.003)	(0.012)		(1.530)	(1.294)	(0.194)
om00-144	20	6	0.0595	0.1347	23.80	43.77	2.64	17.71	0.2385	11.56	0.0140	0.0673	100	53.79	55.24	3.08
			(0.081)	(0.022)	(0.849)	(1.135)	(0.125)	(0.804)	(0.012)	(0.420)	(0.022)	(0.004)		(2.028)	(1.519)	(0.147)
om00-145b	20	5	0.0046	0.0356	26.17	41.86	2.26	17.18	0.2149	12.23	0.0000	0.0454	100	55.92	51.76	2.59
			(0.003)	(0.008)	(1.084)	(1.610)	(0.375)	(0.511)	(0.014)	(0.243)	(0.000)	(0.012)		(1.212)	(1.986)	(0.425)

sample	Width	N	SiO_2	TiO_2	Al_2O_3	Cr_2O_3	Fe_2O_3	FeO	MnO	MgO	CaO	NiO	Total	Mg#	Cr#	Fe3+#
om00-146	20	6	0.0109	0.0448	25.55	42.71	2.32	16.47	0.2124	12.62	0.0015	0.0608	100	57.74	52.86	2.66
			(0.018)	(0.008)	(0.783)	(1.324)	(0.253)	(0.793)	(0.022)	(0.444)	(0.003)	(0.020)		(2.031)	(1.530)	(0.291)
om00-147	20	5	0.0186	0.0871	23.47	44.13	2.77	17.60	0.2440	11.63	0.0012	0.0559	100	54.10	55.78	3.22
			(0.012)	(0.006)	(0.794)	(1.085)	(0.166)	(0.354)	(0.012)	(0.162)	(0.003)	(0.014)		(0.837)	(1.435)	(0.190)
om00-148	20	5	0.0147	0.0805	22.23	45.49	2.70	17.82	0.2687	11.35	0.0000	0.0610	100	53.16	57.86	3.16
			(0.003)	(0.010)	(0.397)	(0.356)	(0.156)	(0.412)	(0.005)	(0.286)	(0.000)	(0.020)		(1.203)	(0.597)	(0.192)
om99-21	20	6	0.0010	0.4796	18.50	46.34	5.85	17.28	0.2798	11.16	0.0043	0.1120	100	53.52	62.69	7.01
			(0.003)	(0.022)	(0.305)	(0.486)	(0.468)	(0.464)	(0.011)	(0.323)	(0.004)	(0.019)		(1.387)	(0.454)	(0.580)
om99-22	20	7	0.0336	0.4773	19.34	46.04	5.72	15.77	0.2918	12.23	0.0050	0.0993	100	58.02	61.50	6.78
			(0.013)	(0.023)	(0.199)	(0.264)	(0.318)	(0.336)	(0.014)	(0.240)	(0.007)	(0.017)		(0.996)	(0.239)	(0.389)
om99-23	20	8	0.0000	0.4342	18.01	47.38	5.78	16.18	0.2486	11.86	0.0047	0.1064	100	56.64	63.84	6.90
			(0.000)	(0.012)	(0.333)	(0.476)	(0.180)	(0.475)	(0.017)	(0.312)	(0.004)	(0.012)		(1.367)	(0.627)	(0.222)
om99-24	20	6	0.0110	0.4796	20.31	44.68	5.96	15.97	0.2851	12.20	0.0005	0.1070	100	57.67	59.61	7.04
			(0.009)	(0.019)	(0.477)	(0.751)	(0.258)	(0.396)	(0.019)	(0.224)	(0.001)	(0.016)		(1.051)	(0.954)	(0.307)
om99-25	20	10	0.0000	0.4563	19.71	46.16	5.35	15.46	0.2454	12.51	0.0021	0.1109	100	59.06	61.11	6.31
			(0.000)	(0.016)	(0.247)	(0.285)	(0.192)	(0.595)	(0.016)	(0.414)	(0.003)	(0.019)		(1.737)	(0.366)	(0.238)
om99-27	20	9	0.0000	0.4493	20.37	45.37	5.57	15.02	0.2385	12.87	0.0010	0.1120	100	60.42	59.91	6.55
			(0.000)	(0.016)	(0.293)	(0.291)	(0.064)	(0.282)	(0.016)	(0.205)	(0.003)	(0.015)		(0.828)	(0.492)	(0.076)
om99-28	20	12	0.0019	0.4927	22.15	43.78	4.77	16.08	0.2865	12.33	0.0010	0.1011	100	57.75	57.00	5.59
			(0.003)	(0.023)	(0.438)	(0.631)	(0.441)	(0.319)	(0.017)	(0.207)	(0.003)	(0.015)		(0.887)	(0.793)	(0.514)
om99-29	20	8	0.0000	0.5137	21.35	43.48	5.82	16.52	0.2560	11.97	0.0015	0.0943	100	56.35	57.74	6.85
			(0.000)	(0.010)	(0.360)	(0.347)	(0.276)	(0.574)	(0.021)	(0.405)	(0.002)	(0.012)		(1.679)	(0.517)	(0.343)
om99-30	20	11	0.0154	0.4653	21.56	43.24	5.72	16.85	0.3055	11.75	0.0019	0.1000	100	55.42	57.36	6.74
			(0.024)	(0.031)	(0.422)	(0.841)	(0.552)	(0.556)	(0.023)	(0.370)	(0.003)	(0.022)		(1.595)	(0.845)	(0.667)
om99-31	20	8	0.0000	0.4865	23.03	43.32	3.97	17.02	0.2399	11.86	0.0000	0.0820	100	55.39	55.79	4.64
			(0.000)	(0.036)	(0.521)	(0.466)	(0.333)	(0.412)	(0.023)	(0.305)	(0.000)	(0.015)		(1.230)	(0.754)	(0.403)
om99-32	20	9	0.0072	0.4262	19.07	45.36	5.99	17.94	0.3260	10.77	0.0051	0.1011	100	51.70	61.47	7.18
			(0.009)	(0.025)	(0.382)	(0.753)	(0.534)	(0.612)	(0.017)	(0.427)	(0.004)	(0.017)		(1.840)	(0.732)	(0.659)
om99-33	20	7	0.0000	0.2837	21.81	44.43	4.20	17.47	0.2508	11.47	0.0013	0.0850	100	53.93	57.75	4.94
			(0.000)	(0.011)	(0.319)	(0.633)	(0.406)	(0.639)	(0.020)	(0.404)	(0.002)	(0.020)		(1.780)	(0.655)	(0.479)
om99-34	20	11	0.0000	0.4911	20.95	44.01	5.97	15.77	0.2687	12.38	0.0000	0.1458	100	58.32	58.49	7.02
			(0.000)	(0.009)	(0.104)	(0.175)	(0.169)	(0.239)	(0.019)	(0.160)	(0.000)	(0.018)		(0.681)	(0.171)	(0.200)
om99-35	20	5	0.0000	0.5179	23.00	43.26	3.80	17.62	0.2638	11.43	0.0012	0.1127	100	53.61	55.78	4.45
			(0.000)	(0.025)	(0.283)	(0.343)	(0.329)	(0.333)	(0.020)	(0.235)	(0.002)	(0.020)		(0.982)	(0.452)	(0.384)

sample	Width	N	SiO_2	TiO_2	Al_2O_3	Cr_2O_3	Fe_2O_3	FeO	MnO	MgO	CaO	NiO	Total	Mg#	Cr#	Fe^{3+}#
om99-36a	20	13	0.0084	0.1772	18.81	49.11	2.89	17.48	0.2736	11.18	0.0023	0.0780	100	53.28	63.66	3.44
			(0.009)	(0.009)	(0.289)	(0.181)	(0.253)	(0.556)	(0.016)	(0.369)	(0.003)	(0.014)		(1.610)	(0.409)	(0.302)
om99-36b	20	7	0.0000	0.1624	20.46	47.71	2.41	17.71	0.2349	11.24	0.0008	0.0630	100	53.08	61.00	2.85
			(0.000)	(0.012)	(0.491)	(0.559)	(0.165)	(0.499)	(0.027)	(0.309)	(0.002)	(0.010)		(1.386)	(0.835)	(0.199)
om99-36c	20	6	0.0143	0.2030	21.13	47.27	2.06	17.69	0.2835	11.29	0.0000	0.0600	100	53.23	60.01	2.43
			(0.009)	(0.013)	(0.278)	(0.330)	(0.202)	(0.140)	(0.018)	(0.095)	(0.000)	(0.015)		(0.397)	(0.455)	(0.240)
om94-100	WT	5	0.0228	0.0634	26.93	40.23	3.43	15.92	0.2691	13.04	0.0065	0.0891	100	59.35	50.06	3.90
			(0.002)	(0.007)	(0.884)	(0.946)	(0.258)	(0.597)	(0.016)	(0.312)	(0.002)	(0.018)		(1.473)	(1.397)	(0.301)
om94-101	WT	5	0.0334	0.0520	24.80	42.89	2.80	16.80	0.2953	12.24	0.0107	0.0763	100	56.50	53.72	3.23
			(0.009)	(0.006)	(0.689)	(0.819)	(0.517)	(0.613)	(0.019)	(0.373)	(0.005)	(0.004)		(1.637)	(1.109)	(0.600)
om94-102	WT	7	0.0195	0.0551	34.71	33.18	2.42	14.42	0.2243	14.85	0.0002	0.1192	100	64.72	39.07	2.64
			(0.013)	(0.004)	(0.840)	(0.963)	(0.579)	(0.707)	(0.012)	(0.495)	(0.001)	(0.012)		(1.872)	(1.246)	(0.625)
om94-103	WT	5	0.0229	0.0572	24.15	42.83	3.32	17.57	0.2743	11.67	0.0039	0.0999	100	54.22	54.34	3.86
			(0.006)	(0.011)	(0.615)	(0.464)	(0.163)	(0.458)	(0.010)	(0.351)	(0.005)	(0.005)		(1.383)	(0.892)	(0.202)
om94-104	WT	10	0.0035	0.0278	24.38	43.14	3.08	16.76	0.2594	12.26	0.0036	0.0803	100	56.59	54.29	3.56
			(0.005)	(0.024)	(0.866)	(0.607)	(0.433)	(0.213)	(0.024)	(0.225)	(0.008)	(0.015)		(0.744)	(1.190)	(0.514)
om94-106	WT	4	0.0178	0.0418	23.75	44.66	2.38	16.30	0.2820	12.48	0.0093	0.0805	100	57.72	55.78	2.76
			(0.021)	(0.004)	(0.481)	(0.232)	(0.159)	(0.588)	(0.023)	(0.444)	(0.014)	(0.016)		(1.746)	(0.623)	(0.192)
om94-114	WT	5	0.0387	0.2821	24.61	41.99	3.63	17.10	0.2703	11.96	0.0191	0.1084	100	55.48	53.39	4.20
			(0.014)	(0.120)	(1.092)	(0.965)	(0.364)	(1.333)	(0.021)	(0.849)	(0.015)	(0.015)		(3.650)	(1.681)	(0.429)
om94-115	WT	6	0.0270	0.0403	20.83	47.42	2.95	15.98	0.2770	12.37	0.0024	0.0976	100	57.98	60.43	3.45
			(0.004)	(0.003)	(0.212)	(0.433)	(0.230)	(0.428)	(0.013)	(0.294)	(0.003)	(0.010)		(1.233)	(0.407)	(0.275)
om94-52	WT	5	0.0167	0.0757	32.16	36.01	2.36	14.49	0.2229	14.53	0.0094	0.1342	100	64.12	42.89	2.61
			(0.005)	(0.002)	(0.567)	(0.678)	(0.320)	(0.325)	(0.012)	(0.198)	(0.003)	(0.013)		(0.822)	(0.881)	(0.351)
om94-53	WT	11	0.0156	0.0797	25.73	42.49	2.26	16.52	0.2635	12.54	0.0094	0.0928	100	57.50	52.57	2.60
			(0.012)	(0.012)	(1.380)	(1.468)	(0.544)	(0.452)	(0.012)	(0.337)	(0.007)	(0.018)		(1.298)	(2.156)	(0.636)
om94-55	WT	4	0.0000	0.0534	30.13	36.88	3.54	15.19	0.2175	13.87	0.0002	0.1173	100	61.94	45.10	3.95
			(0.000)	(0.004)	(0.256)	(0.312)	(0.188)	(0.212)	(0.011)	(0.165)	(0.000)	(0.004)		(0.607)	(0.376)	(0.216)
om94-59	WT	5	0.0362	0.1320	25.67	42.36	2.43	16.43	0.2763	12.55	0.0170	0.1122	100	57.66	52.56	2.79
			(0.005)	(0.017)	(1.780)	(1.834)	(0.185)	(0.394)	(0.009)	(0.257)	(0.002)	(0.009)		(1.002)	(2.791)	(0.231)
om94-60	WT	5	0.0019	0.0587	40.09	27.72	2.47	12.94	0.1651	16.37	0.0012	0.1755	100	69.27	31.69	2.62
			(0.003)	(0.007)	(1.093)	(1.708)	(0.561)	(0.121)	(0.005)	(0.139)	(0.002)	(0.013)		(0.348)	(1.923)	(0.582)
om94-61	WT	5	0.0182	0.1030	29.17	39.69	2.02	14.29	0.2268	14.35	0.0113	0.1236	100	64.16	47.73	2.27
			(0.002)	(0.009)	(1.220)	(1.117)	(0.275)	(0.211)	(0.006)	(0.158)	(0.001)	(0.006)		(0.539)	(1.726)	(0.316)

sample	Width	N	SiO_2	TiO_2	Al_2O_3	Cr_2O_3	Fe_2O_3	FeO	MnO	MgO	CaO	NiO	Total	Mg#	Cr#	Fe3*#
om94-64	WT	5	0.1676	0.1216	26.60	40.31	3.39	16.37	0.2654	12.66	0.0094	0.1102	100	57.96	50.41	3.88
			(0.320)	(0.003)	(0.449)	(0.935)	(0.381)	(0.617)	(0.011)	(0.342)	(0.006)	(0.025)		(1.575)	(0.972)	(0.441)
om94-65	WT	7	0.0325	0.0898	20.59	46.71	3.24	17.87	0.2881	11.12	0.0013	0.0614	100	52.58	60.34	3.83
			(0.032)	(0.003)	(0.406)	(0.436)	(0.242)	(0.539)	(0.012)	(0.382)	(0.001)	(0.010)		(1.609)	(0.650)	(0.292)
om94-67	WT	6	0.0000	0.0097	37.27	30.51	2.53	13.93	0.1521	15.50	0.0000	0.1173	100	66.48	35.46	2.72
			(0.000)	(0.007)	(1.173)	(1.312)	(0.254)	(0.270)	(0.013)	(0.258)	(0.000)	(0.011)		(0.781)	(1.694)	(0.267)
om94-69	WT	5	0.0000	0.2119	20.56	44.56	6.34	15.07	0.2689	12.87	0.0000	0.1321	100	60.35	59.25	7.43
			(0.000)	(0.008)	(0.535)	(0.405)	(0.761)	(0.419)	(0.013)	(0.341)	(0.000)	(0.009)		(1.300)	(0.518)	(0.927)
om94-72	WT	5	0.0000	0.0533	33.59	32.35	4.13	15.58	0.1858	13.99	0.0000	0.1142	100	61.54	39.27	4.56
			(0.000)	(0.014)	(1.447)	(1.350)	(0.463)	(0.496)	(0.017)	(0.457)	(0.000)	(0.018)		(1.502)	(1.965)	(0.531)
om94-73	WT	5	0.0248	0.0658	28.31	38.46	3.80	15.62	0.2119	13.41	0.0031	0.0976	100	60.46	47.69	4.29
			(0.053)	(0.006)	(1.141)	(1.134)	(0.349)	(0.357)	(0.016)	(0.305)	(0.007)	(0.017)		(1.078)	(1.737)	(0.405)
om94-74	WT	5	0.0301	0.0641	32.75	35.20	2.46	14.70	0.2129	14.47	0.0051	0.1164	100	63.69	41.90	2.72
			(0.062)	(0.008)	(1.140)	(1.266)	(0.122)	(0.479)	(0.012)	(0.382)	(0.011)	(0.011)		(1.345)	(1.708)	(0.123)
om94-76	WT	7	0.0356	0.1327	12.20	51.81	5.95	21.85	0.3944	7.53	0.0130	0.0785	100	38.06	74.01	7.48
			(0.002)	(0.005)	(0.447)	(0.553)	(0.153)	(0.406)	(0.019)	(0.269)	(0.003)	(0.010)		(1.276)	(0.890)	(0.207)
om94-78	WT	5	0.0279	0.2990	20.28	41.10	9.15	17.52	0.3282	11.11	0.0111	0.1659	100	53.06	57.62	10.88
			(0.005)	(0.013)	(0.821)	(1.406)	(0.803)	(0.765)	(0.010)	(0.538)	(0.003)	(0.016)		(2.289)	(1.682)	(0.992)
om94-79	WT	5	0.0017	0.0336	32.76	33.93	3.63	15.15	0.1884	14.20	0.0094	0.0986	100	62.54	41.00	4.00
			(0.002)	(0.014)	(1.268)	(1.560)	(0.701)	(0.688)	(0.026)	(0.544)	(0.021)	(0.009)		(1.947)	(2.034)	(0.751)
om94-80	WT	5	0.0088	0.3440	17.01	46.07	6.67	20.68	0.3842	8.76	0.0016	0.0747	100	43.03	64.48	8.16
			(0.010)	(0.037)	(0.675)	(1.772)	(0.689)	(1.238)	(0.014)	(0.769)	(0.001)	(0.014)		(3.624)	(1.798)	(0.863)
om94-81	WT	5	0.0099	0.0935	25.80	41.42	3.31	16.41	0.2528	12.64	0.0019	0.0556	100	57.86	51.85	3.80
			(0.022)	(0.003)	(0.477)	(1.140)	(0.735)	(0.410)	(0.012)	(0.303)	(0.004)	(0.006)		(1.193)	(1.135)	(0.831)
om94-83	WT	3	0.0640	0.3709	20.45	46.61	6.12	9.62	0.2059	16.37	0.0116	0.1793	100	75.17	60.50	7.01
			(0.034)	(0.009)	(1.527)	(0.420)	(3.276)	(3.193)	(0.013)	(1.919)	(0.015)	(0.010)		(8.349)	(1.603)	(3.714)
om94-87	WT	6	0.0111	0.0553	28.35	39.03	3.15	15.72	0.2439	13.33	0.0015	0.1118	100	60.18	48.02	3.56
			(0.003)	(0.006)	(0.753)	(0.622)	(0.251)	(0.224)	(0.019)	(0.189)	(0.001)	(0.005)		(0.659)	(1.055)	(0.295)
om94-91	WT	8	0.0206	0.0715	21.70	45.33	3.61	17.29	0.2811	11.59	0.0099	0.1039	100	54.43	58.36	4.24
			(0.003)	(0.003)	(0.532)	(0.522)	(0.175)	(0.189)	(0.010)	(0.149)	(0.003)	(0.008)		(0.578)	(0.866)	(0.211)
om94-98	WT	10	0.0359	0.0540	29.81	37.84	2.79	15.46	0.2204	13.66	0.0022	0.1201	100	61.15	46.00	3.13
			(0.032)	(0.007)	(0.897)	(1.107)	(0.370)	(0.537)	(0.017)	(0.421)	(0.002)	(0.013)		(1.546)	(1.470)	(0.399)
om94-99	WT	5	0.0031	0.4469	12.00	49.23	9.36	19.56	0.3780	8.91	0.0012	0.1047	100	44.80	73.35	11.72
			(0.007)	(0.011)	(0.350)	(0.850)	(0.364)	(1.211)	(0.029)	(0.822)	(0.002)	(0.007)		(3.823)	(0.803)	(0.494)
om98-120b		2	0.0016	0.2373	22.42	43.17	4.30	18.95	0.2740	10.56	0.0000	0.0844	100	49.85	56.37	5.07
			(0.002)	(0.002)	(0.854)	(1.343)	(0.447)	(0.109)	(0.009)	(0.155)	(0.000)	(0.008)		(0.510)	(1.703)	(0.505)

Table B3 - Orthopyroxene Compositions

Sample	SiO_2	TiO_2	Al_2O_3	Cr_2O_3	FeO	MnO	MgO	CaO	Na_2O	NiO	Total
om00-75	57.14	0.0355	1.1441	0.5877	5.1	0.1004	33.37	2.1459	0.0197	0.1142	99.76
om00-75	57.56	0.0374	1.2188	0.5539	5.28	0.1738	33.25	1.8624	0.0078	0.1074	100.05
om00-75	57.33	0.0418	1.2195	0.5204	5.48	0.1235	33.68	1.6732	0.0095	0.0956	100.17
om00-75	57.21	0.0354	1.2109	0.5473	5.39	0.1192	33.43	1.6808	0.0081	0.0864	99.72
om00-75	57.19	0.0444	1.4586	0.6056	5.33	0.1422	33.85	2.3336	0.0227	0.1012	101.08
om00-75	57.28	0.0406	1.4817	0.5628	5.75	0.1293	34.51	0.964	0	0.0822	100.8
om00-75	57.75	0.0447	1.3531	0.4991	5.67	0.1244	35.02	0.5209	0	0.0934	101.08
om00-75	57.7	0.0361	1.336	0.5276	5.42	0.1329	34.42	1.4287	0.0093	0.0966	101.12
om00-75	57.68	0.0271	1.2732	0.5051	5.69	0.1227	34.76	0.9204	0	0.0974	101.08
om00-76	57.65	0.0513	1.4636	0.5804	5.37	0.1228	34.25	1.4855	0.0282	0.0972	101.1
om00-76	57.83	0.0483	1.4065	0.5633	5.29	0.1361	34.24	1.8157	0.0215	0.0911	101.45
om00-76	57.85	0.0578	1.1514	0.455	5.4	0.1337	35.11	0.6679	0	0.1062	100.93
om00-76	57.61	0.0594	1.3693	0.5202	5.35	0.1237	34.6	0.8068	0.0041	0.0869	100.53
om00-76	57.77	0.0424	1.2504	0.4937	5.34	0.1204	35.13	0.4167	0	0.1104	100.67
om00-76	57.63	0.0567	1.2759	0.4889	5.4	0.1426	35	0.8219	0.0046	0.0742	100.9
om00-76	57.55	0.0498	1.2807	0.451	5.5	0.1354	34.71	0.9631	0	0.0643	100.7
om00-86.4	57.56	0.0284	1.338	0.467	5.33	0.1151	34.86	0.9328	0	0.0821	100.71
om00-86.4	57.56	0.0284	1.338	0.467	5.33	0.1151	34.86	0.9328	0	0.0821	100.71
om00-86.4	57.25	0.03	1.4895	0.5891	5.16	0.1243	34.3	1.4378	0.0188	0.0812	100.49
om00-86.4	57.47	0.0207	1.4851	0.5706	5.33	0.1317	34.66	0.8699	0	0.083	100.63
om00-86.4	57.75	0.03	1.263	0.4384	5.33	0.1242	34.9	0.9117	0	0.089	100.84
om00-86.4	57.38	0.0256	1.5131	0.5443	5.31	0.1167	34.52	0.9866	0	0.0932	100.49
om00-86.4	57.33	0.0373	1.4464	0.557	5.07	0.1298	33.89	2.0126	0.0061	0.0798	100.55
om00-88.1	57.09	0.0394	1.5115	0.5891	5.15	0.1087	34.07	1.5648	0.0038	0.0887	100.22
om00-88.1	57.32	0.0355	1.306	0.4559	5.36	0.12	34.71	0.9592	0.0045	0.0733	100.35
om00-88.1	57.25	0.0422	1.3585	0.5497	5.45	0.1235	34.97	0.6466	0	0.0972	100.49
om00-88.1	57.51	0.0396	1.4028	0.5502	5.32	0.1406	34.69	0.8113	0	0.0957	100.56
om00-88.1	57.64	0.0388	1.3993	0.5115	5.44	0.1242	35.08	0.6239	0.0009	0.0736	100.94
om00-89	57.71	0.034	1.5681	0.5109	5.41	0.1348	34.93	0.6379	0	0.0925	101.02
om00-89	57.78	0.0313	1.6609	0.6042	5.34	0.1258	34.65	1.0302	0	0.0832	101.31
om00-89	57.49	0.02	1.6943	0.5851	5.42	0.1088	34.87	0.6693	0.0033	0.0931	100.95
om00-89	57.51	0.0219	1.552	0.5354	5.32	0.1283	34.92	0.5769	0	0.0817	100.65
om00-89	57.61	0.0272	1.5383	0.538	5.44	0.1262	34.79	0.6643	0	0.0793	100.81
om00-90	57.92	0.0293	1.6593	0.5706	5.63	0.1176	34.69	0.5818	0	0.0806	101.27
om00-90	57.3	0.0259	1.7035	0.6669	5.52	0.1103	34.57	0.6867	0.0009	0.1079	100.7
om00-90	57.63	0.0253	1.5507	0.5836	5.64	0.13	34.91	0.5548	0	0.098	101.12
om00-90	57.68	0.0237	1.5238	0.5828	5.54	0.1247	34.48	1.0324	0	0.0879	101.08
om00-90	57.71	0.0269	1.5487	0.5727	5.55	0.1288	34.79	0.719	0	0.0987	101.14
om00-90	57.76	0.0306	1.5857	0.5912	5.55	0.1294	34.58	0.8683	0	0.1118	101.21
om00-90	57.44	0.0114	1.7418	0.6083	5.35	0.1204	34.61	0.5227	0	0.0527	100.46
om00-141.2	55.18	0.0361	3.24	0.8094	7.81	0.1766	32.32	0.453	0.0089	0.0612	100.09
om00-141.4	55.41	0.0422	3.38	0.8563	7.93	0.1616	32.35	0.4382	0.0145	0.058	100.64
om00-141.4	55.28	0.0515	3.09	0.8466	7.88	0.1967	31.81	0.974	0	0.0704	100.2
om00-141.4	55.44	0.048	3.25	0.8845	7.72	0.1701	32.34	0.4303	0	0.0572	100.34
om00-143.2	57.35	0.0108	1.6673	0.5965	5.65	0.16	33.89	1.5285	0.026	0.0911	100.97
om00-143.2	56.98	0.0199	1.7586	0.6012	5.76	0.1486	33.48	1.9972	0.016	0.1024	100.87
om00-143.2	57.3	0.0245	1.6257	0.5667	5.5	0.1364	32.9	2.637	0.0071	0.0952	100.79
om00-143.2	57.37	0.0243	1.778	0.5968	5.95	0.1463	34.26	0.677	0.0128	0.1067	100.93
om00-143.2	57.24	0.0208	1.7374	0.5672	5.81	0.1533	33.95	1.5204	0.0049	0.1031	101.11
om00-143.2	57.49	0.0323	1.7179	0.5197	5.93	0.1487	34.03	1.0338	0.0123	0.0862	101
om00-144	57.19	0.036	1.8233	0.5529	5.83	0.1583	33.69	1.84	0.0255	0.074	101.22
om00-144	56.99	0.0408	1.8262	0.5774	5.58	0.1294	32.75	2.986	0.0204	0.0818	100.98

Sample	SiO_2	TiO_2	Al_2O_3	Cr_2O_3	FeO	MnO	MgO	CaO	Na_2O	NiO	Total
om00-144	57.06	0.0458	1.751	0.5803	5.71	0.1477	33.11	2.3079	0.0326	0.0715	100.82
om00-144	57.15	0.0462	1.6951	0.6204	6.03	0.1661	33.89	1.0933	0.0181	0.0834	100.79
om00-165a	57.09	0.0506	1.9796	0.5969	5.71	0.1202	33.73	1.6387	0	0.0686	100.99
om00-165a	57.22	0.0423	1.9698	0.5567	5.85	0.1296	34.61	0.6125	0.0003	0.0732	101.06
om00-165a	56.99	0.0427	1.8207	0.5535	5.47	0.1308	33.59	2.029	0.0021	0.086	100.71
om00-168	57.09	0.0448	1.9198	0.6255	5.73	0.1335	33.69	1.7367	0.0087	0.0877	101.06
om00-168	56.83	0.0477	2.0653	0.6572	5.99	0.1427	34.62	0.6057	0	0.0798	101.04
om00-168	56.97	0.0539	1.9535	0.5502	5.88	0.1439	34.47	0.7099	0.0236	0.0785	100.84
om00-166b	57.08	0.0771	1.9977	0.5951	5.73	0.1413	34.26	0.8172	0.0187	0.0721	100.78
om00-166b	57.21	0.0761	2.0073	0.5789	5.83	0.1435	34.74	0.6322	0	0.0974	101.31
om00-166b	56.9	0.0811	2.1678	0.6627	5.65	0.15	33.77	1.3338	0.0324	0.08	100.82
om00-166b	57.09	0.0672	1.939	0.6188	5.69	0.1592	34.68	0.4677	0.0048	0.0918	100.81
om00-173	57.34	0.0657	2.1139	0.6632	6.31	0.1785	34.41	0.5116	0.0025	0.0777	101.67
om00-173	57.41	0.0757	1.7105	0.3799	6.4	0.1525	34.36	0.5965	0	0.0689	101.16
om00-173	57.05	0.0731	2.0851	0.6112	6.3	0.1463	34.35	0.682	0	0.0679	101.36
om00-173	56.77	0.1065	2.0438	0.6337	5.66	0.154	31.73	4.3	0.0237	0.0737	101.5
om00-173	57.12	0.0872	2.0924	0.591	6.27	0.1661	33.87	0.9468	0	0.0805	101.22
om00-173	57.36	0.0845	2.0351	0.5393	6.17	0.1548	33.96	1.2936	0	0.077	101.67
om00-173	57.25	0.0778	2.1297	0.5639	6.29	0.1657	34.31	0.6585	0	0.0819	101.53

Table B4 - Clinopyroxene Compositions

Sample	SiO_2	TiO_2	Al_2O_3	Cr_2O_3	FeO	MnO	MgO	CaO	Na_2O	NiO	Total
om00-86.4	54.82	0.0575	1.4943	0.8108	1.9024	0.0938	18.03	23.25	0.3258	0.0845	100.86
om00-86.4	54.49	0.0663	1.4656	0.813	1.796	0.0692	18.05	23.6	0.3532	0.0746	100.77
om00-86.4	54.38	0.0732	1.7044	1.0224	1.7481	0.066	17.57	23.47	0.3888	0.0659	100.49
om00-86.4	54.59	0.081	1.6888	1.06	1.597	0.0757	17.58	23.67	0.3863	0.0776	100.8
om00-86.4	54.42	0.0768	1.6834	0.9957	1.5505	0.0689	17.62	23.87	0.3661	0.0811	100.73
om00-88.1	54.19	0.1122	1.5768	0.8851	1.6376	0.08	17.9	24.11	0.3785	0.0743	100.94
om00-88.1	54.85	0.0953	1.4743	0.7847	1.7704	0.0911	17.85	23.89	0.3602	0.0762	101.24
om00-88.1	54.61	0.1058	1.3451	0.9549	1.6124	0.0821	17.9	23.79	0.3354	0.0539	100.78
om00-90	54.45	0.0721	1.8929	1.0589	1.7942	0.0704	17.66	23.82	0.354	0.0856	101.25
om00-90	54.95	0.0762	1.5978	0.7974	1.8114	0.0892	17.93	23.89	0.314	0.0837	101.54
om00-90	54.34	0.0967	1.9743	1.0969	1.6927	0.0594	17.36	23.88	0.3604	0.0483	100.91
om00-141.2	52.7	0.2052	3.2	1.0983	2.2854	0.1006	16.69	23.99	0.1846	0.0537	100.52
om00-141.2	52.86	0.2128	3.15	1.0946	2.6703	0.1189	17.77	22.55	0.1441	0.0589	100.64
om00-141.2	52.75	0.2052	3.19	1.0736	2.2639	0.119	16.86	23.68	0.1705	0.0638	100.38
om00-141.2	52.75	0.2136	3.16	1.1323	2.1861	0.1181	16.68	23.97	0.1713	0.0508	100.44
om00-141.2	52.77	0.204	3.16	1.0967	2.3165	0.1069	16.79	23.92	0.1726	0.0563	100.59
om00-141.2	53.12	0.228	3.2	1.1088	2.2235	0.1061	16.8	23.94	0.1659	0.0551	100.95
om00-141.2	52.81	0.2276	3.19	1.1538	2.1655	0.1076	17.12	23.59	0.1713	0.0696	100.61
om00-141.2	53.11	0.1948	2.9686	1.0438	2.1673	0.1048	16.99	23.94	0.1846	0.0468	100.76
om00-141.4	53.15	0.2085	2.914	1.0241	2.5243	0.1205	18.2	22.63	0.1804	0.0615	101.01
om00-141.4	53.41	0.2145	3.11	1.0998	2.5526	0.1315	17.87	23.05	0.1599	0.0493	101.66
om00-141.4	53.18	0.1995	3.06	1.1772	2.5135	0.1131	16.75	23.7	0.1502	0.053	100.89
om00-141.4	52.86	0.2178	3.27	1.2287	2.5355	0.1063	16.76	23.85	0.1493	0.0649	101.04
om00-141.4	52.74	0.228	3.29	1.1602	2.5257	0.1035	16.9	23.64	0.1633	0.0631	100.81
om00-141.4	53.59	0.1952	2.56	0.683	2.4598	0.108	17.5	23.68	0.1568	0.064	101
om00-141.4	53.13	0.2111	3.17	1.1561	2.343	0.1068	16.71	23.94	0.161	0.0581	100.99
om00-141.4	52.82	0.2032	3.11	1.1415	2.4656	0.1067	16.99	23.34	0.1467	0.0661	100.39
om00-142.1	54.03	0.1236	1.7565	1.1063	2.0913	0.1179	17.41	23.54	0.2621	0.0751	100.51
om00-142.1	54.14	0.1272	1.8019	1.0609	2.1538	0.1103	17.43	23.75	0.2505	0.0832	100.91
om00-142.1	53.84	0.1277	1.5664	1.007	2.1532	0.1066	17.65	23.68	0.253	0.074	100.46
om00-142.1	54.26	0.1266	1.671	1.0259	2.246	0.0993	17.89	23.51	0.2099	0.0626	101.1
om00-143.2	54.11	0.0598	2.0983	1.0293	1.9648	0.1152	17.33	24.18	0.2224	0.0729	101.19
om00-143.2	54.45	0.058	2.0333	0.9534	2.3269	0.0971	17.99	22.95	0.1689	0.0861	101.12
om00-165a	53.74	0.0963	2.3602	0.9821	2.1426	0.1015	17.31	23.71	0.238	0.0607	100.74
om00-165a	53.81	0.0958	2.1652	1.0459	1.9354	0.0999	17.45	24.02	0.2688	0.0646	100.95
om00-165a	54.01	0.0883	2.3083	1.0376	2.0688	0.1085	17.43	23.9	0.2764	0.0616	101.29
om00-171	53.53	0.3352	2.6864	0.9573	2.0991	0.0985	16.99	24.64	0.2041	0.0801	101.61
om00-171	53.5	0.2267	2.5695	1.0009	2.3455	0.1208	17.22	23.97	0.2108	0.0688	101.24
om00-171	54.12	0.2277	2.4397	0.8957	2.8621	0.1227	18.89	21.34	0.1829	0.0657	101.16
om00-171	54.38	0.2141	1.9419	0.6618	2.1929	0.0935	17.72	24.11	0.2127	0.0762	101.6
om00-170	54.47	0.1672	1.2136	0.4138	2.054	0.0824	18.12	24.69	0.158	0.0663	101.44
om00-170	53.63	0.2534	2.23	0.862	2.0465	0.0876	17.43	24.58	0.2217	0.0799	101.43
om00-170	53.87	0.2227	2.0462	0.7836	2.33	0.1035	17.24	24.26	0.1853	0.0691	101.11
om00-170	53.78	0.2249	2.0417	0.7443	2.2437	0.1023	17.35	24.32	0.1794	0.0463	101.04
om00-168	53.94	0.133	2.1767	0.957	2.0788	0.1102	17.55	23.86	0.2989	0.0736	101.17
om00-168	54.22	0.1415	1.7041	0.8003	1.9982	0.0917	17.77	23.94	0.2623	0.071	101
om00-166b	54.08	0.187	2.2827	0.7211	2.4077	0.0765	18.97	22.18	0.2103	0.0643	101.18
om00-166b	53.39	0.2056	2.8226	1.1404	2.0311	0.1066	17.16	23.48	0.2706	0.0622	100.67
om00-166b	53.89	0.2214	2.4845	1.0837	1.829	0.0877	17.32	24.09	0.2436	0.0698	101.31
om00-173	54.1	0.2045	2.5363	1.0543	2.1553	0.1026	17.4	23.75	0.2781	0.0758	101.66
om00-173	53.96	0.1829	2.291	0.9309	2.3161	0.1115	17.44	23.89	0.2589	0.088	101.48
om00-173	54.14	0.1897	2.3292	0.9835	2.311	0.1251	17.21	23.73	0.2105	0.0677	101.3

Chapter 4

MICROSTRUCTURAL EVOLUTION IN NATURALLY-DEFORMED DUNITES: GRAIN BOUNDARY SLIDING AND THE STRENGTH OF THE SHALLOW MANTLE

Abstract:

Systematic variations in texture and microstructure observed in naturally deformed peridotites from the Oman ophiolite are used to constrain the rheology of the shallow mantle beneath oceanic spreading centers. A comparison of harzburgites with dunites bodies of different sizes suggests that melt generation and focused melt transport have a significant influence on the dominant deformation mechanism during corner flow. We combine multiple samples from transects across several lithologic bodies to establish representative composite textures and lattice preferred orientations of coarse-grained naturally deformed peridotites. Harzburgites are typically finer-grained and exhibit a strong {0kl}[100] lattice preferred orientation and relatively small grain size. In contrast, dunites show a systematic transition in microstructure and grain size from the fine-grained {0kl}[100] harzburgite texture in the smallest dunites to a coarse-grained, (010)[100] lattice preferred orientation in the widest dunites. In the context of laboratory data, these observations indicate that the harzburgites were deforming by dislocation-accommodated grain boundary sliding, whereas strain in the dunites was accommodated increasingly by dislocation creep as dunite width increased. Given the well-constrained spreading center environment associated with the ophiolite prior to obduction, we infer that the observed transition in deformation mechanism was induced by grain growth associated with dunite formation and melt transport with an the increased time-integrated melt flux in wider dunites. The inferred onset of grain boundary sliding implies the viscosity of the shallow mantle beneath oceanic spreading centers may be much lower than that predicted by extrapolation of dislocation creep flow laws, except in regions of highly focused melt transport.

Introduction:

Correlations between the orientation of seismic anisotropy in the oceanic upper mantle and large-scale plate motions suggest that an anisotropic fabric develops as the result of flow in the asthenosphere [*Hess*, 1964]. Laboratory experiments have demonstrated that dislocation creep can produce a crystallographic alignment, or lattice preferred orientation (LPO), in deforming aggregates [e.g., *Carter and Avé Lallemant*, 1970], which is the source of the observed anisotropy [e.g., *Nicolas and Christensen*, 1987]. Because olivine is the most abundant, and potentially weakest, phase in the upper mantle, much work has been devoted to understanding the development of lattice preferred orientation and its relationship to seismic anisotropy and mantle dynamics.

Laboratory experiments have identified a variety of mechanisms which accommodate strain within olivine aggregates [*Frost and Ashby*, 1982; *Karato et al.*, 1986]; each one dominant under a unique combination of conditions (i.e. temperature, oxygen fugacity, differential stress, grain size). Sustained deformation by the dominant mechanism induces the crystallographic alignment. As a result, the LPO, developed as strain accumulates in the deforming aggregate, is uniquely related to the dominant rheology.

Although deformation mechanisms are well defined at laboratory conditions and timescales, the experimental uncertainties become large when extrapolated to geologic scales. To better constrain the rheology, we depend on observations from naturally-deformed rocks with a reasonably well defined tectonic history. Using the observed relationship between deformation mechanism and the resultant microstructure we can infer the rheology, even when the deformation conditions are poorly known.

We examine dunites and harzburgites from the mantle section of the Oman ophiolite to constrain the deformation mechanisms which operate in melting region beneath mid-ocean ridges. The Oman ophiolite is a nearly continuous section of lithosphere formed at an oceanic spreading center [e.g. *Boudier and Coleman*, 1981; *Glennie et al.*, 1974; *Nicolas et al.*, 2000]. The extensive structural and petrologic mapping conducted in this region as well as the low extents of physical and chemical

weathering (in comparison to abyssal peridotites) make Oman ideal for the study of naturally deformed peridotites.

Microstructural analysis:

Although a few studies have reported peridotite fabrics from various stratigraphic levels within the mantle section of the Oman ophiolite [*Boudier and Coleman*, 1981; *Dijkstra et al.*, 2002], they focused primarily on flow geometry relative to the paleo-ridge. In most other studies, a large majority of the samples come from just below or within the crust-mantle transition zone [*Boudier et al.*, 1988; *Boudier and Nicolas*, 1995; *Jousselin and Mainprice*, 1998; *Jousselin et al.*, 1998; *Nicolas*, 1986; *Nicolas et al.*, 1980]. As a result, many of the samples with reported LPOs have clearly been affected by melt impregnation, containing abundant interstitial plagioclase and/or clinopyroxene and an indeterminate amount of cumulate olivine. The effects of melt impregnation are evident in the abundance of weak or incoherent LPOs.

To avoid complications associated with melt impregnation, all samples in this study lie, stratigraphically, at least 1 km below the crust-mantle transition zone and are overlain by residual harzburgite. The peridotite samples are completely devoid of plagioclase, have only trace amounts of clinopyroxene, and preserve olivine forsterite contents between 89 and 92, observations which preclude melt impregnation.

Dunites vary in size, from less than 1 cm to 100 m, follow a power-law relationship describing their abundance as a function of width [*Braun and Kelemen*, 2002]. To encompass this range of sizes, we examined several dunites ranging from ~1 cm to 50 m wide, as well as the adjacent harzburgites all from within ~600 meters of each other in the Wadi Lufti region of the Samail massif. Here we report the results from 4 lithologic bodies: three dunites, 3 m, 25 m, and 50 m wide, and the surrounding harzburgite.

Lattice preferred orientations as well as grain size and grain shape distributions were measured in multiple samples from each lithologic body. Oriented samples were collected from transects across several dunites and into the surrounding harzburgite with

a sample spacing of ~50 cm. From each sample, thin sections were cut perpendicular to the mean regional dunite/harzburgite contact and parallel to the mean spinel lineation as determined from the average orientations of 59 dunites and 57 spinels (figure 1). The dunite/harzburgite contacts were chosen as a fabric reference because they have a relatively uniform orientation in this transposed mantle section and the orthopyroxene foliation is not readily evident in outcrop. However, crystal shape preferred orientations (discussed below) suggest that the actual shear plane may have been inclined to this chosen reference plane.

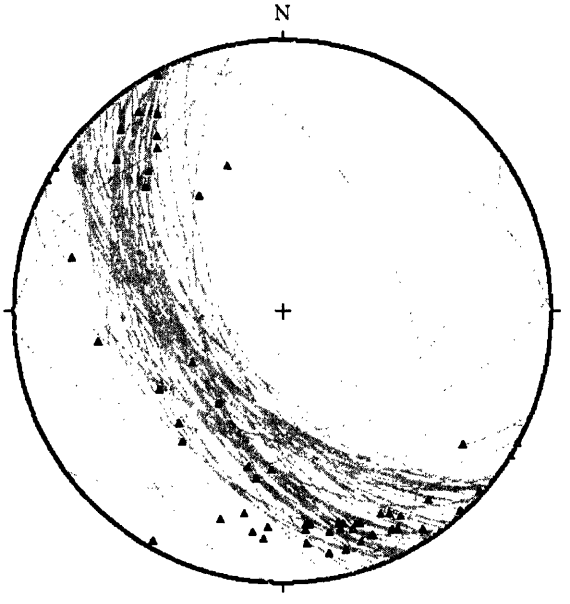

Figure 1: Lower hemispheric, equal-area projection of macroscopic structures in the Wadi Lufti peridotites. The foliation defined by dunite/harzburgite contacts (great circles, N=59) contains the spinel lineation (Δ, N=57). All samples were cut perpendicular to the mean dunite/harzburgite contact (142/58) and parallel to the mean spinel lineation (11-158).

The lattice preferred orientation for each sample was determined using electron backscatter diffraction (EBSD) [*Adams et al.*, 1993] on a JEOL 840 scanning electron microscope equipped with an HKL Technologies backscatter detector. Because the grains in many samples can be quite large (up to 40 mm on a side), multiple thin sections are required to obtain a statistically representative number of grains [*Ben-Ismail and Mainprice*, 1998]. Therefore, data from several samples across each transect were

concatenated to characterize the microstructures. For each section, we indexed each grain interactively (rather than use a completely automated technique) measuring one orientation per grain. This method provides sufficiently extensive sample coverage while reducing errors associated with misindexing and the interference of alteration phases. However, this method limits any extrapolations to bulk rock properties, such as seismic anisotropy, because the volumetric distribution of orientations has been excluded.

In preparation for EBSD, each thin section was polished for approximately 2 hours with 0.02 μm colloidal silica then thinly coated with gold. The coating (<2 sec in an evaporative coater) was sufficient to mitigate the effects of serpentine on surface charging without interfering with the quality of the diffraction patterns. Beam currents with the LaB_6 or tungsten filaments were 10-60 nA with a ~20 kV accelerating voltage and ~23 mm working distance. Pole figures and quantitative crystallographic measurements, described below, were generated using the method of *Mainprice and Silver* [1993].

Grain size and grain shape data were collected separately using digital photomicrographs of many thin sections. Grain boundaries were defined by hand using a digitizing tablet and suites of co-registered digital images for each thin section in 6 or 10 distinct orientations of cross-polarized light. Grain area and perimeter are directly measured from the binary grain boundary images. The grain size is expressed as the diameter of a circle of the equivalent area to avoid biased estimates of size or number associated with grain boundary tortuosity or line intercept sampling density. Composite grain size distributions for each lithologic body are constructed in a manner similar to the orientation data. Grain size data from as many as 8 separate thin sections are concatenated to establish a statistically significant, and approximately equal, number of grains in each lithologic body. Grain orientations are defined by the direction of the major axis of the best-fitting ellipse. In each sample suite, the composite shape preferred orientation was compiled from the same grain boundary images as used for grain size analysis.

Results:

In the following section, we delineate the differences in microstructure observed in four lithologic units: residual mantle harzburgite, and three dunites 3, 25, and 50 meters wide. The textures, grain size distributions, and lattice preferred orientations vary systematically with dunite width, suggesting heterogeneity in the manner by which deformation was accommodated in the shallow mantle.

1. Texture and Grain Size

The textures observed in thin section range from strongly porphyroclastic to coarse granular, suggesting large differences in the extent or style of deformation [*Nicolas and Poirier*, 1976]. Samples from the harzburgite 'protolith' (figure 2a) and the 3 m wide dunite (figure 2b) are dominated by small subgrain-free grains less than 3 mm in diameter. The few large porphyroclasts are generally smaller than those in the larger dunites. Orthopyroxenes in the harzburgite are seldom kinked suggesting a relatively high temperature during deformation [*Ji et al.*, 2001; *Skrotzki*, 1994]. The 25 m wide dunite (figure 2c) is porphyroclastic, with numerous smaller recrystallized grains surrounding larger porphyroclasts. Samples from the largest, 50 m, dunite (figure 2d) are mildly porphyroclastic to coarse granular.

Large olivine grains (>5 mm), common in both the 25 and 50 m wide dunites, often preserve one or two of the following textures: 1) Large grains surrounded by clusters of smaller grains. In some cases, pairs of large grains with identical extinction angles are separated by a narrow band of much smaller grains, suggesting dynamic recrystallization during deformation has split previously larger grains. 2) Large grains with irregular and interpenetrating boundaries, a texture typical of diffusion-induced grain-boundary migration [*Evans et al.*, 1986]. 3) Large olivines completely surrounding multiple inclusions of spinel or other small olivines, suggestive of significant grain growth. 4) Large olivines with distinct subgrains or exhibiting undulose extinction.

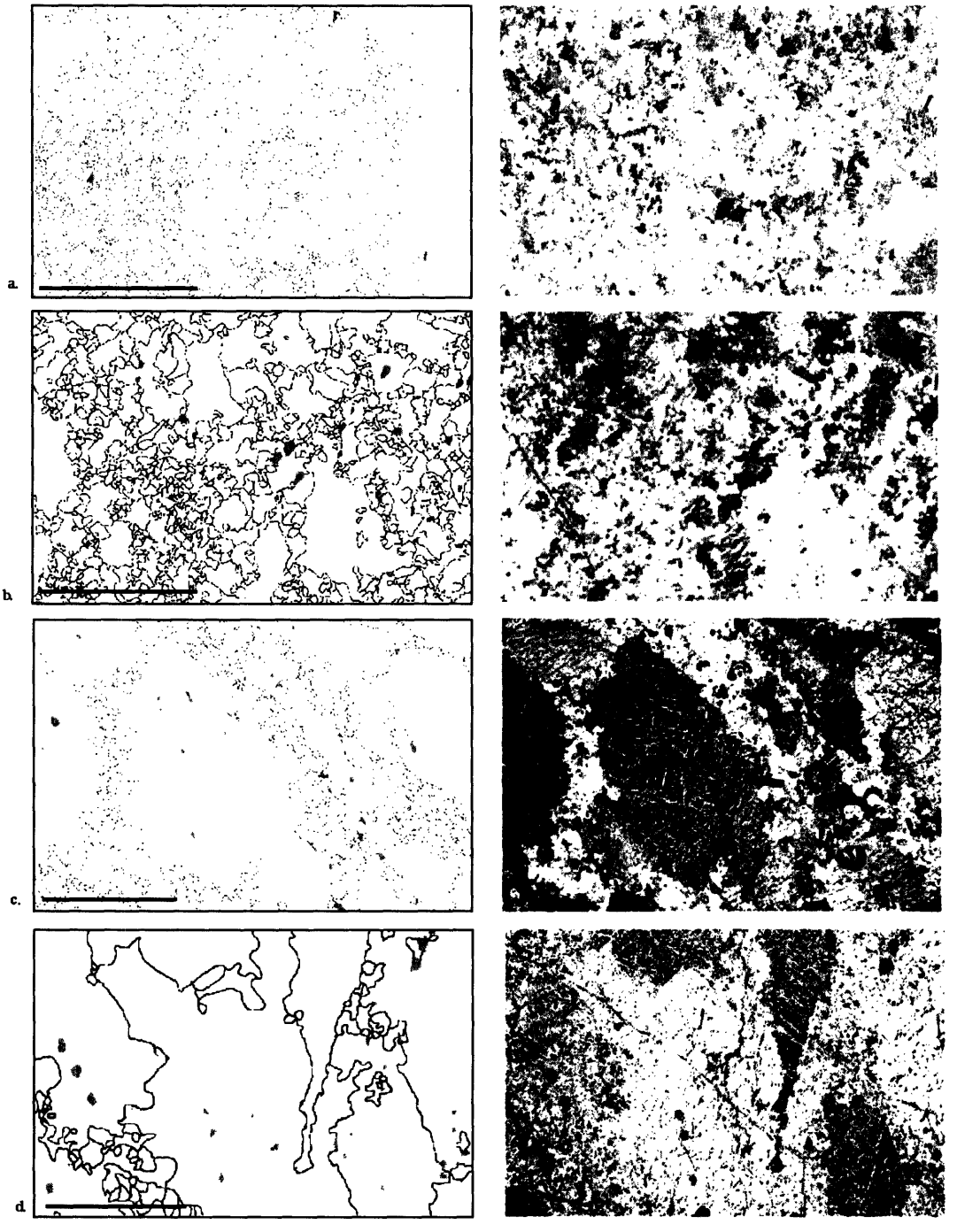

Figure 2: Optical micrographs of representative samples from the a) harzburgite, b) 3 m wide dunite, c) 25 m wide dunite, and d) 50 m wide dunite. Each micrograph is paired with the grain boundary image derived from multiple photographs in various orientations of polarized light.

Grain size increases systematically with increasing dunite width. Composite grain size distributions (figure 3) exhibit a progression toward larger grain sizes in wider dunites. For each lithologic body, data were compiled from a sufficient number of thin sections to obtain approximately equivalent numbers of grains. The mean olivine grain size in the harzburgite is 0.43 mm, and increases with dunite width from 0.68 mm in the 3 m dunite, to 0.83 mm in the 25 m dunite and 1.26 mm in the 50 m dunite. (figure 3a) The maximum observed grain size also varies with width, from 5.18 mm in the harzburgite increasing to 7.9, 18.3, and 26.7 mm in the 3, 25, and 50 m dunites, respectively. A full listing of the quantitative characteristics of the grain size distributions are listed in table 1.

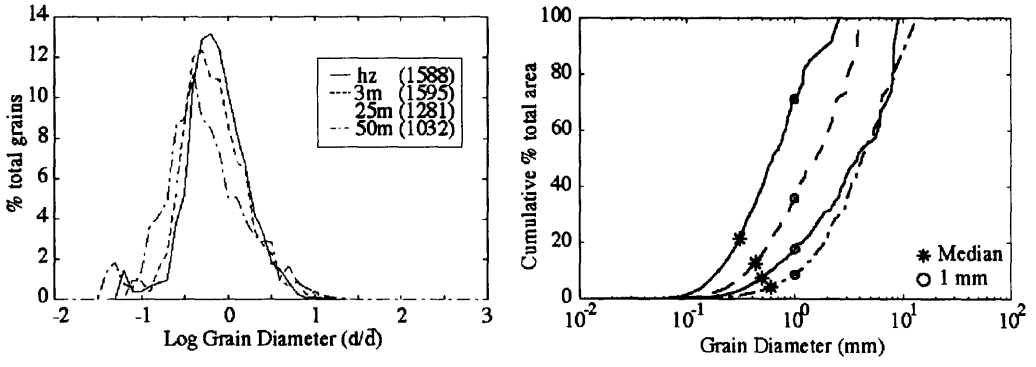

Figure 3: a) Grain size distributions for the harzburgite and 3 m, 25 m, and 50 m wide dunites. Grain size is plotted as the grain size, d, normalized by the mean grain size, $\bar{d}$, for each lithologic suite. Although the distributions all have a similar shape, the mean grain size increases by a factor of three from the harzburgite to the widest dunite, and the maximum grain size increases by more than an order of magnitude. Because of the variation in grain size, more thin sections were required to assemble populations of equivalent size in the wider dunites (see table 1). b) Cumulative area distribution for grains smaller than size, d. As dunite width increases, the area occupied by small grains decreases while the size and abundance of large grains increases. The abundance of grain smaller than the median (✳) and 1 mm (O) are shown for reference.

The differences in grain size between the lithologic bodies are emphasized in the areal distribution of grain size in the thin sections (figure 3b). The total area occupied by small grains decreases with increasing dunite width. With increasing width, the more of the area is occupied by increasingly larger grains. For example, the median grain size, which is 0.3-0.6 mm, occupies less than 20% of the area in each body. In contrast, grains less than 2 mm occupy ~90% of the area in the harzburgite, whereas they only account

for ~20% of the area in the widest dunite. This shift in the areal distribution of grain size is critical to the resultant rheology.

Grain size	50m du	20m du	3m du	hz
# points	1032	1281	1595	1588
# samples	8	4	3	1
mean	1.26	0.83	0.68	0.43
median	0.60	0.49	0.43	0.30
max	26.70	18.30	7.86	5.18
std dev	2.04	1.38	0.83	0.43
kurtosis	43.44	69.69	28.49	28.87
skewness	5.18	7.03	4.34	3.92

LPO data	50m du	25m du	3m du	hz	hz (opx)
# grains	948	434	238	225	66
# samples	10	7	3	3	3
mean J	1.9	1.5	1.7	1.8	3.0
mean K	10.34	2.31	0.58	0.50	3.73

Table 1: Compiled grain size and LPO statistics for each lithologic suite.

2. Deformation Microstructures

The lattice preferred orientations as determined by EBSD, also vary systematically with dunite width while the inferred magnitude of strain remains constant. The olivine LPOs exhibit a transition from hexagonal symmetry in the harzburgite and small dunite to orthorhombic symmetry in the widest dunite. Despite the changes in the shape of the LPO, the strength of the LPO and the orientation of the finite strain ellipse remain constant across all sample suites.

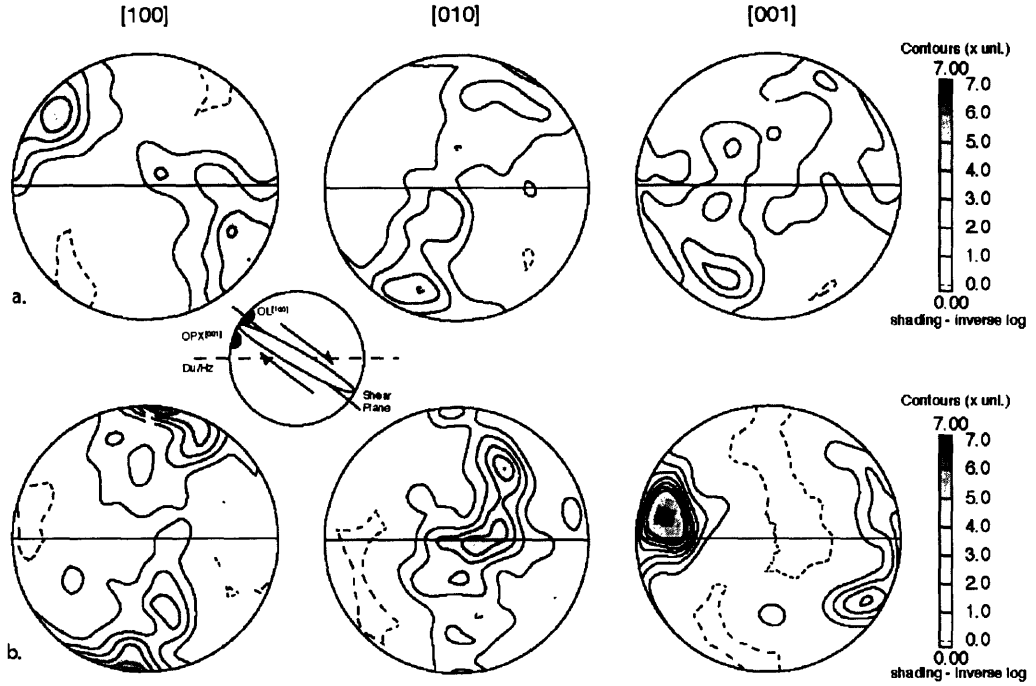

Figure 4: Lattice preferred orientation of a) olivine and b) orthopyroxene in harzburgite from Wadi Lufti, Oman. The olivines exhibit a strong {0*kl*}[100] LPO with the same shear sense as that indicated by the (100)[001] orthopyroxene texture. The inset shows the shear sense and orientation of the shear plane (solid line) and finite strain ellipse relative to the dunite/harzburgite contact (dashed horizontal line). All pole figures are lower hemispheric, equal area projections.

In the harzburgite, the olivine LPO exhibits [010] and [001] girdles about a distinct [100] point maximum (figure 4a). Numerical models for dislocation creep in polycrystalline aggregates indicate the girdled pattern results from simultaneous strain accumulation on two separate slip systems, (010)[100] and (001)[100], [*Tommasi et al.*, 2000; *Wenk and Tomé*, 1999], and is commonly denoted as {0*kl*}[100]. The olivine [100] maximum is inclined ~45 degrees to the plane of the dunite/harzburgite contact along the trend of the spinel lineation (figure 4, inset). The coexisting orthopyroxene (figure 4b) exhibits a strong orthorhombic LPO indicative of deformation on (100)[001], the easy slip system in orthopyroxene [*Mackwell*, 1991]. The sense of shear is the same as that preserved in the olivine, although the [001] lies closer to the plane of the dunite/harzburgite contact.

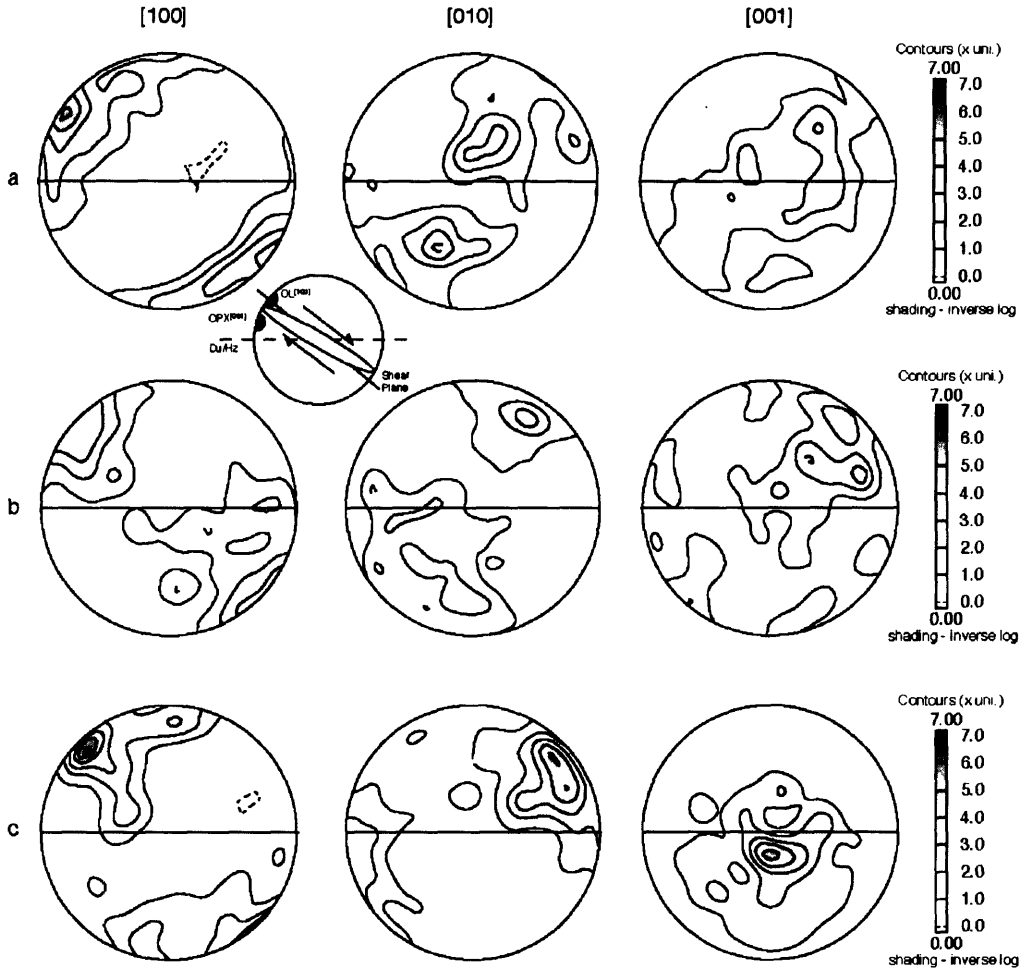

Figure 5: Olivine lattice preferred orientations from a) 3 m, b) 25 m, and c) 50 m wide dunites from Wadi Lufti, Oman. With increasing dunite width, the LPO changes from the girdled {0*kl*}[100] texture indicative of GBS to (010)[100] texture typical of dislocation creep. See figure 4 caption for explanation of inset

In the dunites, we observe a progressive transition in the LPO with increasing dunite width. The small 3 m wide dunite exhibits an LPO with girdles in [010] and [001] about the [100] direction (figure 5a) similar to, although less girdled than, the harzburgite (figure 4a). The LPO in these rocks is also similar to that observed in the experiments of Bystricky et al. [2000]. In contrast, the large 50 m wide dunite has a distinct orthorhombic LPO indicative of strain accommodation dominantly on (010)[100] (figure

5c). This orthorhombic symmetry is the same as observed in the experiments of Zhang and co-workers [1995; 2000].

The 25 m wide dunite shows a more complex LPO, intermediate between the 3 m and 50 m wide dunites (figure 5b). A comparison between the LPOs preserved in large grains and small grains in the 25 m wide dunite shows that the LPO is a mixture of the hexagonal and orthorhombic patterns. The grains larger than ~3 mm (Figure 6a) exhibit an orthorhombic (010)[100] LPO, whereas finer-grained regions in the same thin sections (Figure 6b) exhibit a girdled {0*kl*}[100] pattern. Despite the variation in [010] and [001] pole figures, the orientation of the [100] maximum in all dunite samples is the same as in the harzburgites.

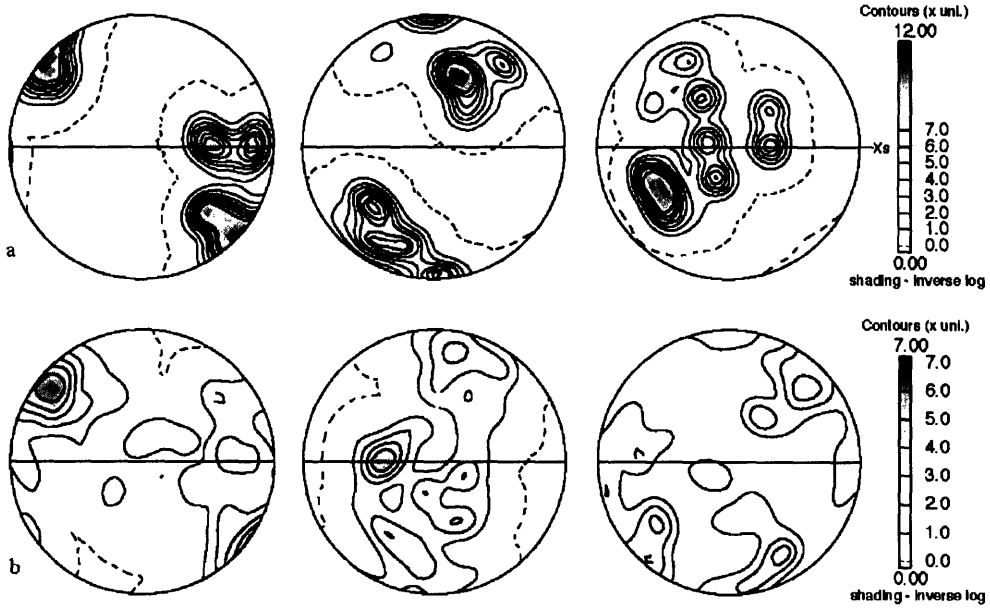

Figure 6: Variation in LPO for populations of different grain sizes from the same rocks. Samples shown here are from the 25 m wide dunite. a) Grains larger than 3 mm (N=41) exhibit a clear orthorhombic (010)[100] LPO. b) In contrast, grain smaller than 3 mm (N=114) record a girdled {0*kl*}[100] LPO.

We can quantify the differences in LPO shape using orientation distribution analysis. The shape factor, K, is based on the eigenvalues of the orientation tensor [*Mainprice and Silver*, 1993; *Woodcock and Naylor*, 1983]. As point maxima develop, K

increases toward infinity. In contrast, as the pole figure becomes girdled, *K* asymptotically approaches zero. As illustrated in figure 7, the *K* factor changes from 0.50 in the harzburgite to 0.58, 1.67, and 10.34 in the 3, 25, and 50 m dunites, respectively.

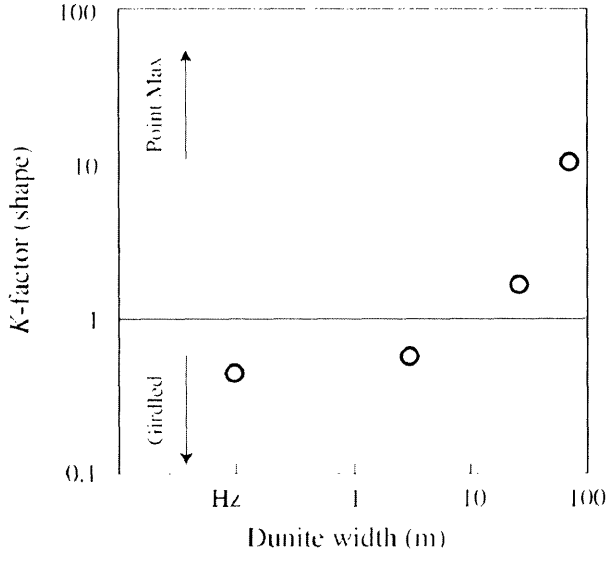

Figure 7: Quantitative textural analysis [*Mainprice and Silver*, 1993] indicates a distinct transition in LPO shape (*K*) from girdled to point maxima with increasing dunite width.

3. Magnitude and Orientation of Shear

We infer the orientation of the shear plane using crystal shape- and lattice-preferred orientation data derived from digital grain boundary images. This technique was originally developed using peridotites from Oman [*Nicholas*, 1989]. Experiments demonstrate that in a deforming aggregate, grains oriented for easy slip will lengthen in the direction of shear, imparting a foliation and an LPO to the minerals which accommodate the strain. With increasing strain, the elongation direction of the finite strain ellipse and the orientation of the olivine [100] maximum rotate toward the shear plane. The experiments by Zhang and Karato [1995] and Bystricky et al. [2000] show that the [100] maximum rotates completely into the shear plane after only ~150% strain, regardless of the differences in the final LPO. Moreover, the LPO rotates more rapidly than the finite strain ellipse with increasing strain.

Our data indicate that the shear plane is inclined relative to the dunite/harzburgite contacts. Measurements of the orientation of the circumscribing ellipse enclosing grains greater than 2 mm imply the finite strain ellipse is inclined ~30 degrees from the mean orientation of the dunite/harzburgite contacts (figure 8). Grains smaller than 2 mm show no clear shape preferred orientation.

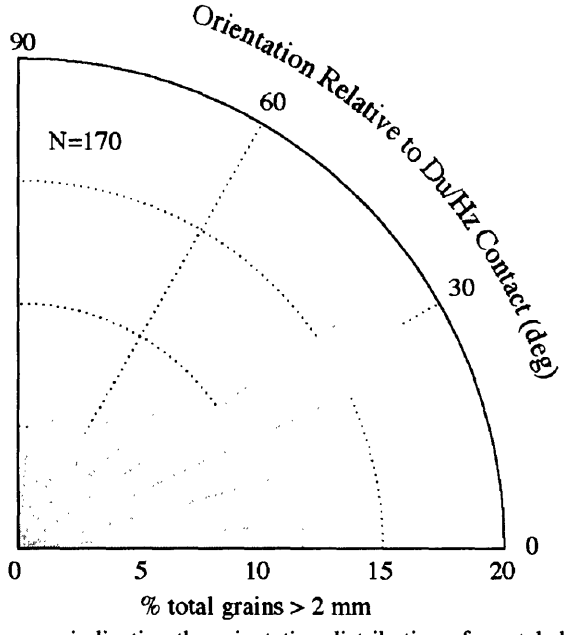

Figure 8: Rose diagram indicating the orientation distribution of crystal shapes. Using digital grain boundary images (figure 2), the orientation of each grain is determined from the major axis the best-fitting ellipse. For grains larger than 2 mm, the crystal shape foliation is oriented 30 degrees from the dunite/harzburgite contact.

Because the experiments demonstrate that the orientation of the LPO reaches steady state after only moderate strains, we assume that the olivine [100] maximum represents the shear direction. The olivine LPO data (figures 4a and 5a-c) show that the [100] maximum is consistently inclined ~45°to the dunite/harzburgite contact orientation. Subtracting the difference in orientation between the observed crystal-shape foliation and the lithologic contacts from the inclination of the [100] maximum, we infer the foliation lies only about 15° out of the shear plane.

Quantitative and relative indicators of the magnitude of strain show no significant differences between dunites of different widths, despite the variations in grain size and LPO. The orientation of the finite strain ellipsoid relative to the shear plane as well as the LPO strength are observed to vary with increasing strain during laboratory experiments [*Zhang*, 1995; 2000]. However, the orientation of the finite strain ellipse and olivine [100] maximum in the naturally deformed samples do not vary substantially. Based on the Zhang and Karato [*Zhang and Karato*, 1995] data, a difference of 15° between the olivine [100] maximum and the finite strain ellipse occurs either at strains less than 50%, as the LPO departs from stress control, or at strains significantly greater than 350%, when the orientation of the finite strain ellipse approaches the saturated LPO already aligned with the shear direction.

The similar strengths of the LPOs also indicate no significant variation in strain between the sample suites. The *J*-index reflects the strength of the LPO by quantifying the homogeneity in the distribution of crystallographic orientations [*Mainprice and Silver*, 1993]. Both the Zhang et al. [1995] and Bystricky et al. [2000] experiments demonstrate that the *J*-index increases with increasing strain. However, in the naturally deformed samples, the measured *J*-indices are nearly equivalent (1.5-1.9) with no clear relationship to the width of the dunite. The lack of variation in the *J*-index, finite strain ellipse, or [100] maximum suggests that all the samples were deformed approximately equally or the strains are sufficiently large that LPOs have become saturated, and further strain accumulation does not significantly affect the LPO. The well developed LPOs with the nearly equivalent *J*-indices and a small difference between the finite strain ellipse and the [100] maximum suggest that the strain in all of the rocks is large (>350%).

Discussion:

1. Relating Deformation Mechanism and LPO

Peridotites from Wadi Lufti, Oman exhibit two distinct patterns of lattice preferred orientation, common amongst naturally-deformed peridotites, which correlate with the grain size of the rocks in which they occur. The grain size and LPO also vary

with dunite width. Specifically, we observe an {0*kl*}[100] LPO in conjunction with smaller grain sizes in the harzburgite (figure 4a) and 3 m wide dunite (figure 5a), as well as in the fine-grained (<2 mm) areas of the 25 m wide dunite (figure 6b). By contrast, coarse grained rocks, which comprise most of the area of wide dunites, exhibit (010)[100] textures.

Observations of both {0*kl*}[100] and (010)[100] lattice preferred orientations are common among naturally deformed harzburgites. A brief review of the literature regarding peridotite petrofabrics in Oman [*Ben-Ismail and Mainprice*, 1998; *Boudier et al.*, 1988; *Boudier and Coleman*, 1981; *Boudier and Nicolas*, 1995; *Ceuleneer et al.*, 1988; *Ceuleneer and Rabinowicz*, 1992; *Dijkstra et al.*, 2002; *Jousselin and Mainprice*, 1998; *Jousselin et al.*, 1998; *Nicolas*, 1986; *Nicolas et al.*, 1980] shows that half of the harzburgite samples which have a significant texture exhibit {0*kl*}[100] LPOs. As with our data, the LPO is also correlated with dunite size. Small dunites (described as intercalated with harzburgite on a centimeter to decimeter scale) show the {0*kl*}[100] texture. Despite the lack of explicit width information, rocks described simply as 'dunite' generally exhibit (010)[100] patterns. Unfortunately, grain size data for these samples were not reported, so correlations between LPO and grain size are impossible to determine from the literature alone.

Both orthorhombic (010)[100] and hexagonal {0*kl*}[100] LPOs are also observed in laboratory experiments on dry olivine aggregates in simple shear. Despite only moderate differences in deformation conditions, the experiments indicate that the distinct lattice preferred orientations correlate with significant differences in both the microstructural and mechanical properties of the aggregate. Samples deformed at 1300°C yield an orthorhombic LPO and a uniform grain size distribution about 1/3 the size of the starting material [e.g. *Zhang and Karato*, 1995; *Zhang et al.*, 2000]. Samples with the orthorhombic LPO also exhibit larger heterogeneities in dislocation density and evidence for migrating grain boundaries [*Lee et al.*, 2002] . In contrast, samples deformed at the same strain rate and confining pressure, but at 1200°C and slightly higher stress, yield the hexagonal {0*kl*}[100] LPO and a bimodal grain size, with the coarser grains similar in

size to the starting material and the finer grains an order of magnitude smaller [*Zhang et al*, 2000; *Bystricky et al.*, 2000]. Additionally, the fine-grained regions exhibit lower and more homogenous dislocation densities and an abundance of thermodynamically unstable 4-grain junctions indicative of grain switching [*Lee et al.*, 2002].

In the following discussion, we focus on experimentally-derived flow laws and the results of numerical models for the deformation of polycrystalline aggregates to discern how the differences in grain size and deformation conditions affect the rheology of the deforming aggregate and subsequently which deformation mechanisms contribute to the observed lattice preferred orientations observed in Oman.

Empirical constitutive laws derived from the deformation of oriented single crystals [*Bai et al.*, 1991; *Durham and Goetze*, 1977] predict (001)[100] slip may be as easy or easier than the (010)[100] slip system in olivine. Figure 9 depicts the flow laws for the three dominant slip systems extrapolated into the range of upper mantle conditions. Although the (010)[001] slip system exhibits the slowest strain rate at all conditions, the relative strain rates on the easier two slip systems varies with the deformation conditions. At high temperatures (>1350°C), the (010)[100] slip system unequivocally exhibits the fastest strain rates. However, over the range of conditions predicted for the melting region beneath mid-ocean ridges (1200-1300°C and oxygen fugacites between the Fayalite-Magnetite-Quartz and Nickel-Nickel Oxide buffers [*Carmichael and Ghiorso*, 1986]) the dominant slip system is equivocal. Given the uncertainty in the measured activation energies, the flow laws predict the (001)[100] slip system is as weak or weaker than (010)[100].

These relative differences in strain rate are independent of the differential stresses driving deformation, because all three flow laws have the same stress dependence. Therefore, the single crystal flow laws allow for the predominance of (001)[100] at all stresses down to temperatures as low as 1100°C. However, the predicted strain rates for the (010)[100] slip system again become significantly higher than for (001)[100] slip at low temperatures, power-law break down occurs below ~1000°C [*Frost and Ashby*, 1982; *Kameyama et al.*, 1999] and these constitutive laws would no longer be applicable.

Therefore, over the range of conditions expected in the melting region beneath ridges, the (001)[100] slip system is equally, if not more, likely to dominate strain accumulation, and subsequently control the LPO.

However, experiments performed in the dislocation creep regime are most commonly dominated by (010)[100] creep [*Carter and Avé Lallemant*, 1970; *Hirth and Kohlstedt*, 1995; *Nicolas et al.*, 1973; *Zhang et al.*, 2000]. Numerical models of LPO development suggest that this discrepancy between the relative activities of the slip

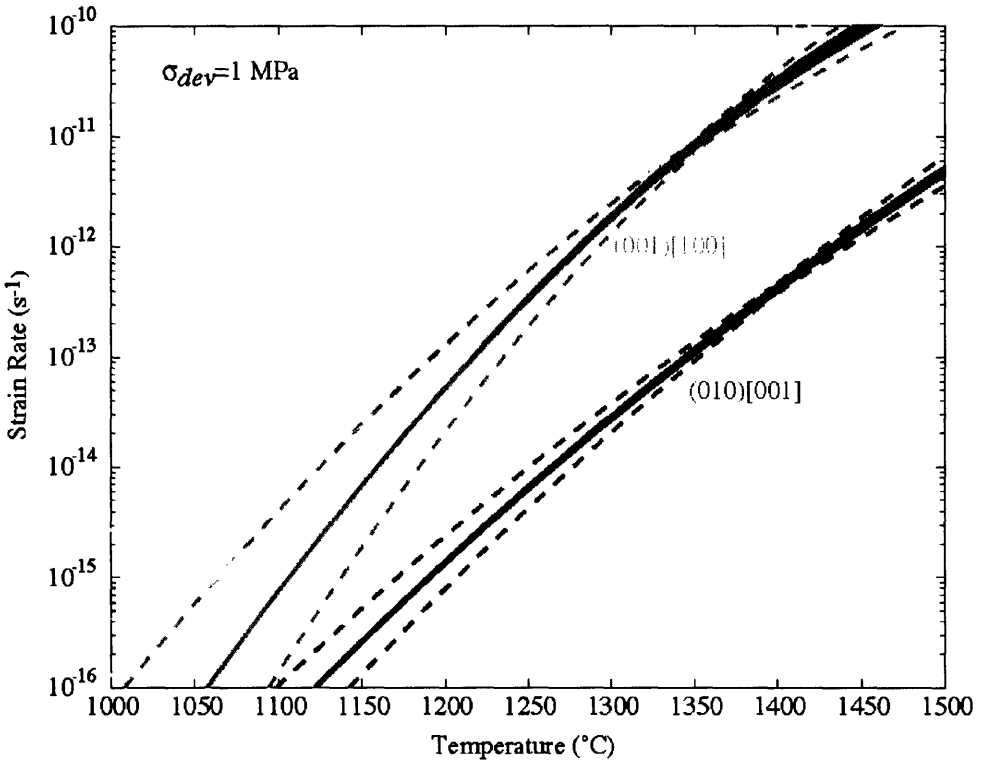

Figure 9: Constitutive laws for individual slip systems in olivine extrapolated to upper mantle conditions from the experiments of Bai et al [1991]. Over the range of temperatures and oxygen fugacities (QFM-NNO) predicted for the oceanic spreading center environment, the (001)[100] slip system is equivalent or weaker than the (010)[100] slip system, traditionally predicted to be the easiest slip system in olivine. If grain switching sufficiently relaxes strain compatibility criterion, then both (010)[100] and (001)[100] can contribute equally to the formation of an LPO.

systems and predominance of the (010)[100] texture is the result of strain compatibility requirements. Specifically, requiring slip on (010)[001] – the hardest slip system in olivine – geometrically inhibits significant strain accumulation on (001)[100].

Viscoplastic self-consistent (VPSC) models reproduce the orthorhombic (010)[100] LPO when stringent strain compatibility requirements are imposed, even when (001)[100] and (010)[100] are equivalently weak [*Tommasi et al.*, 2000; *Wenk and Tomé*, 1999]. Tommasi et al [*Tommasi et al.*, 2000] show that, with increasing strain, the progressively increasing need to deform poorly-oriented grains on the hardest slip system reduces (001)[100] activity, suppressing its expression in the LPO.

When the strain compatibility criterion is relaxed, however, an {0*kl*}[100] LPO develops. VPSC models indicate that relaxed conditions mitigate the geometrical interactions which arise when slip on the hardest slip system is required. Relaxation, manifest as strain accumulation by intercrystalline processes (e.g. dynamic recrystallization, grain boundary migration, or grain boundary sliding), reduces the requirement for slip on (010)[001]. The activity of (001)[100] subsequently increases [*Tommasi et al*, 2000; *Kaminski and Ribe*, 2001]. As a result, models with relaxed strain compatibility show that girdled {0*kl*}[100] textures develop and persist to higher strains with increasing relaxation [*Tommasi et al.*, 2000; *Wenk and Tomé*, 1999]. Therefore, based on the single crystal data and numerical models, we infer that the transition in LPO from (010)[100] to {0*kl*}[100] observed in the peridotites from Oman is due to a relaxation of strain compatibility.

The onset of dislocation-accommodated grain boundary sliding (GBS), in which grain switching relaxes strain compatibility, may be responsible for the transition in LPO from orthorhombic to hexagonal symmetry observed in both laboratory experiments and naturally-deformed rocks. GBS is a grain-size sensitive creep mechanism which outpaces dislocation creep at small grain sizes [*Hirth and Kohlstedt*, 1995]. Although no direct data exist on the LPO induced by GBS, the mechanical and microstructural data which define GBS match those observed in laboratory experiments which exhibit an {0kl}[100] LPO, suggesting deformation by GBS generates the hexagonally symmetric LPO, with girdles in [010] and [001].

At constant stress, strain rates for experiments which generate hexagonal LPOs are higher than for experiments which produce orthorhombic (010)[100] patterns [*Zhang*

et al, 2000; *Bystricky et al*, 2001]. Similarly, strain rates for olivine during GBS are as much as 30 times higher than those observed in coarse-grained samples deforming by dislocation creep under similar conditions (see [*Hirth and Kohlstedt*, 2003] for a review). During dislocation creep, strain rate is limited by slip on the hardest system (i.e., (010)[001]). In contrast, during GBS, microstructural analysis of experimental samples indicates that strain rate is instead limited by deformation on the easiest slip system (i.e., (010)[100]) [*Hirth and Kohlstedt*, 1995].

GBS experiments and the samples with {0kl}[100] textures indicate extensive grain switching accommodated by dislocation migration. Both Lee et al [2002] and Hirth and Kohlstedt [1995] observe an abundance of 4-grain junctions which implies grain switching was inherent to strain accumulation in both cases. Despite the small grain size, grain switching is accommodated by dislocation motion and not by diffusion. Stress exponents and activation energies measured during GBS match those for dislocation creep, and the observed gradients in dislocation density coupled with a strong crystallographic fabric indicate that dislocations are highly mobile [*Hirth and Kohlstedt*, 2003; *Hirth and Kohlstedt*, 1995]. Therefore grain switching in fine-grained aggregates allows for significantly higher strain rates than those predicted for grain-size-independent dislocation creep by alleviating the requirement for slip on the hardest slip system.

The small grain sizes observed in samples with the {0kl}[100] LPO may reflect the transition to grain size sensitive GBS. During GBS, a decrease in grain size at constant stress increases the strain rate by shortening the translation distance required for grains to switch positions. The coexistence of abundant 4-grain junctions with relatively small grain sizes observed in samples with {0kl}[100] textures, suggests that the reduced grain size may be required for the onset of the deformation mechanism responsible for the LPO. The data from Oman corroborate this assertion. Figure 6 shows LPOs collected from fine- and coarse-grained regions of the same rocks. Because the deformation conditions were otherwise the same for both regions, the grain size differences must be responsible for the differences in LPO.

Single crystal flow laws and VPSC models show that the {0*kl*}[100] LPO results from relaxed strain compatibility conditions which may arise from grain switching during GBS. Grain switching and grain size sensitive creep, which distinguishes GBS from nominal dislocation creep, are consistent with the observations from the laboratory experiments which exhibit the {0kl}[100] LPO [*Bystricky et al.*, 2000; *Zhang et al.*, 2000]. We therefore infer that the shared dominance of both (010)[100] and (001)[100] slip during GBS results in a girdled {0*kl*}[100] LPO. By extension, the transition from {0kl}[100] to (010)[100] LPO coupled with in increase in grain size observed in naturally deformed peridotites suggests that the fine-grained harzburgites and small dunites record deformation by GBS, whereas the coarse-grained wide dunites record deformation by nominal dislocation creep.

2. Effects of Melt Generation and Transport on Grain Size

Melting and melt transport are most likely responsible for the observed changes in grain size which subsequently control the dominant deformation mechanism during corner flow. Geochemical data [*Dick*, 1977; *Kelemen and Dick*, 1995; *Kelemen et al.*, 1997], field observations [e.g. *Braun and Kelemen*, 2002; *Kelemen et al.*, 2000a; *Kelemen et al.*, 2000b], and numerical models [*Aharonov et al.*, 1995; *Spiegelman et al.*, 2001] indicate that dunites are the remnants of high porosity channels formed from harzburgite by reactive porous flow of silica-undersaturated basaltic melt. In Oman, replacive dunites are generally tabular features which lie sub-parallel to the crust-mantle transition zone and define the prominent macroscopic foliation [*Boudier and Coleman*, 1981; *Lippard et al.*, 1986]. From these constraints, it is inferred that the dunites formed as near-vertical conduits in the melting region. Although the microstructures recorded in the rocks presented here record the flow of the depleted mantle away from the spreading center, the systematic variations in grain size and LPO with dunite width suggest that the changes in deformation mechanism are related to melting and melt transport processes which occurred prior to corner flow.

Maintaining a critically small grain size is essential to the onset of GBS. If during deformation, grain size reduction by dynamic recrystallization outpaces grain growth, the decreasing grain size will drive the system into the diffusion creep regime, potentially erasing the preexisting LPO [*Warren et al*, in prep]. However, during diffusion creep dynamic recrystallization is not occurring, which allows grain growth to drive the system back into the dislocation creep regime. This balance has led to the notion that steady-state deforming aggregates will tend toward grain sizes at the boundary between diffusion creep and dislocation creep regimes [*De Bresser et al.*, 2001]. Although the grain size data from Oman straddle the boundary between the diffusion creep and dislocation creep fields (figure 10), the microstructures indicate that near this boundary, peridotites likely deform by GBS with an LPO distinct from either end member.

In the harzburgite, the small olivine grain size is partly maintained by the presence of pyroxene. The presence of a distributed second phase pins olivine grain size by preventing grain boundary migration from smoothing heterogeneities in surface and internal strain energy (i.e. Zener pinning) [*Evans et al.*, 2001]. Grain growth may be further inhibited at the onset of melting if melt also serves as a pinning phase [*Hirth and Kohlstedt*, 1995].

The increase in grain size observed from harzburgite to dunite results from melt generation and reactive porous flow. Melt generation reduces the mass and size of the pyroxenes, mitigating the pinning effect. However, the degree of melting inferred from the composition of MORB and abyssal peridotites is too small to completely transform harzburgite into dunite. Dunites instead form by reaction between primitive melts and residual harzburgite, and this reaction process can increase grain size. During ascent, silica-undersaturated melt dissolves orthopyroxene and precipitates a nearly equivalent mass of olivine [*Kelemen*, 1990]. Experiments indicate that during melt-rock reaction, olivine nucleation is slow relative to growth, and the dunite formation process preferentially increases the size of preexisting grains [*Daines and Kohlstedt*, 1994]. The large and abrupt change in grain size commonly observed across harzburgite/dunite boundaries in the Oman samples likely reflects this process (see right side of figure 2a).

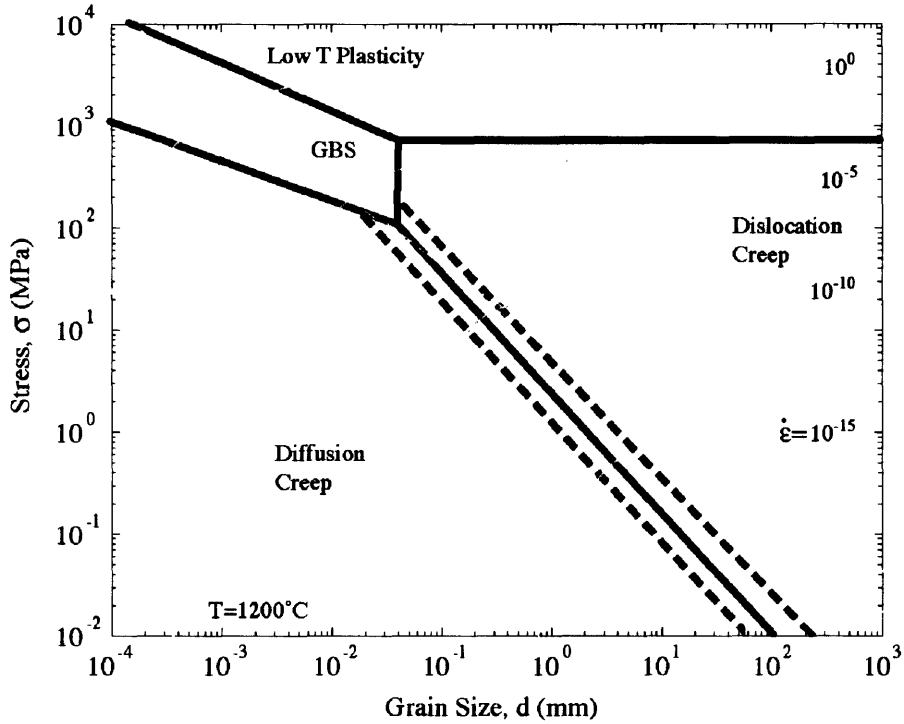

Figure 10: Deformation mechanism map for dry olivine at 1200 °C [*Hirth and Kohlstedt*, 2003]. The range in grain size observed in peridotites from Oman is shown by the light gray field. The coarse-grained dunites fall in the dislocation creep field consistent with the observed (010)[100] LPO. However, the finer-grained rocks are predicted to be in the diffusion creep field, but exhibit a {0*kl*}[100] LPO indicative of GBS. The dark gray field indicates the grain size range over which the girdled LPO is observed. Therefore, we infer that the GBS field extends down along the boundary between dislocation and diffusion creep (dashed field). Extrapolated grain size piezometers [*Karato et al.*, 1980; *Van der Wal et al.*, 1993] (dashed lines) predict stresses on order of 1 MPa during deformation of the coarse-grained wide dunite.

Upon complete dissolution of the pinning pyroxene, olivine grains can grow with time. Numerical models of the reaction infiltration instability show that dunites grow wider with time by reaction along their boundaries [e.g. *Spiegelman et al.*, 2001]. Therefore the correlation between olivine grain size and dunite width suggests that wider dunites formed before, and thus deeper in the melting column, than narrow ones.

Static grain growth models suggest that there is sufficient time for dunites to grow grains as large as those observed in Oman, however the effects of deformation would mitigate much of its effect. Figure 11 shows the time required for a 1 mm olivine grain to grow to the maximum observed grain size in dunites. For normal grain growth with a

grain size exponent of 3 at 1200°C [*Karato*, 1989], the observed maximum grain sizes can be attained in approximately 100 years, for narrow dunites, and ~4000 years for the widest dunites. If the grain size exponent were 2, the time required to normal grain growth to reach the largest grain size reported here would be on order of 5 Ma. Regardless of the grain size exponent, these times fall well below the maximum residence time for solid material in the melting region, which is approximately 1-10 Ma for spreading rates of 120-10 mm/yr, respectively [*Braun and Kelemen*, 2002]. However, grain growth estimates are only applicable under static conditions.

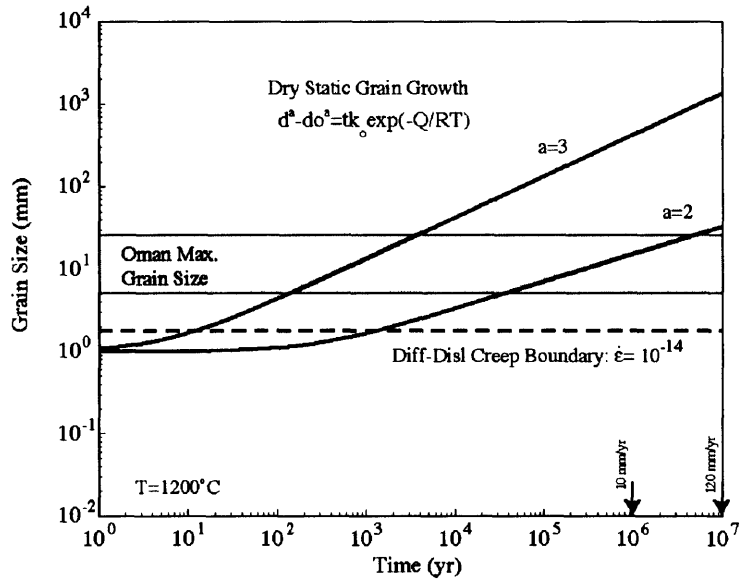

Figure 11: Predictions for the evolution of grain size at 1200°C based on the exponential growth models [*Karato*, 1989]. Solid lines show the timescale for grain growth using a grain size exponent of 2 or 3. Regardless of the grain size exponent, the time required for a 1 mm olivine grain to grow to the size of the largest olivines observed in Oman (gray box) is shorter than the residence time of solid material in the melting region beneath a mid-ocean ridge (arrows). For comparison, the steady-state dynamically-recrystallized grain size at the boundary between the dislocation and diffusion creep fields at 1200°C and a strain rate of 10^{-14} s^{-1} is shown (dashed line).

Dynamic recrystallization during deformation would substantially reduce the grain size. If, as de Bresser [*De Bresser et al.*, 2001] suggests, the grain size is fixed to the diffusion creep-dislocation creep boundary, extrapolation of olivine flow laws [*Hirth and Kohlstedt*, 2003] to 1200°C and a strain rate of 10^{-14} s^{-1}, indicates the recrystallized grain size would be only ~2 mm (figure 11). To achieve a steady state dynamically

recrystallized grain size equivalent to the maximum observed grain sizes, the deformation conditions would be in excess of 1500°C or at strain rates less than 10^{-16} s^{-1}.

Because the dunites were active melt conduits prior to corner flow, the presence of melt could substantially enhance grain boundary mobility, offsetting the effects of dynamic recrystallization. The observed irregular and interpenetrating grain boundaries and numerous spinel inclusions within large grains in the wide dunites (figure 2d) are consistent with substantial growth due to high grain boundary mobility in the presence of melt [*Evans et al.*, 2001].

The systematic increase in grain size with dunite width may therefore be related to an increase the time-integrated melt flux through wider dunites. Because larger grains impose a higher permeability [*Von Bargen and Waff*, 1986], local variations in grain size would increase the melt flux in coarse-grained dunites. The continual dissolution and reprecipitation of olivine by the passing melt can result in substantial grain growth (i.e. zone refining), such that it outpaces grain size reduction associated with dynamic recrystallization. The increased permeability also translates into a larger total volume of melt integrated over the lifetime of the dunite. This hypothesis of a larger melt/rock ratio in wider dunites is independently corroborated by geochemical data collected on these same rocks which show systematic compositional variations with dunite width [*Braun and Kelemen*, in prep].

3. Viscosity Variations in Naturally-Deformed Peridotites

We propose that melt generation and reactive melt transport are what change the grain size in dunites. However, their affect on peridotite rheology, as preserved in these samples, is not realized until after the melt has left the dunites. Although the grain size variations can be used infer a systematic increase in the porosity within the dunites, the decrease in viscosity due to the presence of melt during deformation is inconsistent with the observed textures. Instead, the viscosity variations implied by the onset of GBS predicts that harzburgites are weaker than dunites. Based on the microstructural data

presented here, we can constrain the grain size at which the transition to GBS is likely to occur in the mantle.

Direct extrapolation of the empirically-derived pieziometric relationships for stress as a function of grain size [*Karato et al.*, 1980; *Van der Wal et al.*, 1993] predict the differential stresses estimated for the Oman peridotites are in the range of 0.3-10 MPa (figure 10). If flow in the shallow mantle beneath mid-ocean ridges is forced by the divergent motion of the overlying plates and the plate velocity (i.e. strain rate) is presumed constant, then this predicted variation in stress implies local viscosity variations of more than an order of magnitude. Based on the laboratory observations of the effects of melt on olivine rheology [*Hirth and Kohlstedt*, 2003; *Hirth and Kohlstedt*, 1995; *Kelemen et al.*, 1997], viscosity variations this large are possible if the melt fraction in the large dunites were 5-7% higher than in the small dunites and surrounding harzburgites.

A variation in melt content with dunite width is consistent with melt flux estimates from large scale field observations but inconsistent with the microstructures presented here. Dunite size distribution statistics from Oman suggest that the porosity within dunite conduits may increases systematically in proportion to the width of the conduit, with the maximum porosity in the widest dunites estimated to be ~4% higher than in the small ones [*Braun and Kelemen*, 2002].

If the porosity variations were present during deformation, then the large dunites were at least order of magnitude less viscous than the surrounding harzburgite. As a consequence of the substantially lower viscosity, the wide dunites would experience greater strain localization than narrow dunites. However, the textures presented here indicate the opposite. The widest dunites exhibit coarse-grained, protogranular textures (figure 2d) with little area occupied by small recrystallized grains (figure 3b), whereas the harzburgites and small dunites exhibit abundant small dynamically recrystallized grains. Therefore, the grain sizes do not likely reflect viscosity variations associated with melt present during deformation.

Instead, the microstructures and lattice preferred orientations suggest that, because of GBS, strain may be preferentially partitioned into the harzburgite and small dunites. Laboratory data indicate that strain rates during GBS are as much as on order of magnitude faster than during dislocation creep at the same temperature and stress [*Hirth and Kohlstedt*, 1995]. Considering all the rocks presented here are situated within several hundred meters of one another, it is possible that the range in differential stresses is not as large as that explicitly predicted by grain size piezometery. If stresses were constant across the different lithologies and the fine grained rocks were deforming by GBS, then the harzburgite and fine-grained dunites would have a lower viscosity.

Using the grain size in the wide dunites to provide an estimate of the stresses during deformation, we can use the grain size dependence of the microstructures to estimate the width of the GBS field under geologic conditions. Above a grain size of about 2 mm, grain shapes are largely equant (figure 8) and the LPO becomes orthorhombic (figure 6) indicative of dislocation creep. In peridotites with grain sizes below 2 mm, the {0*kl*}[100] LPO dominates. From the data collected here this girdled LPO persists in grains as small as 500 μm, although this lower bound is not well characterized. Interestingly, the grain size predicted at the boundary between diffusion and dislocation creep at 1200°C and a strain rate of 10^{-14} s^{-1} falls right within these bounds. Figure 10 illustrates the interpreted width of the GBS field based on the grain size and LPOs observed in Oman.

Further analysis of both naturally and experimentally deformed rocks is required to test this inference, as it may have significant implications for the advection of the shallow mantle beneath spreading centers. Several empirical tests regarding the strength of mixtures of olivine and pyroxene have shown that strain rates of olivine-orthopyroxene aggregates increase with increasing orthopyroxene content [e.g. *Ji et al.*, 2001; *Kohlstedt and Zimmerman*, 1996; *Lawlis*, 1998; *McDonnell et al.*, 2000]. Existing data on the resultant microstructures in such controlled experiments indicate that orthopyroxene is deforming by dislocation creep where as the olivines are dominated by GBS [*Fliervoet et al.*, 1999]. These experiments, however, were done in uniaxial compression to strains

less than 24%, and the LPOs show evidence for diffusion creep as well as GBS. Although quantitative estimates of the relative viscosities are obscured by the saturated LPOs, our data indicate that dunites and harzburgites can deform by different deformation mechanisms under similar conditions.

Numerical models which incorporate GBS [*Braun et al.*, 2000; *Choblet and Parmentier*, 2001] predict a significant change in the advective patterns in the shallow mantle beneath mid-ocean ridges. The large viscosity increase associated with dehydration during melting is countered by the onset of GBS, yielding a region of buoyancy driven flow which becomes more pronounced with decreasing spreading rate. As a result, these models can reproduce a variety of geophysical observations, including the observed depth variations in seismic anisotropy [e.g. *Gaherty et al.*, 1996] and the short wavelength of gravity anomalies at slow spreading ridges [e.g. *Lin and Phipps Morgan*, 1992], which cannot be generated by models which rely solely on deformation by diffusion or dislocation creep.

Conclusions:

Analysis of texture, microstructure, and grain size indicate that peridotites from the Oman ophiolite show a transition in deformation mechanism from grain boundary sliding to dislocation creep induced by melt generation and migration. By compiling composite textural and microstructural measurements from suites of samples, we can quantitatively compare the microstructures in coarse-grained naturally-deformed peridotites. The harzburgites are fine-grained with a strongly recrystallized texture and a girdled {0*kl*}[100] lattice preferred orientation, which we suggest is the result of dislocation-accommodated grain boundary sliding. Coupled to an increase in their width, dunites exhibit an increase in grain size, a weaker porphyroclastic texture, and a transition from {0*kl*}[100] to an orthorhombic (010)[100] LPO indicative of dislocation creep. Because dunites form and grow by reaction of harzburgite with ascending melts, we ascribe the transition in deformation mechanism to changes in grain size induced by larger time-integrated melt-rock ratios in wider dunites.

Bibliography:

Adams, B.L., S.I. Wright, and K. Kunze, Orientation imaging: the emergence of a new microscopy, *Mettall. Trans., 24A*, 819, 1993.

Aharonov, E., J.A. Whitehead, P.B. Kelemen, and M. Spiegelman, Channeling instability of upwelling melt in the mantle, *J. Geophys. Res., 100*, 20,433-20,450, 1995.

Bai, Q., S.J. Mackwell, and D.L. Kohlstedt, High-temperature creep of olivine single crystals; 1, Mechanical results for buffered samples, *J. Geophys. Res., 96* (2), 2441-2463, 1991.

Ben-Ismail, W., and D. Mainprice, An olivine fabric database: An overview of upper mantle fabrics and seismic anisotropy, *Tectonophysics, 196*, 145-158, 1998.

Boudier, F., G. Ceuleneer, and A. Nicolas, Shear zones, thrusts and related magmatism in the Oman ophiolite: Initiation of thrusting on an oceanic ridge, *Tectonophysics, 151*, 275-296, 1988.

Boudier, F., and R.G. Coleman, Cross section through the peridotite in the Samail ophiolite, southeastern Oman mountains, *J. Geophys. Res., 86*, 2573-2592, 1981.

Boudier, F., and A. Nicolas, Nature of the Moho transition zone in the Oman ophiolite, *J. Petrol., 36*, 777-796, 1995.

Braun, M.G., G. Hirth, and E.M. Parmentier, The effects of deep damp melting on mantle flow and melt generation beneath mid-ocean ridges, *Earth Planet. Sci. Lett., 176*, 339-356, 2000.

Braun, M.G., and P.B. Kelemen, Dunite distribution in the Oman Ophiolite; implications for melt flux through porous dunite conduits, *Geochem., Geophys., Geosyst. 3* (11), 21, 2002.

Bystricky, M., K. Kunze, L. Burlini, and J.-P. Burg, High shear strain of olivine aggregates: Rheological and seismic consequences, *Science, 290*, 1564-1567, 2000.

Carmichael, I.S.E., and M.S. Ghiorso, Oxidation-reduction relations in basic magma: a case for homogeneous equilibria, *Earth Planet. Sci. Lett., 78*, 200-210, 1986.

Carter, N.L., and H.G. Avé Lallemant, High temperature flow of dunite and peridotite, *Geol. Soc. Am. Bul., 81*, 2181-2202, 1970.

Ceuleneer, G., A. Nicolas, and F. Boudier, Mantle flow patterns at an oceanic spreading centre: The Oman peridotites record, *Tectonophys., 151*, 1-26, 1988.

Ceuleneer, G., and M. Rabinowicz, Mantle flow and melt migration beneath oceanic ridges: Models derived from observations in ophiolites, *Mantle Flow and Melt Generation at Mid-Ocean Ridges, Geophysical Monograph, 71*, 123-154, 1992.

Choblet, G., and E.M. Parmentier, Mantle upwelling and melting beneath slow spreading centers; effects of variable rheology and melt productivity, *Earth Planet. Sci. Lett., 184* (3-4), 589-604, 2001.

Daines, M.J., and D.L. Kohlstedt, Transition from porous to channelized flow due to melt/rock reaction during melt migration, *Geophys. Res. Lett., 21*, 145-148, 1994.

De Bresser, J., J. Ter Heege, and C. Spiers, Grain size reduction by dynamic recrystallization: Can it result in major rheological weakening?, *Int. J. Earth Sci., 90* (1), 28-45, 2001.

Dick, H.J.B., Partial melting in the Josephine Peridotite; I, The effect on mineral composition and its consequence for geobarometry and geothermometry, *Am. J. Sci.*, *277* (7), 801-832, 1977.

Dijkstra, A.H., M.R. Drury, and R.M. Frijhoff, Microstructures and lattice fabrics in the Hilti mantle section (Oman Ophiolite): Evidence for shear localization in the crust-mantle transition zone?, *J. Geophys. Res.*, *107* (11), 2002.

Durham, W.B., and C. Goetze, Plastic flow of oriented single crystals of olivine, 1, Mechanical data, *J. Geophys. Res.*, *82*, 5737-5753, 1977.

Evans, B., R.S. Hays, and N. Shimizu, Diffusion induced grain-boundary migration migration in calcite, *Geology*, *14*, 60-63, 1986.

Evans, B., J. Renner, and G. Hirth, A few remarks on the kinetics of static grain growth in rocks, *Int. J. Earth Sci. (Geol. Rundshc.)*, *90*, 88-103, 2001.

Fliervoet, T.F., M.R. Drury, and P.N. Chopra, Crystallographic preferred orientations and microstructures in some olivine rocks deformed by diffusion or dislocation creep, *Tectonophysics*, *303*, 1-27, 1999.

Frost, H.J., and M.F. Ashby, *Deformation-Mechanism Maps: The plasticity and creep of metals and ceramics*, 168 pp., Pergamon, Oxford, 1982.

Gaherty, J.B., T.H. Jordan, and L.S. Gee, Seismic structure of the upper mantle in a Central Pacific corridor., *J. Geophys. Res.*, *101*, 22291-22309, 1996.

Glennie, K.W., M.G.A. Boeuf, M.W. Hughes Clarke, M. Moody-Stuart, W.F.H. Pilaar, and B.M. Reinhardt, *Geology of the Oman mountains*, 423 pp., 1974.

Hess, H., H., Seismic anisotropy of the uppermost mantle under oceans, *Nature*, *203*, 629-631, 1964.

Hirth, G., and D. Kohlstedt, L., Rheology of the upper mantle and the mantle wedge: a view from the experimentalists, in *The Subduction Factory*, edited by J.M. Eiler, 2003.

Hirth, G., and D.L. Kohlstedt, Experimental constraints on the dynamics of the partially molten upper mantle 2. Deformation in the dislocation creep regime, *J. Geophys. Res.*, *100*, 15,441-15,449, 1995.

Ji, S., Z. Wang, and R. Wirth, Bulk flow strength of forsterite-enstatite composites as a function of forsterite content, *Tectonophysics*, *341* (1-4), 69-93, 2001.

Jousselin, D., and D. Mainprice, Melt topology and seismic anisotropy in mantle peridotites of the Oman ophiolite, *Earth Planet. Sci. Lett.*, *164*, 553-568, 1998.

Jousselin, D., A. Nicolas, and F. Boudier, Detailed mapping of a mantle diapir below a paleo-spreading center in the Oman Ophiolite, *J. Geophys. Res.*, *103* (8), 18,153-18,170, 1998.

Kameyama, M., D.A. Yuen, and S.-I. Karato, Thermal-mechanical efects of low-temperature plasticity (the Peierls mechanism) on the deformation of a viscoelastic shear zone, *Earth Planet. Sci. Lett.*, *168*, 159-172, 1999.

Karato, S.-I., Grain growth kinetics in olivine aggregates, *Tectonophysics*, *168*, 255-273, 1989.

Karato, S.-I., M.S. Paterson, and J.D. FitzGerald, Rheology of synthetic olivine aggregates: Influence of grain size and water, *J. Geophys. Res.*, *91*, 8151-8176, 1986.

Karato, S.-I., M. Toriumi, and T. Fjuii, Dynamic recrystallization of olivine single crystals during high-temperature creep, *Geophys. Res. Lett.*, *7*, 649-652, 1980.

Kelemen, P.B., Reaction between ultramafic rock and fractionating basaltic magma. I. Phase relations, the origin of calc-alkaline magma series, and the formation of discordant dunite, *J. Petrol.*, *31*, 51-98, 1990.

Kelemen, P.B., M. Braun, and G. Hirth, Spatial distribution of melt conduits in the mantle beneath oceanic spreading ridges; observations from the Ingalls and Oman ophiolites, *Geochem., Geophys., Geosyst.*, *1*, 21 (DOI:1999GC000012), 2000a.

Kelemen, P.B., M.G. Braun, and G. Hirth, Spatial distribution of melt migration features in the upper mantle, and implications for melt transport and crustal accretion processes, in *Second RIDGE workshop on mantle flow and melt generation beneath mid-ocean ridges: Constraints from MELT and other observations*, Brown University, Providence, RI, 2000b.

Kelemen, P.B., and H.J.B. Dick, Focused melt flow and localized deformation in the upper mantle: Juxtaposition of replacive dunite and ductile shear zones in the Josephine peridotite, SW Oregon, *J. Geophys. Res.*, *100*, 423-438, 1995.

Kelemen, P.B., G. Hirth, N. Shimizu, M. Spiegelman, and H.J.B. Dick, A review of melt migration processes in the adiabatically upwelling mantle beneath spreading ridges, *Phil. Trans. Roy. Soc., Lond. A*, *355*, 283-318, 1997.

Kohlstedt, D.L., and M.E. Zimmerman, Rheology of partially molten mantle rocks, *Ann. Rev. Earth Planet. Sci.*, *24*, 41-62, 1996.

Lawlis, J.D., High temperature creep of synthetic olivine-enstatite aggregates, PhD thesis, Penn State University, University Park, PA, 1998.

Lee, K.-H., Z. Jiang, and S.-I. Karato, A scanning electron microscope study of the effects of dynamic recrystallization on lattice preferred orientation, *Tectonophysics*, *351*, 331-341, 2002.

Lin, J., and J. Phipps Morgan, The spreading rate dependence of three-dimensional mid-ocean ridge gravity structure, *Geophys. Res. Lett.*, *19*, 13-16, 1992.

Lippard, S.J., A.W. Shelton, and I.G. Gass, *The ophiolite of Northern Oman*, 178 pp., Blackwell, Oxford, 1986.

Mackwell, S.J., High-Temperature rheology of enstatite: Implications for creep in the mantle, *Geophys. Res. Lett.*, *18*, 2027-2031, 1991.

Mainprice, D., and P.G. Silver, Interpretation of SKS-waves using samples from the subcontinental lithosphere, *Phys. Earth Planet. Inter.*, *78*, 257-280, 1993.

McDonnell, R.D., C.J. Peach, H.L.M.v. Roermund, and C.J. Spiers, Effect of varying enstatite content on the deformation behavior of fine-grained synthetic peridotite under wet conditions, *J. Geophys. Res.*, *105*, 13535-13553, 2000.

Nicholas, A., *Structures of ophiolites and dynamics of oceanic lithosphere*, 367 pp., Kluwer Academic Press, Boston, 1989.

Nicolas, A., Structure and petrology of peridotites: Clues to geodynamic environment, *Rev. Geophys.*, *24*, 875-895, 1986.

Nicolas, A., F. Boudier, and J.-L. Bouchez, Interpretation of peridotite structures from ophiolitic and oceanic environments, *Am. J. Sci.*, *280-A*, 192-210, 1980.

Nicolas, A., F. Boudier, and A.M. Boullier, Mechanisms of flow in naturally and experimentally deformed peridotites, *Am. J. Sci., 273*, 853-876, 1973.

Nicolas, A., F. Boudier, B. Ildefonse, and E. Ball, Accretion of Oman and United Arab Emirates ophiolite - Discussion of a new structural map, *Marine Geophys. Res., 21*, 147-179, 2000.

Nicolas, A., and N.I. Christensen, Formation of anisotropy in upper mantle peridotites - A review, in *Composition, structure and dynamics of the lithosphere-asthenosphere system*, edited by K. Fuchs, and C. Froidevaux, pp. 111-123, American Geophysical Union, Washington, D.C., 1987.

Nicolas, A., and J.-P. Poirier, *Crystalline plasticity and solid state flow in metamorphic rocks*, 444 pp., John Wiley & Sons, New York, 1976.

Skrotzki, W., Defect structure and deformation mechanisms in naturally deformed augite and enstatite, *Tectonophysics, 229*, 43-68, 1994.

Spiegelman, M., P.B. Kelemen, and E. Aharonov, Causes and consequences of flow organization during melt transport: The reaction infiltration instability, *J. Geohys. Res., 106*, 2061-2078, 2001.

Tommasi, A., D. Mainprice, G. Canova, and Y. Chastel, Viscoplastic self-consistent and equilibrium-based modeling of olivine preferred orientations, *J. Geophys. Res., 105*, 7893-7908, 2000.

Van der Wal, D., P. Chopra, M. Drury, and J. Fitz Gerald, Relationships between dynamically recrystallized grain size and deformation conditions in experimentally deformed olivine rocks, *Geophys. Res. Lett., 20* (14), 1479-1482, 1993.

Von Bargen, N., and H.S. Waff, Permeabilities, interfacial areas and curvatures of partially molten systems: results of numerical computations of equilibrium microstructures, *J. Geophys. Res., 91*, 9261-9276, 1986.

Wenk, H.-R., and C.N. Tomé, Modeling dynamic recrystallization of olivine aggregates deformed in simple shear, *J. Geophys. Res, 104*, 25513-25527, 1999.

Woodcock, N.H., and M.A. Naylor, Randomness testing in three-dimensional orientation data, *J. Struct. Geol., 5* (5), 539-548, 1983.

Zhang, S., and S.-I. Karato, Lattice preferred orientation of olivine aggregates deformed in simple shear, *Nature, 375*, 774-777, 1995.

Zhang, S., S.-I. Karato, J. FitzGerald, U.H. Faul, and Y. Zhou, Simple shear deformation of olivine aggregates, *Tectonophysics, 316*, 133-152, 2000.

Chapter 5

THE EFFECTS OF DEEP DAMP MELTING ON MANTLE FLOW AND MELT GENERATION BENEATH MID-OCEAN RIDGES

Reprinted from *Earth and Planetary Science Letters*, Vol. 176, M.G. Braun, G. Hirth, and E.M. Parmentier, "The effects of deep damp melting on mantle flow and melt generation beneath mid-ocean ridges", 339-356 (2000), with permission from Elsevier.

Abstract

We explore the implications of experimental constraints on mantle rheology and the thermodynamics of melting for mantle flow and melt generation beneath a mid-ocean ridge. Numerical models are used to investigate the effects of 1) rheologies affected by dehydration during melting, the presence of melt, and a transition in creep mechanism to grain boundary sliding, and 2) variations in the rate of melt production. Water in the mantle deepens the peridotite solidus, producing a region of damp melting between approximately 70 and 120 km depth. Extraction of water during melting can increase mantle viscosity by as much as two orders of magnitude. At the same time, the presence of melt can decrease the mantle viscosity. A decrease in recrystallized grain size due to the presence of melt can promote a transition in the dominant deformation mechanism to grain boundary sliding limited by creep on the easiest slip system for olivine, resulting in an additional order of magnitude decrease in viscosity. The increase in viscosity associated with dehydration significantly inhibits buoyant mantle flow in the dry melting region. However, buoyantly driven flow is predicted in the damp melting region if the viscosity in this depth interval is on the order of 10^{18} Pa s; a viscosity this low can be achieved if a transition to grain boundary sliding occurs after the onset of damp melting. Previous models suggest that crustal thickness variation with spreading rate is a consequence of conductive cooling at the top of the melting region. If melt productivity is higher, so that more melt is produced at greater depth, then the influence of spreading rate on crustal thickness is reduced even in the absence of buoyant upwelling. Rheology has a significant effect on the size and shape of the melting region and the strain distribution beneath the ridge at a given spreading rate. For example, buoyant upwelling in the damp melting region localizes melt production and induces a region of strong elongation in finite strain ellipses between 50 -120 km, offering an explanation for the apparent difference in seismic anisotropy inferred from body and surface waves in the MELT experiment. The models indicate that the magnitude of the effects of buoyant flow in the damp melting region become increasingly prominent at slower spreading ridges. If lattice-preferred orientations produced by deep buoyant flow are incorporated into the lithosphere as it thickens by conductive cooling, then anisotropy in old lithosphere may be greater for lithosphere created at slower spreading rates.

Introduction

In this study, we use numerical models to explore the implications of experimental constraints on mantle rheology and the thermodynamics of melting on mantle flow beneath spreading centers. In particular, we investigate the rheological effects of changes in viscosity associated with the extraction of water during melting, the presence of an interstitial melt phase, and possible changes in deformation mechanism. In addition, we examine the significance of variable melt production rates on the amount of melt produced. The results of these models are used to discuss how data on crustal thickness, seismic velocity and anisotropy, and geochemistry can be used to constrain the rheology and melting of upwelling mantle.

Water is present in the earth's mantle [*Bell and Rossman*, 1992; *Kohlstedt et al.*, 1996] in sufficient quantities to affect the rate and depth of melting during adiabatic decompression. A first order effect of water on melting is depression of the peridotite solidus. The water content of the oceanic mantle is sufficient to promote a region of 'damp melting' beneath spreading ridges at depths between ~70-120 km, followed by anhydrous melting above ~70 km [*Hirth and Kohlstedt*, 1996]. Therefore the size of the melting region is expanded relative to that expected for anhydrous mantle.

The interval of damp melting can also affect melt production rates. Thermodynamic models indicate that the rate of isentropic melting of peridotite is initially slow but increases rapidly, to as much as 2-3%/kb, after incompatible components are extracted [*Asimow et al.*, 1997]. This productivity estimate is similar to rates calculated from inversions of geochemical data on mid-ocean ridge basalt (MORB) [*McKenzie and O'Nions*, 1991] and significantly greater than the average productivity previously estimated from thermodynamic calculations [*McKenzie and Bickle*, 1988; *Turcotte and Ahern*, 1978]. Because melting is initially buffered by a limited amount of water, the productivity during damp melting is low [*Hirth and Kohlstedt*, 1996]. Melting in the damp region also results in extraction of other incompatible components. This scenario may lead to greater melt production rates deeper in the melting column than under anhydrous conditions. Increasing the magnitude of melt productivity also increases the depth of phase exhaustion (e.g. clinopyroxene out) [*Dick and Fisher*, 1984], which has potentially important implications for the influence of thermal conduction, and subsequent truncation of the top of the melting region, on the variation of crustal thickness with spreading rate.

In addition to changing the melting behavior, the presence of water significantly reduces the viscosity of olivine aggregates. Because water is an incompatible component

during melting, the extraction of water from olivine, due to the presence of melt, can result in an increase in mantle viscosity [*Karato*, 1986]. Petrologic constraints on the water content of the MORB source region, in conjunction with experimental data on the effect of water on viscosity and the solubility of water in peridotite and MORB, indicate that the extraction of water during melting beneath mid-ocean ridges results in an increase in viscosity by a factor of ~100 [*Hirth and Kohlstedt*, 1996]. These effects have been suggested to promote the creation of a compositional lithosphere at the ridge axis [*Gaherty et al.*, 1999; *Hirth and Kohlstedt*, 1996; *Phipps Morgan*, 1997].

The effective viscosity of partially molten peridotite is also dependent on the retained melt fraction. A moderate decrease in viscosity is observed when small amounts of interstitial melt are present, in both the diffusion creep [*Cooper and Kohlstedt*, 1984; *Hirth and Kohlstedt*, 1995b] and dislocation creep regimes [*Hirth and Kohlstedt*, 1995a; *Kohlstedt and Zimmerman*, 1996]. With melt contents in excess of ~5%, viscosity decreases by more than an order of magnitude.

An additional decrease in viscosity may arise if the onset of melting promotes a decrease in the dynamically recrystallized grain size and a concomitant transition in deformation mechanism. Microstructural observations indicate the presence of melt inhibits grain growth in olivine-basalt aggregates [*Faul*, 1997; *Hirth and Kohlstedt*, 1995a]. Thus, the dynamically recrystallized grain size may decrease with continued deformation after the onset of melting. Extrapolation of experimental flow laws to stresses and strain rates appropriate for the upper mantle indicates the transition from creep at a grain size of 1-10 mm [*Karato et al.*, 1986], similar to the observed range of grain size in natural peridotites [*Mercier*, 1980; *Nicolas and Boudier*, 1995]. Experimental studies indicate that the dominant deformation mechanism at this transition is grain boundary sliding limited by creep on the easiest slip system in olivine [*Hirth and Kohlstedt*, 1995a]. Creep rates observed for this mechanism are approximately an order of magnitude greater than those for dislocation creep at the same stress. Therefore, if grain size reduction is sufficient to promote a transition to the grain boundary sliding process, an additional decrease in viscosity of as much as an order of magnitude may result, even at low melt fractions.

Model Formulation, Parameters, and Analysis

1. Governing Equations

The models in our study are based on solutions of the following set of governing equations:

$$\frac{\partial u_i}{\partial x_i} = -\dot{M} \tag{1}$$

$$\frac{\partial T}{\partial t} = \kappa \nabla^2 T - u_i \frac{\partial T}{\partial x_i} - \frac{\Delta H_{fus}}{c_p} \dot{M} \tag{2}$$

$$-\frac{\partial p}{\partial x_i} + \frac{\partial \tau_{ij}}{\partial x_i} + \rho g_i = 0 \tag{3}$$

$$\frac{\partial F}{\partial t} + u_i \frac{\partial F_i}{\partial x_i} = \dot{M} \tag{4}$$

expressing, respectively, conservation of mass, conservation of energy, mechanical equilibrium for variable viscosity, and advection and production due to melting of mantle depletion (F). In these equations, u_i is the mantle velocity, $\dot{M}$ is the rate of melt production, T is temperature, t is time, κ is the thermal diffusivity, ΔH_{fus} is the latent heat of fusion, c_p is the specific heat at constant pressure, p is pressure, τ_{ij} is the deviatoric stress tensor defined as

$$\tau_{ij} = 2\eta\left(\frac{\partial u_i}{\partial x_j} + \frac{\partial u_j}{\partial x_i}\right), \tag{5}$$

g_i is the acceleration due to gravity, and η is the viscosity. The density, ρ, is a function of temperature, composition (i.e. depletion), and retained melt fraction ϕ:

$$\rho = \rho_0(1 - \alpha T - \gamma F) - \Delta\rho\phi, \tag{6}$$

where ρ_0 is the reference density of the mantle, α is the coefficient of thermal expansion, γ is a ratio that accounts for the change in density of the residue owing to preferential extraction of Fe versus Mg during melting [*Oxburgh and Parmentier*, 1977], and $\Delta\rho$ is the density difference between the solid and melt.

2. Model Configuration

Steady state solutions are obtained numerically using a hybrid finite element-finite difference formulation. The equations for buoyant viscous flow are solved using a standard penalty function method with linear rectangular elements. The equations for energy conservation and melt depletion are solved with second order finite difference approximations [*Barnouin-Jha*, 1996]. Advection of scalar variables (e.g., temperature, depletion) is accomplished using an upwind-differencing method with high order

corrections to reduce artificial diffusion [*Smolarkiewicz*, 1983]. Steady state solutions are calculated on a 41x81 node mesh with non-uniform, rectangular elements within a vertical plane beneath a spreading center perpendicular to the axis. Node spacing decreases toward the ridge axis from both depth and off-axis providing resolution of better than 2 km near the ridge axis in a domain 300 km by 300 km. Continuity of velocity is imposed between the mantle and the crust above, such that material at the top of the domain is moving only horizontally at the prescribed spreading rate. Material entering the base of the domain is assumed to be flowing only vertically, without resistance from the deeper mantle. Symmetry is assumed along the vertical boundary beneath the axis, and the off-axis velocity boundary conditions are defined by an analytical, passive-flow solution.

The temperature of incoming material at the bottom is determined by a prescribed potential temperature (1350°C) and a adiabatic gradient (0.3°C/km). The temperature along the top boundary is set to 0°C. The temperature distribution is controlled by the competing effects of conductive heat loss from above and advective heat transport from below.

3. Melting and Rheology

Melting occurs when the temperature of the adiabatically upwelling solid exceeds the solidus temperature at a given pressure. The amount of melt generated for a given amount of adiabatic decompression is given by

$$F = F_{damp}\left(\frac{T - T_{damp}}{T_{dry} - T_{damp}}\right), \tag{7}$$

in the damp melting region, and by

$$F = \left(\frac{\partial F}{\partial T}\right)_p \left(T - T_{dry}\right) + F_{damp} \tag{8}$$

in the dry melting region. The amount of melt generated in the dry melting region is adjusted through use of the isobaric melt productivity,$(\partial F/\partial T)_p$. The total melt fraction produced in the damp region (F_{damp}) is set to 0.01, based on the analysis of the effect of water on melting beneath

spreading centers [*Hirth and Kohlstedt*, 1996]. The damp and dry solidi, respectively, are defined as

$$T_{damp} = 900°C + \left(\rho_m g Z_m + \rho_c g Z_c\right)\left(\frac{dT}{dP}\right)_{damp} \tag{9}$$

$$T_{dry} = 1100°C + \left(\rho_m g Z_m + \rho_c g Z_c\right)\left(\frac{dT}{dP}\right)_{dry} \tag{10}$$

where Z_m is the depth beneath the crust-mantle boundary, and ρ_m is the density of the mantle. The solidi account for the thickness (Z_c) and the density (ρ_c) of the crust.

The rate of melt production expressed as a function of depth is,

$$\dot{M} = u_z \frac{dF}{dz}, \tag{11}$$

where u_z is the solid upwelling rate and dF/dz is the amount of melt produced per unit depth over which decompression occurs.

One-dimensional melting models for adiabatic upwelling of dry and damp mantle are illustrated in Figure 1. The total depletion in both models is limited to 18%; this value is assumed to be the amount of melt produced prior to the exhaustion of clinopyroxene. With this constraint and a constant productivity of 1%/kbar, melting of an anhydrous mantle extends from the intersection of the adiabat with the dry solidus (~70 km) to within 5-10 km of the crust-mantle boundary (Figure 1a). In contrast, melting influenced by the presence of water initially proceeds slowly (~0.1%/kb) above the damp solidus (~120 km) and continues at a higher productivity (2%/kbar) above the dry solidus (Figure 1b). With the higher melt productivity in this model, phase exhaustion due to adiabatic decompression occurs ~30 km below the crust-mantle boundary.

We assume that melt migrates vertically through the permeable shallow mantle according to Darcy's law, and that the rate of melt extraction balances the production of melt [*Jha et al.*, 1994], thus

$$\frac{K\Delta\rho g}{\eta} = \int_z \dot{M} dz \tag{12}$$

where K is the permeability, defined as

$$K = \frac{d^2 \bar{\phi}^n}{C}. \tag{13}$$

The characteristic spacing of melt tubules, d, is assumed to be on the order of the grain size, $\bar{\phi}$ is the mean melt fraction, n=2, and C, is a geometrical constant indicative of a melt topology distributed along the edges of tetrakaidekahedral grains [*Cheadle*, 1993; *Von Bargen and Waff*, 1986]. The permeability in the passive flow model, K, is approximately $3\text{x}10^{-13}\text{m}^2$ for a melt fraction of 0.03. Assuming a permeability model based on melt

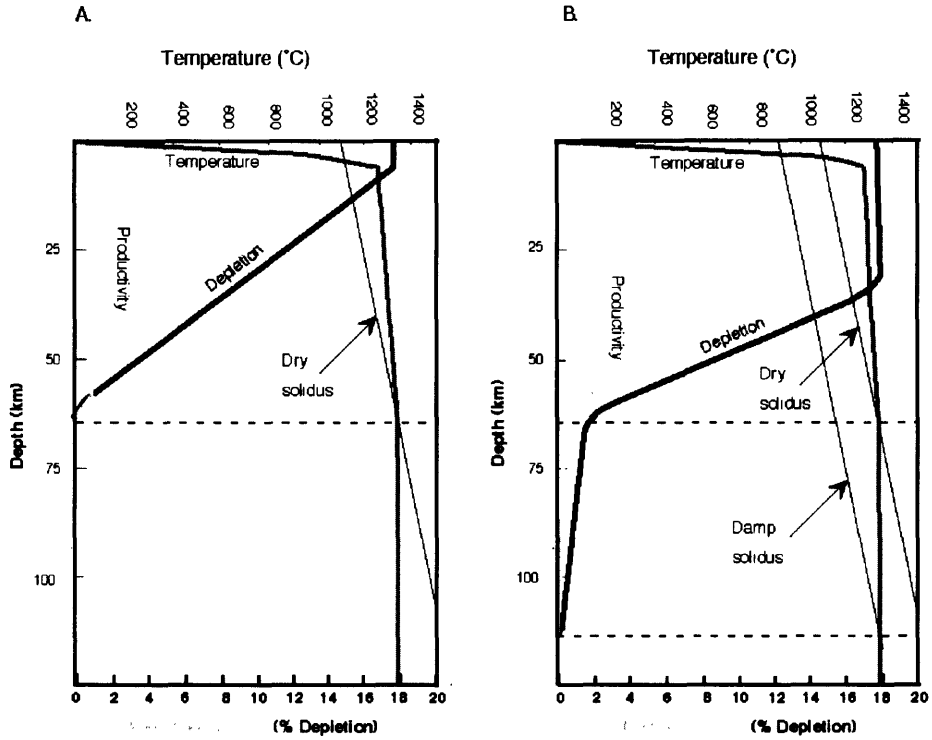

Figure 1. Schematic melt production and mantle depletion profiles beneath a ridge axis for (a) melting only above the dry solidus at a productivity of 1%/kb and (b) melting that includes the effects of water and increased productivity (2%/kb) above the dry solidus; melt productivity in the damp melting region is 0.1%/kb. In each figure, the melt productivity, mantle depletion, and temperature are shown as a function of depth. The dashed lines indicate depths where the mantle adiabat crosses the damp and dry solidi. The region of melt generation is deeper with increased productivity.

topology with isotropic surface energies and a single phase, this permeability is consistent with a grain size of approximately 2 mm [*Von Bargen and Waff*, 1986], which is in the range estimated for the mantle. The actual permeability could be lower than we have used owing to the effects of second phases [*Toramaru and Fujii*, 1986] and anisotropic wetting [*Faul*, 1997]. The effective permeability could also be larger if the grain size were larger or melt were efficiently segregated into high porosity channels [*Kelemen et al.*, 1997].

The mantle viscosity is parameterized as a function of temperature,T, pressure, P, melt fraction, ϕ, and water content,Ω, using the relationship:

$$\eta = A\exp\left(\frac{Q+PV}{RT}\right) * \exp(-a\phi) * \Omega \quad , \qquad (14)$$

The temperature and pressure dependence of viscosity are controlled by the activation energy (Q=265 kJ/mol) and activation volume (V=5x10^{-6} m^3/mol). The activation terms are reduced by a factor of two relative to experimental values as a linear approximation for a non-linear rheology [*Christensen*, 1984]. The pre-exponential term

$$A = \frac{\eta_{ref}}{\exp\left(\frac{Q + V\rho_0 g Z_{xdamp}}{RT_{xdamp}}\right)} \qquad (15)$$

defines a reference condition, where η_{ref} is the viscosity of the mantle as it crosses the solidus, Z_{xdamp} is the depth at which the adiabat crosses the damp solidus, T_{xdamp} is the absolute temperature at Z_{xdamp}, and R is the ideal gas constant.

Following [*Kelemen et al.*, 1997], the effect of melt fraction on viscosity is described by the relationship:

$$\frac{\eta}{\eta_o} \sim \exp(-a\phi) \qquad (16)$$

where η_o is the viscosity of the material at the same pressure and temperature neglecting the effects of melt, and a is a constant between 30 and 45 based on experimental observations [*Hirth and Kohlstedt*, 1995a; *Kohlstedt and Zimmerman*, 1996]. For a=45, 5% melt results in an order of magnitude decrease in viscosity. This empirical relationship holds for melt percentages up to at least 10%, but may be valid up to some greater, rheologically critical melt percentage above which the aggregate no longer deforms as a solid.

The viscosity increase that results from the extraction of water during melting is parameterized with the variable Ω. Water is extracted from the mantle gradually during damp melting, until the upwelling mantle crosses the dry solidus and productivity subsequently increases. At this point water is extracted more rapidly. In the damp melting regime, Ω increases linearly with F up to a maximum factor of η_{damp}/η_o. After crossing the dry solidus, Ω is set to η_{dry}/η_o, reflecting the increase in viscosity associated with the extraction of the remaining water from the matrix; η_{dry} is the anhydrous mantle viscosity at the reference pressure and temperature. In all models, we set η_{damp}/η_o=10 and η_{dry}/η_o,=100.

Implicit in the hypothesis that grain boundary sliding can be promoted by a decrease in recrystallized grain size after the onset of melting, is that sufficient strain is accumulated to achieve a steady-state grain size. Experimental observations show that following a change in deformation conditions, 5-10% strain is required to develop a new steady state grain size [*Van der Wal*, 1993]. To determine if this strain criterion is met, and therefore

the viscosity decrease is justifiable, we calculate strain accumulation along solid-flow streamlines using a finite difference method based on velocity gradients around each node [*Barnouin-Jha*, 1996; *McKenzie*, 1979]. These calculations indicate that 5% strain is achieved within the damp melting region, even if the reference viscosity is 10^{25} Pa s (a proxy for passive flow). Therefore, in models that explore the influence of grain boundary sliding, we assume that the dynamically recrystallized grain size in the presence of melt is small enough to promote the transition in creep mechanism and that additional strain is accumulated rapidly enough that the steady-state flow law is applicable. Therefore, the viscosity is reduced by an order of magnitude anywhere melt is present.

The finite strain calculation can also be used to determine regions where a lattice preferred orientation of olivine may develop beneath the ridge axis. The development of a lattice preferred orientation in olivine during plastic deformation by dislocation creep has a significant effect on the seismic, and potentially electromagnetic [*Evans et al.*, 1998], properties of ridges observed at the surface. Even when subject to the transitional creep mechanism, deformation is still limited by dislocation motion in the easiest slip system and may result in the development of a significant lattice preferred orientation. For each model, we calculate finite strain accumulation along flow lines, starting from an initially strain-free state at a depth of 200 km.

The cumulative effects of dehydration, melt, and grain boundary sliding on viscosity structure beneath a ridge are schematically illustrated in Figure 2. The influence of temperature and pressure have been omitted for simplicity in plotting. Cooling of the solid due to melting results in a small increase in viscosity (Figure 2a). Without dehydration, the presence of melt decreases the viscosity (Figure 2b). Dehydration alone produces a viscosity profile reflecting the changes in water content during damp and dry melting (Figure 2c). The viscosity profile that includes both the effects of melt and water demonstrates that the influence of dehydration is significantly greater than the effect of the presence of melt, unless the melt fraction is very large (e.g. >0.1) (Figure 2d). However, the additional effect of a transition in creep mechanism to grain boundary sliding mitigates the influence of dehydration and results in a low viscosity region beneath the dry solidus (Figure 2e).

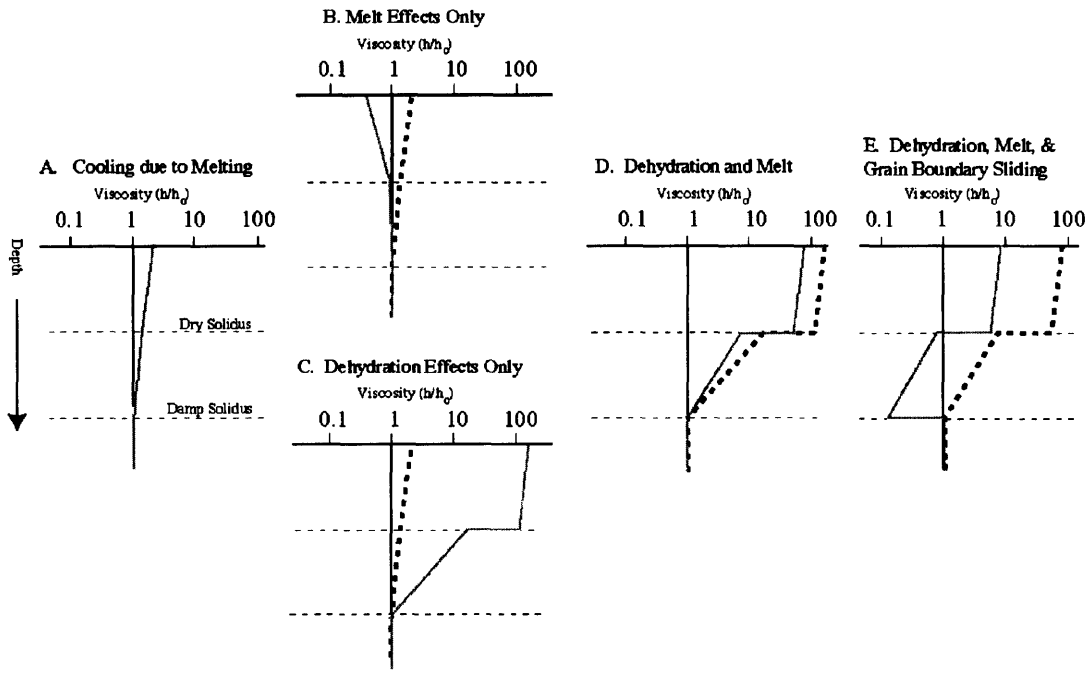

Figure 2. Normalized viscosity versus depth profiles show the effects of melting on the viscosity of an initially damp mantle. (a) Viscosity increase due to cooling during decompression melting. (b) Viscosity decrease due to the presence of melt (with maximum melt content of ~3%); the profile in (a) is shown as a dashed line. (c) Viscosity increase due to the effects of dehydration; the profile from (a) is shown as a dashed line. (d) The solid line shows the combined effects of melt and dehydration relative to the profile that includes only the effects of dehydration (dashed line). (e) Composite viscosity profile (solid line) that includes a change in deformation mechanism from dislocation creep to grain-boundary sliding, as well as the effects of melt and dehydration, resulting in a low viscosity region beneath the dry solidus; the dashed line is the profile shown in (d). In each plot, the depths of the damp and dry solidi are shown by horizontal dotted lines.

4. Crustal Production

For each model we calculate the crustal thickness, mean melt fraction, mean pressure of melting, and mean degree of melting. The crustal thickness is calculated by dividing the volume rate of melt generation by the spreading rate. The mean pressure ($\overline{P}$) and degree ($\overline{F}$) of melting are defined as

$$\overline{P} = \rho_m g \left(\frac{\int_a z \dot{M} da}{\int_a \dot{M} da} \right) + \rho_c g Z_c \qquad (17)$$

$$\overline{F} = \frac{\int_a F\dot{M} da}{\int_a \dot{M} da} \tag{18}$$

where a is the area of the melting region [*Forsyth*, 1993; *Langmuir et al.*, 1992].

5. Quantification of Buoyant Flow

We evaluate the magnitude of buoyant flow by comparing the upwelling velocities determined from the models to those determined for a passive flow solution at the same spreading rate by the relationship

$$\beta_z = \frac{1}{L}\int_L \frac{w_{model}}{w_{passive}} dz \tag{19}$$

where L is the height of the melting region, and w is the vertical component of velocity beneath the axis. This buoyancy index, β_z, becomes large for highly focused flow and approaches unity for passive-like flow. For these calculations, $w_{passive}$ is taken from the results of a model with a reference viscosity of 10^{25} Pa s and for which no effects of melt or dehydration were included.

Results

Steady state solutions for numerical models illustrating the progressive superposition of rheological effects shown in Figure 2 are presented in Figures 3, 4, and 5. Data for these models (e.g., mean melt fraction, crustal thickness) are summarized in Table 1 and in Figures 6a-d.

1. Passive Solution

To assess the component of buoyancy driven flow in each model solution, we first calculate the solution for a system with a high reference viscosity (η_{ref}=10^{25} Pa s) to use as a proxy for passive flow (Figure 3a). The resulting solid flow streamlines closely resemble the analytical solution for corner flow with constant viscosity [*Reid and Jackson*, 1981]. In addition, the melting region has a roughly triangular shape that extends ~110 km deep and ~225 km off axis. This result becomes our non-buoyant solution ($\beta_z \equiv 1$) to which we compare other velocity fields.

2. Base Rheology

The solution for the 'base' model, upon which we build the more realistic rheologies, is illustrated in Figure 3b. The reference viscosity for this model is $5x10^{18}$ Pa s, and the melting function is illustrated in Figure 1b. Compared to the passive model, the crust is thicker because buoyancy driven flow results in greater upwelling rates in the melting region and thus more material is melted. Buoyant localization of melting also limits the extent of melting off-axis to 100 km. Focusing of solid flow toward the ridge axis induces vertically oriented finite strain ellipse elongation directions under the ridge axis, similar to previous results [*Blackman et al.*, 1996]. The largest finite strains are produced in material that passes through the outer edge of the damp melting region. This flow results in region of very high strain between depths of 80 and 150 km off axis.

3. Melt-Only

The 'melt-only' rheology builds upon the base rheology with the added effect of a viscosity reduction due to the presence of melt. (Figure 3c) The decrease in mantle viscosity due to the presence of melt, in conjunction with the density contrast between the melt and mantle, enhances the upwelling velocity, inducing more focused solid flow (β_z=2.44 compared to 1.51 for the base rheology) and stronger vertical elongations of finite strain ellipses in the shallow melting region. The increased solid flux leads to higher melt fractions which further decreases the viscosity. This positive feedback leads to increased crustal production (Table 1) and higher melt fractions concentrated in a smaller, shallower melting region, relative to the base rheology. The buoyant feedback can be discerned in the depression of the isodepletion contours outside the melting region and more shallowly focused flow streamlines delineated by the finite strain ellipses shown in Figure 3c. If the permeability were higher, the effects of buoyant flow would be diminished. For example, with an order of magnitude increase in permeability for the model with the rheology shown in figure 3c, the buoyancy is significantly diminished (β_z=1.48).

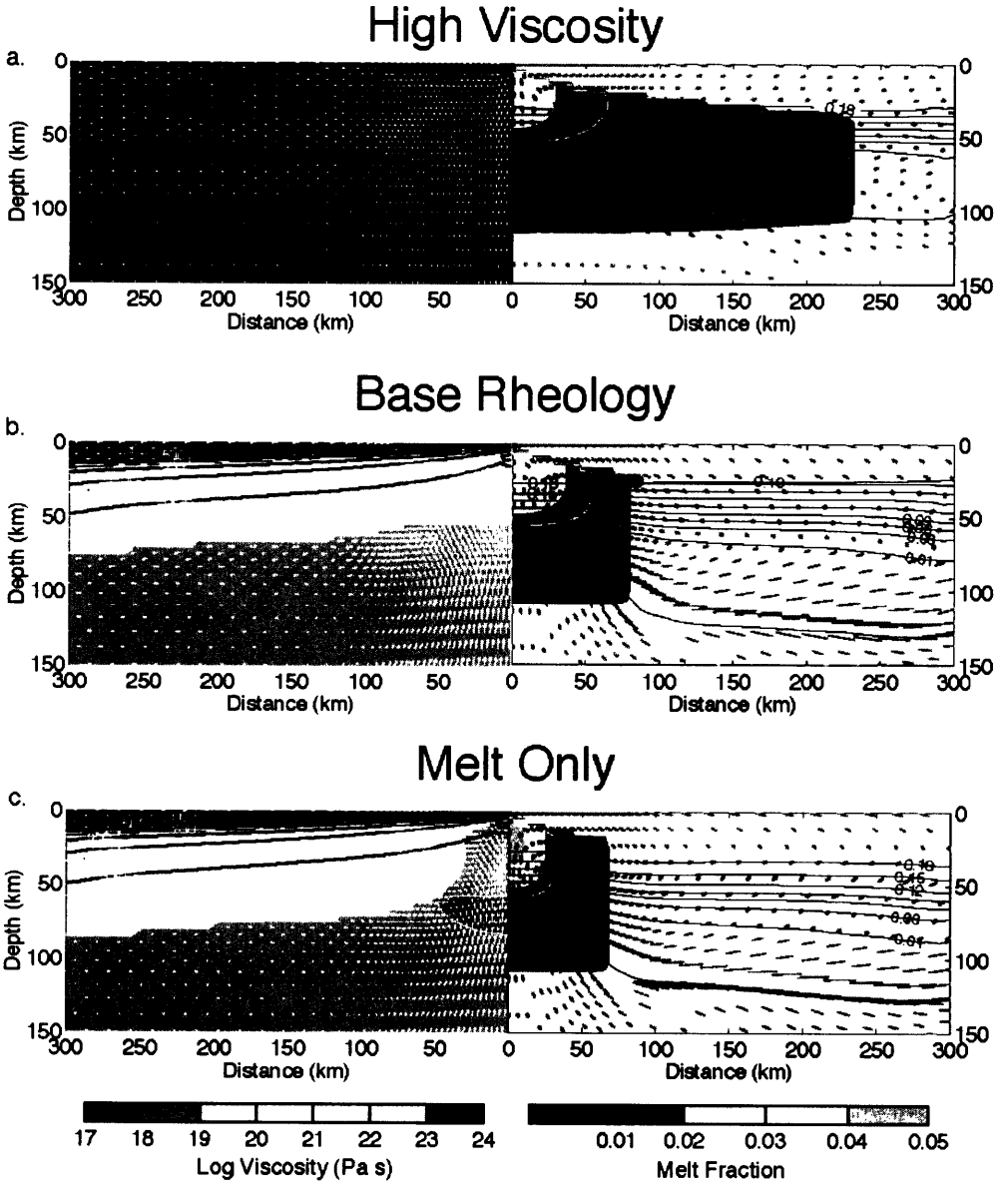

Figure 3. Model results for temperature- and pressure-dependent viscosity, including damp melting and increased melt productivity (2%/kb). The half spreading rate in each case is 50 mm/yr. Filled contours in the left panels represent the mantle viscosity, and black lines depict isotherms (200°C intervals) for a potential temperature of 1350° and an adiabatic gradient of 0.3°C/km. Solid flow streamlines, as depicted by the finite strain ellipses (red ovals), are determined by the calculated velocity field (white vectors). Velocity vector length is equal to the half-spreading rate along the top boundary. Filled contours on the right panel show the steady-state melt fraction (> 0.1%) overlain by isodepletion contours (black lines). (a) Model for a system with a reference viscosity of 10^{25} Pa s used as a proxy for passive flow. (b) Model with a

reference viscosity of $5x10^{18}$ Pa s used as a basis of comparison for models which include other rheologic effects. (c) Model including the effects of viscosity reduction due to the presence of melt. The feedback between melt generation and viscosity reduction produces a region of focused flow that extends from depths of 10 to 150 km beneath the axis and a diagnostic pattern of strain accumulation.

4. Dehydration-Only

Focused upwelling in the melting region is strongly inhibited by the increase in viscosity due to the extraction of water. The resulting passive-like flow (β_z=1.05) is characterized by horizontally stratified viscosity and depletion structures throughout the melting region. Calculated finite strain ellipses are similar to those of the passive solution (Figure 3a). The amount of melt generated, and therefore crustal thickness, is reduced because the increased viscosity reduces the solid flux through the melting region. In addition, the lack of focusing permits melting to take place further off axis, since still-fertile material continues to advect upward. The reduced melt fractions averaged over the larger melting region result in a lower mean melt fraction relative to the base model.

5. Dehydration and Melt

When the rheological effects of dehydration and melt are combined (Figure 4a), the viscosity increase due to dehydration dominates the decrease due to the presence of melt, creating a passive-like flow pattern. The viscosity structure in the melting region mirrors the primary melting zone, as in the melt-only model; however, the viscosities above the dry solidus are two orders of magnitude higher, inhibiting buoyant flow. As a result of the higher viscosity, the mean melt fraction decreases and the melting region widens to ~170 km off-axis, similar to the passive model. Because of the smaller melt fraction and higher viscosity, the effects of buoyancy (β_z=1.19) and the overall magnitude of finite strain are diminished. Decreasing the reference viscosity to $2x10^{18}$ Pa s is sufficient to generate very focused upwelling in both the damp and dry melting regimes (Figure 4b). The damp melting region becomes much narrower and the high velocity gradients induce much stronger finite strain than in the higher viscosity counterpart. The deep buoyant flux is also reflected in the larger crustal thickness, higher melt fraction, and lower mean degree of melting.

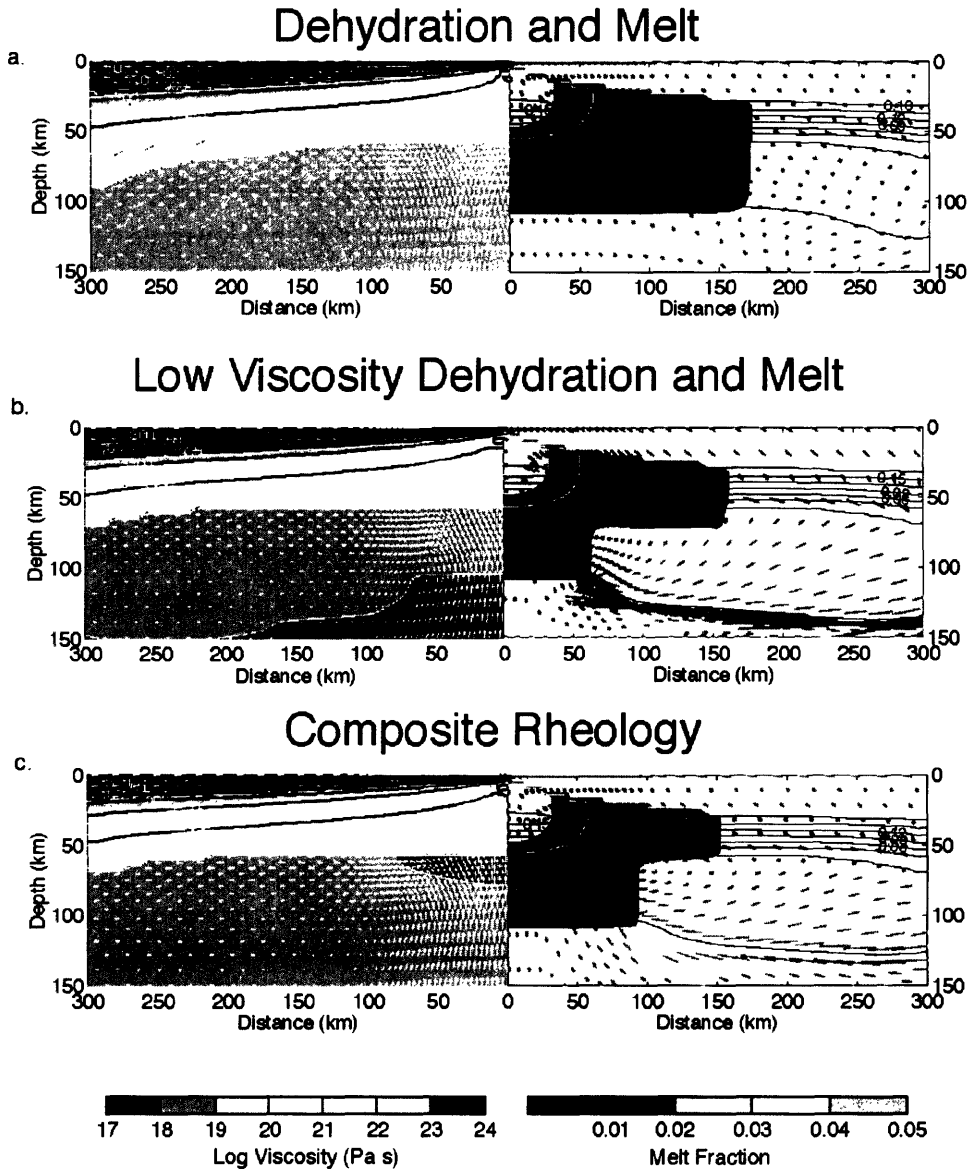

Figure 4. Models including the effects of dehydration beneath the ridge axis. The half spreading rate in each case is 50 mm/yr. The model variables are plotted the same as described in figure 3. (a) Model with a reference viscosity of $5x10^{18}$ Pa s including the effects of dehydration and melt. (b) Model with a reference viscosity of $2x10^{18}$ Pa s including the effects of dehydration and melt. (c) Model with a reference viscosity of $5x10^{18}$ Pa s including the effect of a transition to grain boundary sliding, as well as the effects of dehydration and melt. Since the effects of dehydration dominate those of melt, the viscosity and velocity structures resemble more passive-like flow above the dry solidus. Even with lower reference viscosities, buoyant flow is restricted to depths beneath the dry solidus.

6. Composite Rheology

An additional decrease in viscosity due to a change in creep mechanism from dislocation creep to grain boundary sliding limited by creep on the easiest slip system in olivine allows for focused, buoyancy-driven flow, but only in the damp melting region (Figure 4c). In the damp melting region, the influence of grain boundary sliding dominates over the effect of dehydration (e.g., Figure 2e), resulting in a lower viscosity. The low effective viscosity permits strongly focused flow, narrowing the width of the damp melting region and generating a finite strain pattern similar to the base model.

The velocity field rapidly changes to more passive-like flow as the viscosity increases above the dry solidus. The melt region also broadens as material diverted away from the axis continues to melt due to the small vertical component of flow. Relative to the dehydration and melt model, the mean melt fraction and the mean pressure of melting are slightly higher, and the mean degree of melting and crustal thickness remain approximately the same (Table 1). The difference in β_z between the composite model and the dehydration and melt model is associated with buoyant flow in the damp melting regime (compare Figure 4c to 4a). Thus, because only small amounts of melt are produced in this region, the difference in crustal thickness between these two models is small.

7. Variation with Spreading Rate

There is a strong effect of spreading rate on the flow field determined for the composite rheology (Figure 5). As the spreading rate decreases, the solid flow becomes more focused, and the melt region narrows significantly. The mean degree of melting drops off and the melt production below the dry solidus increases slightly (Figure 6d) at very slow spreading rates. The buoyancy index, β_z, is also greatest at slow spreading rates, with buoyancy increasing significantly at rates below 30 mm/yr (Figure 6c). These results suggest that buoyant localization of melting at slow spreading ridges occurs in the damp melting region. The spreading rate at which the rapid increase in buoyancy occurs coincides with the spreading rate at which the crustal thickness begins to deviate from a relatively constant value.

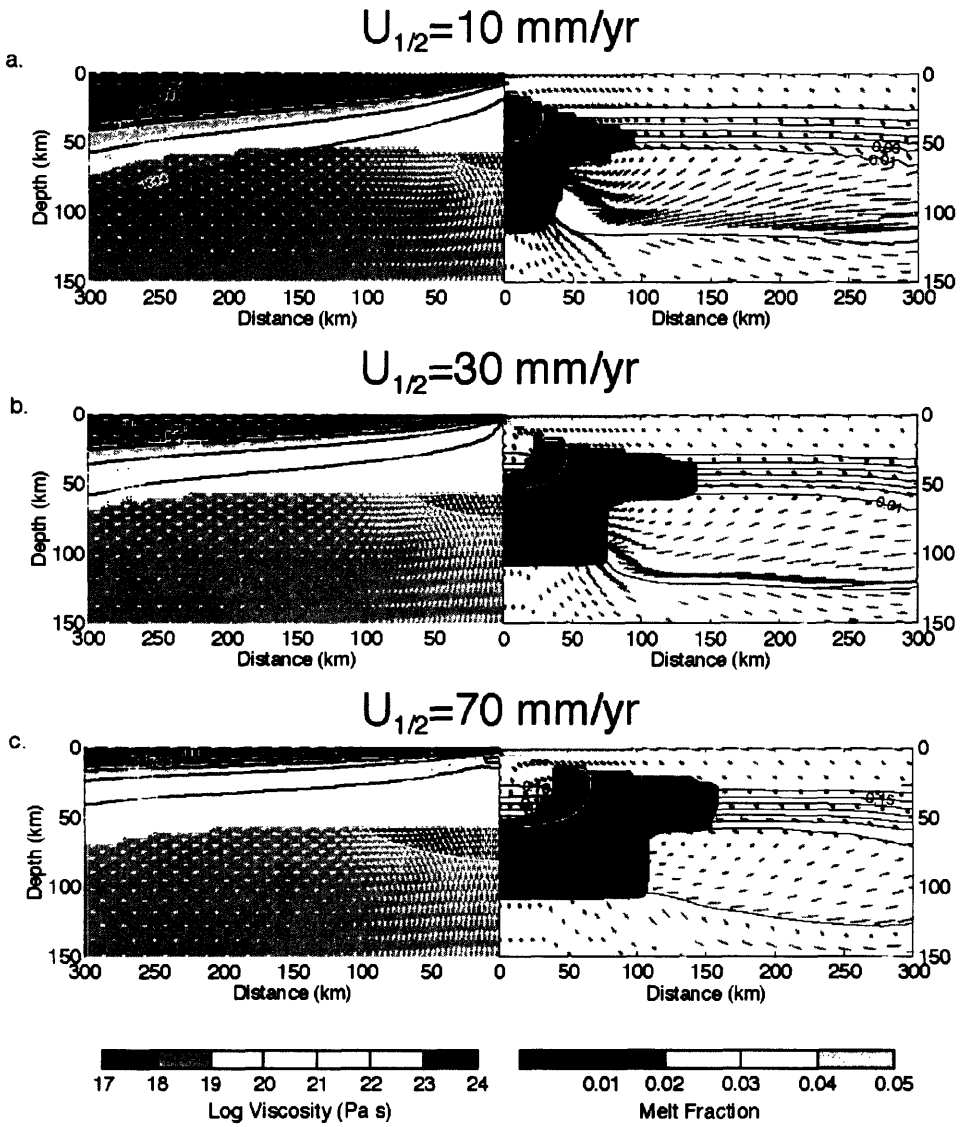

Figure 5. Variation with spreading rate of models with a rheology including the effects of dehydration, melt, and grain boundary sliding (the same rheology as in figure 4c). The model variables are plotted the same as described in figure 3. Buoyant localization of solid flow and melt generation at depth increases as the half spreading rate decreases. The magnitude and localization of strain also increases with decreasing spreading rate.

Discussion

The results of these models provide important insights into the interpretation of geophysical and geochemical observations established for the global ridge system. In this section we discuss the implications of our results on the interpretation of crustal thickness variations, the seismic structure of the mantle beneath ridges, the chemistry of MORB, and the dynamics of melt migration.

1. Crustal Thickness Variation

The effect of spreading rate on crustal thickness depends on the magnitude of buoyant upwelling and the melt productivity. Buoyancy driven upwelling can be sufficient to inhibit conductive cooling, allowing melting to proceed to shallower depths. Previous studies have suggested that this effect is responsible for the lack of variation in crustal thickness with spreading rate [*Forsyth*, 1992; *Sotin and Parmentier*, 1989]. Alternatively, if melt productivity is higher, so that more melt is produced at greater depth (e.g. Figure 1b), then conductive cooling will have a smaller effect on the amount of melt produced. Therefore, for passive flow the influence of spreading rate on crustal thickness is smaller for higher melt productivites (Figure 6b).

The percentage of melt produced in the damp melting region increases with increasing buoyancy (β_z) for a variety of rheologic models. The increased role of buoyancy with decreasing spreading rate is reflected in a modest increase in the percent of melt produced in the presence of garnet with decreasing spreading rate (Figure 6d). We assume that all melt generated at pressures greater than 2.5 GPa is produced in the presence of garnet.

2. Interpretation of Seismic Data

Rheology has a significant effect on the predicted size and shape of the melting region and the finite strain distribution beneath the ridge at a given spreading rate. Our model results provide a basis to interpret the observed dimensions of the melting region and seismic anisotropy. The size of the melting region determined from the Mantle Electromagnetic and Tomography (MELT) experiment along the East Pacific rise is consistent with passive-like flow [*Forsyth et al.*, 1998a; *Toomey et al.*, 1998]. Our models suggest that, for geophysically constrained values of mantle viscosity, the large lateral extent of the melting region results from the transition to passive-like flow due to the effects of dehydration (compare Figures 3b, c, and 4a).

Our models also illustrate a possible explanation for the apparent inconsistency between the magnitudes of anisotropy interpreted from shear wave splitting and surface wave analyses of anisotropy in the MELT region. Although the relationship between lattice preferred orientation and finite strain is not fully resolved, the direction and degree of anisotropy is coupled to the orientation and magnitude of finite strain, especially at large strains [*Wenk et al.*, 1989; *Zhang and Karato*, 1995]. The finite strains calculated from these models can be used to predict lattice-preferred orientation, and therefore, seismic anisotropy in the mantle [*McKenzie*, 1979; *Ribe*, 1989]. Rayleigh wave data from the MELT region [*Forsyth et al.*, 1998b] imply less anisotropy than that determined from body waves [*Wolfe and Solomon*, 1998]. The short (25 s) period surface waves are sensitive

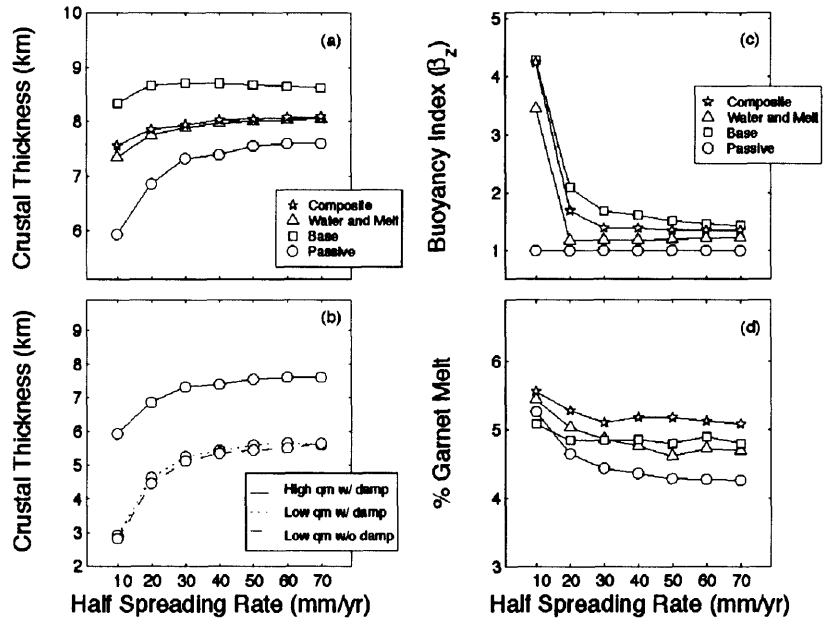

Figure 6. Characteristic model results as a function of spreading rate. (a) Variation in crustal thickness with spreading rate for the 'base' (□), 'composite' (★), 'dehydration and melt' (△), and high viscosity passive (○) rheologies assuming complete extraction of melt. (b) Effects of melt productivity on the variation in crustal thickness for the high viscosity passive rheology. 2%/kb (solid line) with damp melting, 1%/kb with damp melting (dashed line), and 1%/kb without damp melting (dotted line). (c) Buoyancy index as a function of spreading rate . (d) Percentage of melt generated in the presence of garnet. Crustal thickness is constant, except at very slow spreading rates, for rheologies which promote buoyant upwelling. The thinner crust for the composite and dehydration and melt models relative to the base rheology is due to the restriction of buoyant upwelling to depths below the dry solidus. By removing the effects of buoyancy (by using a high reference viscosity) the crustal thickness is decreased further and becomes more strongly spreading rate dependent. Crustal thickness increases with increased productivity. The decrease in crustal thickness with decreasing spreading rate occurs at higher spreading rates for lower productivities. Finally, the percentage of melt produced in the presence of garnet is greatest at slow spreading rates or for rheologies that limit buoyancy to the damp melting region.

to anisotropy only within the upper 100 km, whereas body waves integrate over greater depth. The 'hidden' anisotropy indicated by the shear wave splitting can be associated with the buoyant flow in the damp melting region (Figure 5c). A preferred alignment of melt pockets can also contribute to seismic anisotropy [e.g. *Blackman et al.*, 1996; *Zimmerman et al.*, 1999]. However, we emphasize that the strong horizontal fabric in the depth interval of 100-150 km occurs outside the melting region where melt has likely been extracted.

Variation in the arrival times of vertically-incident body waves and the magnitude of anisotropy should increase at slower spreading rates. Strong vertical elongation directions resulting from increased buoyancy driven flow at slow spreading rates could result in earlier arrival times, relative to an isotropic medium, for vertically propagating waves directly beneath the ridge axis (Figure 5a). Similarly, strong horizontal elongation directions would induce later arrival times off-axis. Therefore, variations in arrival times should be greatest at slow spreading rates. In addition, greater horizontal elongation with decreasing spreading rate could lead to a detectable increase in the magnitude of anisotropy between 50-120 km. If this lattice-preferred orientation is incorporated into the lithosphere as it thickens by conductive cooling, then the anisotropy in old lithosphere may be greater for lithosphere created at slower spreading rates.

3. Geochemistry of MORB

Damp melting that generates near-fractional, small-degree melts at depths between 70 and 120 km is consistent with geochemical constraints from radiogenic isotopic ratios and rare earth element (REE) patterns in MORB glasses and melt inclusions. In the presence of garnet, melting at these depths can explain the $^{176}Hf/^{177}Hf$ and $^{143}Nd/^{144}Nd$ excesses [*Salters and Hart*, 1989], light-REE-enriched trace element patterns [*Hirschmann and Stolper*, 1996], and secular disequilibria observed among uranium-series isotopes ($^{230}Th/^{238}U$ and $^{226}Ra/^{230}Th$) [*Beattie*, 1993; *Salters and Longhi*, 1999] in MORB. Buoyant focusing of mantle flow and melt generation below 70 km (Figure 4a-c) could enhance these garnet signatures. As the spreading rate decreases, buoyancy localizes melt production beneath the axis, increasing the likelihood that this melt will be extracted to form crust at the ridge axis, regardless of the mechanism of melt migration. In addition a greater fraction of the total melt produced is derived from the damp melting region (Figure 6f). Therefore, as spreading rate decreases, the garnet signatures observed in MORB may be more pronounced. However the mean pressure of melting appears to be controlled

predominantly by melt productivity and varies only by 10-30 MPa for the range of rheology and spreading rates examined in this study.

4. Mantle Flow and Melt Migration

A change from 2- to 3-dimensional convective structure in the shallow mantle has been suggested as an explanation for the morphologic and geophysical characteristics of fast and slow spreading ridges [*Jha et al.*, 1994; *Parmentier and Phipps Morgan*, 1990]. The length-scale of segmentation at slow spreading ridges and wavelength of 'bulls-eye' mantle Bouguer anomalies derived from along-axis variation in crustal thickness [*Lin and Phipps Morgan*, 1992] have been attributed to 50-100 km wavelength convective instabilities in the upper mantle [*Kuo and Forsyth*, 1988; *Lin et al.*, 1990]. However 3-dimensional models with simpler rheologies do not generate such short wavelength instabilities [*Barnouin-Jha et al.*, 1995]. In our models (Figure 5), the increase in viscosity associated with dehydration decreases the column height over which buoyant flow occurs [*Choblet and Parmentier*, 2001]. The shorter column height could lead to shorter along-axis wavelengths of buoyant upwelling.

The viscosity structure produced by dehydration can also influence melt migration. Pressure gradients induced by 'corner flow' associated with plate spreading can result in ridgeward melt migration if the viscosity in the melting region were on the order of 10^{21} Pa·s [*Phipps Morgan*, 1987; *Spiegelman and McKenzie*, 1987]. The viscosity increase associated with dehydration can result in viscosities in this range over the majority of the melting region.

Conclusions

This series of numerical models demonstrates the importance of rheology and melt productivity on crustal production and the dynamics of mantle flow beneath mid-ocean ridges.

Owing to the effects of dehydration, buoyant circulation is limited to depths beneath the dry solidus despite a substantial retained melt fraction. This is significant if the mantle viscosity is sufficiently small (~10^{18} Pa·s); a viscosity this low can be achieved if a transition to grain boundary sliding occurs after the onset of damp melting.

We also examine the spreading rate dependence of models that incorporate more realistic rheologies and deep, damp melting. The crustal thickness calculated in these models varies with spreading rate only at very low spreading rates, as is observed in

available seismic data. This invariance is due to a buoyancy enhanced flux of mantle through the melting region and an increased melt productivity deep in the melting column. Strain accumulation calculations indicate that a significant lattice-preferred orientation would develop as deep as 150 km, as a result of buoyant flow in the damp melting region. The magnitude of this effect increases with decreasing spreading rate, indicating that the seismic properties observed at the ridge and anisotropy preserved in the lithosphere could also vary systematically with spreading rate.

Acknowledgments:

The authors would like to thank Kopal Barnouin-Jha for her early work in developing the computer code and Peter Kelemen, Marc Spiegelman, Chad Hall, and Marc Hirschmann for their enthusiasm and assistance during the course of this project. We would also like to thank Donna Blackman and Shun-Ichiro Karato for their provocative comments during review. This work was funded in part by NSF graduate research fellowship 2277600 and grants EAR-9405845 and OCE-9521113.

Bibliography:

Asimow, P., M. Hirschmann, and E. Stolper, An analysis of variations in isentropic melt productivity, *Phil. Tran. Roy. Soc. London, A, 355*, 255-281, 1997.

Barnouin-Jha, K., Mantle convection and melt generation: theoretical studies of flow in the shallow mantle, PhD thesis, Brown University, Providence, RI, 1996.

Barnouin-Jha, K., E.M. Parmentier, and D.W. Sparks, Buoyant mantle upwelling and crustal production at oceanic spreading centers: on-axis segmentation and off-axis melting, *J. Geophys. Res., 102*, 11,979-11,989, 1995.

Beattie, P., Uranium- thorium disequilibria and partitioning on metling of garnet peridotite, *Nature, 363*, 63-65, 1993.

Bell, D.R., and G.R. Rossman, Water in earth's mantle: the role of nominally anhydrous minerals, *Science, 255*, 1391-1397, 1992.

Blackman, D.K., J.-M. Kendall, P.R. Dawson, H.-R. Wenk, D. Boyce, and J. Phipps-Morgan, Teleseismic imaging of subaxial flow at mid-ocean ridges: traveltime effects of anisotropic mineral texture in the mantle, *Geophys. J. Int., 127*, 415-426, 1996.

Cheadle, M.J., The physical properties of texturally equilibrated partially molten rocks, *Eos, 74*, 283, 1993.

Choblet, G., and E.M. Parmentier, Mantle upwelling and melting beneath slow spreading centers; effects of variable rheology and melt productivity, *Earth Planet. Sci. Lett., 184* (3-4), 589-604, 2001.

Christensen, U., Convection with pressure- and temperature-dependent non-newtonian rheology, *Geophys. J. Roy. Astr. Soc., 77*, 343-381, 1984.

Cooper, R.F., and D.L. Kohlstedt, Sintering of olivine and olivine-basalt aggregates, *Phys. Chem. Mineral, 11*, 5-16, 1984.

Dick, H.J.B., and R.L. Fisher, Mineralogic studies of the residues of mantle melting: Abyssal and alpine-type peridotites, in *Kimberberlites II: the mantle and crust - mantle relationships*, edited by J. Kornprobst, pp. 295-308, Elsevier, 1984.

Evans, R.L., A.D. Chave, G. Heinson, A. WHite, H. Tob, T. Goto, H. Utada, P. Tarits, N. Seama, K. Baba, J.H. Filloux, M. Unsworth, and J. Booker, The MELT experiment electromagnetic data: preliminary inverson and modeling results, *Eos*, *79*, S232, 1998.

Faul, U.H., Permeability of partially molten upper mantle rocks from experiments and percolation theory, *J. Geophys. Res.*, *102*, 10,299-10,311, 1997.

Forsyth, D.W., Geophysical constraints on mantle flow and melt generation beneath mid-ocean ridges, in *Mantle flow and melt generation beneath mid-ocean ridges*, edited by J.P. Morgan, D.K. Blackman, and J.M. Sinton, pp. 1-66, American Geophysical Union, 1992.

Forsyth, D.W., Crustal thickness and the average depth and degree of melting in fractional melting models of passive flow beneath mid-ocean ridges, *J. Geophys. Res.*, *98*, 16-73-16079, 1993.

Forsyth, D.W., D.S. Scheirer, S.C. Webb, L.M. Dorman, J.A. Orcutt, A.J. Harding, D.K. Blackman, J.P. Morgan, R.S. Detrick, Y. Shen, C.J. Wolfe, J.P. Canales, D.R. Toomey, A.F. Sheehan, S.C. Solomon, and W.S.D. Wilcock, Imaging the deep seismic structure beneath a mid-ocean ridge: The MELT experiment, *Science*, *280*, 1215-1218, 1998a.

Forsyth, D.W., S.C. Webb, L.M. Dorman, and Y. Shen, Phase velocity of rayleigh wave in the MELT experiment of the east pacific rise, *Science*, *280*, 1235-1238, 1998b.

Gaherty, J.B., M. Kato, and T.H. Jordan, Seismological structure of the upper mantle: a regional comparison of seismic layering, *Earth Planet. Sci. Lett.* *110*, 21-41, 1999.

Hirschmann, M.M., and E.M. Stolper, A possible role for garner pyroxenite in the origin of the "garnet signature" in MORB, *Contrib. Mineral. Petrol.*, *124*, 185-208, 1996.

Hirth, G., and D.L. Kohlstedt, Experimental constraints on the dynamics of the partially molten upper mantle 2. Deformation in the dislocation creep regime, *J. Geophys. Res.*, *100*, 15,441-15,449, 1995a.

Hirth, G., and D.L. Kohlstedt, Experimental constraints on the dynamics of the partially molten upper mantle: Deformation in the diffusion creep regime, *J. Geophys. Res.*, *100*, 1981-2001, 1995b.

Hirth, G., and D.L. Kohlstedt, Water in the oceanic upper mantle: implications for rheology, melt extraction and the evolution of the lithsphere, *Earth Planet. Sci. Lett.*, *144*, 93-108, 1996.

Jha, K., E.M. Parmentier, and J. Phipps-Morgan, The role of mantle-depletion and melt-retention buoyancy in spreading-center segmentation, *Earth Planet. Sci. Lett.* *125*, 221-234, 1994.

Karato, S.-I., Does partial melting reduce the creep strength of the upper mantle?, *Nature*, *319*, 309-310, 1986.

Karato, S.-I., M.S. Paterson, and J.D. FitzGerald, Rheology of synthetic olivine aggregates: Influence of grain size and water, *J. Geophys. Res.*, *91*, 8151-8176, 1986.

Kelemen, P.B., G. Hirth, N. Shimizu, M. Spiegelman, and H.J.B. Dick, A review of melt migration processes in the adiabatically upwelling mantle beneath spreading ridges, *Phil. Trans. Roy. Soc., Lond. A*, *355*, 283-318, 1997.

Kohlstedt, D.L., H. Keppler, and D.C. Rubie, Solubility of water in a, b, and g phases of $(Mg,Fe)_2SiO_4$, *Contrib. Mineral. Petrol.*, *123*, 345-357, 1996.
Kohlstedt, D.L., and M.E. Zimmerman, Rheology of partially molten mantle rocks, *Ann. Rev. Earth Planet. Sci.*, *24*, 41-62, 1996.
Kuo, B.-Y., and D.W. Forsyth, Gravity anomalies of the ridge-transform system in the south atlantic between 31 and 34.5 degrees South: Upwelling centers and variations in crustal thickness, *Marine Geophy. Res.*, *10*, 205-232, 1988.
Langmuir, C.H., E.M. Klein, and T. Plank, Petrological systematic of mid-ocean ridge basalts: Constraints on melt generation beneath ocean ridges, in *Mantle flow and melt generation beneath mid-ocean ridges*, edited by J.P. Morgan, D.K. Blackman, and J.M. Sinton, pp. 183-281, American Geophysical Union, 1992.
Lin, J., and J. Phipps Morgan, The spreading rate dependence of three-dimensional mid-ocean ridge gravity structure, *Geophys. Res. Lett.*, *19*, 13-16, 1992.
Lin, J., G.M. Purdy, H. Schouten, J.-C. Sempere, and C. Zervas, Evidence from gravity data for focused magmatic accretion along the mid-Atlantic ridge, *Nature*, *344*, 627-632, 1990.
McKenzie, D., Finite deformation during fluid flow, *Geophys. J. Roy. Astr. Soc.*, *58* (3), 689-715, 1979.
McKenzie, D., and M.J. Bickle, The volume and composition of melt generated by extension of the lithosphere, *J. Petrol.*, *29*, 625-679, 1988.
McKenzie, D., and R.K. O'Nions, Partial Melt Distributions from Inversion of Rare Earth Element Concentrations, *J. Petrol.*, *35* (5), 1021-1091, 1991.
Mercier, J.-C., Magnitude of the continental lithospheric stresses inferred from rheomorphic petrology, *J. Geophys. Res.*, *85*, 6293-6303, 1980.
Nicolas, A., and F. Boudier, Mapping oceanic ridge segments in Oman ophiolite, *J. Geophys. Res.*, *100*, 6179-6197, 1995.
Oxburgh, E.R., and E.M. Parmentier, Compositional and density stratification in the oceanic lithosphere --causes and consequences, *J. Geol. Soc. Lond.*, *133*, 343-354, 1977.
Parmentier, E.M., and J. Phipps Morgan, Spreading rate dependence of three-dimensional structure in oceanic spreading centers, *Nature*, *348*, 325-328, 1990.
Phipps Morgan, J., Melt migration beneath mid-ocean spreading centers, *Geophys. Res. Lett.*, *14*, 1238-1241, 1987.
Phipps Morgan, J., The generation of a compositional lithosphere by mid-ocean ridge melting and its effect on subsequent off-axis hotspot upwelling and melting, *Earth Planet. Sci. Lett.*, *146*, 213-232, 1997.
Reid, I., and H.R. Jackson, Oceanic spreading rate and crustal thickness, *Marine Geophys. Res.*, *5*, 165-172, 1981.
Ribe, N.M., Seismic Anisotropy and mantle flow, *J. Geophys. Res.*, *94*, 4213-4223, 1989.
Salters, V.J.M., and S.R. Hart, The hafnium paradox and the role of garnet in the source of mid-ocean-ridge basalts, *Nature*, *342*, 420-422, 1989.
Salters, V.J.M., and J. Longhi, Trace element partitioning during the initial stages of melting beneath mid-ocean ridges, *Earth Planet. Sci. Lett.*,, *166*, 15-30, 1999.
Smolarkiewicz, P.K., A fully multidimensional positive definite advection transport algorithm with small implicit diffusion, *J. Comp. Phys.*, *54*, 325-362, 1983.

Sotin, C., and E.M. Parmentier, Dynamical effects of compositional and thermal density stratification beneath spreading centers, *Geophys. Res. Lett.*, *16*, 835-839, 1989.

Spiegelman, M., and D. McKenzie, Simple 2-D models for melt extraction at mid-ocean ridges and island arcs, *Earth Planet. Sci. Lett.*,, *83*, 137-152, 1987.

Toomey, D.R., W.S.D. Wilcock, S.C. Solomon, W.C. Hammond, and J.A. Orcutt, Mantle Seismic structure beneath the MELT region of the east pacific ridge from P and S wave tomography, *Science*, *280*, 1224-1227, 1998.

Toramaru, A., and N. Fujii, Connectivity of melt phase in a partially molten peridotite, *J. Geophys. Res.*, *91*, 9239-9252, 1986.

Turcotte, D.L., and J.L. Ahern, A porous flow model for magma migration in the asthenosphere, *J. Geophys. Res.*, *83*, 767-772, 1978.

Van der Wal, D., Deformation processes in mantle peridotites, PhD Thesis, University of Utrecht, Utrecht, 1993.

Von Bargen, N., and H.S. Waff, Permeabilities, interfacial areas and curvatures of partially molten systems: results of numerical computations of equilibrium microstructures, *J. Geophys. Res.*, *91*, 9261-9276, 1986.

Wenk, H.-R., G. Canova, A. Molinari, and U.F. Kocks, Viscoplastic modeling of textural development in quartzite, *J. Geophys. Res.*, *94*, 17895-17906, 1989.

Wolfe, C.J., and S.C. Solomon, Shear-wave splitting and implications for mantle flow beneath the MELT region of the east pacific rise, *Science*, *280*, 1230-1232, 1998.

Zhang, S., and S.-I. Karato, Lattice preferred orientation of olivine aggregates deformed in simple shear, *Nature*, *375*, 774-777, 1995.

Zimmerman, M.E., S. Zhang, D.L. Kohlstedt, and S.-I. Karato, Melt distribution in mantle rocks deformed in shear, *Geophys. Res. Lett.*, *26*, 1505-1508, 1999.

Chapter 6

Implications of Chemical and Microstructural Variations in Dunite Conduits on the Permeability and Melt Flux Beneath Mid-Ocean Ridges

Introduction

The segregation and transport of basaltic melt from its source deep beneath mid-ocean ridges is both efficient and rapid. Although mid-ocean ridge basalt (MORB) is an mixture of near-fractional melts derived over a range of pressures [*Johnson et al.*, 1990; *McKenzie and O'Nions*, 1991], the major element composition of primitive basalts, which form the bulk of the oceanic crust, implies that these primitive liquids traverse the uppermost 20-30 km of the mantle without significant chemical interaction with the rocks through which they pass [*Elthon*, 1989; *O'Hara*, 1965; *Stolper*, 1980]. Additionally, ^{230}Th excesses observed in recently erupted lavas indicate that some melts are segregated from their source at depths greater than 75 km and ascend to the surface with rates on order of a meter per year [e.g. *Beattie*, 1993; *McKenzie*, 1985; *Sims et al.*, 2002].

Geochemical and petrologic data from abyssal and ophiolitic peridotites suggest that dunites (rocks with > 90% olivine) accommodate the chemically-isolated transport of primitive melts to the surface via porous flow [*Kelemen et al.*, 1997]. Dunites are ubiquitous in residual mantle peridotites and often exhibit compositions in equilibrium with primitive MORB [*Braun and Kelemen*, in prep; *Dick*, 1977; *Kelemen et al.*, 1995]. These geochemical data, in conjunction with field observations [e.g. *Braun and Kelemen*, 2002; *Kelemen et al.*, 2000], and numerical models [*Aharonov et al.*, 1995; *Spiegelman et al.*, 2001] indicate that dunites are the remnants of high porosity channels formed from harzburgite by reactive porous flow of basaltic melt.

By constraining the permeability of dunites, we can address whether an interconnected network of porous dunite conduits can deliver the volume of unequilibrated melts required to form the oceanic crust on timescales short enough to preserve the excess ^{230}Th. Permeability estimates are derived from a combination of field

and microstructural observations from dunites in the Oman ophiolite. The extensive exposures of gabbroic crust and residual mantle peridotite in the Oman ophiolite were created at a submarine spreading center [e.g. *Nicolas et al.*, 2000]. The geochemical characteristics observed in Oman peridotites closely follow those documented in abyssal peridotites [*Godard et al.*, 2000; *Kelemen et al.*, 1997] suggesting that the igneous processes which formed the Oman rocks are similar to those that occur beneath mid-ocean ridges. Additionally, the Oman ophiolite offers extensive outcrops which preserve structural details impossible to observe in active spreading environments.

Observations regarding the widths of dunites and their grain size distributions in Oman can be used to constrain the permeability and melt capacity of the transport network. First, measurements of dunite widths in the mantle section of the ophiolite constrain the size and distribution of porous conduits which comprise the network [*Braun and Kelemen*, 2002]. Dunites in the Samail, Wadi Tayin, and Muscat massifs of the Oman ophiolite range in size from several millimeters to approximately 100 m wide. In these regions, a power-law relationship exists between the width of dunites and their abundance. Extrapolation of the power-law successfully predicts the abundance of wide dunites on length scales of entire massifs, providing confidence that the additional extrapolation to mid-ocean ridge length scales probably represents the dunite abundance in the melting region.

Additionally, microstructural analyses on the same peridotites document an increase in grain size with dunite width, likely induced by increased melt migration prior to corner flow [*Braun and Hirth*, in prep]. The significant increase in grain size observed across harzburgite/dunite boundaries is consistent with laboratory experiments which show that the increase in olivine mass associated with opx dissolution results in an increase in olivine grain size during reaction [*Daines and Kohlstedt*, 1994]. Normal grain growth [e.g.*Atkinson*, 1988] can account for much of the grain size variation once dunite formation is complete, because the pinning orthopyroxene phase has been removed [*Olgaard and Evans*, 1986]. The time required for normal grain growth [*Karato*, 1989]

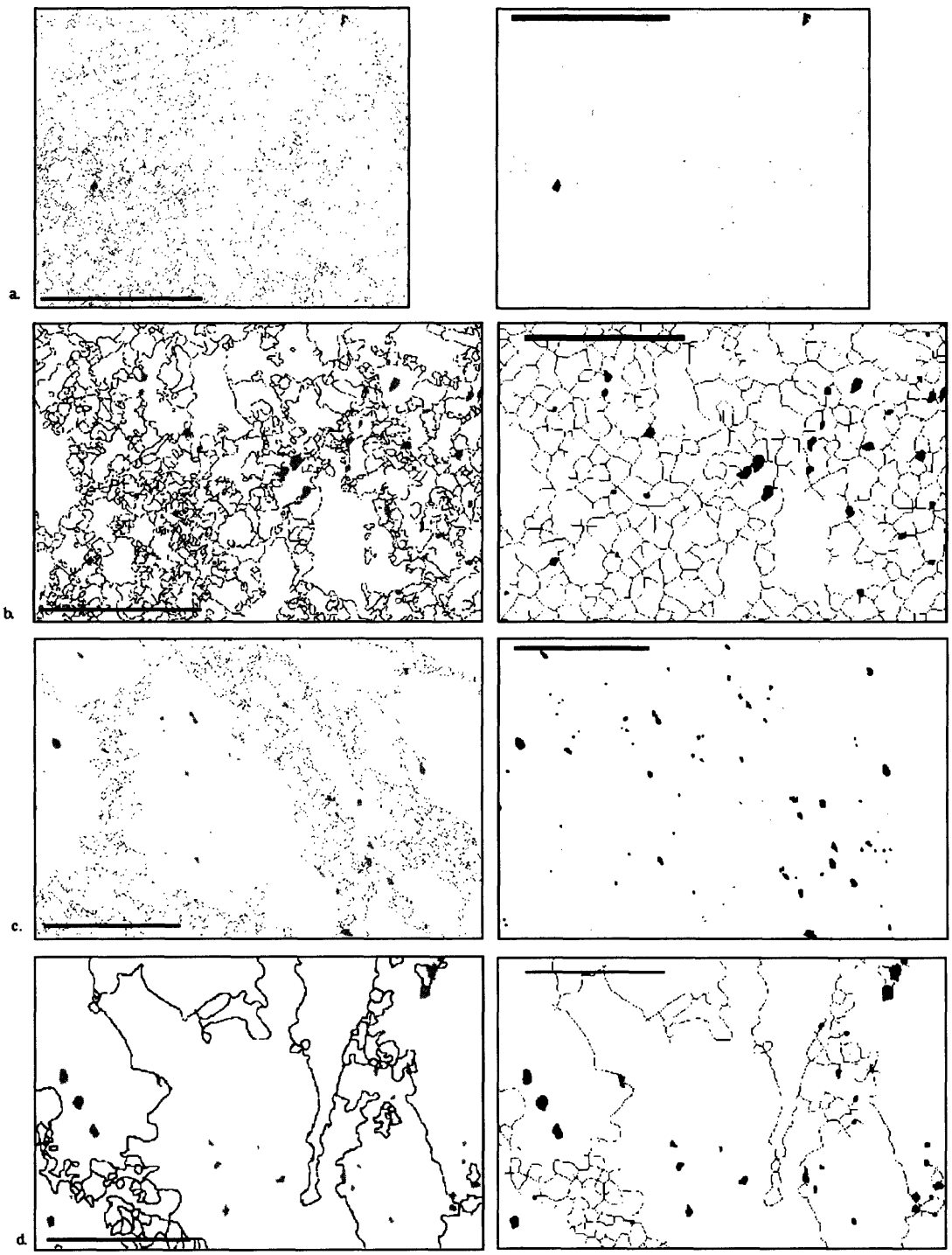
a.
b.
c.
d.

Figure 1. Grain boundary images of representative thin sections from the (a) harzburgite, (b) 3 m wide dunite, (c) 25 m wide dunite, (d) 50 m wide dunite. Images in the left column are traced directly from the thin section. Images in the right column are the result of the grain growth algorithm described in the text. Scale bar in all images is 10 mm. Black represents spinel, white is olivine, and gray is orthopyroxene

to produce grains as large as the observed maxima is well within the ascent time of peridotite in the melting region [*Braun and Kelemen*, 2002]. Even though the peridotite was deforming during its ascent, the common occurrence of spinel and small olivine inclusions within large olivine grains (figure 1) suggests that grain boundary mobility was greatly enhanced, perhaps by the presence of melt, mitigating the grain size reduction effects of dynamic recrystallization [*Braun and Hirth*, in prep].

These grain size variations in conjunction with the dunite abundances are what best constrain the permeability of the porous dunite conduits. Grain sizes were measured from grain boundary images and have been corrected for thin-sectioning and the effects of low temperature recrystallization to better represent the actual grain size distribution under asthenospheric conditions. In an attempt to remove the abundant small grains associated with dynamic recrystallization at high stress and low temperature [*Karato et al.*, 1980; *Van der Wal et al.*, 1993], the edges of grains were "eroded" using image analysis techniques until olivines smaller than 1 mm were removed. The eroded grains were then dilated, restoring the remaining grains to their original size. This threshold grain size of 1 mm was chosen because it reflects the boundary between dislocation and diffusion creep at the conditions at which the rocks were deformed (1200°C, 1MPa differential stress, and a strain rate of 10^{-14} s^{-1}) as inferred from lattice preferred orientations [*Braun and Hirth*, in prep].

The effects of the dynamic recrystallization correction on representative thin sections with different grain size distributions are illustrated in figure 1. Fine-grained regions exhibit a more uniform grain size and euhedral shapes. The size of large grains is virtually unaffected, however, short wavelength undulations in grain boundaries are smoothed. The dynamic recrystallization correction changes the grain size distributions

as well (figure 2). To convert the measured (apparent) grain size to a more representative 3-dimensional grain size, we multiply the grain sizes by 1.5 [*Pannozo*, 1982; *Gunderson and Jensen*, 1983; *Renner et al.*, 2003]. Figure 2a depicts the corrected grain size data as a function of dunite width. Although the variations in mean and median grain size, observed in the raw data, have been obscured by the dynamic recrystallization correction, the maximum grain size still clearly exhibits an increases from 4.5 mm in the harzburgite to 12, 29, and 39 mm in the 3, 25 and 50 m wide dunites, respectively. However, percolation theory indicates that the maximum grain size is not likely the primary control on permeability. Instead, the permeability of porous aggregates with non-uniform grain sizes is better represented by the "backbone" grain size, which is what remains after truncating the largest and smallest grains from the distribution. Lacking an accurate analytical or empirical relationship between the grain size distribution and permeability, I have chosen to use the grain size which defines 50% of the cumulative area of the sample (figure 2b) as representative of the aggregate in the Kozney-Carmen permeability relationship [e.g. *Von Bargen and Waff*, 1986; *Wark and Watson*, 1998]. In the Oman peridotites, 50% of the sample is occupied by grain smaller than 2.25 in the harzburgite and 4.8, 7.4, and 10.95 mm in the 2, 25, and 50m dunites, respectively.

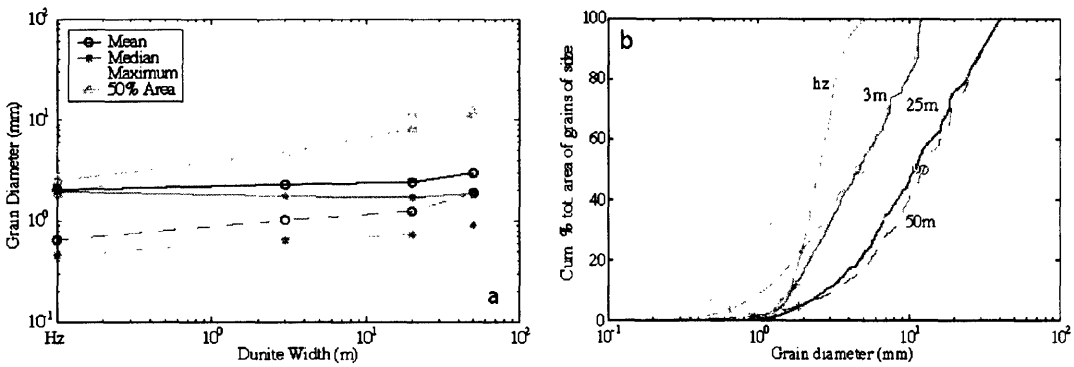

Figure 2. Increase in grain size with increasing dunite width as shown by several statistical measures. (a) Variation in mean, median, maximum, and '50% area' grain size. Dashed lines indicate the measured values and solid lines indicate grain sizes corrected for the effects of dynamic recrystallization at high stress. (b) Cumulative area as function of grain size. * denotes the median grain size in each population. O designates the grain size above and below which 50% of the total area is occupied.

Permeability and the Melt Flux in a Dunite Network

1. Constraints on Dunite Permeability

Hierarchical interconnection is typical of coalescing tributary systems observed in nature, from river basins [e.g. *Dodds and Rothman*, 2000; *Tokunaga*, 1978] to arterial systems [e.g. *Schreiner et al.*, 1997] and have also been observed in dissolution channeling experiments [*Hoefner and Fogler*, 1988]. The spatial distribution of dunites, the clustering behavior in particular, suggests that dunites are also hierarchically interconnected with respect to their size, forming a coalescing network. The overall percentage of dunite in the mantle section of the Oman ophiolite is 5-15%, however, the dunites appear to be arranged in clusters with proportions approaching 40-70% of the peridotite locally. Clusters typically contain a few large dunites which are surrounded and intersected by smaller dunites, which are in turn connected to even smaller dunites. Deformation associated with corner flow and obduction has substantially reduced the intersection angles between dunites, and in several cases, dunites cross each other. However, given the uncertainties in the orientation of the dunites relative to the spreading center under which they formed, we infer from their spatial distribution that the dunites formed a coalescing network of channels which focused melt transport to the ridge axis.

Within this context of a coalescing network, Braun and Kelemen [*Braun and Kelemen*, 2002] derive a method for estimating the total melt flux that the dunites can supply, given the abundances measured in the field. In the following section, I expand upon that analysis by incorporating the grain size data and comparing the resultant permeability and flux estimates to the volume and velocity constraints required by crustal thickness and ^{230}Th excesses in MORB.

The total melt flux through a network of interconnected, porous dunites can be estimated by integrating the predicted flux in a dunite of a given width with the observed abundance of dunites that width. The 2-dimensional flux (area per unit time per unit length) in an individual dunite, J_w, can be defined as

$$J_w = \phi v w , \qquad (1)$$

which is the product of the dunite width, w, and the Darcy flux

$$\phi v = \frac{K}{\eta}\Delta\rho g, \qquad (2)$$

where $\Delta\rho g$ is the driving pressure gradient owing to melt buoyancy, η is the melt viscosity, and the permeability, K, is a function of porosity, ϕ, grain size, d, and geometry, C:

$$K = \frac{\phi^n d^2}{C}. \qquad (3)$$

Empirical determination of rock permeabilities indicate that n=3 and C=200 [*Wark and Watson*, 1998], which is consistent with the laboratory estimates of Renner et al. [*Renner et al.*, 2003]. The viscosity of basalt is on the order of 10 Pa·s [*Bottinga and Weill*, 1972].

For Oman, Braun and Kelemen [2002] show that the number of dunites, f_w, within a length scale, L, is related to the width of the dunite, w, by the power-law relationship

$$f_w = \frac{aD}{w^{D+1}}L \qquad (4)$$

where D is the ratio of narrow dunites to wide dunites and a is constant which reflects the percentage of dunite within the mantle. By definition, the fraction of dunite within L meters is

$$\frac{1}{L}\int_{w_{min}}^{w_{max}} f_w w dw. \qquad (5)$$

Figure 3 shows the predicted relationship between a and the percentage of dunite in a given outcrop along with the measured abundances in each of the locations used for the power-law determination. The prediction fits the majority of the dunite abundance measurements quite well. The two "apparent" exceptions to the prediction, from the airphoto (17% dunite) and from Lufti outcrop #10 (68% dunite), can both be fit by adjusting the prediction parameters to those specific for the outcrop rather than using the mean values for all Oman. First, both datasets have higher D values than the rest of the regions analyzed [*Braun and Kelemen*, 2002]. Additionally the abundance prediction depends on the range in dunite width used for integration. Despite the large variation in the true dunite size distribution as observed on the ground, only dunites wider than

several meters can be accurately resolved in the airphoto. Using the values for listed in Braun and Kelemen [2002] and integrating only over dunites from 5 to 100 m, the prediction passes through the data point (dashed line). Outcrop #10 is small and contains only a few dunites which span a small range in width. Reintegration of (5) with more appropriate values of D, w_{min} and w_{max} moves the predicted curve toward the data point. The remaining misfit between the data and the prediction likely reflects error in the estimates of D and a from such a small sample of the population, as indicated by the low correlation coefficient obtained for the fit.

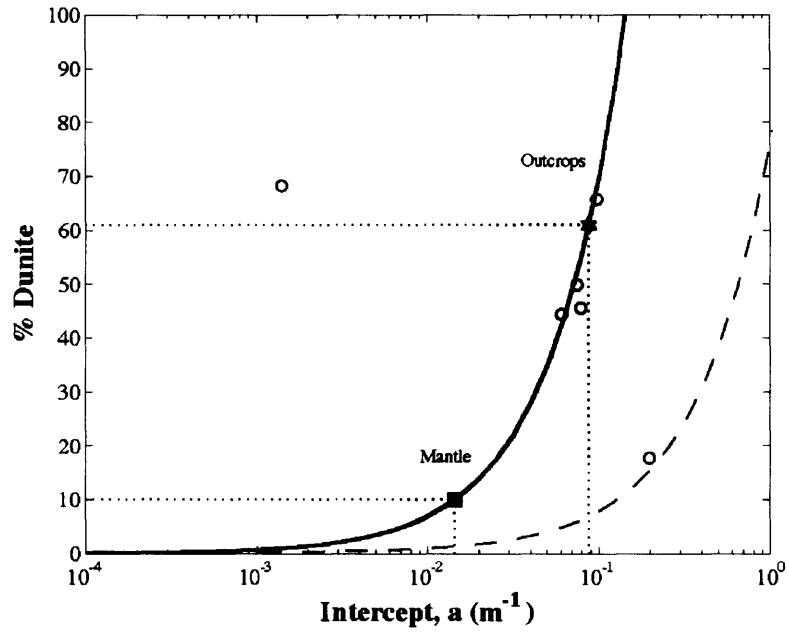

Figure 3. Percentage of dunite in outcrop as a function of 'intercept' value, a, in the power-law size/frequency distribution (eqn 4). Circles indicate the abundance of dunite in each of the data sets used in fitting the power-law and the associated value of a [*Braun and Kelemen*, 2002]. The solid line is the theoretical prediction based on D=1.11 and dunites ranging from 0.1 to 100 m wide. The mean a as reported by Braun and Kelemen is shown with a ✱. The intercept value given a dunite abundance of 10% in the mantle is shown with a ■. Dashed line is the predicted abundance curve for the airphoto data. See text for description.

Because the dunite size/frequency statistics were collected from regions in which the local proportion of dunite (20-70%) was much higher than the average for the whole mantle section (5-15%), the power-law "intercept" value, a, is corrected to 0.015 to approximate the regional dunite proportion.

The total melt flux can thus be expressed as the product of the melt flux J_w, and the number of dunites, f_w, integrated over the observed range in dunite widths, or

$$J_{tot} = \int_{w_{min}}^{w_{max}} f_w J_w dw . \qquad (6)$$

2. Network Permeability Models

In this section, the permeability distributions predicted by each of four models are used to compute the total unequilibrated melt flux to the ridge and velocity at which that melt is transported in comparison to the observed geophysical and geochemical constraints. Based on the dunite distribution data, Braun and Kelemen introduce two permeability models for the solution of (3): one in which both porosity and grain size are constant and independent of dunite width and another in which flux conservation requires that the porosity varies with dunite width. However, the textural observations from Oman indicate that grain size, d, also varies with dunite width, and should be incorporated into the permeability distribution.

If all melt is transported via dunites, then the observed oceanic crustal thickness requires that the dunite network supply a flux of 60-900 m^3/yr of melt per meter of ridge axis, depending on spreading rate [*Braun and Kelemen*, 2002]. Because of the pyroxene-undersaturated bulk composition of primary MORB, a large fraction of the total melt flux in dunites must remain isolated from chemical interaction with the surrounding harzburgite. Based on the inferred time scale for upwelling beneath the Oman paleo-spreading center and dunite porosities less than 5%, the minimum dunite width which can maintain the major element disequilibrium is approximately 5 m [*Braun and Kelemen*, 2002]. Additionally, if ^{230}Th excesses are created by small degrees of melting in the presence of garnet [e.g. *Beattie*, 1993], then melts must segregate from their source at small porosities and migrate to the surface from 75-120 km depth in less than 5 half-lives of ^{230}Th ($t_{1/2}$=75,380 yr). This isotopic constraint requires melt velocities of 0.2-1.2 m/yr. A viable flux model must satisfy all three of these requirements.

Model 1: The simplest permeability model is one in which both grain size and porosity are constant in all dunites and the melt flux varies linearly with width. Using a

grain size of 2 mm, as is observed in the harzburgites in Oman, integration of (1) predicts the total melt flux through a dunite network is sufficient to create the oceanic crust provided dunites have porosities of ~2-6% (figure 4a). With 3% porosity, the permeability of a dunite is ~$5x10^{-13}$ m^2 independent of width (figure 5a). At this level of permeability the melt velocity is 0.27 m/yr (figure 5b), barely satisfying the velocity constraint required by the ^{230}Th excesses. With a porosity greater than 6% or grain size larger than 4 mm, the melt velocities exceed 1 m/yr. However, regardless of porosity or grain size, the fraction of the total flux which would remain unequilibrated is only 22%, implying that primary MORB traveling through such a network would not be far from pyroxene saturation.

Model 2: Incorporating the observed grain size variations with dunite width increases the permeability and melt flux in wide dunites. The textural data from the Oman dunites (figure 2) show a power-law dependence of grain size on dunite width of the form

$$d = pw^m \qquad (7)$$

where p=0.004 and m=0.2268, derived from a least-squares fit to the "50% area" data (figure 2a). Substituting (7) into (3) and reintegrating (6) yields higher total melt flux than Model 1 and fits the mid-ocean ridge flux constraints at lower porosities (figure 4b). The ~5-fold increase in grain size increases the permeability of wide dunites from $5.3x10^{-13}$ to $1.7x10^{-11}$ m^2 (with ϕ=3%), allowing melt velocities to easily exceed the ^{230}Th-excess constraint in all dunites wider than a few centimeters (figure 5b). However, the fraction of unequilibrated flux still only accounts for ~67% of the total melt flux.

Model 3: By incorporating the requirement that melt flux is conserved where dunites coalesce, Braun and Kelemen, [2002] derived a dependence of porosity on dunite width of the form

$$\phi = \phi_{\max}\left(\frac{w}{w_{\max}}\right)^{D/n}. \qquad (8)$$

By fixing the maximum porosity, ϕ_{max}, in the widest observed dunite, w_{max} (100 m in Oman), the porosities in dunites of all other widths are specified. Since the majority of

the flux in this model is passing through wide dunites, the fraction of unequilibrated melt is 95% of the total (figure 4c). However, the total melt flux is lower than either Model 1 or 2 because the porosity, and therefore the permeability (figure 5a), is smaller in narrower dunites. Therefore, the mid-ocean ridge flux constraint is met only at large porosities (ϕ_{max}> 6%).

It is possible, at the porosities which satisfy the crustal production requirement (ϕ_{max}> 6%), to get melt velocities within the range required by the Th data. Such high porosities are larger than those inferred for the distributed porosity in shallow mantle beneath mid-ocean ridges, [e.g. *Forsyth*, 1992; *Toomey et al.*, 1998], but would be undetectable if confined within bodies less than 100 m across [*Hung et al.*, 2000]. However, the high porosities would result in a either a substantial viscosity reduction and localized strain in the wide dunites or high compaction rates [*Renner et al.*, 2003] and rapid expulsion of the melt from the dunite. Based on laboratory experiments, the effective viscosity, $\eta = \eta_{ref} \exp(-\alpha\phi)$ of a dunite with ϕ=6% would be a factor of 8 lower than a melt-free olivine aggregate η_{ref} (α=30-40) [*Hirth and Kohlstedt*, 2003; *Hirth and Kohlstedt*, 1995]. Localized deformation in the dunites as a result of a viscosity reduction is inconsistent with the porphyroclastic and coarse granular textures observed in the wide dunites [*Braun and Hirth*, in prep]. Rather than plastic deformation of the solid, high porosities can increase the compaction rate such that the volumetric strain rate due to the expulsion of melt exceeds that of the deforming solid. The volumetric strain rate,

$$\dot{\varepsilon} \approx \frac{K}{\mu \delta_c} \Delta P,$$

is dependent upon the permeability, K, the melt viscosity, μ, and the length scale, δ_c, over which a pressure gradient, ΔP, can be transmitted. The compaction length scale as defined by [*McKenzie*, 1984] is

$$\delta_c = \sqrt{\frac{\eta}{\mu} K}.$$

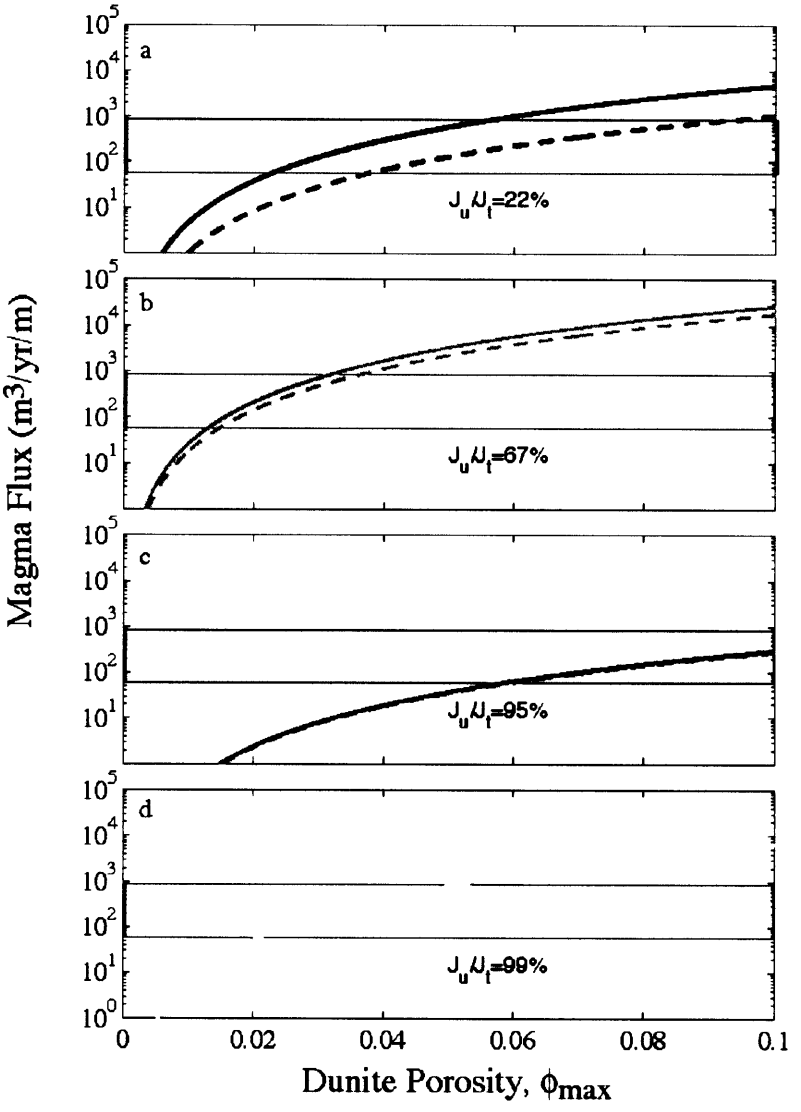

Figure 4. Total flux as a function of porosity through an interconnected network of dunites with the abundances measured in Oman for four different permeability models as compared to the observed mid-ocean ridge magma flux (gray box). The total melt flux through the network, J_t, is shown as a solid line, and the unequilibrated melt flux, J_u, (defined in the text) is shown as a dashed line. a) Model 1: Given a constant grain size (d=2mm) and porosity in all dunites, the fraction of unequilibrated melt (J_u/J_t) is only 22%. (b) Model 2: With constant porosity, and grain size dependent on dunite width (7), the total flux increases and 67% of the flux remains unequilibrated. (c) Model 3: Grain size is constant (d=2mm) and porosity varies with dunite width as described by (8). The x-axis defines the maximum porosity in the widest dunite. The total flux is smaller but more remains unequilibrated. (d) Model 4: Total flux when both grain size and porosity vary with dunite width (9). In this model, the mid-ocean ridge fluxes are matched at moderate porosities and nearly all the flux remains unequilibrated.

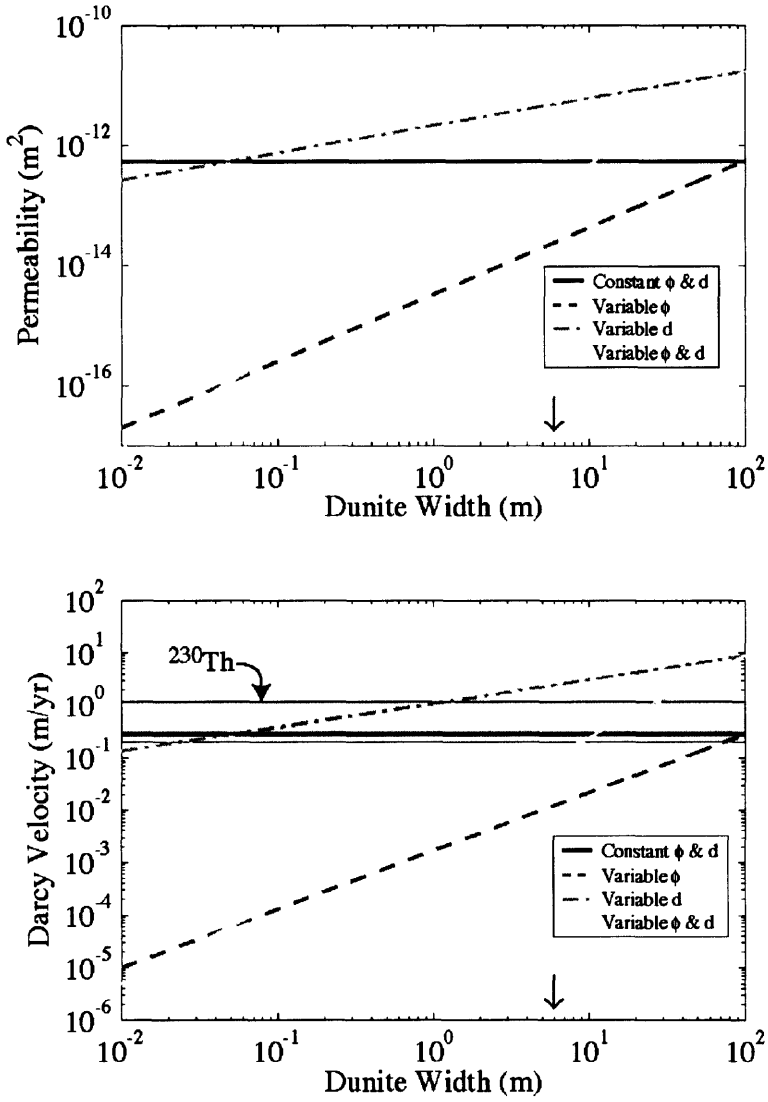

Figure 5. (a) Permeability and (b) velocity for each of the four models. In all cases, the porosity (or maximum porosity) is 3% and the grain size is 2 mm where held constant. Only the model which incorporates grain size and porosity variations satisfies both the melt velocity constraints imposed by the observation of ^{230}Th excesses (gray box) and maintains a significant fraction of unequilibrated melts (figure 4).

For ϕ=6%, μ=40 Pa·s, and $\Delta P=\Delta\rho g$, the compaction length is ~2 km and $\dot{\varepsilon}=8\text{x}10^{-12}$ s^{-1}. Therefore, dunites would compact at a rate more than 800 times faster than the surrounding mantle is deforming (~10^{-14} s^{-1}), rapidly expelling melt and reducing the porosity. Smaller porosities would mitigate the viscosity reduction and/or compaction

rate effects. However, the melt velocities would fall well below those required by the magma flux (figure 4c) and ^{230}Th excess (figure 5b) constraints.

Model 4: To account for the observed grain size variations as well as the flux conservation constraints, Model 4 combines the grain size variation with dunite width with the porosity variations inferred from the dunite size/frequency statistics. Substituting both (7) and (8) into (3) and reintegrating (6) yields

$$J_{tot} = \frac{DaL\Delta\rho g}{\eta C} \frac{\phi_{\max}^{n} p^{n}}{w_{\max}^{D}(2m+1)} \left[w_{\max}^{2m+1} - w_{\min}^{2m+1} \right]. \qquad (9)$$

The porosity decrease with decreasing width reduces the total melt flux relative to Model 2, satisfying the mid-ocean ridge flux requirement over a wide range of ϕ_{max} (2-5%) (figure 4d). Additionally, ~99% of the total melt flux remains unequilibrated because of the high permeabilities (figure 5a) associated with the combined porosity and grain size increases. As a result, the melt velocities meet or exceed the ^{230}Th velocity constraints in all dunites greater than ~8 m wide even with only 3% porosity in the widest dunite (figure 5b).

3. Uncertainties in Dunite Grain Size and Abundance

This thesis represents the first systematic investigation of dunite microstructure, composition, distribution, and abundance. However, these data are not complete and thus the permeabilities models presented here accompanied by two key uncertainties. First, the characterization of the olivine grain size distributions is limited to only a few dunites which makes definitive correlations with dunite width difficult. Second, the exact proportion of dunites in the shallow mantle is unknown [*Kelemen et al*, 1997]. In light of these uncertainties, we can estimate the sensitivity of the calculations presented above on the assumed grain size and dunite proportion.

It is uncertain whether or not the small grains in wide dunites (e.g. figure 1c) were part of the high temperature deformation texture and therefore present when the dunite was an active melt conduit. Although grains smaller than ~2 mm exhibit an LPO with the same sense of shear as large grains and consistent with deformation at geologic strain

rates (~10^{-14} s^{-1}) by dislocation-accommodated grain boundary sliding at 1000-1300°C [*Braun and Hirth*, in prep], it is possible that they formed during dynamic recrystallization at much lower temperature (800-1000°C) and commensurately higher stress (~100-10 MPa, respectively). If it were the case that the small grains formed after the dunites were active melt conduits, then the large grains in the wide dunites directly reflect the grain size which controls the permeability rather than the area-defined value reported here.

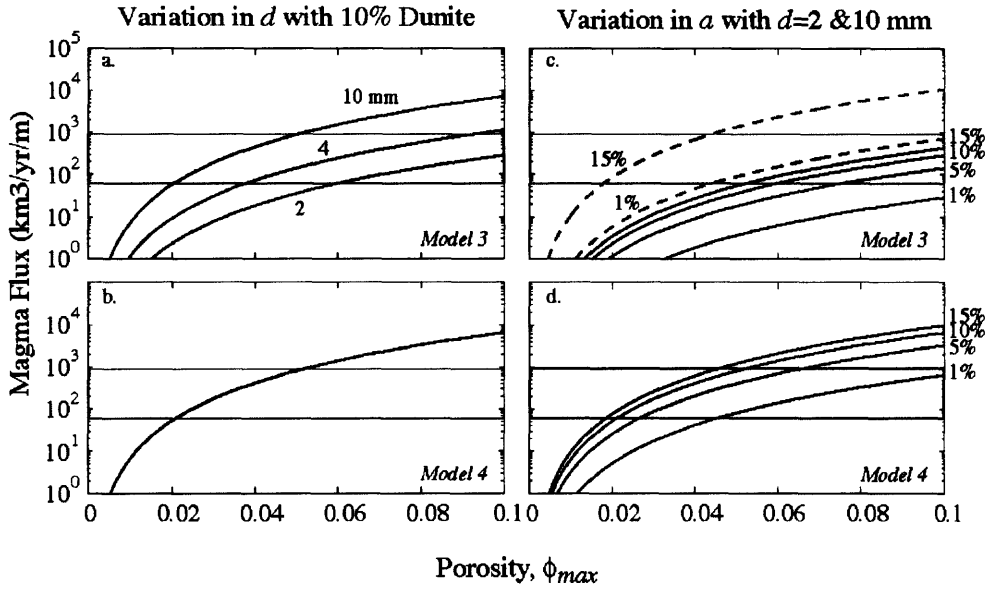

Figure 6. Changes in the unequilibrated melt flux relative to the estimated ridge flux (gray box) based on potential variations in the permeability model. For reasonable variations in grain size and dunite abundance, a interconnected network of dunites can supply an adequate magma flux to form the oceanic crust. Increasing olivine grain size, *d*, increases the flux in (a) the constant grain size model relative to (b) the model in which grain size varies with width as measured in thin section. For either (c) a fixed grain size or (d) a power-law grain size distribution, increasing the total percentage of the mantle occupied by dunites increases the total flux. Solid lines are for d=2 mm, dashed for d=10 mm. Even if dunites represent only 1% of the shallow mantle, Model 4 still satisfies the mid-ocean ridge melt flux constraints.

Figure 6 a&b examines the effects of variations in grain size on the melt flux assuming a fixed dunite abundance of 10%. Increasing the grain size from 2 to 10 mm increases the total melt flux predicted by Model 3 by nearly two orders of magnitude. If the wide dunites are populated entirely by grains ~10 mm in diameter, then a maximum porosity of only 2-5% in the widest dunites is required to satisfy the mid-ocean ridge

magma flux constraint. In contrast, if the dunite grain size is only 2 mm, then the required porosities would be significantly higher, as discussed above. The melt flux predicted by Model 4 would remain unchanged, since the grain size is assumed to be a function of the dunite width. Insufficient data exist to better constrain the potential variation in the power-law exponent, m, in (7). With the current observations, Model 4 satisfies the mid-ocean ridge melt flux constraint with maximum porosities in the widest dunites between approximately 2 and 5%.

Dunite abundance as measured directly from field observations range from 5-15% averaged over the available exposures in Oman [Boudier, 1981 #210; Lippard, 1986 #211], with higher proportions of dunite in individual clusters [Braun, 2002 #6422]. However, Kelemen et al [, 1997 #32] argue that the transposed mantle near the base of the crust contains the core of what previously was the upwelling mantle in the melting region. Therefore, the dunites observed in the field may well represent all the dunites that existed in the melting region. If the exposed stratigraphic thickness in Oman is about 10% of the total height of the melting column, then the abundance of dunites in the melting region may be as low as 1%.

Figure 6 c&d illustrates the effect of dunite abundance on the predicted flux of unequilibrated melt. If the total proportion of dunites in the melting region were as low 1% then Model 3 could not satisfy the mid-ocean ridge magma flux constraint at realistic porosities. However, if the grain size were 10 mm then a mantle with 1% dunite could match the observed ridge flux. In the case where both grain size and porosity vary as function of dunite width, a mantle with 1% dunite could meet the observed ridge flux, but porosities in wide dunites would be quite large, especially at fast spreading ridges.

4. Independent Melt Flux Constraints

The inferred increase in melt flux associated with the increase in permeability is consistent with the geochemical composition of dunites which provide a proxy for the amount of melt which passed through them [*Braun and Kelemen*, in prep]. Analyses of dunites from Oman show systematic variations in composition with dunite width. With

increasing width, the olivine Mg# decreases, the Ni content drops and both the TiO_2 content and Cr# of spinels increase markedly. The widest dunites have compositions which are in major, minor, and to a lesser extent, trace element equilibrium with the liquid parental to the Oman basalts.

Mass balance calculations for interaction between residual harzburgite and the liquid parental to the Oman lavas can reproduce these systematic variations with increasing amounts of melt-rock reaction. Reactive porous flow dissolves orthopyroxene (opx), precipitates olivine, and increases the liquid mass [*Kelemen*, 1990], all of which is recorded by variations in the olivine Mg#. Because of its relatively high Mg#, the dissolution of opx contributes more Mg than Fe to the remaining phases. Additionally, based on the relative partitioning of Fe and Mg between melt and olivine [*Gaetani and Grove*, 1998], Mg is preferentially incorporated into the olivine while the liquid becomes an increasingly large reservoir for Fe. Because opx has only a trace amount of Ni, the increase in olivine mass by reaction serves only to dilute the NiO concentration. Additionally, the contribution of Cr from the dissolving opx and the liquid dramatically increases the spinel Cr# during reaction. Once opx dissolution is complete, interaction of the resulting dunite with an increasing volume of melt drives the Mg# and NiO content down toward equilibrium with the primitive liquid. Similarly, the TiO_2 content in the spinel increases until it reaches equilibrium with the primitive liquid. While the composition of the narrow dunites suggests only about 1-2 times the rock mass in liquid passed through, the composition of the widest dunites is consistent with time-integrated melt-rock ratios as high as 1000.

The range in the time-integrated melt-rock ratio inferred from geochemistry is larger than that predicted solely by variations in permeability. The melt-rock ratio over the life of the dunite is up to 10^3 times larger in wide dunites than narrow ones. However, the instantaneous melt flux as inferred from the permeability is only ~100 times larger in wide dunites. Therefore, large dunites must form earlier (i.e. deeper in the melting column) and remain active longer than small ones. This notion is consistent with dunite growth with time by reaction along their margins and with grain growth models

which require more time to grow the larger grains in wider dunites. Additionally, the formation of high permeability dunites high in the melting column

Conclusions

Dunite size/frequency statistics coupled with observed systematic grain size variations in Oman peridotites provide a framework to determine the melt capacity of a network of porous dunite conduits and their ability to preserve major element disequilibrium with the shallow mantle and excess radiogenic ^{230}Th observed in MORB. Four permeability models are examined with respect to their ability to satisfy these chemical and volumetric constraints. The model in which both porosity and grain size vary systematically with dunite width produces both an unequilibrated melt flux sufficient to generate 6 km of oceanic crustal gabbro and the high melt velocities required to maintain ^{230}Th excesses with sustainable maximum porosities consistent with microstructural constraints. The grain size and dunite width distributions imply that the permeability of dunites ranges from less than 10^{-16} m^2 for dunites narrower than 100 cm to as high as 10^{-11} m^2 in dunites 100 m wide. Based on the distribution of porosity and grain size in a interconnected network of porous dunites which conserve flux, the bulk of the melt transport is accommodated in conduits with permeabilities between $1.5x10^{-13}$ and $1.7x10^{-11}$ m^2.

Bibliography

Aharonov, E., J.A. Whitehead, P.B. Kelemen, and M. Spiegelman, Channeling instability of upwelling melt in the mantle, *J. Geophys. Res.*, *100*, 20,433-20,450, 1995.

Atkinson, H.V., Theories of normal grain growth in pure single phase systems, *Acta Metall.*, *36*, 469-491, 1988.

Beattie, P., Uranium-thorium disequilibria and partitioning on melting of garnet peridotite, *Nature*, *363*, 63-65, 1993.

Bottinga, Y., and D.F. Weill, The viscosity of magmatic silicate liquids: a model for calculation, *Amer. J. Sci.*, *272*, 438-475, 1972.

Braun, M.G., and G. Hirth, Microstructural Evolution in Naturally-Deformed Dunites: Grain Boundary Sliding and the Strength of the Shallow Mantle, *J. Geophys. Res.*, in prep.

Braun, M.G., and P.B. Kelemen, Dunite distribution in the Oman Ophiolite; implications for melt flux through porous dunite conduits, *Geochem., Geophys., Geosyst., 3* (11), 21, 2002.

Braun, M.G., and P.B. Kelemen, Dunites as conduits for primitive melt transport: Inferences from the geochemistry of Oman peridotites, *J. Geophys. Res.*, in prep.

Daines, M.J., and D.L. Kohlstedt, Transition from porous to channelized flow due to melt/rock reaction during melt migration, *Geophys. Res. Lett., 21*, 145-148, 1994.

Dick, H.J.B., Partial melting in the Josephine Peridotite; I, The effect on mineral composition and its consequence for geobarometry and geothermometry, *Amer. J. Sci., 277* (7), 801-832, 1977.

Dodds, P.S., and D.H. Rothman, Scaling, universality, and geomorphology, *Ann. Rev. Earth Planet. Sci., 28*, 571-610, 2000.

Elthon, D., Pressure of origin of primary mid-ocean ridge basalts, in *Magmatism in the Ocean Basins*, edited by A.D. Saunders, and M.J. Norry, pp. 125-136, Geological Society, 1989.

Forsyth, D.W., Geophysical constraints on mantle flow and melt generation beneath mid-ocean ridges, in *Mantle flow and melt generation beneath mid-ocean ridges*, edited by J.P. Morgan, D.K. Blackman, and J.M. Sinton, pp. 1-66, American Geophysical Union, 1992.

Gaetani, G.A., and T.L. Grove, The influence of water on melting of mantle peridotite, *Contrib. Mineral. Petrol., 131*, 323-346, 1998.

Godard, M., D. Jousselin, and J.-L. Bodinier, Relationships between geochemistry and structure beneath a paleo-spreading center: a study of the mantle section in the Oman ophiolite, *Earth Planet. Sci. Lett., 180*, 133-148, 2000.

Gunderson, H.J.G., and E.B. Jensen, Particle sizes and their distribution etimated rom line- adn point-sampled intercepts, *J. Microsc., 131*, 291-310, 1983.

Hirth, G., and D. Kohlstedt, L., Rheology of the upper mantle and the mantle wedge: a view from the experimentalists, in *The Subduction Factory*, edited by J.M. Eiler, 2003.

Hirth, G., and D.L. Kohlstedt, Experimental constraints on the dynamics of the partially molten upper mantle 2. Deformation in the dislocation creep regime, *J. Geophys. Res., 100*, 15,441-15,449, 1995.

Hoefner, M.L., and H.S. Fogler, Pore evolution and channel formation during flow and reaction in porous media, *AlChE Journal, 34*, 45-54, 1988.

Hung, S.-H., D.W. Forsyth, and D.R. Toomey, Can a narrow, melt-rich, low-velocity zone of mantle upwelling be hidden beneath the East Pacific Rise? Limits from waveform modeling and the MELT experiment, *J. Geophys. Res., 105* (4), 7945-7960, 2000.

Johnson, K.T.M., H.J.B. Dick, and N. Shimizu, Melting in the oceanic upper mantle: an ion microprobe study of diopsides in abyssal peridotites, *J. Geophys. Res., 95*, 2661-2678, 1990.

Karato, S.-I., Grain growth kinetics in olivine aggregates, *Tectonophysics, 168*, 255-273, 1989.

Karato, S.-I., M. Toriumi, and T. Fjuii, Dynamic recrystallization of olivine single crystals during high-temperature creep, *Geophys. Res. Lett.*, *7*, 649-652, 1980.

Kelemen, P.B., Reaction between ultramafic rock and fractionating basaltic magma. I. Phase relations, the origin of calc-alkaline magma series, and the formation of discordant dunite, *J. Petrol.*, *31*, 51-98, 1990.

Kelemen, P.B., M. Braun, and G. Hirth, Spatial distribution of melt conduits in the mantle beneath oceanic spreading ridges; observations from the Ingalls and Oman ophiolites, *Geochem., Geophys., Geosyst., 1*, 21 (paper number 1999GC000012), 2000.

Kelemen, P.B., G. Hirth, N. Shimizu, M. Spiegelman, and H.J.B. Dick, A review of melt migration processes in the adiabatically upwelling mantle beneath spreading ridges, *Phil. Trans. Roy. Soc., Lond. A*, *355*, 283-318, 1997.

Kelemen, P.B., N. Shimizu, and V.J.M. Salters, Extraction of mid-ocean ridge basalt from the upwelling mantle by focused flow of melt in dunite channels, *Nature*, *375*, 747-753, 1995.

McKenzie, D., The generation and compaction of partially molten rock, *J. Petrol.*, *25*, 713-765, 1984.

McKenzie, D., 230Th-238U disequilibrium and the melting processes beneath ridges axes, *Earth Planet. Sci. Lett.*, *72*, 149-157, 1985.

McKenzie, D., and R.K. O'Nions, Partial Melt Distributions from Inversion of Rare Earth Element Concentrations, *J. Petrol.*, *35* (5), 1021-1091, 1991.

Nicolas, A., F. Boudier, B. Ildefonse, and E. Ball, Accretion of Oman and United Arab Emirates ophiolite - Discussion of a new structural map, *Marine Geophys. Res.*, *21*, 147-179, 2000.

O'Hara, M.J., Primary magmas and the origin of basalts, *Scot. J. Geol.*, *1*, 19-40, 1965.

Olgaard, D.L., and B. Evans, Effect of second-phase particles on grain growth in calcite, *J. Am. Ceram. Soc.*, *69* (11), 272-277, 1986.

Pannozo, R., Determination of size distributions of spheres from size distributions of circular sections by Monte Carlo methods, *Microscopia Acta*, *86*, 37-48, 1982.

Renner, J., K. Viskupic, G. Hirth, and B. Evans, Melt extraction from partially molten peridotites, *Geochem., Geophys., Geosyst.*, *4* (5), 2003.

Schreiner, W., F. Neumann, M. Neumann, R. Karch, A. End, and S.M. Roedler, Limited bifurcation assymetry in coronary arterial tree models generated by constrained constructuve optimization, *J. Gen. Physiol.*, *109*, 129-140, 1997.

Sims, K.W.W., S.J. Goldstein, J. Blichert-Toft, M.R. Perfit, P. Kelemen, D.J. Fornari, P.J. Michael, M.T. Murrell, S.R. Hart, D.J. DePaolo, G.D. Layne, L. Ball, M. Jull, and J.F. Bender, Chemical and isotopic constraints on the generation and transport of magma beneath the East Pacific Rise, *Geochim. Cosmochim. Acta*, *66* (19), 3481-3504, 2002.

Spiegelman, M., P.B. Kelemen, and E. Aharonov, Causes and consequences of flow organization during melt transport: The reaction infiltration instability, *J. Geophys. Res.*, *106*, 2061-2078, 2001.

Stolper, E., A phase diagram for mid-ocean ridge basalts: preliminary results and implications for petrogenesis, *Contrib. Mineral. Petrol.*, *74*, 13-27, 1980.

Tokunaga, E., Consideration on the composition of drainage networks and their evolution, *Geograph. Rep. Tokyo Metro. Univ.*, *13*, 1-27, 1978.

Toomey, D.R., W.S.D. Wilcock, S.C. Solomon, W.C. Hammond, and J.A. Orcutt, Mantle Seismic strcutre beneath the MELT region of the east pacific ridge from P and S wave tomography, *Science*, *280*, 1224-1227, 1998.

Van der Wal, D., P. Chopra, M. Drury, and J. Fitz Gerald, Relationships between dynamically recrystallized grain size and deformation conditions in experimentally deformed olivine rocks, *Geophys. Res. Lett.*, *20* (14), 1479-1482, 1993.

Von Bargen, N., and H.S. Waff, Permeabilities, interfacial areas and curvatures of partially molten systems: results of numerical computations of equilibrium microstructures, *J. Geophys. Res.*, *91*, 9261-9276, 1986.

Wark, D.A., and E.B. Watson, Grain-scale permeabilities of texturally equilibrated, monomineralic rocks, *Earth Planet. Sci. Lett.*, *164* (3-4), 591-605, 1998.